Investigating the causes of silo honking during discharge

Jesus Chavez-Sagarnaga

Doctor of Philosophy

The University of Edinburgh
May 2005

Abstract

Vibration phenomena in thin metal silos during discharge are associated with a range of problems. Vibrations cause noise pollution and in some cases structural failure. This study focuses on one such phenomena, commonly called "silo honking". Honking refers to intermittent high frequency sounds, similar to a truck horn, that predominantly cause noise pollution. Honking has commonly been reported to occur in tall metal silos designed for mass flow containing polymer granulates at higher stress levels.

An industrial honking silo was extensively instrumented to examine its wall vibration and acoustic response. Spectral analyses of the acceleration and acoustic pressure measurements showed that honking comprises of a fundamental acoustic frequency and a harmonic series of peaks at integer multiples of the fundamental frequency. The results indicated that the sound is generated by the silo walls acting as large speakers and is not due to resonance inside the silo, as in a flute or organ pipe.

The measurements also indicated that during honking the silo vibrates in some of its specific natural modes. Finite element (FE) models were used to examine the free vibration characteristics of the instrumented silo and other silos that were known to honk. Both 3D and axisymmetric models were considered. Considerable attention was focused on the latter as excitations that may cause honking are expected to be axisymmetric. In addition closed form solutions on vibration characteristics of thin cylindrical shells were discussed. The latter were used to develop an understanding of free vibration characteristics and to validate the FE models. The FE models of the simple cylindrical shell were transformed to a real silo structure by incorporating the addition of features such as roof, hopper and thickness variations. The influence of

these implementations was examined. It was found that the introduction of hopper and the roof introduced additional modes and thickness variation made a small change to the natural frequencies. Additionally the influence of the bulk solid stored in the silo was also considered. The analyses indicated that during honking the stored solid is uncoupled from the shell.

Two different sources of excitation that are thought to lead to honking were examined. While pulsating flow was considered using previous studies, slip-stick was examined using Jenike shear tester. Transient dynamic response of the silo structure due to the different locations and directions of pulse loads was examined using FE models. The results showed that dynamic loading on the silo hopper excites frequencies close to the honking fundamental frequency and its harmonics. This suggests that hopper excitation may be the source that leads to honking.

Publications

The following publications have resulted from this research and may be found in Appendix F.

1. Buick, J.M., Chavez-Sagarnaga, J., Zhong, Z., Ooi, J.Y., Pankaj, Campbell, D.M. and Greated, C.A. (2003) "Investigation of silo honking: slip-stick excitation and wall vibration" 16th ASCE Engineering Mechanics Conference, Seattle, paper 625.

2. Buick, J.M., Chavez-Sagarnaga, J., Zhong, Z., Ooi, J.Y., Pankaj, Campbell, D.M. and Greated, C.A. (2005) "Investigation of silo honking: slip-stick excitation and wall vibration" Journal of Engineering Mechanics ASCE, 131, 299-307.

3. Chavez-Sagarnaga, J., Buick, J.M., Ooi, J.Y., Pankaj, Campbell, D.M. and Greated, C.A. (2004) "Frictional properties of pellets and silo wall materials for the investigation of silo honking" Proc. Int. Congress for Particle Technology, PARTEC 2004 (Nuremberg, Ger., March 2004).

4. Buick, J.M., Chavez Sagarnaga, J., Ooi, J.Y., Pankaj, Campbell, D.M. and Greated, C.A. (2004) "Intermittent particle motion on the wall of a model silo during discharge" Proc. Int. Congress for Particle Technology, PARTEC 2004 (Nuremberg, Ger., March 2004).

5. Chavez-Sagarnaga, J. (2004) "Investigating the causes of silo honking during discharge" Presented at the Young Researchers' Conference, The Institution of Structural Engineers (London, England, March 2004).

6. Buick, J.M., Pankaj, Ooi, J.Y., Chavez-Sagarnaga, J., Pearce, A. and Houghton, G. (2004) "Motion of granular particles on the wall of a model silo and the associated wall vibration" J. Phys. D: Appl. Phys., 37, 2751-2760.

Acknowledgements

The author is deeply indebted to Dr. Pankaj not only for his supervision, expert guidance and support in this research work but also for his unconditional help in many personal issues.

The author is very thankful to Dr. Jin Y. Ooi for his supervision and for putting in motivational passion in this project.

The author thanks Dr. J. Mark Holst for his guidance at the beginning of this study.

The author also thanks Dr. James M. Buick for his help in analysis of field measurements data and for valuable discussions. Helpful discussions with Prof. D. Murray Campbell and Prof. Clive A. Greated are gratefully acknowledged.

The financial support provided by The Overseas Research Student Scheme (ORS Award), The School of Engineering and Electronics and my parents is gratefully acknowledged.

The author would like to thank Peter Moon and John Thorman for providing pellets for the laboratory tests. Thanks to Mark Astin for providing plates for the laboratory tests.

The author would like to acknowledge Tim Bell, John Carson, Paul Dean and Karl Jacob for sharing their valuable industrial experience and for helpful discussions during this study.

Thanks are also due to Mark Astin, Ron Dailey, Paul Denby, Michael Duerr, Paul Mayer, Colin Milton, Peter Moon, and John Thorman for many useful discussions throughout the course of this study.

Special thanks to Jesus Chavez Robles and Elvira Sagarnaga de Chavez, my parents, Liliana Chavez Sagarnaga, my sister, and Eloisa Mendoza de Lozano, my mother in law, for their encouragement and prayers. Thanks to the rest of my family and friends for the many types of support they have so kindly given to me.

Lastly I would like to thank my wife, Giovanna, and son, Leonardo, for their patience and endless love. I dedicate this thesis to them and my parents.

Thanks to God for giving me in every day a new motivation to live for.

Contents

List of Figures

List of Tables

Nomenclature

Roman characters

a	Acceleration of upper mass during pulse motion
A, B, C	Amplitude coefficients in the axial, circumferential and radial direction respectively
A_c	Cross section area of cylinder
A_d, R_d, C_d	Vibration of silo wall in the axial, radial and circumferential direction respectively
C_c	Amplitude coefficients in Rayleigh and Love displacement equations
d	Maximum particle linear dimension
D	Cylinder diameter
D_j	Jenike shear cell diameter
E	Young's modulus
f	Frequency in cycles per second
f_h	Honking fundamental frequency
f_p	Pulse frequency
f_r	Ring frequency
g	Gravity constant
h	Thickness
h_s	Effective surcharge head
h_{sh}	Head of material above plane of shock
H_{cr}	Critical height for mass flow occurrence
H_{sh}	Plane of shock height above transition
k	Nondimensional thickness parameter

k_h	Tan Θ
K	Lateral pressure ratio
K_s	Stiffness matrix
L	Cylinder length
L/mR	Axial wavelength parameter
m	Axial half wave number
M	Mass matrix
M_x	Bending moment
n	Circumferential wave number
N_x	Longitudinal membrane force
O_l	Outlet diameter of the hopper
p_{hf}	Wall normal pressure at depth z
p_{ho}	Wall pressure at infinite depth
p_{vf}	Mean vertical stress in solid at depth z
p_{vo}	Vertical stress in solid at infinite depth
p_{wf}	Wall frictional traction at depth z
P_n	Radial support within the stored material
Q	Discharge rate
R	Cylinder radius
Ra	Surface average roughness
SD	Shear Diaphragm boundary condition
t	Time
t_0	Time for motion of upper mass to be initiated
t_T	Total time in dynamic model
T	Period
T_p	Thickness of falling layer
u, v, w	Orthogonal components of displacement
v_p	Average velocity of bulk solid in the cylinder during discharge
x	Length coordinate
$\overline{x}$	Length coordinate measured from the centre section
$X_m(x)$	Beam function
z	Distance below the equivalent surface at full storage condition

z_0	Janssen reference depth

Greek characters

β	Hopper half angle
γ	Bulk unit weight
Δ_t	Time step in dynamic model
Δ_{cy}	Dynamic displacement of consolidated mass in the vertical direction
ε_0	Void fraction at outlet
ε_1	Void fraction at dynamic arch
θ	Rotation coordinate
θ_h	Hopper angle measured from horizontal to hopper wall
Θ	Internal angle of hopper
λ_m	Axial wavelength factor
μ	Wall friction coefficient
ν	Poisson's ratio
ρ	Unit density
ρ_{MAX}	Maximum bulk unit density
ρ_{MIN}	Minimum bulk unit density
ρ_s	Density of solid excluding voids
φ	Eigenvector (mode of vibration)
φ_i	Effective angle of internal friction
φ_w	Wall friction angle
ω	Frequency in radians per second
Ω	Frequency parameter

Chapter 1

Introduction

1.1 General

Huge quantities of bulk materials in the form of granular solids are handled each year throughout the world. During emptying from storage structures, many of these granular solids, such as plastic pellets (Tejchman, 1999), corn (Roberts and Wiche, 1991), coal (Levison and Munch-Andersen, 1994) and rape seeds (Tejchman and Gudehus, 1993) induce significant vibrations and dynamic loads on the storage systems. In addition to these dynamic loads, some thin-walled metal silos storing granular solids, such as PET pellets, nylon pellets and PVC powder, emit very loud intermittent honking sounds during discharge. This honking noise contains much higher frequencies and differs radically in nature from the periodic thumping or banging which can be heard in some silos during discharge. Honking of silos has been a fairly common industrial problem and has been known to exist in thin walled metal silos with differing dimensions and fills in a variety of locations worldwide. As noise pollution becomes increasingly unacceptable, silo honking has become an issue that needs to be addressed. Honking with sound pressure levels in excess of 100-110 dB can cause long term hearing damage if hearing protection is not worn. The intermittent nature of silo honking can cause an unexpected distraction and create further hazards. The noise can also create problems for the local population residing

close to industrial plants and in some cases, has been known to cause curtailment of normal silo operations (fill levels and operating hours).

In recent years, the dynamic effects during silo discharge have been studied to a limited extent and various descriptive terms such as silo vibration, silo quaking, silo music or silo shocks have been used (Roberts and Wiche, 1991; Gudehus and Tejchman, 1992; Roberts, 1993; Tejchman, 1995; Schulze, 1998). However all these studies predominantly focused on the additional dynamic loads induced on the silo structure during flow and did not address, to any significant extent, the acoustic aspects. Indeed a significant number of these studies were on concrete structures rather than on thin-walled metal silos in which honking occurs. A recent study (Tejchman, 1999) examined the displacement and acceleration response of the walls of a honking silo, but did not consider the causes of honking. The two main solutions proposed to date are the installation of waffle sheets (rough wall plates) or a central discharge tube. These silo modifications can be expensive to implement, interfere considerably with the industrial processes, are not well accepted by the industry due their complexity and, since they have been developed for specific silos without a comprehensive understanding of the phenomenon, they may not work in all situations. Moreover, waffle sheets change the flow pattern and introduce additional non-uniform loading on the silo walls that can have serious implications on the structural integrity of thin-walled metal silos. Several sources of the dynamic excitations in silos have been proposed (Gudehus and Tejchman, 1992; Roberts, 1993; Schulze, 1998; Tejchman, 1999). These include slip-stick behaviour between stored solids and silo walls, internal slip-stick behaviour within the stored solids, alternating flow patterns during flow, collapsing arches and solid dilation during flow.

1.2 Cylindrical metal silos

In this section the terminology and some basic aspects associated with cylindrical silo structures and the stored solid are presented. The aspects included are geometry of the silo structure, stored solid data, flow patterns and silo wall pressures.

1.2.1 Elemental geometry

The basic elements of cylindrical metal silos without columns are shown in Fig. 1.1. The range of forms of metal silos has a wide variation; the one shown is typical of the honking silos considered in this study. The terminology associated with Fig. 1.1 is as follows.

Cylindrical shell or barrel. The section with vertical parallel walls above the transition.

Hopper. The converging section at the bottom of a silo to gravitationally direct the solids to the outlet. Conical and wedge hoppers are the most common shapes.

Hopper half angle β. The angle between the vertical axis and the hoper wall.

Outlet. The opening at the bottom of the hopper where the granular solid is discharged.

Skirt. The lower part of the cylindrical shell below the transition.

Transition junction. It is the junction between the hopper and the cylindrical shell.

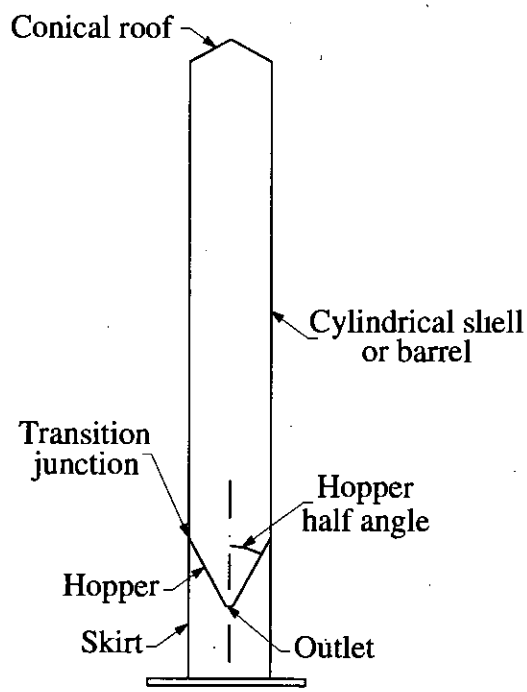

Figure 1.1: Elemental geometry in cylindrical silos.

1.2.2 Data on stored solids

The material properties of the stored solid influence the loads and pressures as well as the flow regimes in a silo. Some of these properties are described as follows.

Bulk unit density ρ. Bulk density is the mass of the bulk solid per unit volume and it is stress dependent. The maximum (ρ_{MAX}) and minimum (ρ_{MIN}) are important parameters for almost all aspects of the silo design. For example the maximum value is used to calculate silo pressures as well as outlet dimensions to avoid trouble flow situations.

Wall friction coefficient μ. The wall friction coefficient is the ratio of the maximum shear stress to the normal pressure on a surface for solid sliding on the silo wall. This parameter is used to calculate silo pressures, flow regimes and other parameters. A procedure for its measurement is described in IChE (1989). This procedure will also be discussed in Chapter 6. The wall friction coefficient μ is related to the wall friction angle φ_w as:

$$\mu = \tan \varphi_w \tag{1.1}$$

Lateral pressure ratio K. It is the ratio of the lateral pressure in the solid near the wall to the vertical pressure within the solid. It is also used to calculate pressures in silos and the Poisson's ratio "ν" using:

$$\nu = \frac{K}{1+K} \tag{1.2}$$

Effective angle of internal friction φ_i. The friction angle within the solid that governs its flow behaviour. It is used to assess, for example, hopper pressures. It is normally measured using the Jenike shear testing procedure described in IChE (1989).

Cohesion. The component of a particulate solid's shear strength, which is independent of the applied normal stress. This parameter is used in conjunction with some other hopper parameters to determine the flow behaviour of the stored solid. Free-flowing solids, such as plastic pellets, do not develop cohesion. Their response is purely frictional.

1.2.3 Flow patterns

Figure 1.2 shows different flow patterns in cylindrical silos. A brief explanation of each of these patterns is described next.

Mass flow. Flow pattern in which all particles are in motion during silo discharge (Fig. 1.2a). The criteria for mass flow to occur is shown in Fig. 1.3 (Rotter, 2001) for conical and wedge hoppers. It is important to note the uncertain region where either mass flow or funnel flow may occur.

Mixed flow. In this flow pattern stationary material rests against the wall in the lower part of the silo while in the upper part the stored solid moves across the entire cross section (Fig. 1.2b). The location of the upper limit of the stationary material on the silo wall is known as the effective transition.

Pipe flow. The particulate solid in motion is surrounded by stationary material, which forms a vertical or nearly vertical flow channel (Fig. 1.2c).

Expanded flow. This pattern is the combination of mass flow at the bottom of the hopper and funnel flow in the upper part (Fig. 1.2d).

Eccentric flow. The shape of eccentric flow varies depending of the conditions causing it. Figure 1.2e shows just one possible cause. Eccentric flow also occurs in the shape of internal pipe flow, mixed flow and pipe flow.

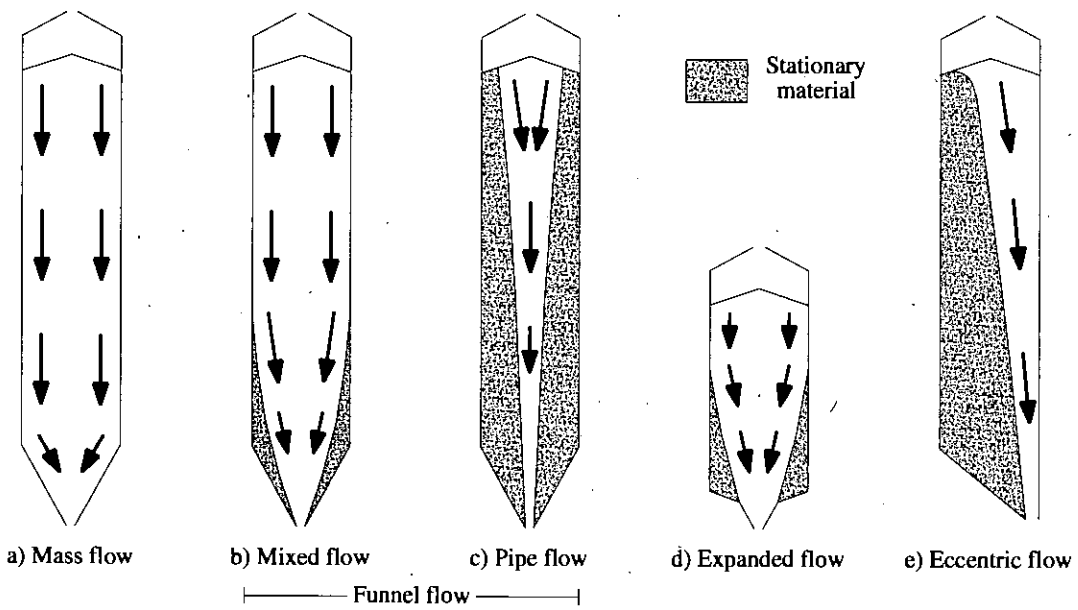

Figure 1.2: Flow patterns (redrawn from Rotter, 2001).

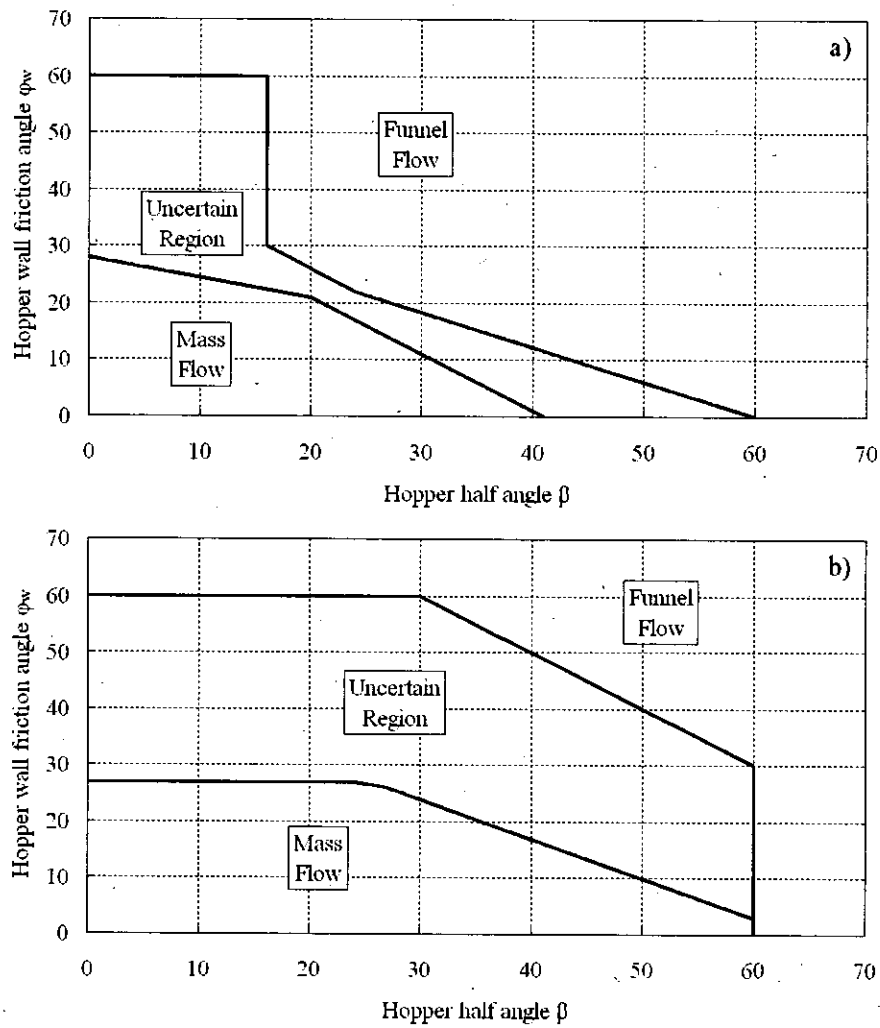

Figure 1.3: Mass flow and funnel flow bounds in a) conical and b) wedge hoppers (angles in degrees), after Rotter, 2001.

1.2.4 Pressures on silo wall

To calculate the pressures on the cylindrical barrel due to the particulate solid, the Janssen theory (Rotter, 2001) is the most commonly used. The behaviour of the stored solid depends on stress level and history. Thus the normal pressure on the silo barrel after symmetrical filling at distance z below the equivalent surface (Fig. 1.4) is given by:

$$p_{hf} = p_{ho}\left(1 - e^{-z/z_o}\right) \tag{1.3}$$

and the wall frictional traction at depth z is given by

$$p_{wf} = \mu p_{hf} = \mu p_{ho}\left(1 - e^{-z/z_o}\right) \tag{1.4}$$

and the mean vertical stress within the stored solid by:

$$p_{vf} = p_{vo}\left(1 - e^{-z/z_o}\right) \tag{1.5}$$

where

$$p_{ho} = \frac{\gamma R}{2\mu} \quad \text{(wall pressure at infinite depth)} \tag{1.6}$$

$$p_{vo} = \frac{\gamma R}{2K\mu} \quad \text{(vertical stress in solid at infinite depth)} \tag{1.7}$$

$$z_o = \frac{R}{2K\mu} \quad \text{(Janssen reference depth)} \tag{1.8}$$

and,

R is the circular silo radius

z is the distance below the equivalent surface at full storage condition (Fig. 1.4)

γ is the unit weight of the stored material ($\gamma = g\rho$)

μ is the wall friction coefficient

K is the lateral pressure ratio

g is the gravity constant.

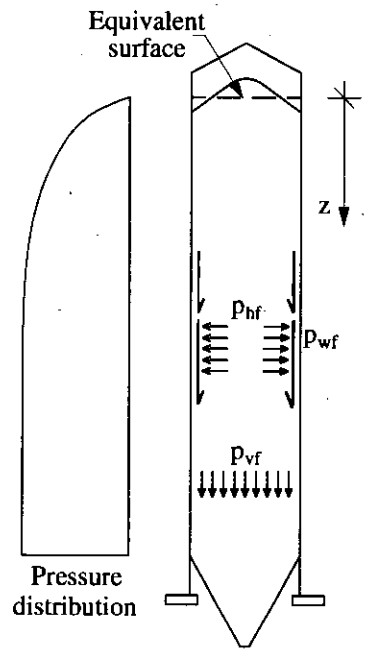

Figure 1.4: Pressure definitions and distribution in tall silos.

1.3 Scope and layout of the thesis

The noise pollution caused by honking has resulted in the shutting down of some silos. In many cases the "honking silos" are filled to less than their capacity, since it has been observed that they do not honk when the fill levels are low. Many industries have resorted to expensive modifications to prevent honking. However the fundamental mechanisms that cause honking are not yet known. The aim of this research project is to develop an understanding of the fundamental mechanism responsible for honking. This will subsequently help in devising appropriate measures to prevent occurrence of this unwanted sound.

The remainder of the thesis is divided into seven Chapters (Chapters 2 to 8) and following describes briefly what they include.

- Chapter 2 reviews the literature on different dynamic phenomena observed in silos during discharge with particular emphasis on honking.

- Acoustic and vibration measurements were taken for a honking industrial silo. Details of these measurements and their analysis are considered in Chapter 3.

- The theory related with the free vibration characteristics of circular cylindrical shells is reviewed in Chapter 4. Different Finite Element (FE) models are validated with this theory.

- The free vibration characteristics of the instrumented honking silo are investigated in Chapter 5 using the Finite Element method (Zienkiewicz and Taylor, 1989). Considerable attention is focused on the axisymmetric behaviour of the silo structure.

- Two different sources of excitation that are thought to lead to honking are examined in Chapter 6: pulsating flow and slip-stick.

- The transient dynamic response of the silo structure subjected to pulse loads at different locations is considered in Chapter 7.

- Chapter 8 discusses the general conclusions drawn from this study as well as recommendations for modifications in existent honking silos.

Chapter 2

Literature review

2.1 Introduction

Dynamic phenomena in metal silos cause a range of problems in industry. Generally these phenomena have been observed during emptying of silo structures and different terms such as "silo quaking" (Roberts, 1993; Roberts and Wensrich, 2002; Tejchman and Gudehus, 1993; Tejchman, 1995, 1998; Schulze, 1998), "silo music" (Roberts and Wensrich, 2002; Tejchman and Gudehus, 1993) and "silo honking" (Roberts and Wensrich, 2002; Tejchman, 1998, 1999) have been used to describe them. Silo quaking is a term generally used to describe loud thudding and banging sounds that are produced during discharge and it has implications on the stability of the silo structure. Considerable research has been directed to understand the quaking phenomenon and will be reviewed first. Silo music and silo honking refer to intense and annoying sounds that predominantly cause noise pollution, though it has been suggested that they can induce weaknesses in the structure (Tejchman, 1999). Research on the honking phenomenon is extremely limited. Some of the research literature available on different dynamic phenomena observed in silos during discharge is considered in the following sections.

2.2 Silo quaking

"Silo quaking" has been described as the phenomenon of loads induced by self excited pulsating flow (Roberts, 1993; Roberts and Wensrich, 2002; Tejchman, 1995, 1998; Schulze, 1998). Pulsations have been observed only when dry granular material is stored. During discharge of cohesive material both pulsations and shocks are observed (Tejchman, 1995, 1998; Tejchman and Gudehus, 1993; Niedostatkiewicz and Tejchman, 2003). It is important to mention that the authors do not provide a strict difference between pulsations and shocks as a shock may take the form of a pulse in the excitation mechanism in a mechanical system (Harris, 1996). The shocks have been mainly related to silo quaking and are often accompanied by a banging sound (Tejchman and Gudehus, 1993; Hardow et al., 1998). Response on the silo wall can be significantly affected by the pulsating flow, especially when any of the natural frequencies of the silo structure matches the pulse frequencies (Roberts, 1993; Roberts and Wensrich, 2002, Niedostatkiewicz and Tejchman, 2003). A range of factors that, alone or combined, may produce pulsating flow have been suggested by previous investigators (Roberts, 1993; Hardow et al., 1998; Roberts and Wensrich, 2002). These factors are: the type of flow pattern during discharge (mass flow, funnel flow, expanded flow or eccentric flow) as shown in Fig. 1.2 and variations in the flow pattern due to changes in the properties of the bulk material; reductions in the stored material density and therefore reduction in magnitude of stresses due to dilation of the bulk material during emptying; internal and boundary friction variations and variations in the flow properties of the bulk solid such as changes in moisture content and particle size distribution. Since structural response depends both on the characteristic of the excitation and that of the silo-fill system not all the dynamic loads induce severe excitations. Amongst other factors the severity of quaking depends on the mass involved (inertia forces) in the rapid deceleration of the bulk material during flow (Schulze, 1998; Hardow et al., 1998). Consequences of quaking include annoying noises which disturb employees and neighbours of industrial plants, quaking induced movements endangering the surrounding structures and in the worse cases failure of the storage structure (Roberts

and Wensrich, 2002; Tejchman, 1995, 1998; Tejchman and Gudehus, 1993; Niedostatkiewicz and Tejchman, 2003).

Quaking has been reported to occur in different flow conditions (mass flow, funnel flow and expanded flow) in storage bins. A brief description of the quaking mechanism in each of them is described next.

Mass flow. It is now generally accepted that a minimum level or critical height H_{cr} is needed to make sure that mass flow occurs in the vertical section of a mass flow hopper (Thomson, 1984; Roberts, 1993). The critical height (H_{cr}) should be between *0.75D* to *1.0D* approximately, where D is the barrel's diameter. During discharge in the mass flow condition, the particulate solid dilates leading to variations in density from the static condition. When $H > H_{cr}$ (see Fig. 2.1) the flow in the cylinder is uniform. When the flow starts to move towards the region close to the hopper, called transition region, the velocity profile changes from uniform to non-uniform. Dilation of the stored material takes place due to the generation of pressures in the hopper. Due to the dilation, the vertical pressure and corresponding horizontal pressure become smaller reducing the support between the bulk material and the cylinder. This pressure reduction produces a momentary drop of the solid generating a load pulse. The cycle is then repeated (Roberts, 1993; Roberts and Wensrich; 2002; Schulze, 1998).

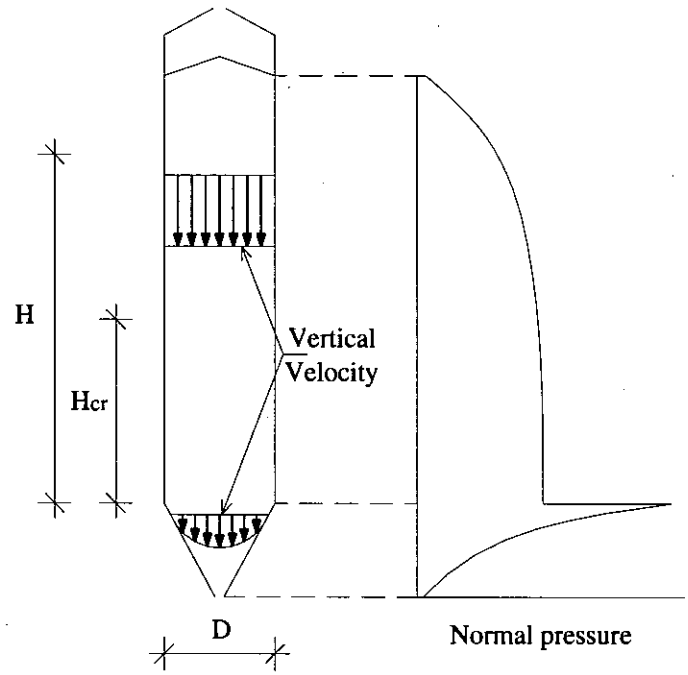

Figure 2.1: Velocity profile and normal pressure distribution in a mass flow silo (redrawn from Roberts, 1993).

Funnel flow. It has been suggested (Roberts, 1993; Roberts and Wensrich; 2002; Schulze, 1998) that a phenomenon similar to that described for mass flow may also occur in tall funnel flow silos where the effective transition intersects the silo wall in the lower region of the silo (Fig. 2.2a). If the material height above the effective transition, with a hopper made of bulk solid, is greater than the critical height (H_{cr}), the same conditions described for the mass flow case are met and quaking may occur.

In squat funnel-flow silos (Fig. 2.2b) where the bulk solid does not move along the walls, the material dilation occurs as it expands in the flow channel. Due to this, the radial support (P_n) given to the stationary material is reduced. If the hopper's angle (θ_h) is large, then an increase of pressure in the flow channel may occur due to the momentary slip of the stationary mass causing quaking. Then the cycle repeats itself (Roberts, 1993; Roberts and Wensrich; 2002; Schulze, 1998).

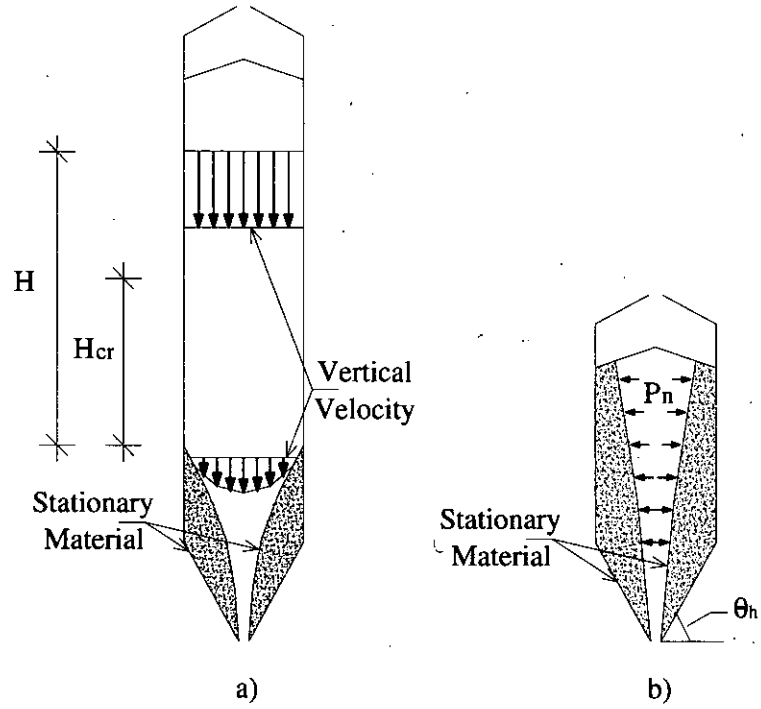

Figure 2.2: Quaking mechanism in a) tall and b) squat funnel flow silos.

Expanded flow. Roberts (1993) also suggested that in expanded flow silos (Fig. 2.3), the upper part of the silo works under funnel flow, while the lower part of the hopper region works under mass flow. If the transition angle (θ_h) is large, silos can experience pulsating loads. Due to segregation, large particles tend to accumulate near of the lower part of the transition wall. When these large particles slide over the wall, they produce load pulsations.

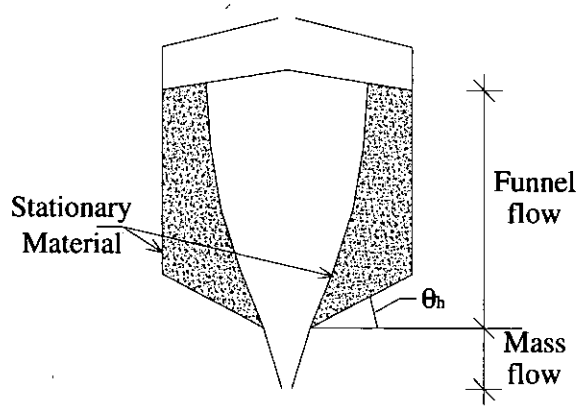

Figure 2.3: Quaking in expanded flow silos (redrawn from Roberts, 1993).

2.3 Silo music

Limited research is available in literature where the term "silo music" has been employed. The manner in which the term is employed generally resembles the "silo honking" phenomenon (which will be reviewed in the next section). Commonly, silo music has been described as an annoying noise with frequencies greater than 20 Hz, which causes noise pollution (Tejchman and Gudehus, 1993; Schulze, 1998; Muite et al., 2004). Roberts and Wensrich (2002) have also described silo music as a variation of silo quaking. It has also been reported to occur when dry granular materials discharge from silos (Tejchman and Gudehus, 1993). The research related to silo music is mostly based on experiments in model silos rather than full-scale measurements or observations (Tejchman and Gudehus, 1993; Muite et al., 2004).

Tejchman and Gudehus (1993) conducted experimental and theoretical studies to investigate different dynamic phenomena in silos during emptying. Model silo experiments were performed in a slender Perspex cylinder fixed to a wooden chest. Two different fillings were used, dry sand and weakly cohesive sand (dry sand and some clay). A geophone transducer fixed on the exterior of the silo near the outlet was used to measure the vibration of the wall. Silo music occurred when dry sand was used in the experiments and the frequencies reported were not constant, they increased with the discharge process. Silo music was thought to emanate from the upper part of the silo during mass flow. However, the authors felt that this could also be because the supporting chest was brought into resonance. No acoustic measurements were undertaken during the study. Both silo music and silo quaking were detected when cohesive sand was used in the experiments. At the beginning of the discharge, the silo vibrations frequencies were higher than those for dry sand. However, later in the emptying process, frequencies of just a few Hertz were associated with non-rhythmical shocks.

The Finite Element method was used (Tejchman and Gudehus, 1993) to model dry sand with inclusion of inertial forces. The study examined the motion of particles due to controlled mass flow and free flow. Some conclusions from their calculations were: the granular bulk material always caused silo music during discharge and

frequency and amplitude of the silo music were influenced by material properties, wall roughness and kind of silo outlet. It was suggested that dynamic effects were transmitted to the silo wall during mass flow, while in funnel flow these effects were damped by the stagnant material. It was suggested that the fundamental frequency due to silo music in silos with smooth walls can be roughly calculated with the frequency formula for the first longitudinal mode of an elastic bar. In essence the study associated silo music to wave motion in the stored solid considered as an elastic body.

Muite et al. (2004) also conducted experimental work to investigate different dynamic phenomena during silo discharge. In their study, different wall materials (aluminium, steel and acrylic) and granular materials (crushed glass, glass beads and sand) were used. The model silos were supported on springs, which were, in turn, attached to a rigid steel frame. The model silos were restricted to oscillate just in the vertical direction using physical constrains. A microphone was placed at the top of the silo model for the detection of acoustic emissions. Vertical acceleration measurements were also undertaken using accelerometers at the silo base and inside the granular material. Pulsations were reported to occur during discharge. However, none of the granular materials produced pulsations in the steel model silo and also pulsations did not occur when sand was discharging from the aluminium model silo. The frequency spectrum of the acoustic signal in the sand-acrylic combination was associated to the resonant frequencies of the air column above the fill level. The authors compared the variation of the air column height with the variation of the quarter wavelength during discharge (similar to an organ pipe with one end closed and the other open) to draw the conclusion that silo music is due to the vibration of the air column inside the silo structure. These findings are contrary to those of Tejchman and Gudehus (1993) where silo music is associated to the vibration of the material column. The authors also conclude that the pulsations observed during the experiments were due to slip-stick and this phenomenon was responsible for generating silo music and silo quaking. However, the slip-stick behaviour was not investigated between the granular and silo wall material by direct shear tests (Purutyan et al., 1994a; Ooi et al., 1999; Buick et al., 2003, 2005). Slip-stick studies

have shown that this behaviour is stress level dependent with large amplitudes of shear stress fluctuations at large normal stress and small amplitudes of fluctuations at low normal stress (Ooi et al., 1999). In model silos the stresses are expected to be fairly low to produce large amplitudes of slip-stick fluctuations.

2.4 Silo honking

The "silo honking" term has been used to describe as a loud annoying noise similar to a truck horn (Tejchman, 1998, 1999; Schulze, 1998; Hupkes, 2003) that emanates from silos during discharge. However, anecdotal evidence suggests that sometimes honking also occurs after a discharge period. The sound level of the honking noise has been reported to be above 100 dB (Tejchman, 1998, 1999; Ooi et al. 1999). Generally, honking is known to occur in cylindrical tall aluminium silos designed for mass flow and storing polymer granulates (Tejchman, 1998, 1999; Schulze, 1998; Hupkes, 2003; Ooi et al., 1999; Roberts and Wensrich, 2002). However, steel silos have also been reported to honk (Tejchman, 1999; Hupkes, 2003). Moreover, the honking phenomenon has been reported to occur only with some polymer granulates (Tejchman, 1998, 1999). Industrial experience indicates (Dean, 2003) that a polymer granulate may produce honking in a particular silo but may not produce honking in another silo. This suggests that honking is due to a combination of factors such as stored material, silo material and silo geometry. Where silo wall accelerations have been measured, the honking noise has been associated to vibrations of the silo wall (Tejchman, 1998, 1999; Hupkes, 2003). Observations on honking industrial silos also indicate that they only honk when they are relatively full and stop honking when the fill level reduces (Hupkes, 2003; Schulze, 1998). Authors suggest that the discharge rate does not appear to influence the honking intensity but increases its frequency of occurrence. The authors also found that at higher outflow rates, honking is more likely to happen while at low rates the noise occurs rarely and unpredictably (Tejchman, 1998, 1999; Hupkes, 2003). However, a different study suggests that a significant reduction in the discharge rate reduces the magnitude of honks (Ooi et al. 1999). In some studies (Tejchman, 1998, 1999; Roberts and Wensrich, 2002), silo honking is assumed to be a resonant effect between the frequencies of pulsations and

some of the natural frequencies of the silo structure. Often it is also suggested that the honking sound emanates predominantly from those parts of the silo structure where there is no fill (Tejchman, 1998, 1999; Hupkes, 2003).

The studies conducted by Tejchman (1998, 1999) are perhaps the most relevant published research on silo honking. In these studies full-scale experiments were conducted on aluminium silos containing polymer granulates. Limited axial and radial acceleration and deformations were measured at the exterior of the silo wall during discharge. Wall acceleration was measured along the height in four different positions, one of them at the base of the supporting structure and the remainder at around mid-height of the structure. Accelerations were also measured in three different circumferential positions near to mid-height of the structure. Vertical and horizontal deformations were also measured at one position on the silo wall at about mid-height of the silo structure. Wall accelerations and deformations were measured with acceleration transducers and strain gauges respectively. Sound pressures inside and outside the silo were also recorded with microphones located on the roof (inside) and the base (outside) of the silo structure. In addition to measurements during discharge the author also reported determination of eigenfrequencies of the empty storage structure by using loud speakers excitation from the roof of the silo structure. Some of the conclusions drawn from these studies are as follows:

- The honking noise occurred in the form of pulses of very short duration (about 0.15 s). The time gap between honking pulses was in the range of 7-15 s.

- Accelerations of the order of $500g$, where g is the acceleration due to gravity, were recorded during honking in the axial (vertical) direction. The maximum vertical wall acceleration during honking decreased with increasing location along the silo height. In general, the peak radial acceleration was smaller than the vertical.

- The author suggests that honking is due to resonance effect between the pulsating stored material and the silo structure. The lowest frequency

registered during honking was 292 Hz, which was reported to match the lowest eigenfrequency measured using a loud speaker in an empty silo.

- Acceleration variations around the silo circumference were reported as not being large.

- The strain increments during honking were found to be small. It was suggested that honking did not put the silo structure in danger but could aid fatigue.

Tejchman (1999) suggested a number of factors that can influence honking. These include type of flow, properties of the stored solid and geometrical and material properties of the silo structure. It has also been suggested that the weather influences the honking behaviour because it was not observed during "strong sun-warming".

Tejchman's (1998, 1999) studies are the only published investigations with measurements during silo honking; however, the study does not address the fundamental mechanism that causes honking. In these studies honking is hypothesised to initiate by self-induced pulsation of the silo fill. It is assumed that with smooth silo walls the shear zone between wall and particulate material is small. This small shear zone is unable to damp out the pulsations created within the stored material during discharge. These pulsations are transferred to the silo wall generating the audible noise or honking. Based on this, the author proposed increasing the wall roughness using waffle sheets along the cylinder's interior at certain height (Fig.2.4) to eliminate honking. The waffle sheets were 2.0 x 0.5 m, thickness of 1.5 mm and a wall roughness of 3 mm. The objective of these rough sheets is to increase the material shear zone along the cylinder wall and damp the pulses due to the bulk material and it is assumed that the shear zone does it. Introduction of waffle sheets has been found to be effective. However this solution is not favoured by the industry as it is expensive and more importantly it changes the flow pattern from mass flow to funnel flow. Since honking has generally been observed only in mass flow silos it appears that the real reason for the efficiency of waffle sheets is this flow pattern change.

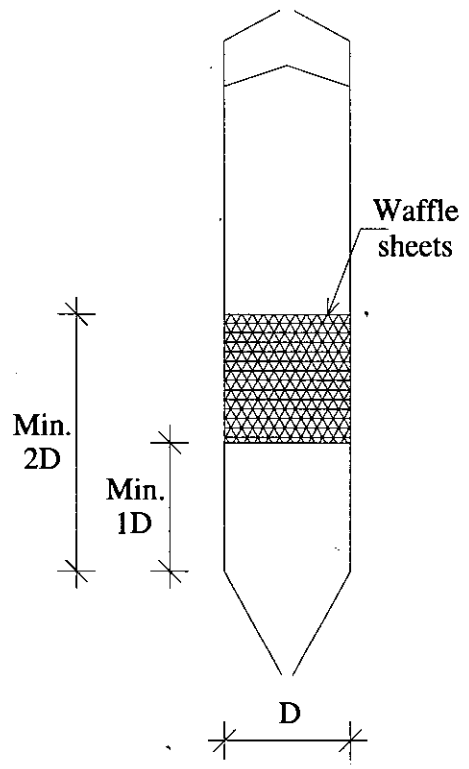

Figure 2.4: Position of waffle sheets to increase the material shear zone (redrawn from Tejchman, 1998,1999).

Ooi et al., (1999) hypothesised that honking originates from the excitations caused by the slip-stick interaction between the stored solid and the silo walls during discharge. Recent shear tests have shown that slip-stick occurs when pellets stored in a honking silo were sheared against aluminium plates. Different normal stress levels, similar to those expected in a real honking silo, were considered in these tests. The slip-stick behaviour was observed to be stress level dependent, with larger fluctuations at higher normal stress and smaller fluctuations at lower stress levels. The shear rate was also investigated during the experiments. The results show that the frequency of fluctuation increased at higher shear rates while the magnitude of fluctuations decreased. The slip-stick behaviour was also influenced by properties of the stored solid and silo wall material. The authors also conducted shear tests on pellets against pellets to examine internal slip-stick and found that this was not significant. Based on the results of the study, the authors suggested that the slip-stick interaction at the silo walls might be the source of excitation that leads to honking.

More tests to examine the frictional properties were conducted as part of this study and are discussed in Chapter 6.

One of the solutions recommended by Ooi et al., (1999) was the installation of a "holey pipe" inside the silo structure (Fig. 2.5). The pipe is perforated with holes, which are arranged in a spiral pattern from top to bottom. The pipe is located in the axisymmetric axis of the silo. The objective of this holey pipe is to force pipe flow of pellets through the pipe by the assumption of reducing shearing against the wall. This too has been found to be effective, but again it is an expensive solution and in a similar way to the waffle sheets it appears that its efficacy is due to the change in flow pattern.

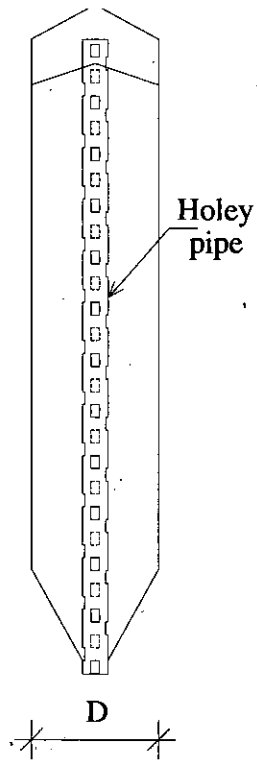

Figure 2.5: Holey pipe to enforce pipe flow.

The main objective of the research studies reviewed here is to describe the honking phenomenon and some hypotheses have emerged about its causes (pulsating flow and slip-stick). Also, from these hypotheses different solutions have been proposed to eliminate the problem, such as waffle sheets and holey pipes. However, the

structural behaviour and response due to any of the hypotheses proposed to cause honking has not been studied. An attempt to find the mode responsible for honking by studying the free vibration characteristics of the silo structure was conducted by Hupkes (2003). However, the research work was unsuccessful concluding that the honking silo wall has to be excited by a load mechanism at the specific honking frequencies (resonance).

Significant part of this research work is based on the study of the free vibration characteristics of the silo structure. Honking has been reported to occur in the form of short pulses (Tejchman, 1998, 1999; Hupkes, 2003) and also the anecdotal evidence of occurrence after a discharge period (when the stored material is static) confirms the occurrence of a pulse load instead of a harmonic load. This supports the assumption that pulse loads excite some of the natural frequencies of the structure. This is investigated in Chapter 7. Meanwhile, results from full-scale measurements and numerical analysis of the free vibration characteristics in a honking silo structure are presented in the following Chapters.

Chapter 3

Full scale measurements and data analysis

3.1 Introduction

This Chapter describes the measurements conducted to understand the honking phenomenon on an industrial honking silo. Silo wall accelerations and acoustic emissions were recorded simultaneously during discharge. The instrumentation arrangements also enabled measurements of the silo wall acceleration at different heights. Spectral analyses of acoustic emission and silo wall vibrations show that during honking a fundamental frequency and a harmonic series of peaks at integer multiples of the fundamental frequency are excited. The latter will be referred as "harmonic response" throughout this thesis. Analyses of the silo response during the entire discharge period (including non-honking durations) were also conducted. These show a different kind of behaviour. Oscillatory motions were found to occur in a fairly periodic manner during the entire discharge period. In the last section, four cases of study are presented where different investigators have instrumented honking silos and identified their frequency content.

3.2 Silo characteristics and instrumentation

3.2.1 Silo characteristics

The instrumented honking aluminium silo is located in an industrial plant that produces polyester films in the U.K. One other silo was also originally honking, but it was modified using a perforated tube (discussed in Chapter 2) to stop the unwanted noise. The instrumented honking silo was 3 m in diameter and 22 m high. It had aluminium walls with thickness (h) varying from 6.2 mm to 4.0 mm as shown in Fig. 3.1. The silo barrel consists of eleven aluminium rings welded together along their circumferences. The height of each ring is 2 m. The silo has a conical roof at the top and a 60° conical hopper at the bottom. It stores polyethylene terephthalate (PET) pellets and is designed to undergo mass flow (all of the particulate solids are in motion during discharge).

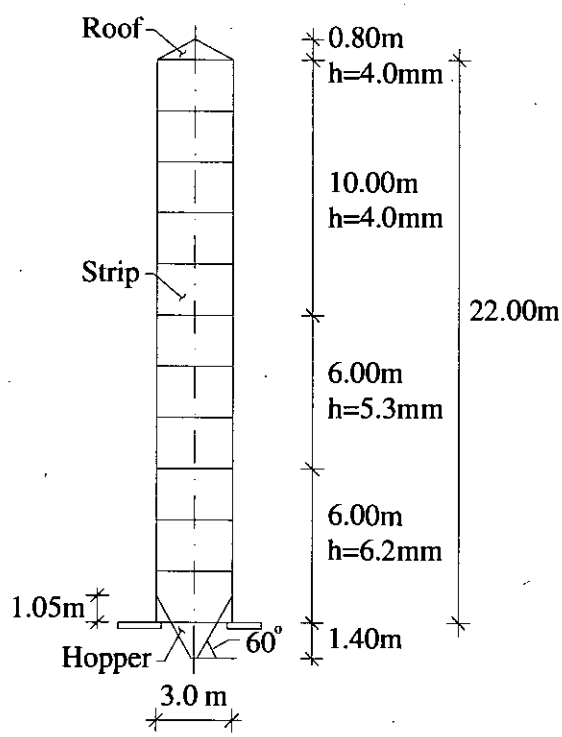

Figure 3.1: Geometry of the honking aluminium silo.

3.2.2 Instrumentation

Two different sets of measurements were obtained during discharge of the honking aluminium silo. The first set of measurements used a tri-axial accelerometer on the silo wall and consisted of three PCB 303A02 accelerometers that were calibrated between 1 and 10 kHz. Above this range they had a maximum error of ± 10% up to 20 kHz. The second set of measurements used accelerometers at different positions along the silo height to record only the radial acceleration of the silo wall. The characteristics of these accelerometers were the same as above. An Audio-Technica microphone ATM33a with an approximately flat frequency response between 200 Hz and 2 kHz and a variation of no more than 5dB between 40Hz and 200 Hz and between 2kHz and 20 kHz was used to measure the acoustic emission. In addition a CEL-254 digital impulse sound level meter with a measurement range of 35-135 dB and a frequency range of 10 Hz to 25 kHz was used to measure the noise level.

Recordings with the tri-axial accelerometer, for the first set of measurements, were conducted by placing it at different positions along the silo height as shown in Fig. 3.2. The positions at which the accelerometer was located were at nearly two meters separation and in a vertical line. The instrumentation arrangement in this way enabled simultaneous measurement of the acceleration in the three directions of the silo wall and the acoustic emission. The three directions of vibration measured on the silo wall were axial (A_d), radial (R_d) and circumferential (C_d), as shown in Fig. 3.2; which indicates the positive directions of the acceleration considered. For the second set of measurements the accelerometers were placed at different positions along the silo height for simultaneous measurements of radial acceleration. The positions used were the same as those for the first set of measurements. The sound level meter was also placed at different heights to examine the variation in sound emission. The microphone was kept at just one position during the two sets of measurements, on the base of the honking silo.

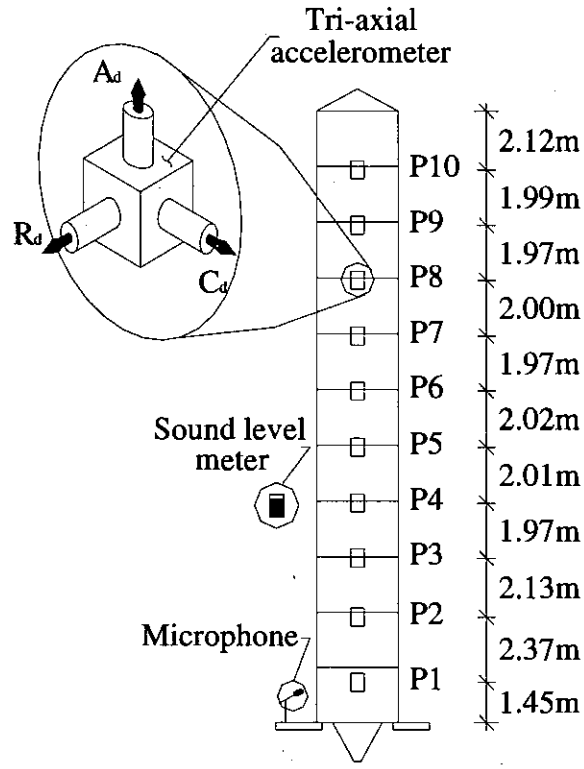

Figure 3.2: Instrumentation of honking silo.

3.3 Acoustic emission and silo wall accelerations

3.3.1 The acoustic emission

In this section the measurements and analysis from the microphone at the base of the silo are considered. The digital acoustic measurements were made at a sampling rate of 12500 samples per second (12.5 kHz). The discharge of the material was noisy with several bangs and honks (bangs outnumbered honks) during the entire process. The acoustic signals for two different discharge periods are shown in Figs. 3.3 and 3.4. The signals were analysed with a MATLAB (Math Works Inc., 1999) code. The code can be found in Appendix A. The data acquisition was triggered when one of the signals exceed a preset threshold. The signals were, however, continuously sampled, enabling the signal just prior to triggering to be recovered from the system's buffer. This enabled the full honking event to be captured including the build-up before the system is triggered (negative time in Figs. 3.3 and 3.4 and

subsequent figures). The typical discharge period lasted for around 7 s and the fill level was maintained between 85% and 100 %. The honks are represented in the graphs by the sudden increase of pressure and its rapid variation (higher frequency). For example, in Fig. 3.3 it is possible to observe the sudden pressure increment and dense areas (representing higher frequencies) in six different positions along the time axis at $t \approx 0.0$, 1.4, 2.6, 3.7, 4.5 and 5.3 s. However, by playing the sound file, nine honks are audible. The pressure increment at $t \approx 2.6$, 3.7 and 4.5 s represents not just one honk but two consecutive honks separated for a very short interval of time. The highest sound level for this discharge period was 104 dB, the loudest honk during the discharge period and during non-honking periods the background noise was in the range of 85-90 dB.

The sound pressure variation in Fig. 3.4 shows a similar behaviour. The plot shows just two sudden changes in pressure at $t \approx 0.0$ and 3.8 s, but in the sound file three honks can be heard, the extra honk takes place between them at $t \approx 1.4$ s. The highest sound level was 106 dB representing the loudest honk during the discharge period.

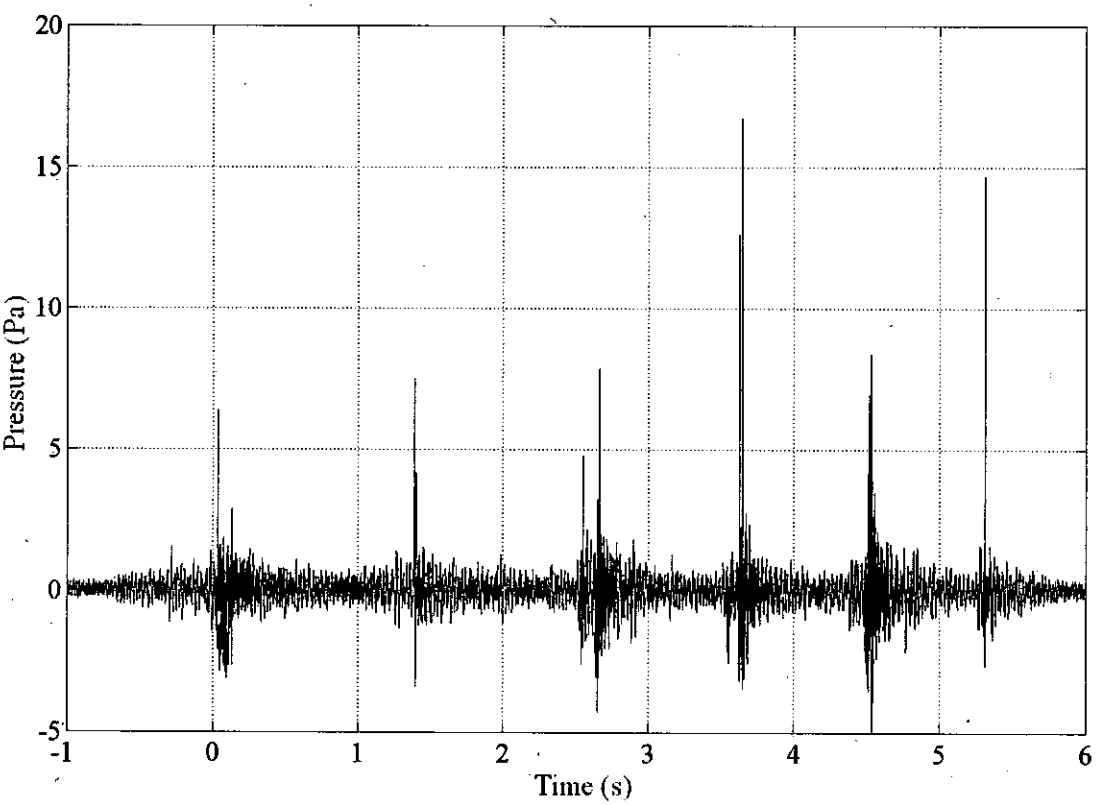

Figure 3.3: Sound pressure measurement in a discharge period (six visible honks).

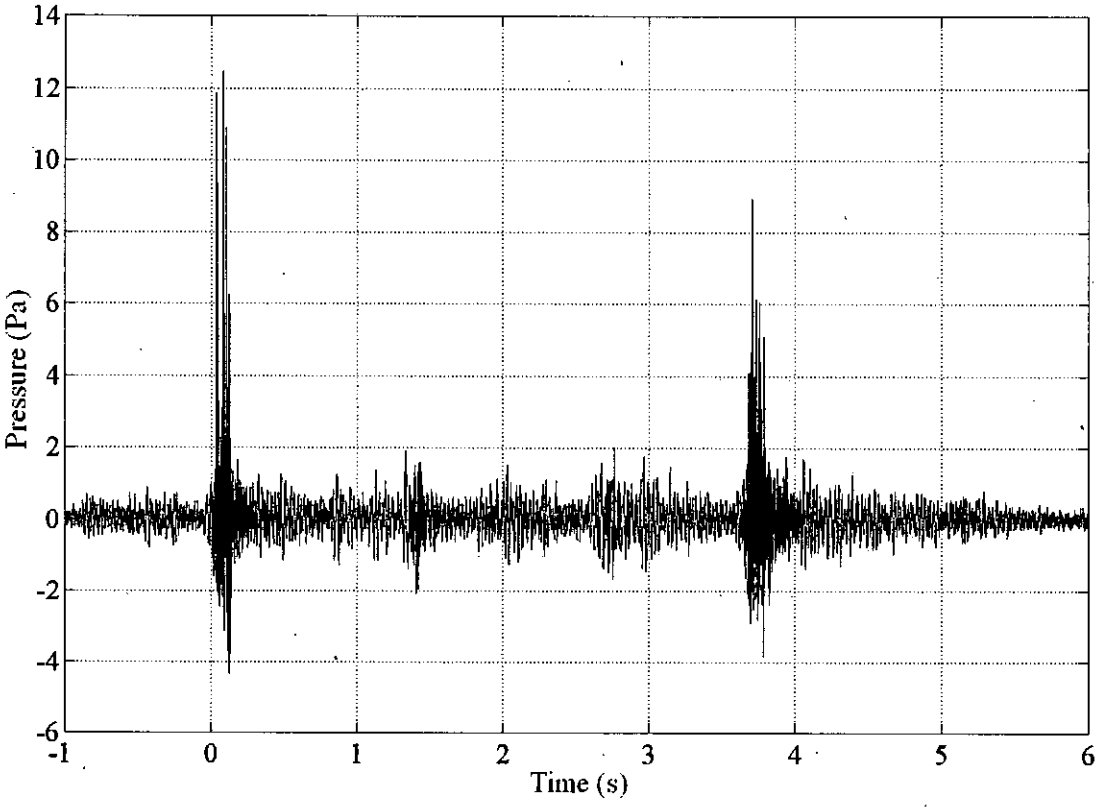

Figure 3.4: Sound pressure measurement in a discharge period (two visible honks).

In order to investigate the behaviour of individual honks, one honk is selected from each discharge period. The two different honks are shown in Fig. 3.5. These honks, shown in Fig. 3.5a and Fig. 3.5b, correspond to the increments in pressure at $t \approx 0.0$ s for Fig. 3.3 and $t \approx 3.8$ s for Fig. 3.4 respectively. The plots show the different stages of the acoustic signal variation with time. For the periods of time between $t \approx 0.0$ - 0.25 s for Fig. 3.5a and $t \approx 3.65$ - 4.0 s for Fig.3.5b the signal varies rapidly. These rapid variations correspond to the honks. However, during the whole ranges of time selected in Figs 3.5a and b slow variation with time (low frequency variation) can also be observed. This variation corresponds to the background noise and it is more evident just before and after each honk.

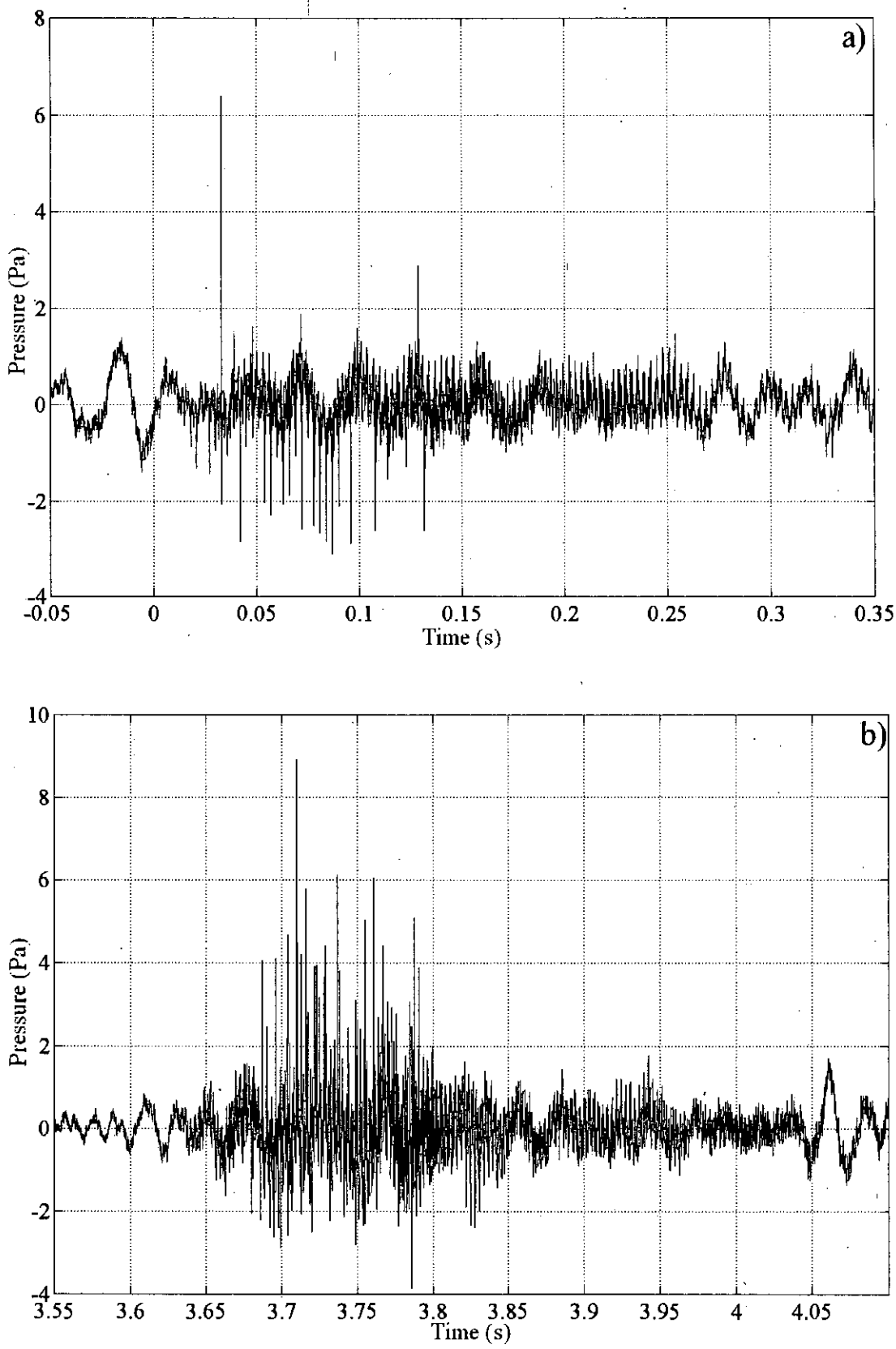

Figure 3.5: Sound pressure measurements for individual honks at a) $t \approx 0.0$ s in Fig. 3.3 and b) $t \approx 3.8$ s in Fig. 3.4.

Spectral analyses of the two honks in Fig. 3.5, from $t \approx$ -0.02 to 0.14 for Fig. 3.5a and from $t \approx$ 3.62 to 3.78 for Fig. 3.5b, were conducted and are shown in Fig. 3.6. The spectra show clear peaks in harmonic series with the acoustic fundamental frequency at 333 Hz. The larger peaks occur at frequencies up to 4000 Hz for Fig. 3.6a and 2500 Hz for Fig. 3.6b, above these frequencies the peaks are relatively equal to those due to the background noise. This aspect will be discussed later. The spectra also show high peaks at frequencies below 60 Hz. These are single peaks with no harmonic response and due to the background noise. This was verified by selecting a non-honking duration during discharge and conducting its spectral analysis. The sound pressure during a non-honking period of time and its frequency spectrum are shown in Fig. 3.7a and 3.7b respectively. The acoustic signal clearly shows the slow variation in time that is particularly apparent just before and after each honk. The acoustic frequencies excited during non-honking periods of time are below 60 Hz. These frequencies exist in the entire discharge duration and can be attributed to the background noise of the industrial plant. Once these frequencies below 60 Hz have been identified as due to the background noise, it is clear that the harmonic response observed in the spectra is due to the honks emanating from the silo. A number of acoustic emissions due to honking were analysed and the behaviour described above was repeatable.

3.3.2 The filtered acoustic emission

Now that the frequency content of the honks has been identified it is possible to remove the background noise by passing it through a high-pass filter. This was done using a Butterworth filter with a cut-off frequency of 200 Hz. This cut-off frequency is low enough to detect the fundamental honking frequency and sufficiently high to eliminate the background noise. The results of the filtered acoustic signals of Figs. 3.3 and 3.4 are shown in Fig. 3.8a and b respectively. From Fig. 3.8a it can be seen that the two honks each at $t \approx$ 2.6 and 3.7 s can now be identified from the time signal. The third double honk at $t \approx$ 4.5 s is still difficult to observe due to small pressure amplitude and time separation. Something similar occurs with the filtered signal in Fig. 3.8b. A variation in pressure is observed at $t \approx$ 1.4 s and in a lesser

extend at $t \approx 2.8$ s, however, the variation in pressure at $t \approx 1.4$ s is a honk while the one at $t \approx 2.8$ s is not. Other acoustic measurements show similar behaviour.

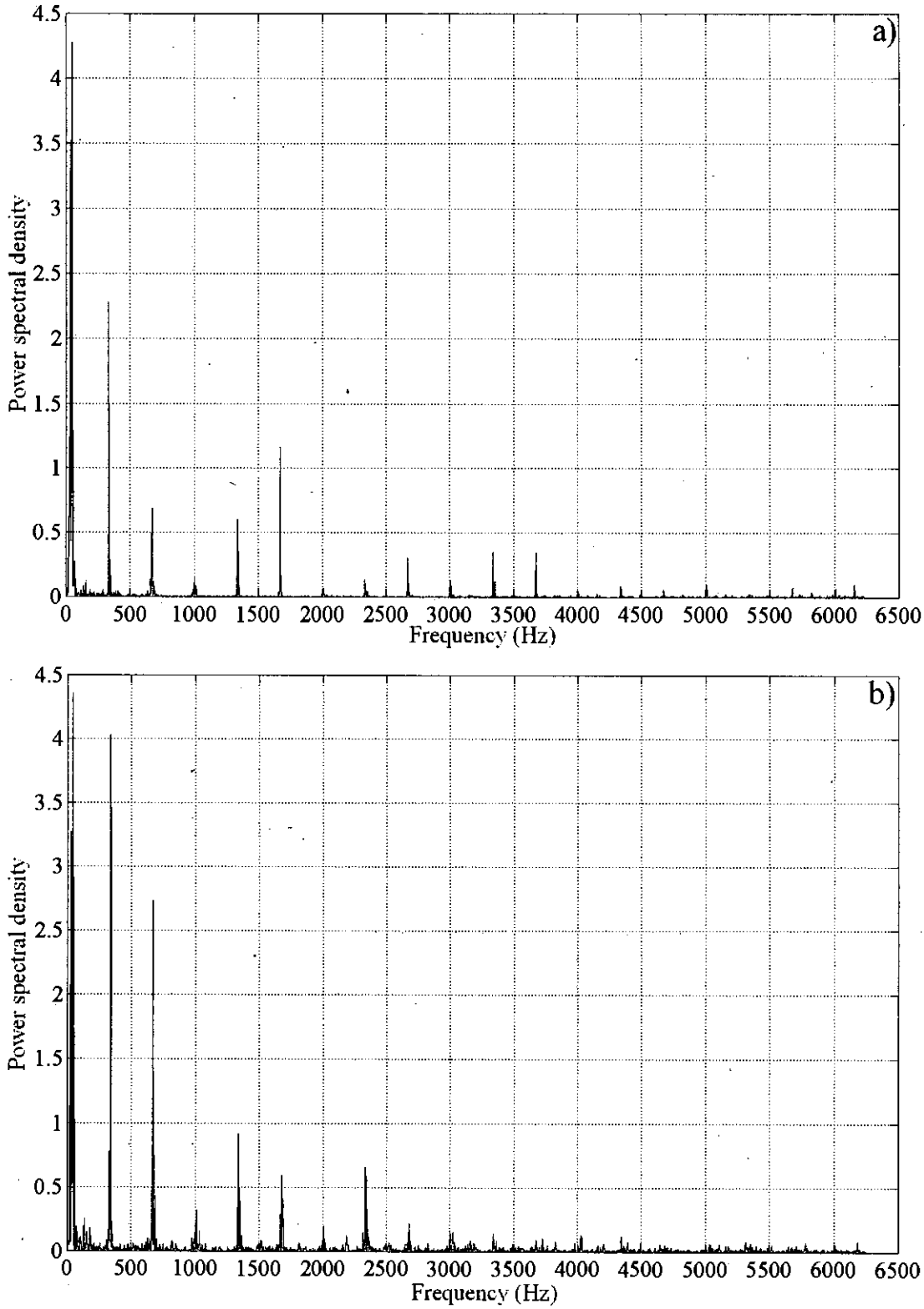

Figure 3.6: Frequency spectra of the acoustic signal for honk a) in Fig. 3.5a and b) in Fig. 3.5b.

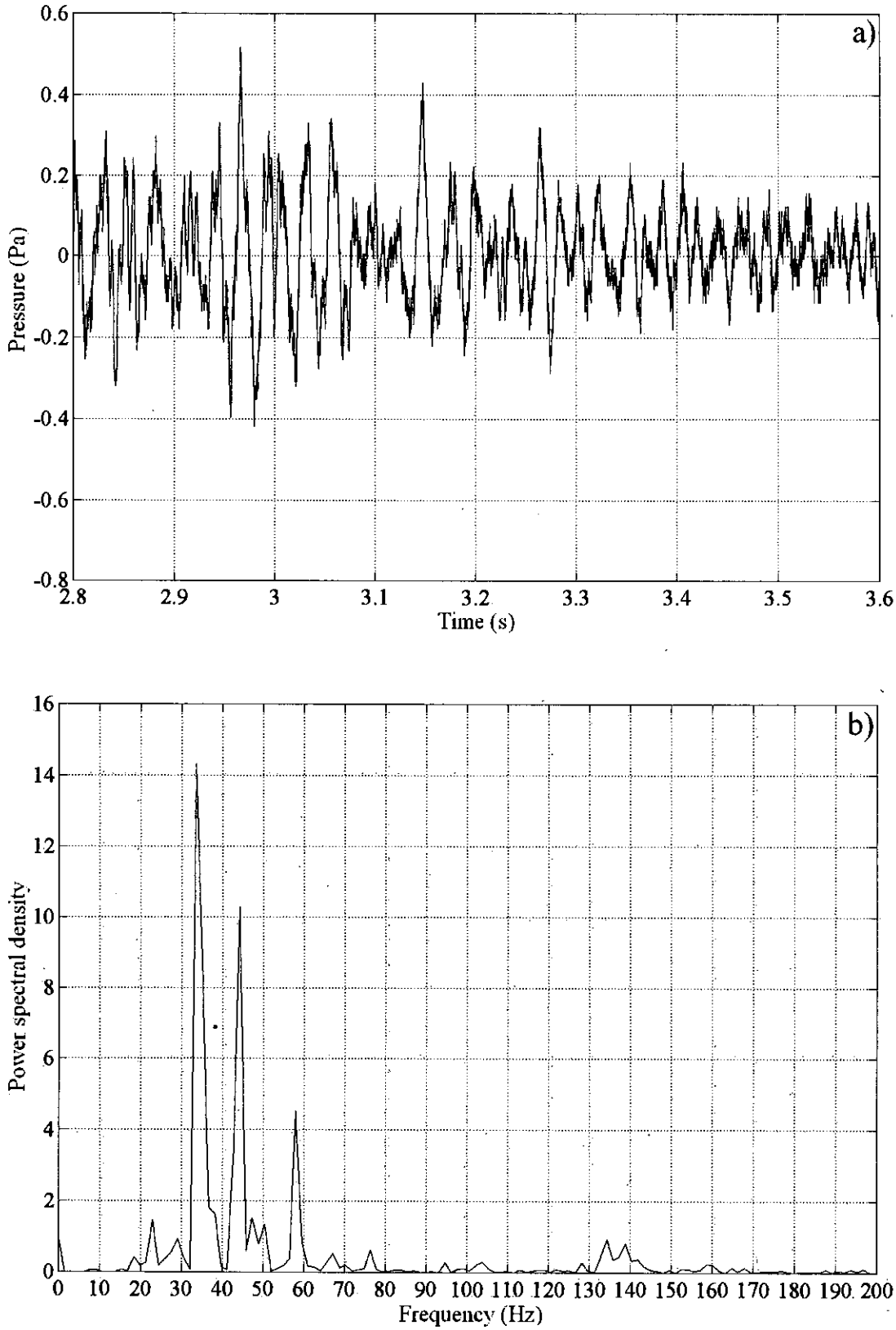

Figure 3.7: Analysis in a non-honking region, a) sound pressure and b) frequency spectrum.

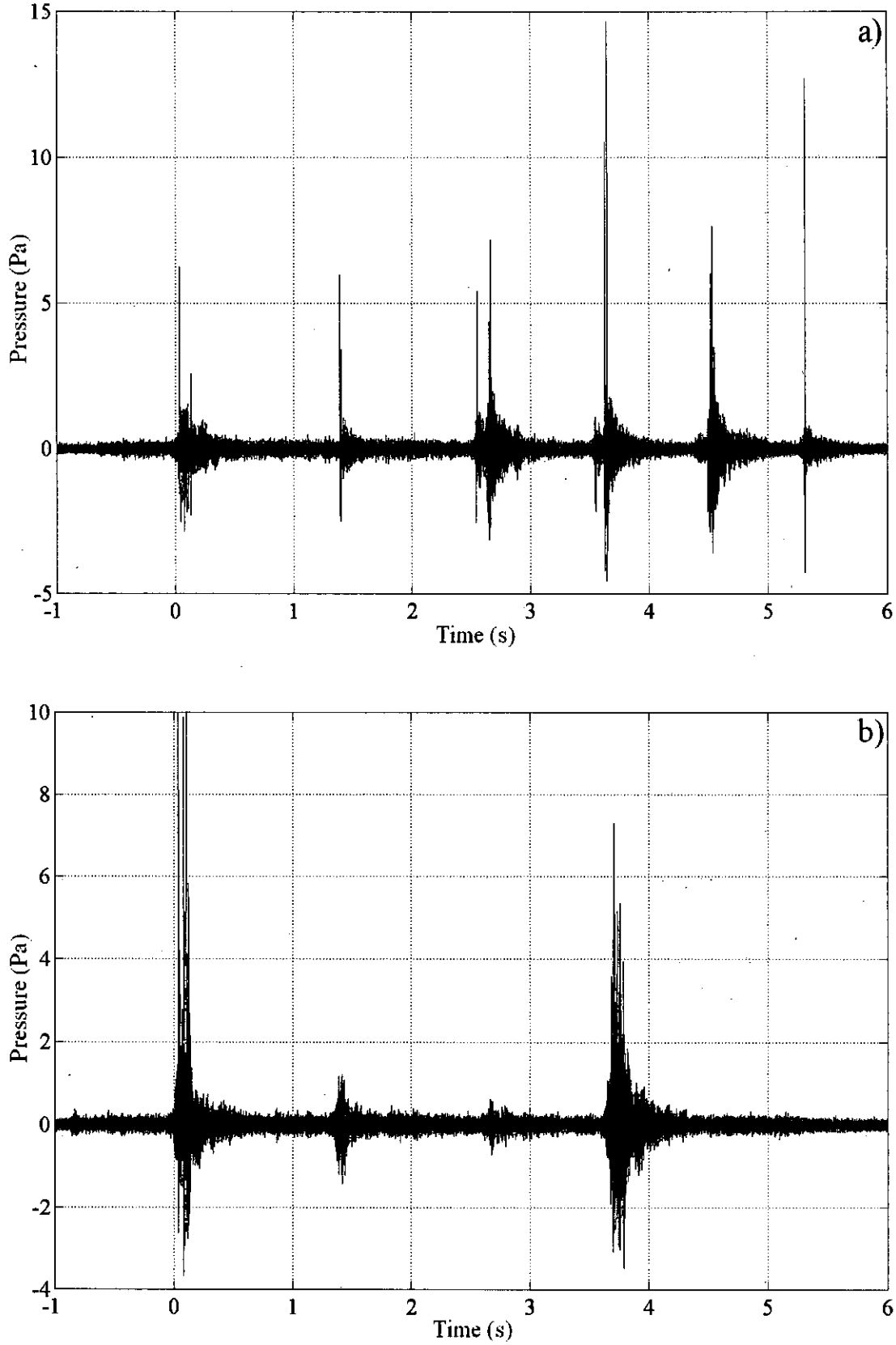

Figure 3.8: Filtered acoustic signals in a) Fig. 3.3 and b) Fig. 3.4.

3.3.3 Wall acceleration during honking

The wall acceleration measurements and their analyses from the tri-axial accelerometer are considered in this section. The same discharge periods as those discussed in the previous sections are selected to enable comparison of the characteristics of the acceleration and acoustic signals. The acceleration signals were also captured at a sampling rate of 12.5 kHz. Figure 3.9 shows the tri-axial acceleration records at two different locations from the silo base for the two discharge periods previously presented. The three acceleration components have been plotted at the same scale to enable easy comparison. For the first discharge period, Fig. 3.9a, it is possible to observe relative higher acceleration amplitudes at $t \approx 0.0$, 1.4, 2.5, 2.7, 3.5, 3.7, 4.4, 4.5 and 5.3 s. These correspond to the audible honking sounds of the acoustic measurements. The three double honks in the sound measurements are clearly visible at $t \approx 2.5$, 3.5 and 4.4 s in this time acceleration plot. Axial and radial components have large acceleration amplitudes in comparison to the circumferential component. For the second discharge period, Fig. 3.9b, the relatively higher acceleration amplitudes are observed at $t \approx 0.0$, 1.4 and 3.8 s corresponding to the honking sounds heard in the acoustic measurements. The honk at $t \approx 1.4$ s can now be easily identified. Again the maximum amplitudes occur in the axial and radial direction. The amplitudes of the honks are extremely variable within the same discharge period and also for different ones. For example honks at $t \approx 4.4$ and 4.5 s in Fig. 3.9a where the peak amplitude in the first one just reaches 500 m/s² while in the second one it exceeds 2000 m/s² in the radial direction.

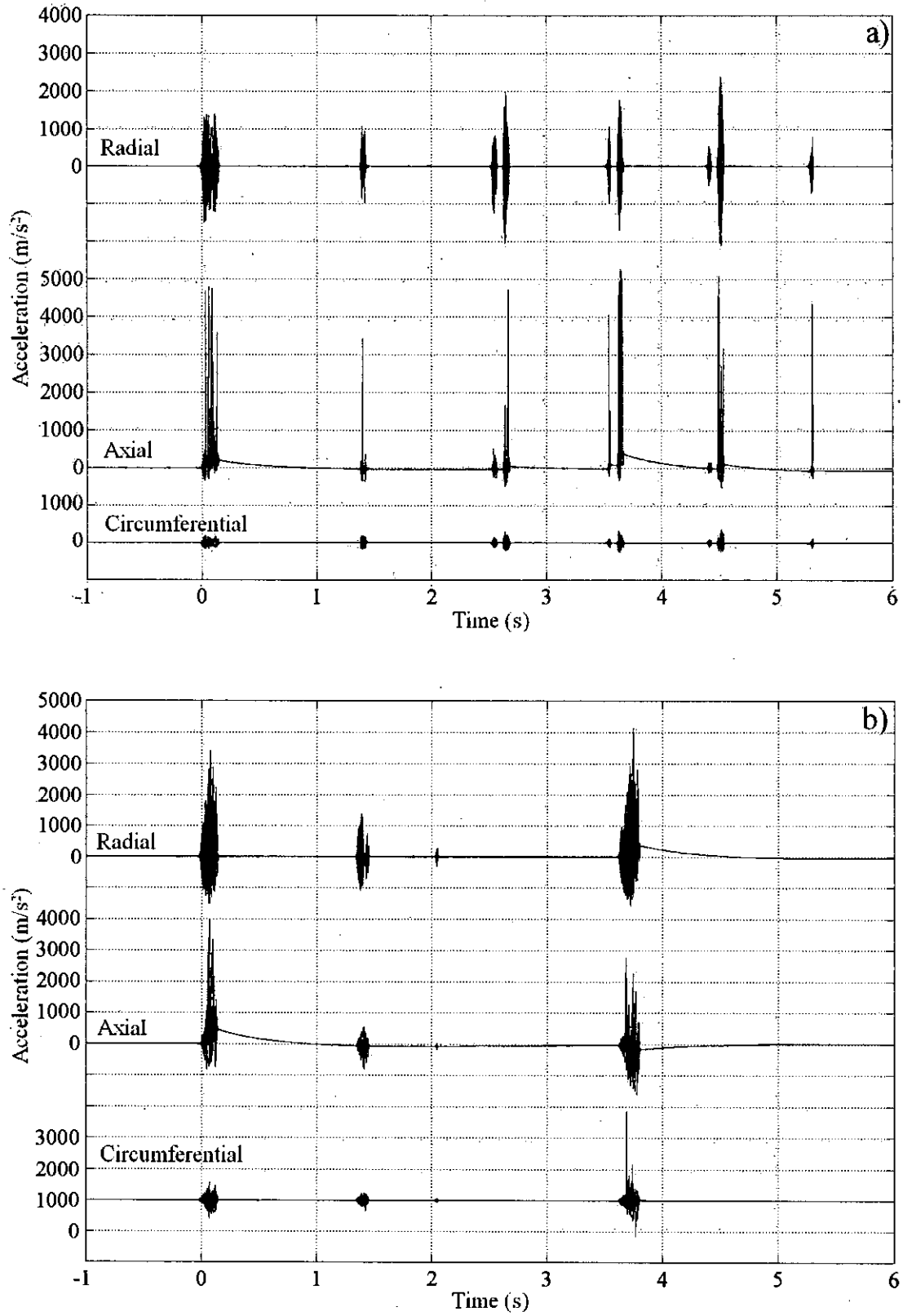

Figure 3.9: Tri-axial acceleration readings at a) P2 ≈ 3.80 m and b) P5 ≈ 9.90 m from silo base for two different discharge periods.

A closer look at individual honk representing acceleration is shown in Fig. 3.10. The honks selected are at $t \approx 0.0$ s of Fig. 3.9a and $t \approx 3.8$ s of Fig. 3.9b. These acceleration readings correspond to the acoustic emissions shown in Fig. 3.5. The radial acceleration readings show rapid oscillatory motions with amplitudes between 1000 and 3000 m/s^2. However, in the axial direction intermittent, non-oscillatory pulse responses can be observed with amplitudes between 2000 and 5000 m/s^2. These correspond to single points in the sampling record with an extremely short pulse duration (less than 80 μs). These cannot be responsible for the acoustic emission since there are no oscillations. In some radial acceleration measurements, these isolated large acceleration peaks were also visible with similar amplitudes of acceleration. Ignoring the intermittent pulses, the relative amplitudes of the radial accelerations are larger than those for axial ones. Generally, this was the case for a number of honks analysed with some honks having similar amplitudes in both directions. The amplitudes of circumferential accelerations are the smallest of all in Fig. 3.10. This was found to be the case for all the honks analysed.

Frequency analysis for the three components of acceleration readings of Fig. 3.10a and b is shown in Fig. 3.11 and 3.12 respectively. The spectra show peaks at regular intervals of 333 Hz for all three components of the wall acceleration, the same harmonic response as their correspondent acoustic emissions. Due to the limited sampling rate some aliasing is evident in the graphs. This is represented by small peaks, which occur approximately mid-way between the peaks separated at 333 Hz. Aliasing effect disappeared in the radial and circumferential direction when the sampling rate was increased to 50 kHz while in the axial direction still some aliasing could be observed (Buick et al., 2005). In the frequency spectra of Fig. 3.11 and Fig. 3.12 for the three acceleration components, while the harmonic interval is 333 Hz, the lowest frequency peaks are typically smaller and often the fundamental peak (333 Hz) is indistinguishable. This is different from their correspondent acoustic spectra where higher peaks occur at lower frequencies. It is important to note that acoustic pressure is related to particle velocity. Integration of wall acceleration signals (to obtain velocity) will amplify low frequency components (Buick et al., 2005).

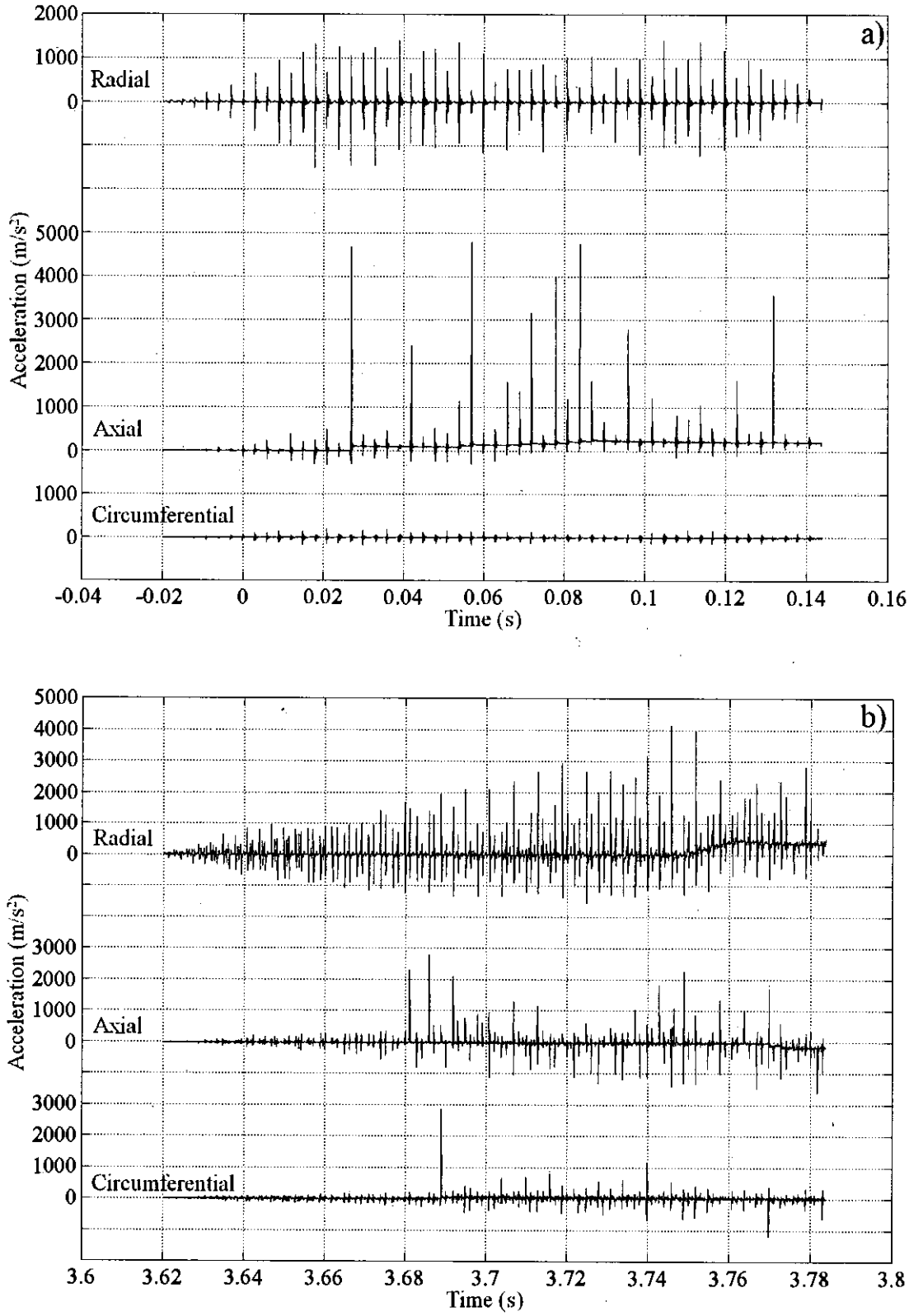

Figure 3.10: Tri-axial acceleration readings for individual honks at a) $t \approx 0.0$ s in Fig. 3.9a and b) $t \approx 3.8$ s in Fig. 3.9b.

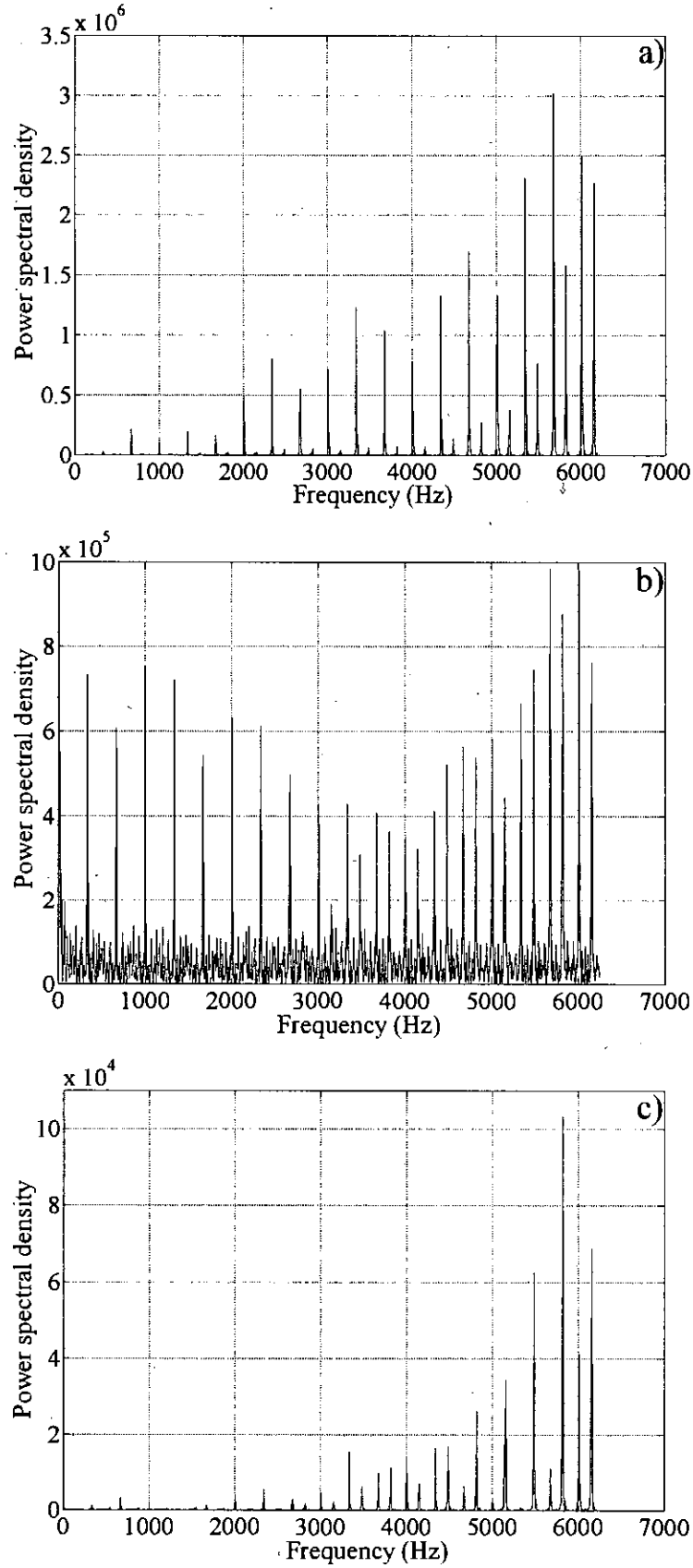

Figure 3.11: Frequency spectra of the acceleration readings in the a) radial, b) axial and c) circumferential direction for honk in Fig. 3.10a.

3.3.4 Wall acceleration at different heights during honking

The second set of observations is discussed in this section. This second arrangement enabled simultaneous measurements of the radial acceleration to investigate the variation of honking along the silo height and the influence of the fill level on the phenomenon. Consider simultaneous recording of radial acceleration at positions P2, P4, P5 and P6 (see Fig. 3.2). Figure 3.13 shows the acceleration at these positions for a typical honk. The silo was filled to 90% of its capacity during this honk. For the four positions shown, the maximum acceleration amplitudes are reached at position P2, the lower part of the silo. The acceleration amplitudes at position P4 are the smallest of all ($\approx$ 200 m/s^2). Generally, this was the case for a number of honks analysed with the silo filled to 90% of its capacity. However some other honks analysed at position P5 also reached similar acceleration amplitudes as those shown in Fig. 3.13 for position P2. The rest of the acceleration readings at higher positions have nearly the same amplitude range as P6. For 90% of silo capacity, the maximum acceleration amplitudes were in the range 1000 - 6000 m/s^2 for a number of honks analysed.

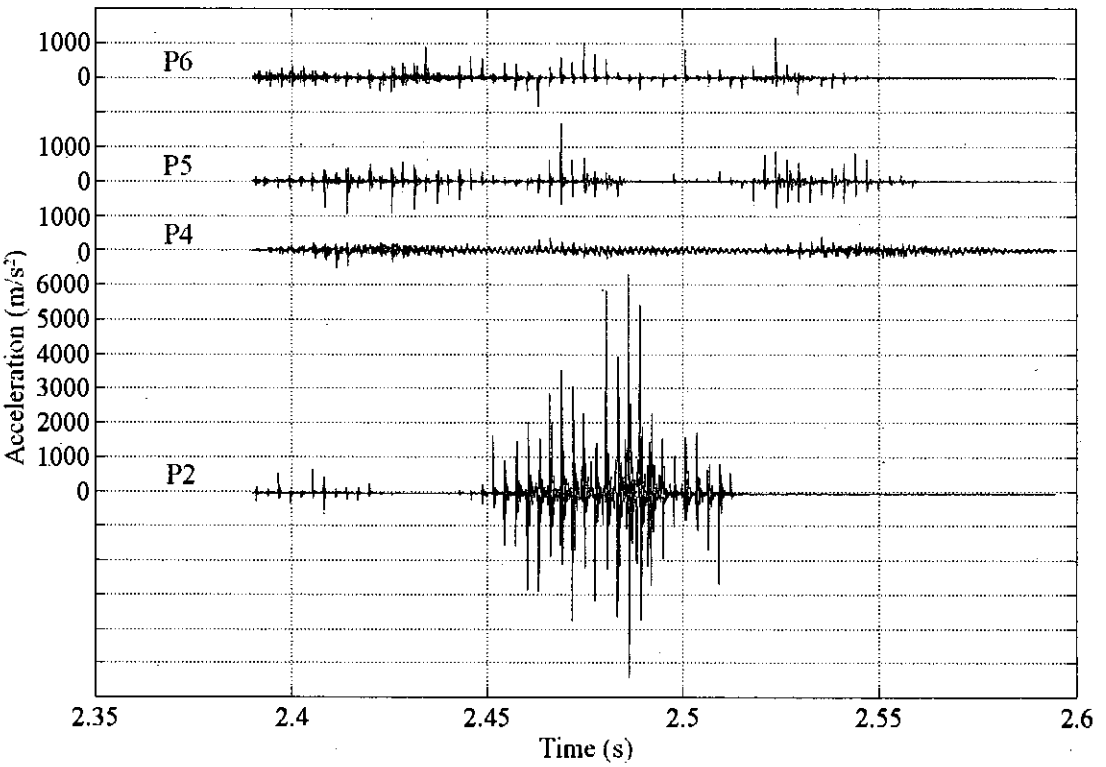

Figure 3.13: Radial acceleration readings for a honk at different positions with 90% silo capacity.

The frequency spectra for the honk of Fig. 3.13 at positions P2, P4, P5 and P6 are shown in Fig. 3.14. The spectra show that the harmonic response is the same as that obtained with the acoustic emission and tri-axial acceleration readings earlier. The honking frequency content does not change with accelerometer position along the silo height. Again, higher harmonics seems to have higher energy content and the fundamental honking frequency is not easily seen in some cases (Fig. 3.14a and 3.14c).

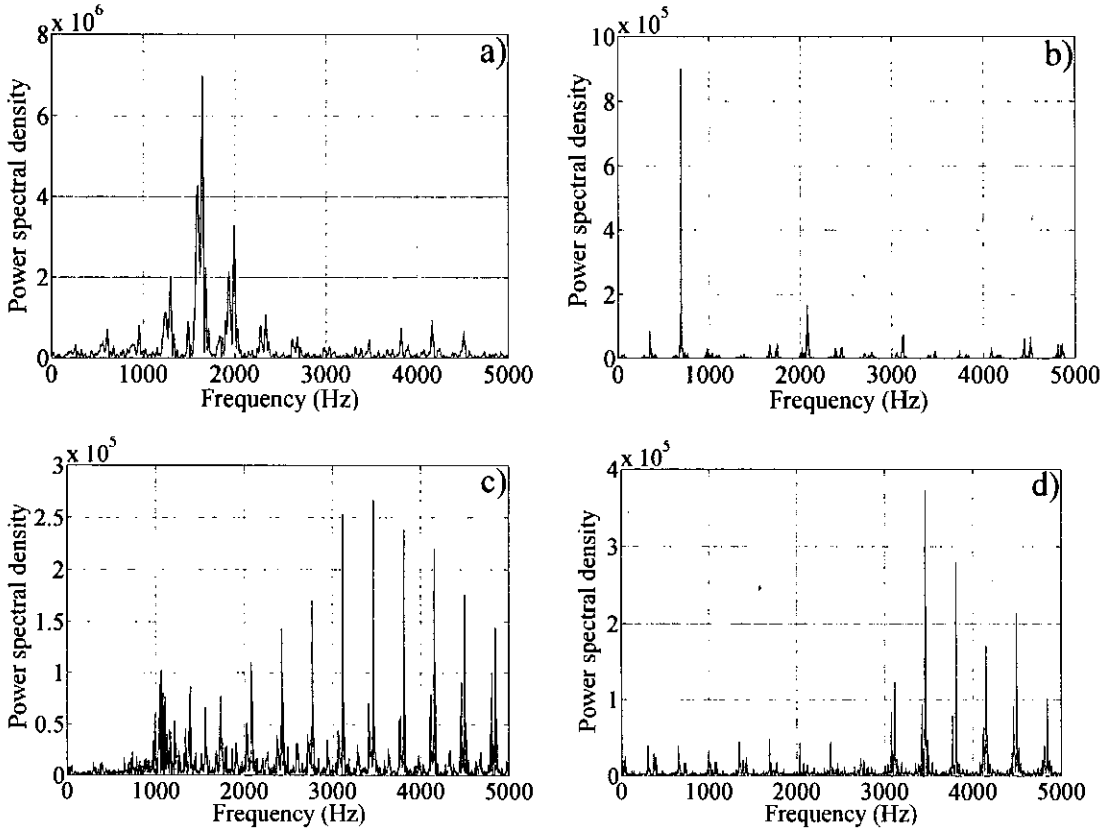

Figure 3.14: Frequency spectra for honk in Fig. 3.13 at a) P2, b) P4, c) P5 and d) P6.

A different honk is shown in Fig. 3.15 for positions P2, P4, P5 and P6 with silo at 60% of its capacity. The maximum acceleration amplitudes in this case are much lower than those for the honk in Fig. 3.13. For a 60% silo capacity, the maximum acceleration amplitudes were between 100 m/s² and 600 m/s² for a number of honks analysed. The frequency spectra for honk in Fig. 3.15 are shown in Fig. 3.16. Once again, the harmonic response is unchanged for this honk. The results show that the frequency content of honking does not change with the fill level variation, indicating that the stored material does not contribute to the honking response of the silo structure. This also indicates that the resonant frequency of the air-column and/or granular solids within the silo will change markedly as the fill level changes; however, no variation in the frequency of honking is observed. Previous published work (Buick et al., 2005), where the radial wall velocity is compared with the velocity variation due to the sound, has shown that honking can be generated by the radial vibration of the silo wall. Thus honking is generated by the motion of the silo

wall acting as a large loud speaker and cannot be likened to a flute or an organ where the sound is generated by resonance of air column inside.

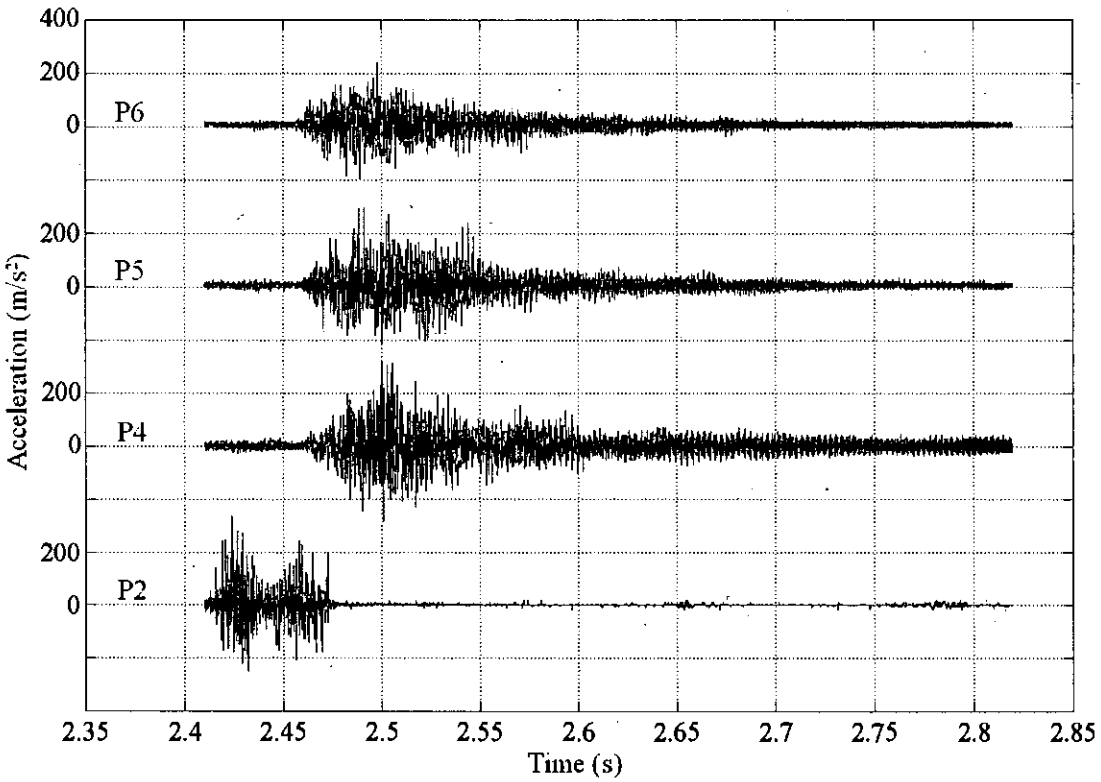

Figure 3.15: Radial acceleration readings for a honk at different positions with 60% silo capacity.

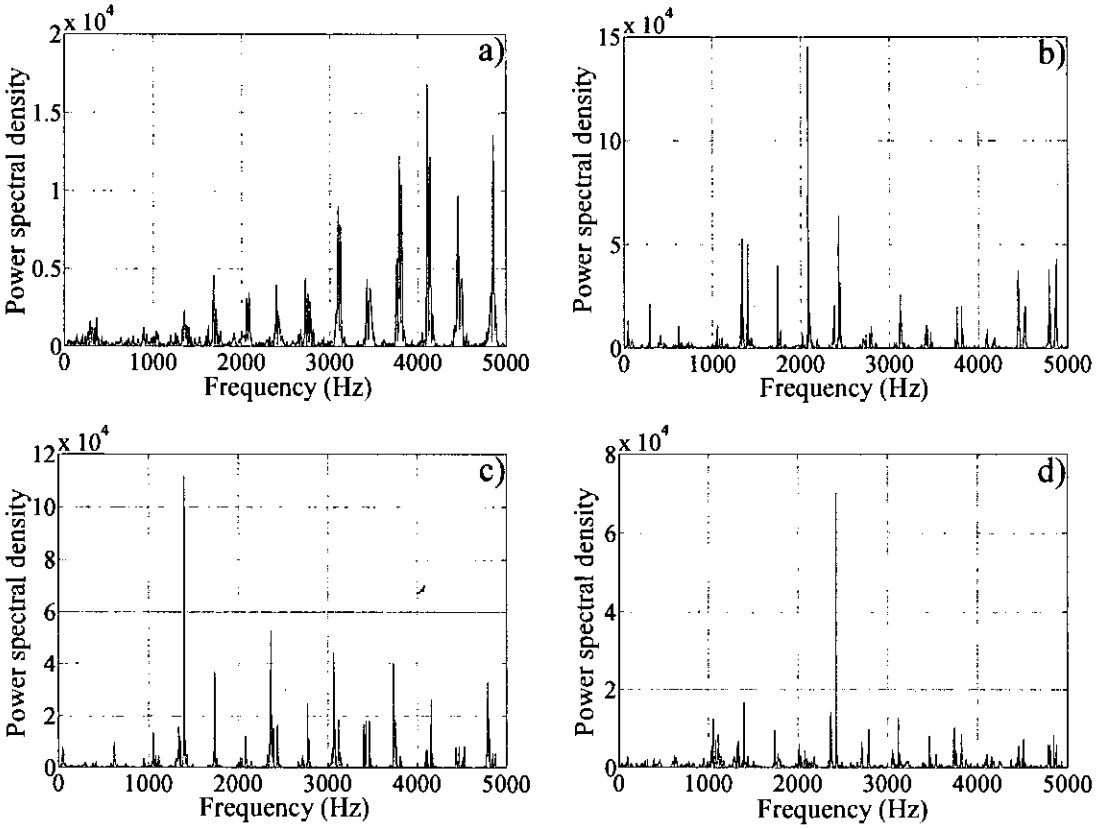

Figure 3.16: Frequency spectra for honk in Fig. 3.15 at a) P2, b) P4, c) P5 and d) P6.

3.3.5 Wall acceleration during non-honking periods

In this section the response during an entire discharge period (not just during a honk) is considered. Once again the measurements taken using the tri-axial accelerometer are used for this purpose. A different kind of behaviour is observed when the entire discharge period is considered. Two typical discharge periods previously shown in Fig. 3.9, with acceleration axes magnified, are shown in Fig. 3.17. The plots are for positions P2 ≈ 3.80 m and P5 ≈ 9.90 m. The relatively high acceleration amplitudes of the honks go off the vertical limits of these graphs. During non-honking periods, at intervals of 0.15-0.20 s (6.66-5 Hz), oscillatory motions of the order 5-10 m/s^2 are observed in the axial and radial directions in Fig. 3.17a. However, in Fig. 3.17b these oscillatory motions do not appear to occur with similar regularity and are mostly in the order of 5-10 m/s^2 in the axial direction and 5-20 m/s^2 in the radial direction (although at $t \approx 2$ s the radial accelerations nearly 300 m/s^2 can be observed). Similar motion with lower amplitudes is also observed in the circumferential direction. These

oscillatory motions are believed to represent the banging noises heard during the discharge process. However, in acoustic measurements they are difficult to identify, in the way they are observed in the acceleration measurements (see Fig. 3.17a), due to the plant background noise. As the plots in Fig. 3.17 show, these periodic oscillatory motions are more evident in the acceleration measurements taken at the lower part of the silo (position P2 in this case). This was the case for a number of readings analysed. Not only the oscillatory motions seem to occur between the range of time mentioned above but also the honks for the reading in Fig. 3.17a. To examine the change of frequency as a function of time wideband spectrograms in the radial and axial accelerations for the entire discharge period were computed and are shown in Figs. 3.18 and Fig. 3.19 for the two discharge readings at P2 and P5 respectively in Fig. 3.17. A wideband spectrogram can be made by selecting a small analysis window and these provide a better time resolution to observe individual pitch periods as vertical lines. The colours in the spectrograms represent different energy levels and for Figs. 3.18 and 3.19 red, orange, yellow, green, cyan and blue have decreasing levels of energy associated with them respectively. The red vertical lines that extend the entire height of the graph represent the honks and show that during honking high energy is associated with a wide range of frequencies. Apart from the honks the spectrograms also show a number of orange or yellow vertical lines spaced at 0.15-0.20 s in Figure 3.18. These lines represent the oscillatory motions seen in Fig. 3.17a. The fairly periodic behaviour in the radial and axial directions can be clearly seen in these spectrograms. Figure 3.19 shows the spectrograms for the radial and axial acceleration readings in Fig. 3.17b. The fairly periodic behaviour is not as clear as it is for the lower position. However, between 1.5 s and 3.8 s the fairly periodic behaviour is observed in both radial and axial spectrograms. It is important to note that in the axial spectrograms (see Figs. 3.18b and 3.19b) lower frequencies (< 500 Hz) are associated with higher energy.

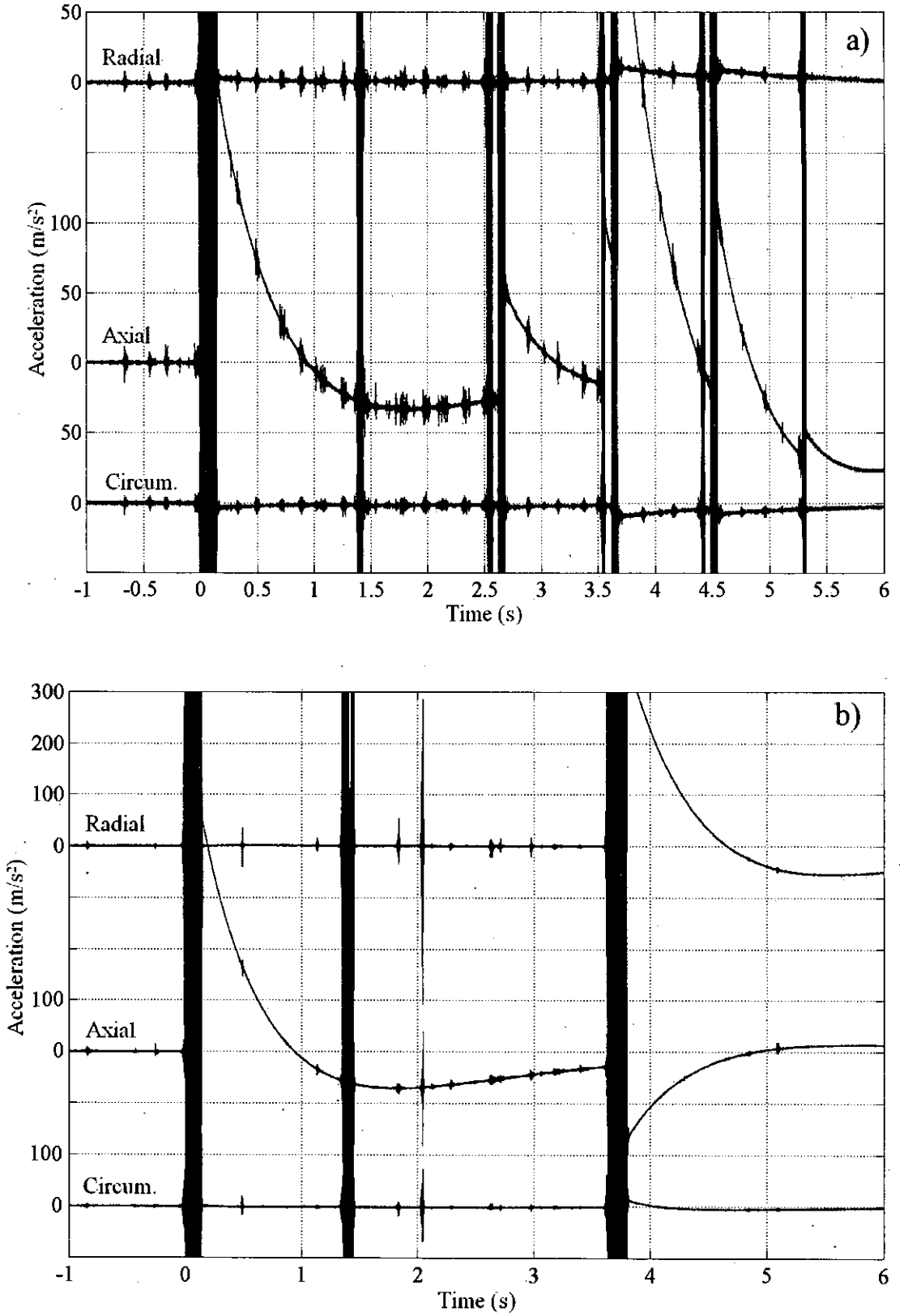

Figure 3.17: Magnification of the tri-axial acceleration reading at a) P2 ≈ 3.80 m and b) P5 ≈ 9.90 m for two different a discharge periods.

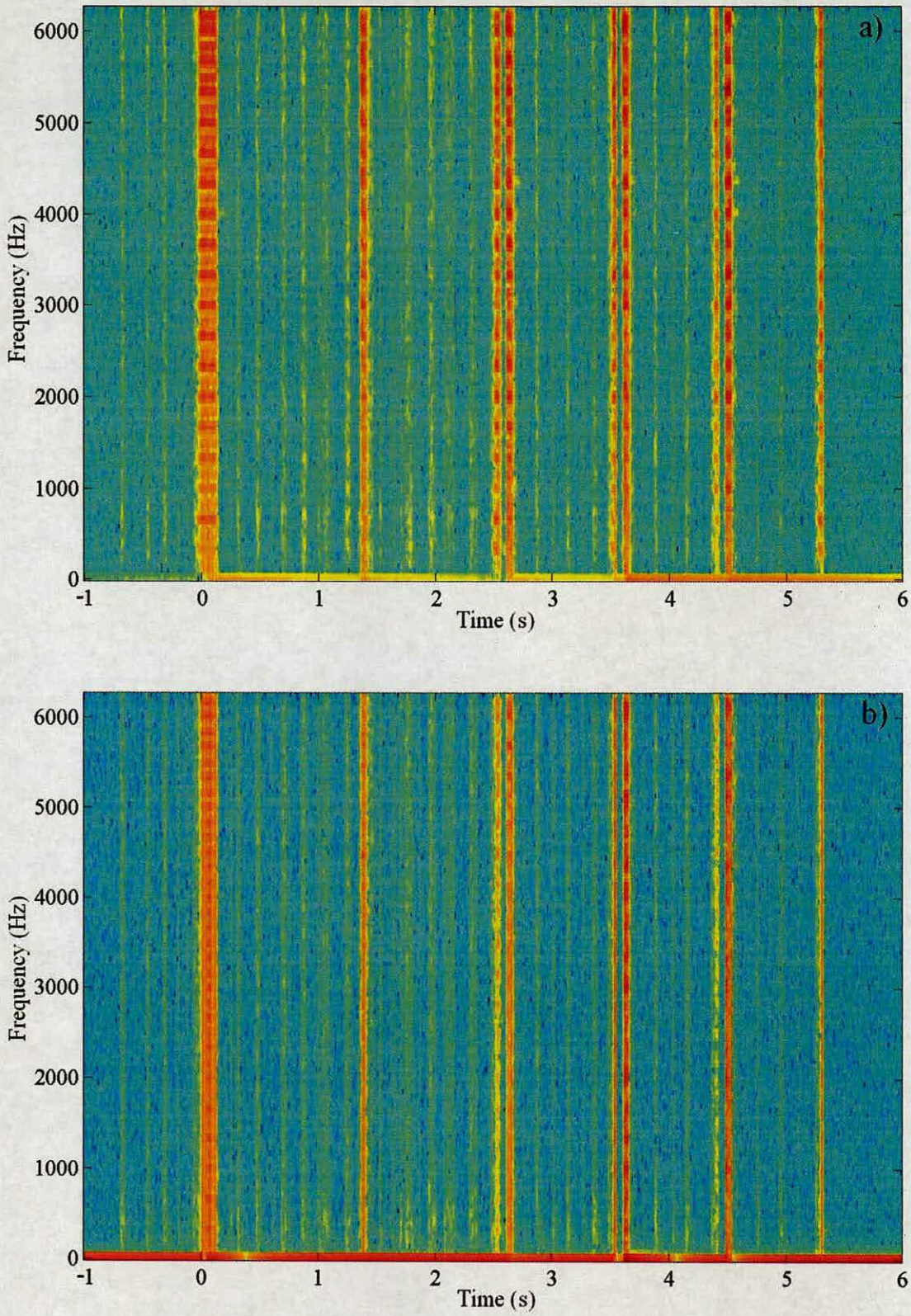

Figure 3.18: Wideband spectrogram for a) radial and b) axial acceleration reading in Fig. 3.17a.

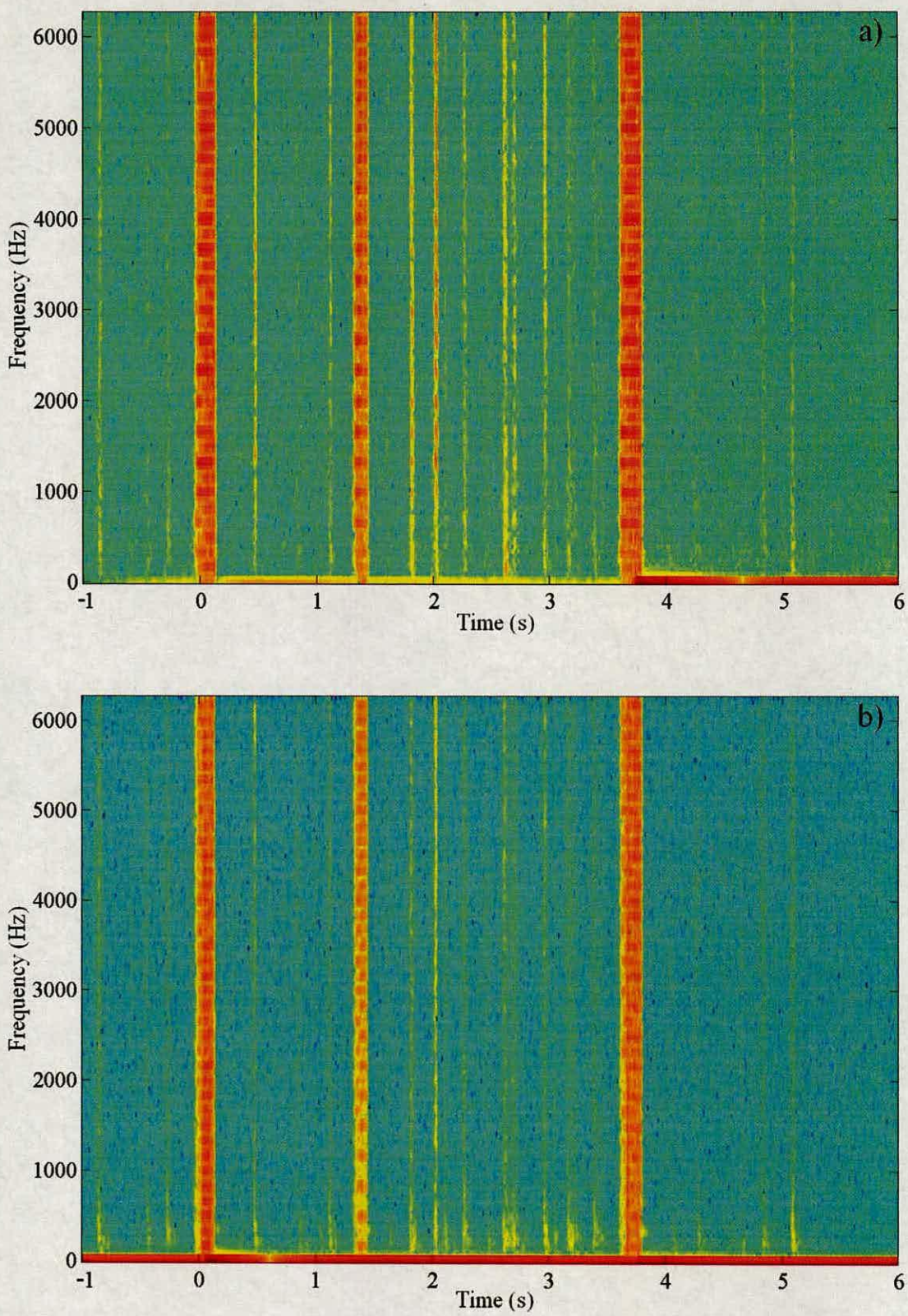

Figure 3.19: Wideband spectrogram for a) radial and b) axial acceleration reading in Fig. 3.17b.

One non-honking period of time from each discharge period of Fig. 3.17 is selected for frequency analysis. The periods of time selected are between 1.5 s and 2.5 s for Fig. 3.17a and between 1.5 s and 3.6 s for Fig. 3.17b. The periods chosen do not include honks. The spectra are presented in Fig. 3.20 and Fig. 3.21 for the non-honking periods in reading of Fig. 3.17a and Fig. 3.17b respectively. Figure 3.20 shows the radial and axial spectra for the non-honking period in Fig. 3.17a (P2). A harmonic response with a fundamental frequency of 333 Hz can be seen in the radial spectrum, however, it is not as clear as in the spectra corresponding to honks shown in previous sections. The harmonic peaks can be observed below 2000 Hz. In the axial spectrum of Fig. 3.20b the harmonic response is not observed as it is in axial spectra during honking. In fact, the axial frequencies with high energy in the non-honking period are below 600 Hz. The spectral analysis for radial acceleration of the selected non-honking period of Fig. 3.17b (P5) shows clear peaks at intervals of 333 Hz. However, the fundamental frequency 333 Hz and second harmonic are not visible in the spectrum. The first visible harmonic is the third one (1000 Hz) with a low energy but the fourth one (1333 Hz) reaches the highest value in energy in the spectrum. For Fig. 3.21b, which is the axial spectrum for the non-honking period of Fig. 3.17b (P5), the behaviour is similar to that in Fig. 3.20b. The frequencies with higher energy are below 600 Hz, harmonic response is not evident in low frequency range. These radial spectra during non-honking periods show that harmonic response occurs even when the silo is not honking. However, it is not clear from these analyses if this harmonic response is present in the entire discharge period or it is just seen in the spectra due to honks and periodic oscillations discussed earlier.

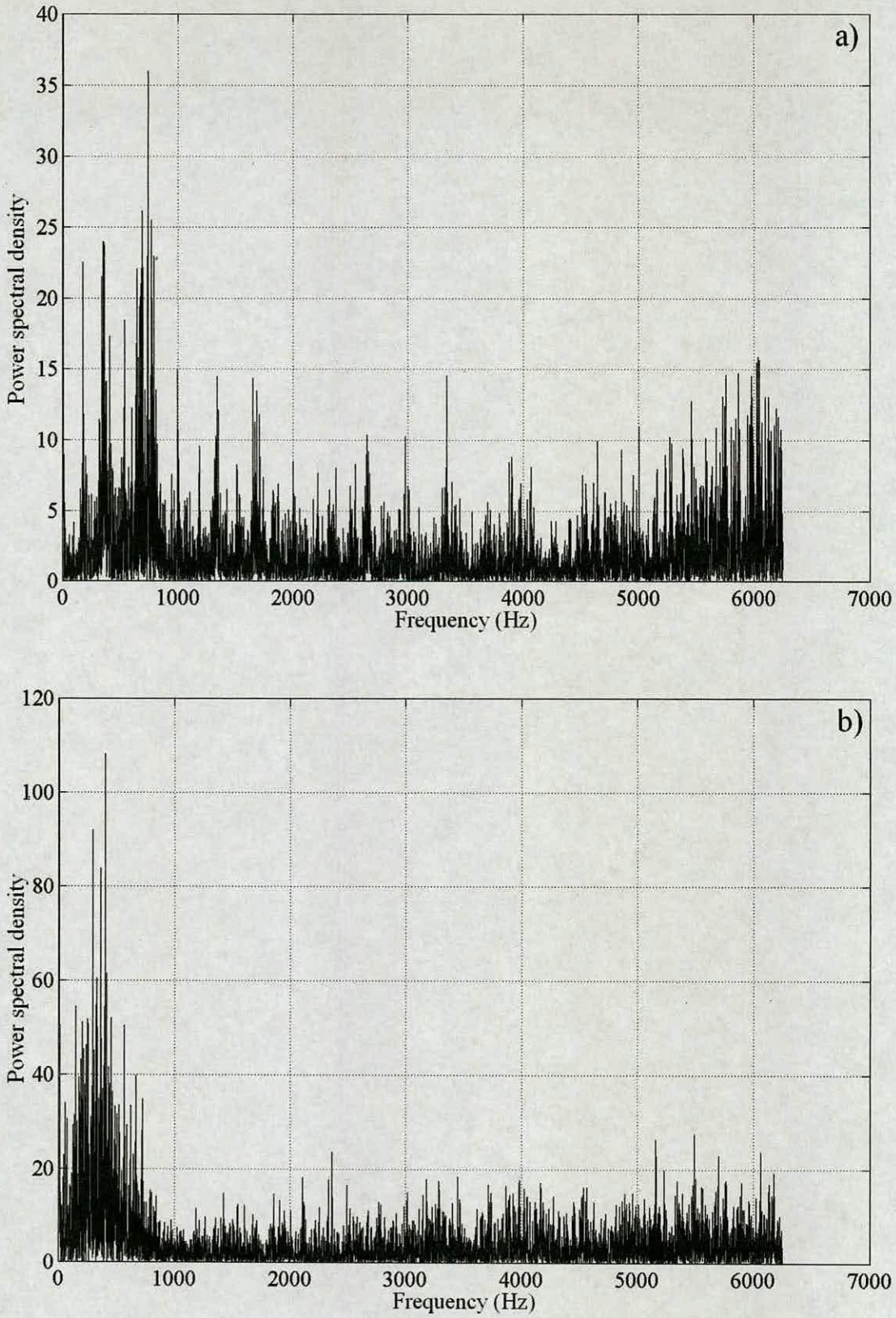

Figure 3.20: Frequency spectra for the non-honking period between 1.5 s and 2.5 s in Fig. 3.17a for the a) radial and b) axial acceleration.

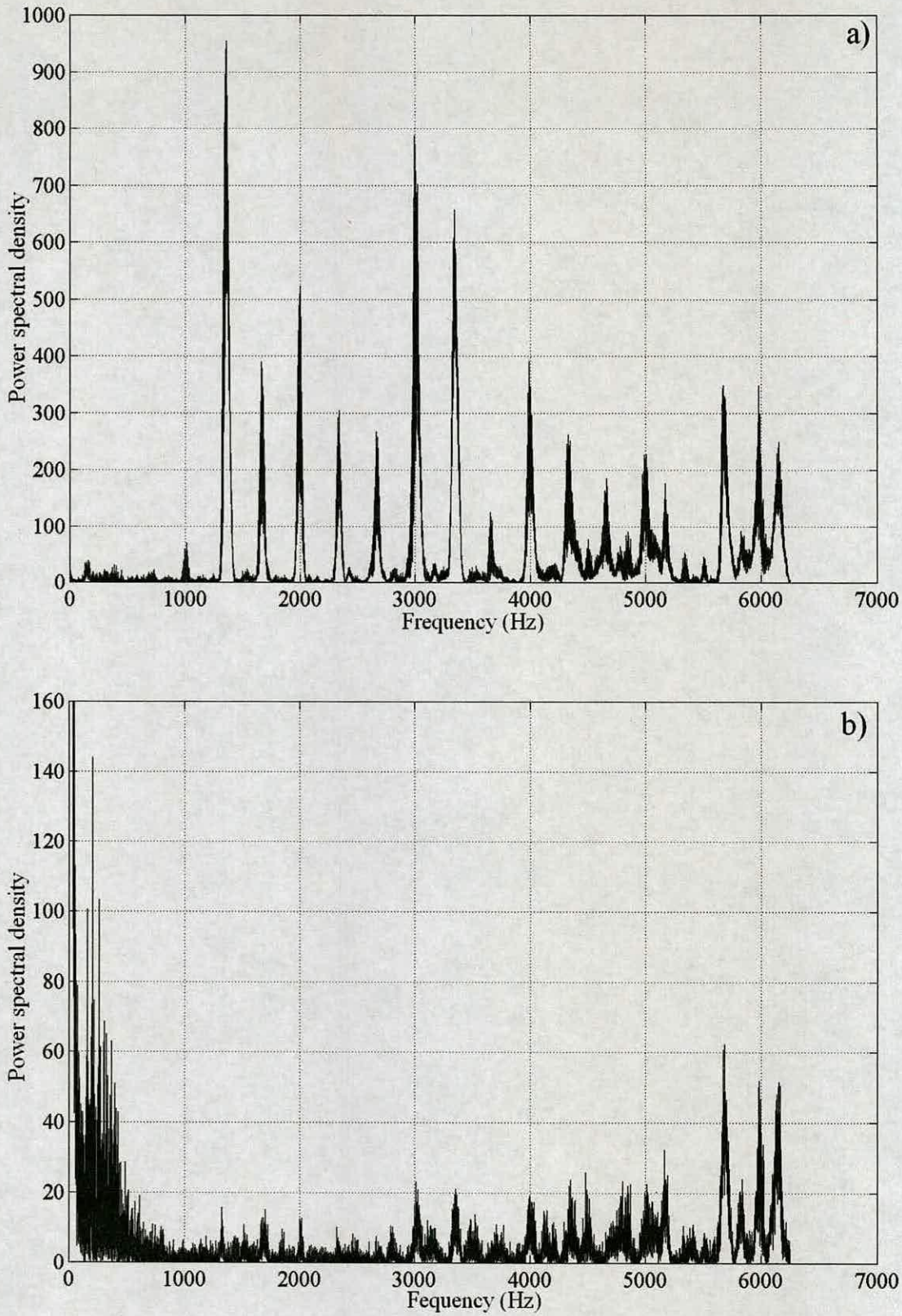

Figure 3.21: Frequency spectra for the non-honking period between 1.5 s and 3.6 s in Fig. 3.17b for the a) radial and b) axial acceleration.

To investigate the harmonic response during non-honking period frequency analyses of a number of periodically occurring oscillatory motions were conducted. The radial and axial frequency spectra for two oscillatory motions in Fig. 3.17a at $t \approx 1.95$ s and Fig. 3.17b at $t \approx 1.82$ s are presented in Figs. 3.22 and 3.23 respectively. The results presented in these figures are typical of these motions. The oscillatory motion in Fig. 3.22 was extracted from the acceleration reading in Fig. 3.17a. It shows a harmonic response in the radial direction (Fig. 3.22a) with clearer peaks below 2000 Hz. However, higher harmonics can also be observed in the spectrum. The axial spectrum in Fig. 3.22b does not show a harmonic response but it shows the highest energy values for frequencies below 600 Hz. The behaviour of this single oscillatory motion matches the behaviour of the whole non-honking period analysed above. In the same way the single oscillatory motion analysed from Fig. 3.17b (P5) shows in Fig. 3.23 similar behaviour to the whole non-honking period. For example in the radial spectrum (Fig. 3.23a) the harmonic response is also observed with clear peaks above 1000 Hz (compare with Fig. 3.21a) and in the axial spectrum (3.23b) the highest energy values again correspond to frequencies below 600 Hz and harmonic peaks are barely observed at higher frequencies.

A different set of frequency analyses is conducted in regions where no oscillatory motion takes place during non-honking periods. The results are presented in Fig. 3.24 and Fig. 3.25 for non-honking periods in Fig. 3.17a (P2) and 3.17b (P5) respectively. A harmonic response is not observed in any of the spectra, neither radial nor axial. These results indicate that harmonic response is not present in the entire discharge period but occurs at periodic intervals. At each interval a honk or oscillatory motion takes place, which contains a harmonic set of frequencies in the radial direction. However, the sound is not always radiated from the structure probably because the necessary amount of energy to produce honking is not always reached.

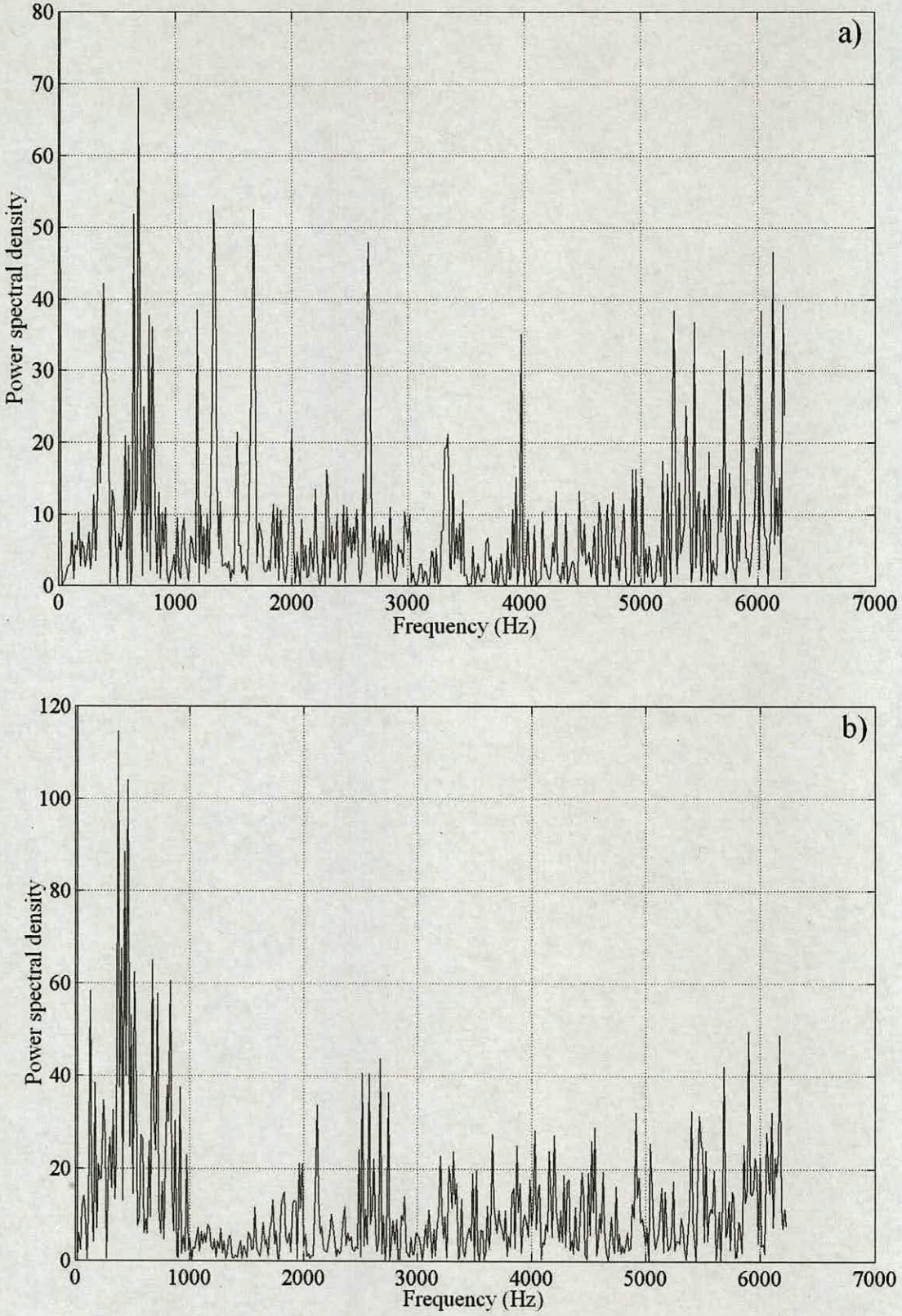

Figure 3.22: Typical frequency spectrum for a single oscillatory motion in Fig. 3.17a during non-honking periods for the a) radial and b) axial acceleration.

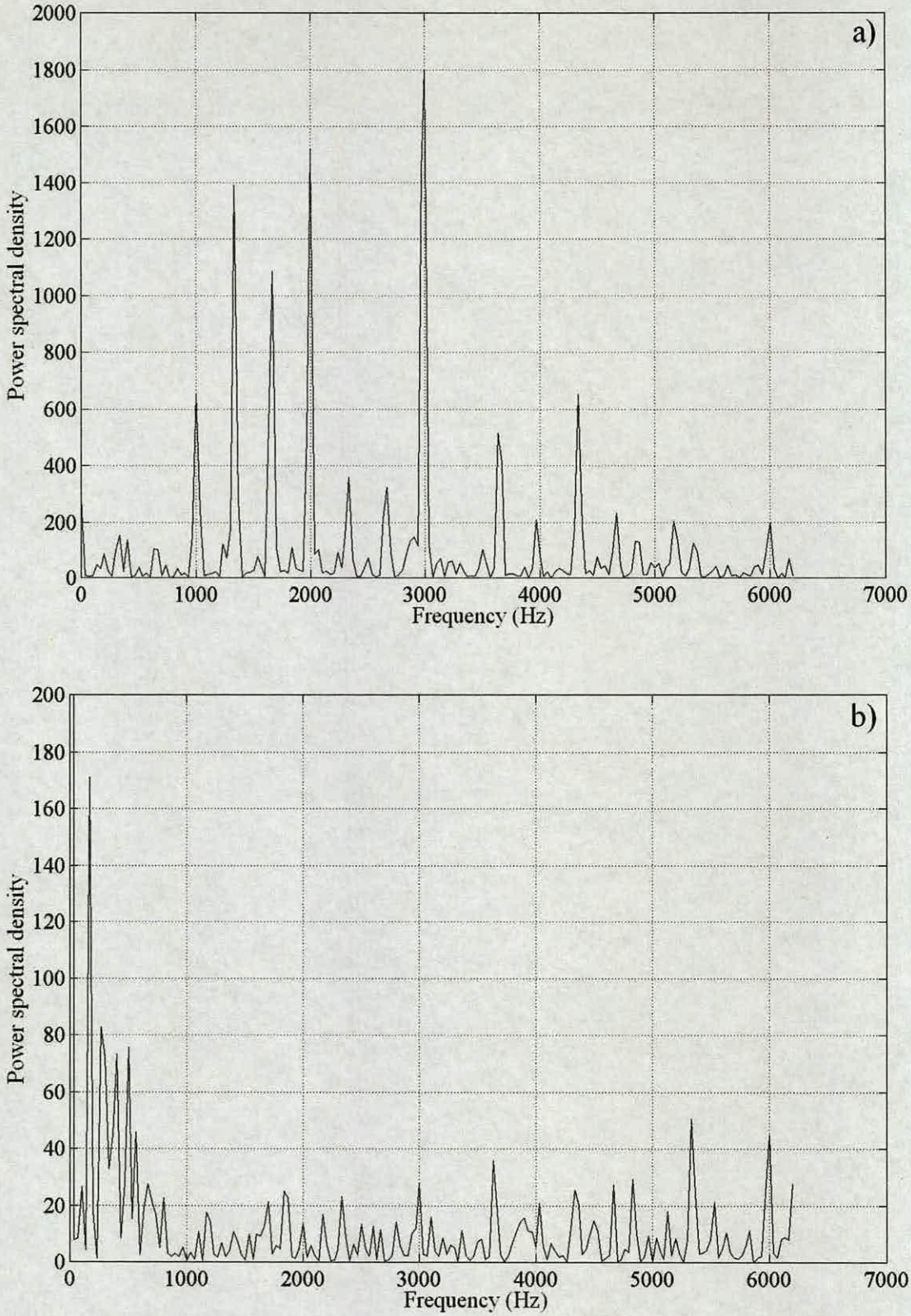

Figure 3.23: Typical frequency spectrum for a single oscillatory motion in Fig. 3.17b during non-honking periods for the a) radial and b) axial acceleration.

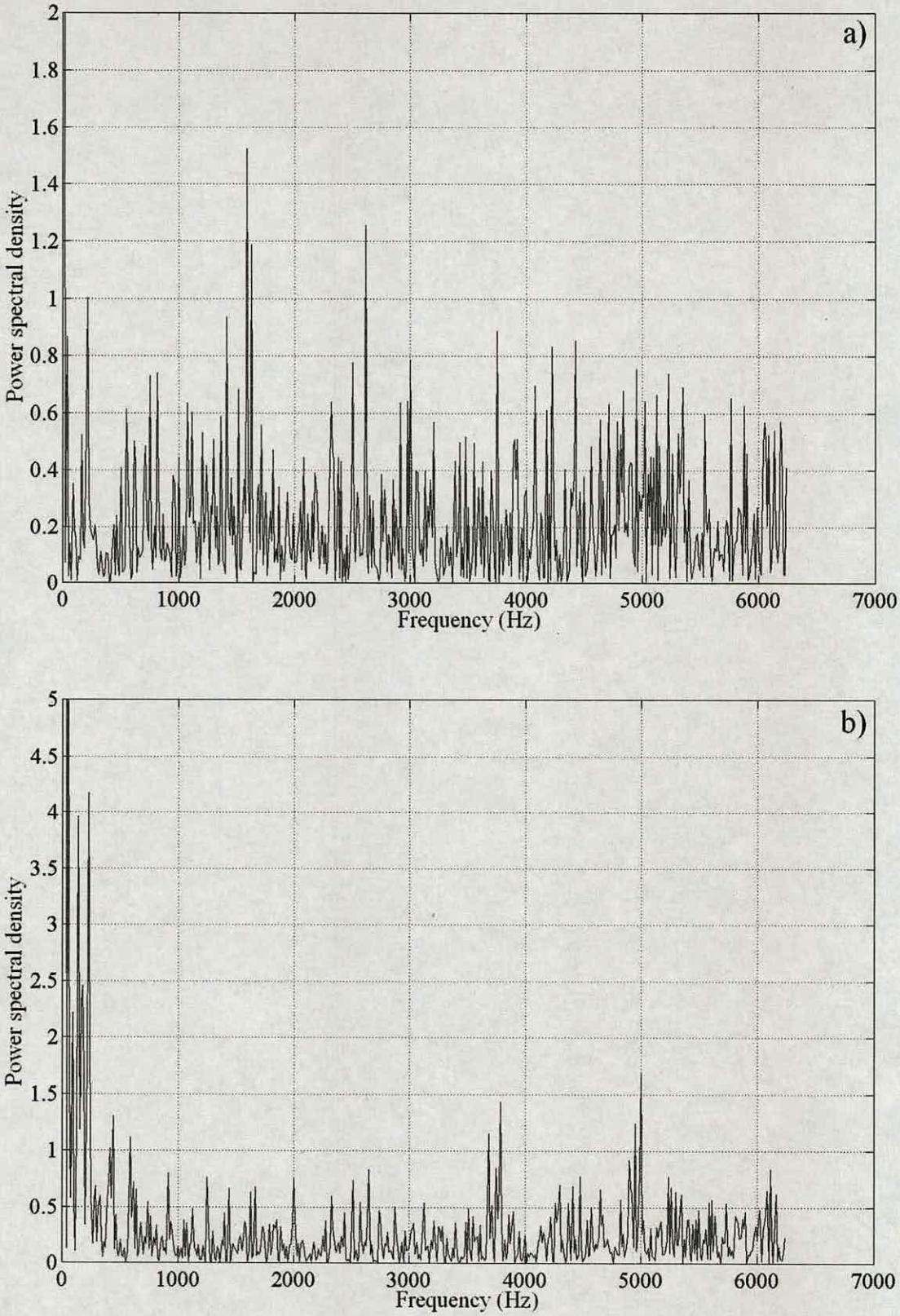

Figure 3.24: Typical frequency spectrum for non-oscillatory motion regions in Fig. 3.17a during non-honking periods for the a) radial and b) axial acceleration.

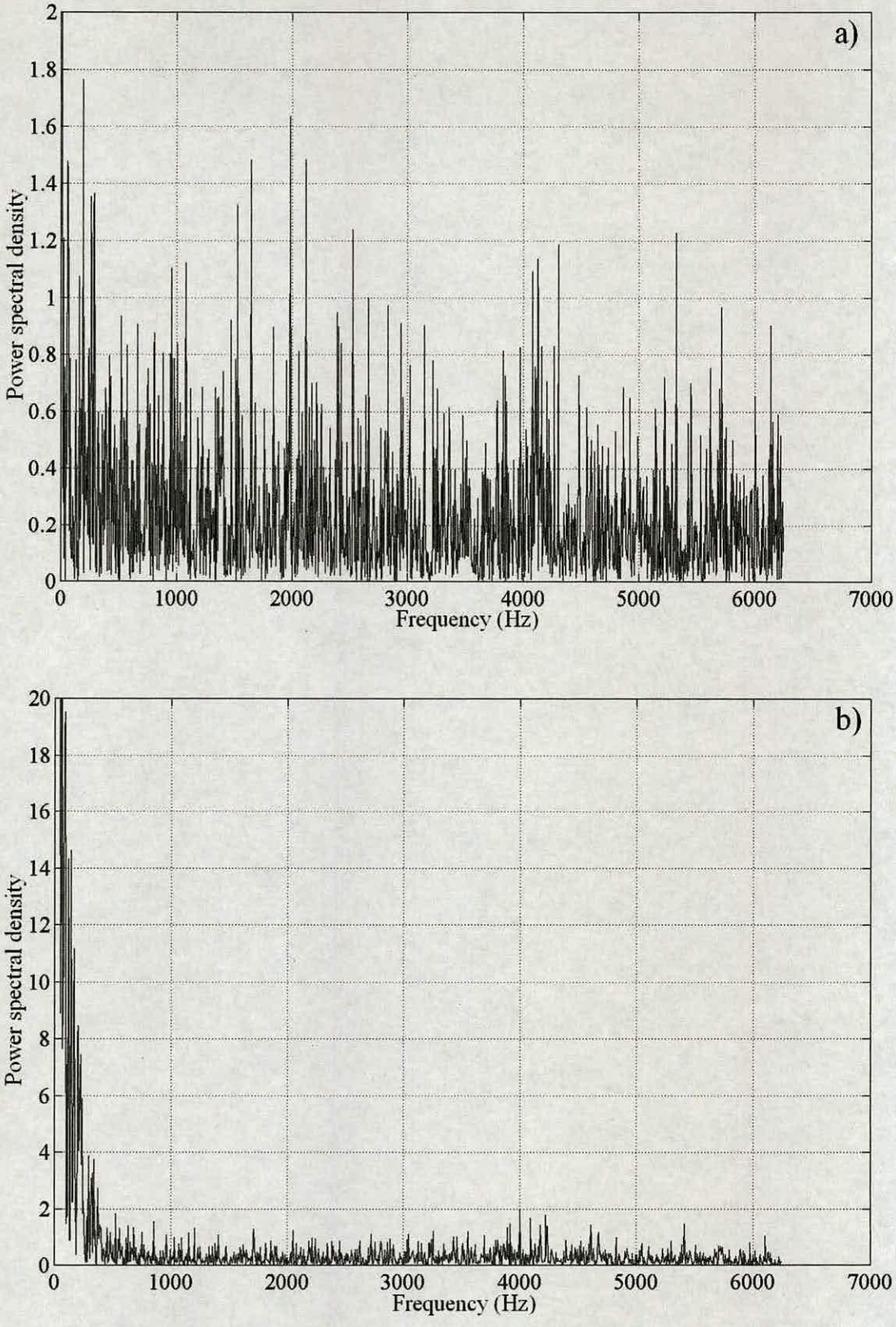

Figure 3.25: Typical frequency spectrum for non-oscillatory motion regions in Fig. 3.17b during non-honking periods for the a) radial and b) axial acceleration.

3.4 Cases of study

Four cases of aluminium silos that have been previously reported to honk are discussed in this section. The geometry of the honking silos is presented in Fig. 3.26. The details of instrumentation and analysis for the first three of these cases can be found in Tejchman (1999) and Hupkes (2003). The geometry and the sound file for Case4 was obtained directly from the concerned industry. These silos have been reported to honk at 292 Hz (Case1), 333 Hz (Case2) and 246 Hz (Case3) as the fundamental honking frequency and their correspondent harmonics. Banging and quaking has been reported for the first three cases in addition to honking, with bangs outnumbering honks. However, the sound file obtained during discharge from silo Case4 shows a much larger number of honks than bangs. Frequency analysis of a typical honk for Case4 is shown in Fig. 3.27. A number of analyses were conducted with the sound file where single honks and a few honks together were analysed. Frequency content in all cases was similar to those shown in Fig. 3.27. The sound spectrum for this case is different from those presented in this Chapter and reported in previous research studies (Tejchman, 1999; Hupkes, 2003) in one respect. For cases 1 to 3 and for the instrumented silo considered earlier in this Chapter the fundamental honking frequency was always present in the honking sound spectrum. However, for the silo in Case4 the fundamental honking frequency is not observed but its second and subsequent harmonics seem to be present. This can be easily deduced from the separation of peaks, which is 240 Hz. If the fundamental acoustic frequency were 480 Hz (first visible peak in the sound spectra of Fig. 3.27) then the subsequent harmonics would be at this separation. There is no apparent explanation for this difference observed in this honking silo with respect to the others. It is interesting to note that the aluminium silo described in Section 3.2.1 and the silo in Case2 both honk at the same fundamental frequency and its correspondent harmonics. The only apparent similarity is the diameter and the hopper angle, which are 3.0 m and 60° respectively in both cases. In fact, it appears that the honking fundamental frequency is inversely proportional to the diameter and is given by $f_h=1000/D$ where f_h is the honking fundamental frequency and D the cylinder

diameter. However, up to now, there is no rational explanation for this relationship. These cases of study will be used further in subsequent Chapters.

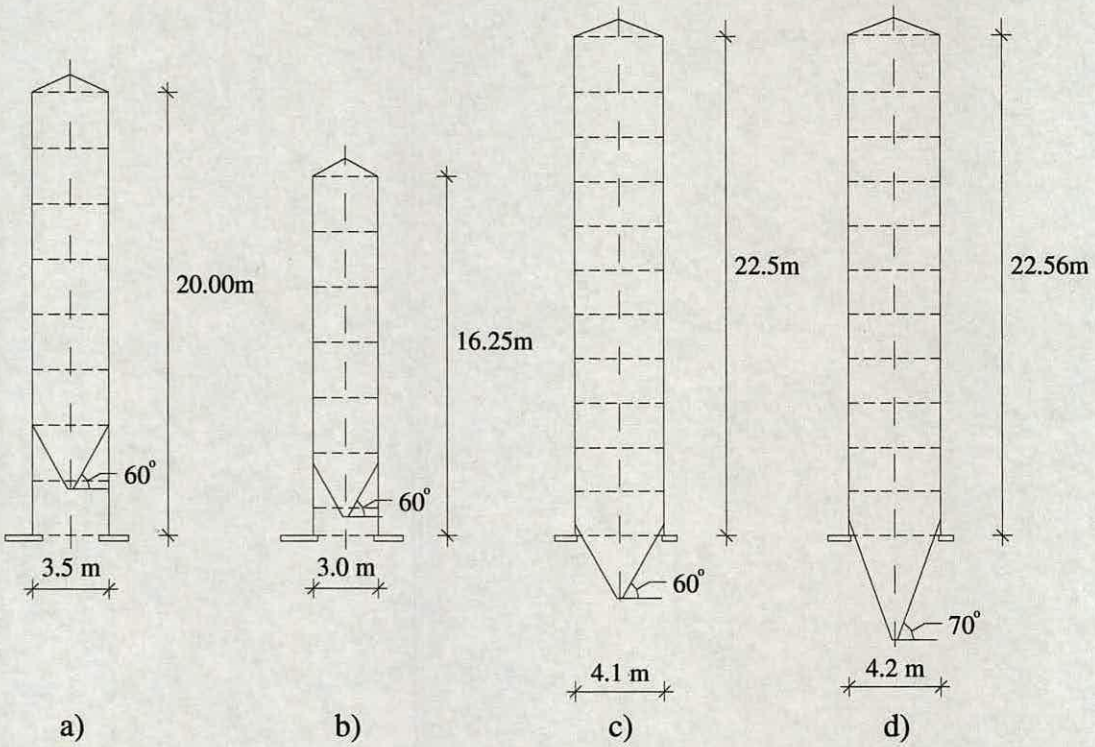

Figure 3.26: Geometry of honking silos reported previously a) Case1 (Tejchman, 1999), b) Case2 (Hupkes, 2003), c) Case3 (Hupkes, 2003) and d) Case4.

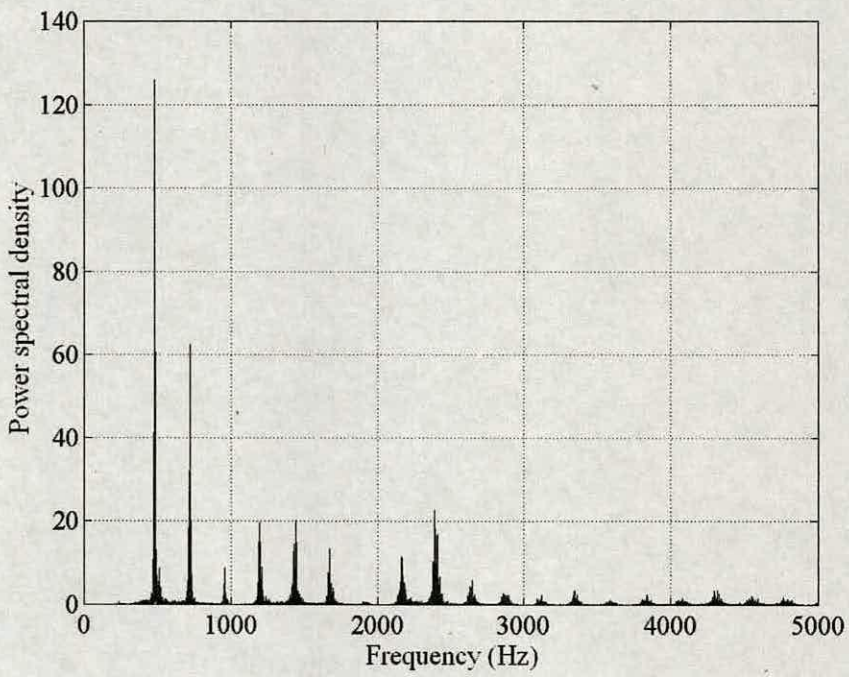

Figure 3.27: Sound spectra analysis for honking silo Case4.

3.5 Conclusions

Measurements using two different instrumentation set-ups were conducted to characterise the honking phenomenon. Acoustic emission and silo wall accelerations in the three directions (radial, axial and circumferential) were recorded simultaneously in the first set of measurements. For the second one, the radial wall vibration was measured simultaneously at different positions along the height. From the digital signal is possible to compare the acoustic and acceleration signals, which is essential to obtain a full picture of the phenomenon since all honks are not identical. Once this comparison was conducted, a further investigation of the height and fill influence on the radial wall vibration was also conducted. The following conclusions can be drawn:

- *Acoustic emission during honking.* Frequency spectra show clear peaks in harmonic series with the acoustic fundamental frequency at 333 Hz for the instrumented silo in this study.

- *Wall acceleration during honking.* During honking large acceleration amplitudes of the order of several hundred times the acceleration due to gravity are observed. The amplitudes of the radial accelerations were generally larger than acceleration amplitudes in the axial direction. The circumferential acceleration was considerably smaller. Frequency spectra of the three components of the acceleration showed the same harmonic response of the structure with peaks at the fundamental frequency and integer multiples of this frequency as the acoustic emission. For the acceleration measurements, the lowest frequency peaks are typically smaller and often the fundamental peak is indistinguishable. The harmonic response of the structure during honking was repeatable for all the honks analysed.

- *Wall acceleration at different heights during honking.* The frequency spectra show that the harmonic response is independent of position of the accelerometer and fill level, indicating that the stored material does not participate in the honking response of the silo structure. This further supports

the assertion that the acoustic emission is due to the wall vibrations acting as a speaker since the frequency of an internal resonance would vary with the fill level.

- *Wall acceleration during non-honking periods.* A different kind of behaviour is observed when the entire discharge period is considered. During non-honking periods relatively small oscillatory motions are observed. These are more evident in the axial and radial directions. These oscillatory motions are thought to represent the banging noises heard during the discharge process. These are more evident in the acceleration measurements taken at the lower part of the silo. The spectra of individual small oscillations during non-honking periods show that harmonic response is present in radial vibration of the silo structure. However, honking sound is not emitted from the structure probably because the necessary amount of energy to produce a honk is not reached. This harmonic response is not observed in the axial spectra during non-honking periods. Moreover, the harmonic response of the silo structure is not observed for periods where oscillatory motions are not apparent in the acceleration response in non-honking periods, indicating that harmonic frequencies are not present during the entire discharge process. The above indicates that honking cannot be due to a steady state harmonic response of the excitation source. The spectrograms of the full discharge readings show a fairly regular period between honks and oscillatory motions suggesting that the same periodic transient excitation is causing them.

Chapter 4

Free vibration characteristics of circular cylindrical shells

4.1 Introduction

This Chapter is intended to review the theory related with the free vibration characteristics of circular cylindrical shells with the aim of understanding their behaviour and validate Finite Element (FE) models of shells having different boundary conditions. The review starts with the equations of motion of cylindrical shells followed by the considerations of cylindrical shells of infinite length and those of finite length with different boundary conditions. Closed form solutions for natural frequencies and vibration modes under different boundary conditions are considered using characteristics of the barrel of the honking silo examined in Chapter 3. The results obtained from the closed form solutions are compared with three-dimensional (3D) and axisymmetric FE models of simple shells. These comparisons are used to validate the FE models, which will be subsequently (in Chapter 5) refined to include roof, hopper and thickness variation that were presented in the honking silo geometry.

4.2 Equations of motion

Before considering the equations of motion it is important to enumerate the basic assumptions introduced by Love (Leissa, 1973) in deriving the equations of motion for thin shells.

- The shell thickness is small compared with the shell radius.
- The displacement is small in comparison with the shell thickness.
- The transverse normal stress that acts on planes parallel to the shell middle surface, which is defined as the surface located midway from two closely spaced curved surfaces that bound the three dimensional body of the thin shell, is neglected.
- The fibres perpendicular to the middle surface remain perpendicular after deformation and do not elongate.

The shell coordinate system (x, θ) to be used is shown in Fig. 4.1, where h is a constant thickness, R is the radius and L is the length of the shell. The middle surface of the shell is taken as the reference surface. The orthogonal components of displacement are defined by u, v and w in the x, θ and radial directions respectively.

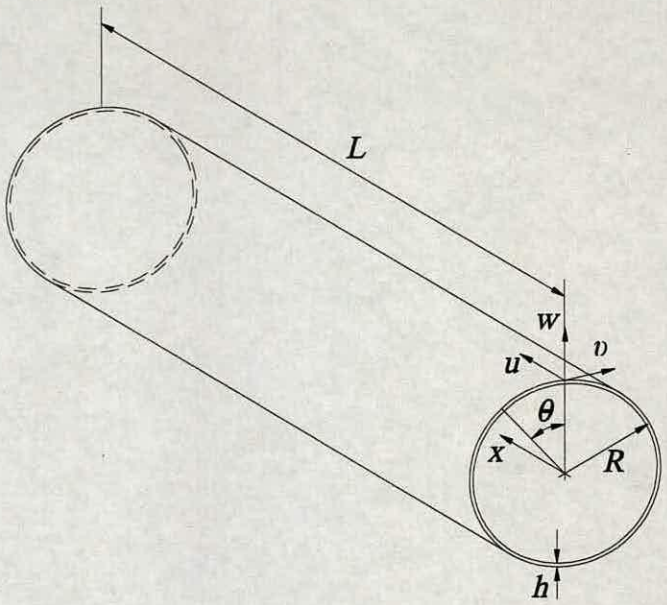

Figure 4.1: Closed circular cylindrical shell and coordinate system (redrawn from Leissa, 1973).

The equations of motion for thin cylindrical shells (for a complete derivation of these equations see Leissa, 1973) can be written in matrix form as:

$$[L]\{u_i\} = \{0\} \tag{4.1}$$

where $\{u_i\}$ is the displacement vector

$$\{u_i\} = \begin{bmatrix} u \\ v \\ w \end{bmatrix} \tag{4.2}$$

and $[L]$ is the matrix differential operator. This operator differs depending on which shell theory is applied to model the vibrational behaviour of circular cylindrical shells. Here the Donnell-Mushtari shell theory (Leissa, 1973) is applied and the operator takes the form

$$[L]=\begin{bmatrix} \frac{\partial^2}{\partial s^2}+\frac{(1-\nu)}{2}\frac{\partial^2}{\partial\theta^2}-\rho\frac{(1-\nu^2)R^2}{E}\frac{\partial^2}{\partial t^2} & \frac{(1+\nu)}{2}\frac{\partial^2}{\partial s\partial\theta} & \nu\frac{\partial}{\partial s} \\ \frac{(1+\nu)}{2}\frac{\partial^2}{\partial s\partial\theta} & \frac{(1-\nu)}{2}\frac{\partial^2}{\partial s^2}+\frac{\partial^2}{\partial\theta^2}-\rho\frac{(1-\nu^2)R^2}{E}\frac{\partial^2}{\partial t^2} & \frac{\partial}{\partial\theta} \\ \nu\frac{\partial}{\partial s} & \frac{\partial}{\partial\theta} & 1+k\nabla^4+\rho\frac{(1-\nu^2)R^2}{E}\frac{\partial^2}{\partial t^2} \end{bmatrix} \tag{4.3}$$

where $\nabla^4 = \nabla^2\nabla^2$ and

$$\nabla^2 \equiv \frac{\partial^2}{\partial s^2}+\frac{\partial^2}{\partial\theta^2} \tag{4.4}$$

$$k = \frac{h^2}{12R^2} \tag{4.5}$$

In a similar way, the material properties of the shell E, ν and ρ represent the Young's modulus, Poisson's ratio and density respectively, t is the time variable and $s = x/R$. It is important to note that in addition to the assumptions introduced by Love, the Donnell-Mushtari shell theory neglects the transverse shear resultant terms (Leissa, 1973). Different theories for thin shells (e.g. Love-Timoshenko, Sanders, etc.) differ from the Donnell-Mushtari theory by the addition of a modifying operator that is multiplied by k, which is very small for small h/R ratios.

4.3 Circular shell of infinite length

Although the infinite shell case does not apply to the particular honking silo presented in Chapter 3, the reasons for examining it are that it is simple and forms the basis for some of the more complicated cases. Assume the displacements of the shell take the form

$$\left.\begin{aligned} u &= A\cos(\lambda_m s)\cos(n\theta)\cos(\omega t) \\ v &= B\sin(\lambda_m s)\sin(n\theta)\cos(\omega t) \\ w &= C\sin(\lambda_m s)\cos(n\theta)\cos(\omega t) \end{aligned}\right\} \tag{4.6}$$

where A, B and C are the amplitudes of vibration in the axial, circumferential and radial directions respectively, λ_m is the axial wavelength factor (to be discussed), n is a positive integer and ω is the natural frequency in radians per second. Equations 4.6 assume that the spatial and time variables can be separated, permitting the normal modes to execute simple harmonic motion. All the points in the shell have the same period and phase of the motion.

Substitution of Equations 4.6 into Equation 4.1 using the Donnell-Mushatari operator of Equation 4.3 permits the factorization of the terms that contain s, θ and t out of each equation. This can be represented in matrix form as:

$$\begin{bmatrix} -\lambda_m^2 - \frac{(1-\nu)}{2}n^2 + \Omega^2 & \frac{(1+\nu)}{2}\lambda_m n & \nu\lambda_m \\ \frac{(1+\nu)}{2}\lambda_m n & -\frac{(1-\nu)}{2}\lambda_m^2 - n^2 + \Omega^2 & -n \\ -\nu\lambda_m & n & 1 + k\left(\lambda_m^2 + n^2\right)^2 - \Omega^2 \end{bmatrix} \begin{bmatrix} A \\ B \\ C \end{bmatrix} = \begin{bmatrix} 0 \\ 0 \\ 0 \end{bmatrix} \tag{4.7}$$

where Ω^2 is the square frequency parameter from which the frequency ω can be calculated using the expression:

$$\Omega^2 = \frac{\rho(1-\nu^2)R^2\omega^2}{E}. \tag{4.8}$$

The natural frequency f in cycles per second (Hz) can also be calculated from the angular frequency ω using

$$f = \frac{\omega}{2\pi} \tag{4.9}$$

Equation 4.7 represents an eigenvalue problem and admits a trivial solution if the amplitudes vector is set equal to zero. However, the interest is to find the nontrivial solution, i.e. to find the values of Ω^2 if they exist (Greenberg, 1998). To find the nontrivial solution, the determinant of the coefficient matrix in Equation 4.7 is set to zero. The problem can then be solved giving λ_m values and obtaining Ω^2 values or vice versa. If the λ_m value is chosen to be $m\pi R/L$ where m is a positive integer then the frequencies of free vibration can be found corresponding to a given wavelength.

4.4 Modes of vibration in circular shells of finite length

Many authors, including Arnold and Warburton (1949), Leissa (1973) and Kraus (1967), have described the vibration forms of closed cylindrical shells vibrating freely and having a finite length. A cylindrical thin shell may be deformed, while vibrating, along its circumference and height. These deformations consist of a number of circumferential waves and axial half waves, denoted by integers n and m respectively as shown in Fig. 4.2. Transversal vibrating sections are shown in Fig. 4.2a where n is equal to 0, 2 and 3. In the axisymmetric mode (n = 0) the circumferential waves and nodal lines are absent. Circumferential nodal lines are the points of zero displacement along the height and axial nodal lines are defined in the same way, but along the circumference. For the cases n = 2 and n = 3 the circumferential waves and nodal lines are easily identified. In a similar way, lateral views of vibrating shells with different boundary conditions are shown in Fig. 4.2b. The shape of the axial half waves is modified by the boundary conditions as shown in the figure, similar to a beam with the same end conditions, where m is equal to 1, 2 and 3. For the Shear Diaphragm (SD) boundary condition the radial and circumferential displacement are restricted to zero.

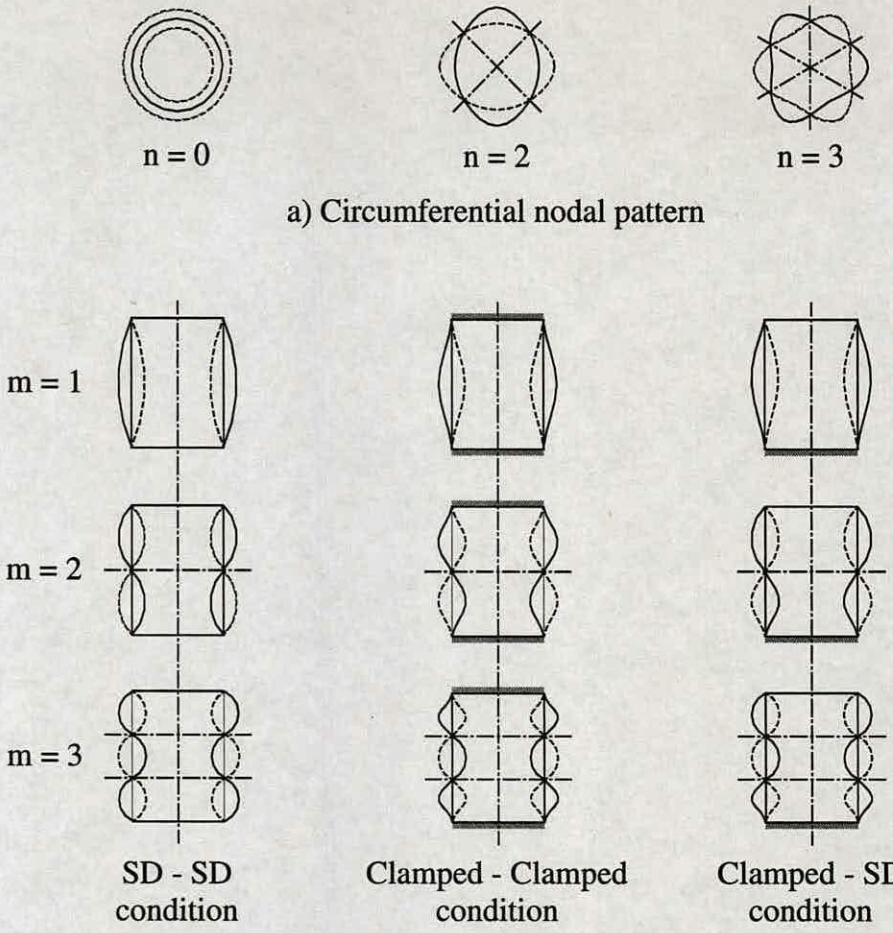

Figure 4.2: Nodal patterns for circular cylindrical shells, a) Circumferential and b) Axial.

4.5 Finite shells with simple boundary conditions

Different authors have proposed simplified equations to calculate the natural frequencies of finite cylindrical shells with various end conditions (Sharma, 1979,1980; Soedel, 1980). It is possible to obtain exact solutions for the frequencies and mode shapes for the free vibration for many different boundary conditions. This can be achieved assuming generalizations of the displacements in Equation 4.6. However, due to the complexity of the procedure and the amount of computational work many authors have used the Rayleigh-Ritz method (Rao, 2004) to obtain natural frequencies and mode shapes in a closed solution form. For example

Gontkevich (Leissa, 1973) used the Rayleigh-Ritz method with beam functions to obtain characteristic equations of cylindrical shells with different boundary conditions. He also used the Donnell-Mushtari shell theory as the basis for the calculations. The conditions considered at either or both ends by the author are clamped, shear diaphragm and free. The displacement functions used by Gontkevich are:

$$\left.\begin{aligned} u &= AX'_m(x)\cos(n\theta)\cos(\omega t) \\ v &= BX_m(x)\sin(n\theta)\cos(\omega t) \\ w &= CX_m(x)\cos(n\theta)\cos(\omega t) \end{aligned}\right\} \tag{4.10}$$

where A, B and C are amplitude coefficients, primes indicate differentiation with respect to the independent variable x and $X_m(x)$ is a beam function which is the mth eigenfunction of free vibration of a beam having the desired boundary conditions. The author obtained a cubic characteristic equation in Ω^2 (see Equation 4.8) of the form:

$$\Omega^6 - K_2\Omega^4 + K_1\Omega^2 - K_0 = 0 \tag{4.11}$$

where

$$K_2 = \frac{\mu_m^2}{\delta_m} + \frac{1}{2}(3-\nu)n^2 + 1 + \frac{1}{2}(1-\nu)\delta_m\mu_m^2 + k\left[n^2 + 2(1-\nu)\delta_m\mu_m^2 + \mu_m^4 - 2n^2\mu_m^2\gamma_m + n^4 + 2n^2\mu_m^2(1-\nu)(\delta_m + \gamma_m)\right] \tag{4.12a}$$

$$\delta_m K_1 = \left[\mu_m^2 + \frac{1}{2}(1-\nu)\delta_m n^2\right]\left[n^2 + \frac{1}{2}(1-\nu)\delta_m\mu_m^2 + 1\right] + \frac{1}{2}(1-\nu)\delta_m^2\mu_m^2 - \nu^2\gamma_m^2\mu_m^2 - n^2\mu_m^2\left[-\frac{\delta_m}{2} + \nu\left(\gamma_m + \frac{1}{2}\delta_m\right)\right]^2 + k\left\{\left[\mu_m^2 + \frac{1}{2}(3-\nu)n^2\delta_m + \frac{1}{2}(1-\nu)\delta_m^2\mu_m^2\right]\left[\mu_m^4 - 2n^2\mu_m^2\gamma_m^2 + n^4 + 2n^2\mu_m^2(1-\nu)(\delta_m + \gamma_m)\right]\right.$$

$$+\left[n^2+2(1-\nu)\delta_m\mu_m^2\right]\left[\mu_m^2+\frac{1}{2}(1-\nu)\delta_m n^2+\delta_m\right]$$

$$-2n^2\delta_m\left(n^2+\mu_m^2[2(1-\nu)\delta_m-\gamma_m\nu]\right)\Big\} \tag{4.12b}$$

$$\delta_m K_0=\frac{1}{2}(1-\nu)\delta_m\mu_m^4\left(1-\gamma_m^2\nu^2\right)+k\Big\{\left[\frac{1}{2}(1-\nu)\delta_m n^2+\mu_m^2\left(1-\gamma_m^2\nu^2\right)\right]$$

$$\left[n^2+2(1-\nu)\delta_m\mu_m^2\right]+\left[\left(\mu_m^2+\frac{1}{2}(1-\nu)\delta_m n^2\right)\left(n^2+\frac{1}{2}(1-\nu)\delta_m\mu_m^2\right)\right.$$

$$\left.-n^2\mu_m^2\left[-\frac{1}{2}\delta_m+\nu\left(\gamma_m+\frac{1}{2}\delta_m\right)\right]^2\right]\left[\mu_m^4-2n^2\mu_m^2\gamma_m+n^4\right.$$

$$\left.+2n^2\mu_m^2(1-\nu)(\delta_m+\gamma_m)\right]-n^2\left[\mu_m^2\delta_m\gamma_m(1-\nu)\nu-2\nu^2\mu_m^2\gamma_m^2\right.$$

$$\left.+2\left(\mu_m^2+\frac{1}{2}(1-\nu)\delta_m n^2\right)\right]\left[n^2+\mu_m^2(2\delta_m(1-\nu)-\gamma_m\nu)\right]\Big\} \tag{4.12c}$$

and

$$\left.\begin{aligned}\mu_m&=\varepsilon_m R/L\\ \delta_m&=\frac{L}{\alpha_m^2}\int_0^L(X_m')^2\,dx\\ \gamma_m&=\frac{L}{\alpha_m^2}\int_0^L X_m''X_m\,dx\end{aligned}\right\} \tag{4.13}$$

The values for ε_m, δ_m and γ_m for the different boundary conditions considered by Gontkevich are listed in Table 4.1 (Leissa, 1973).

Table 4.1: Constants for the Characteristic Equation 4.11 (After Leissa, 1973).

m	Item	SD-SD	Clamped-Clamped	Clamped-Free	Free-Free	Clamped-SD	SD-Free
0	δ_m	-	-	1.321886	-	-	-
1		1.0	0.549880	1.471208	2.211601	0.723422	1.742905
2		1.0	0.746684	1.252875	1.766169	0.856926	1.422809
3		1.0	0.818051	1.181963	1.545592	0.902022	1.293787
4		1.0	0.858553	1.141465	1.424419	0.925136	1.224722
5		1.0	0.884249	1.115749	1.347244	0.939525	1.181899
>5		1.0	$1-\frac{2}{\left(m+\frac{1}{2}\right)\pi}$	$1+\frac{2}{\left(m+\frac{1}{2}\right)\pi}$	$1+\frac{6}{\left(m+\frac{1}{2}\right)\pi}$	$1-\frac{1}{\left(m+\frac{1}{4}\right)\pi}$	$1+\frac{3}{\left(m+\frac{1}{4}\right)\pi}$
0	γ_m	$-\delta_m$	$-\delta_m$	0.244094	-	$-\delta_m$	-
1				-0.603337	-0.549879		-0.723422
2				-0.744024	-0.744024		-0.902022
3				-0.818169	-0.818051		-0.902022
4				-0.858524	-0.858533		-0.925136
5				-0.869100	-0.884249		-0.939525
>5				$-1+\frac{2}{\left(m+\frac{1}{2}\right)\pi}$	$-1+\frac{2}{\left(m+\frac{1}{2}\right)\pi}$		$-1+\frac{1}{\left(m+\frac{1}{4}\right)\pi}$
0	ε_m	-	-	1.875104	-	-	-
1		π	4.730040	4.694090	4.730040	3.926600	3.926600
2		2π	7.853204	7.854757	7.853204	7.068580	7.068580
3		3π	10.995608	10.995541	10.995608	10.21020	10.21020
4		4π	14.137166	14.137168	14.137166	13.35180	13.35180
5		5π	17.278760	17.278800	17.278760	16.49340	16.49340
>5		$m\pi$	$\frac{(2m+1)}{2}\pi$	$\frac{(2m+1)}{2}\pi$	$\frac{(2m+1)}{2}\pi$	$\frac{(4m+1)}{4}\pi$	$\frac{(4m+1)}{4}\pi$

The closed form solution developed by Gontkevich to obtain the natural frequencies of thin circular shells was coded in MATLAB (Math Works Inc., 1999). The code can be found in Appendix A. The results obtained from the closed form solution are used in this Chapter to compare different Finite Element (FE) models for cylindrical shells with different boundary conditions. Particular attention is paid to the case of Clamped-SD boundary condition, which is considered as the condition in the honking silo described in Chapter 3.

4.6 Free-Free boundary condition

The Free-Free boundary condition is the first case considered to produce the simplest FE model. These boundary conditions are also helpful in reviewing the classical inextensional theory, which is one of the best-known theories in thin shells with free ends. Rayleigh (1888, 1945) used this theory assuming that the middle surface does not experience stretching if the shell is sufficiently thin and vibrates in one of its low modes. All the transversal sections of the cylindrical shell vibrate performing the same motion; this means that the generators of the cylinder remain straight during vibration. Rayleigh considered the displacements of the form:

$$\begin{aligned} u &= 0 \\ v &= C_c \sin(n\theta)\cos(\omega t) \\ w &= C_c \cos(n\theta)\cos(\omega t) \end{aligned} \tag{4.14}$$

assuming these to be applicable for long shells, and by equating the maximum strain energy to the maximum kinetic energy obtained the natural frequencies of shells as

$$f = \frac{1}{2\pi}\sqrt{\left[\frac{Eh^2}{12\rho R^4\left(1-\nu^2\right)}\right]\left[\frac{n^2\left(n^2-1\right)^2}{n^2+1}\right]} \tag{4.15}$$

In Equation 4.15 the nodal configuration is represented by the second term inside the radical.

Love (1888) assumed a different set of vibration modes, which is more applicable to shells of arbitrary length. Love assumed displacements to be of the form

$$\begin{aligned} u &= \frac{R}{n} C_c \cos(n\varphi)\cos(\omega t) \\ v &= \bar{x} C_c \sin(n\varphi)\cos(\omega t) \\ w &= n\bar{x} C_c \cos(n\varphi)\cos(\omega t) \end{aligned} \tag{4.16}$$

where $\bar{x}$ is the length coordinate measured from the centre section of the shell (x=$L/2$), to obtain frequencies as

$$f = \frac{1}{2\pi}\sqrt{\left[\frac{Eh^2}{12\rho R^4\left(1-\nu^2\right)}\right]\left[\frac{n^2\left(n^2-1\right)^2}{n^2+1}\right]\left[\frac{1+\dfrac{24(1-\nu)R^2}{n^2L^2}}{1+\dfrac{12R^2}{n^2\left(n^2+1\right)L^2}}\right]} \tag{4.17}$$

The frequency value of Equation 4.17 tends to the value of Equation 4.15 when the ratio $L/R\rightarrow\infty$. Figure 4.3 shows a comparison of the Rayleigh, Love and m = 1 modes in a Free-Free shell. The m = 1 mode occurs once the strain energy due to the stretching of the shell is included as considered by Gontkevich.

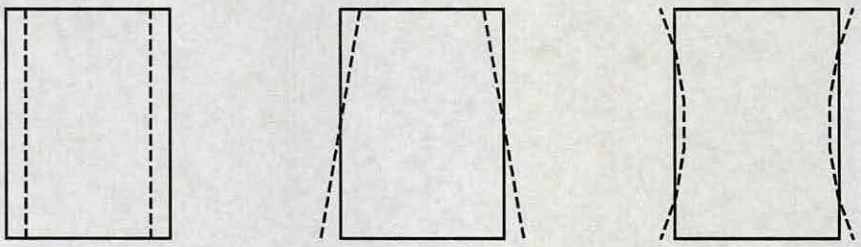

a) Rayleigh b) Love c) m=1

Figure 4.3: Mode shapes of a Free-Free circular cylindrical shell (After Leissa, 1973).

These two frequency equations proposed by Rayleigh, Love and Gontkevich are used to verify a 3D FE model of a simple shell having free ends. The model is constructed using ABAQUS (HKS, 2002) a commercial FE program and it will be the basis for further modifications such as boundary conditions, thickness variation, inclusion of hopper and roof to represent the real characteristics of the instrumented honking silo presented in Chapter 3. Only half of the shell is included in the model with symmetry boundary conditions along the height to reduce the running time. The shell is 3 m diameter and 22 m long. The 3D FE shell model has a total of 8448 elements, 96 columns and 88 rows, and 8633 nodes (see Fig. 4.4). The elements used in the FE

model are S4R5 (HKS, 2002), which is a 4-node three dimensional thin shell element with reduced integration using five degrees of freedom per node except at the nodes that have a boundary condition on a rotational degree of freedom in which case six degrees of freedom are considered per node (HKS, 2002). The aluminium material properties used in the models are Young's modulus $E = 79\text{x}10^9$ Pa, Poisson's ratio $\nu = 0.33$ and mass density $\rho = 2800$ kg/m^3. The closed form solutions require a constant thickness value and for this the thickness of the barrel at midsection ($h = 5.3$ mm) was assumed (see Fig. 3.1). The input file for this model and subsequent FE models can be found in Appendix B.

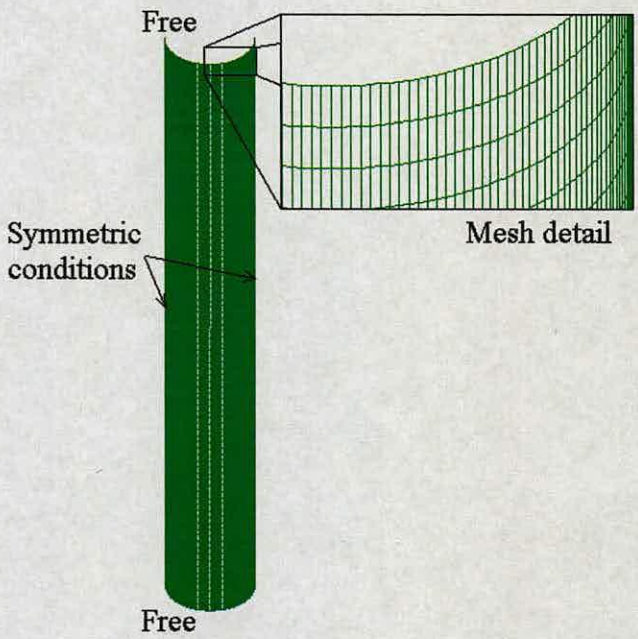

Figure 4.4: Three-dimensional FE shell model.

The eigenvalue problem (Greenberg, 1998) of the discrete shell is of the form

$$\left(-\omega^2 M + K_s\right)\varphi = 0 \tag{4.18}$$

where M is the mass matrix, K_s is the stiffness matrix, φ is the eigenvector (the mode of vibration) and ω^2 is the eigenvalue (square of frequency). The lowest modes obtained with the eigenvalue extraction of the 3D FE model are presented in Table 4.2. These modes are compared with the closed form solutions discussed above

(Rayleigh, Love and Gontkevich) for a shell with free ends. The Table shows the first twenty-five natural frequencies from the FE model and their corresponding value from different closed form solutions. It should be noted that the number of circumferential and axial half waves (n, m) for the FE model are not directly given by the program. These need to be picked up from the evaluated vibration modes. The results in Table 4.2 agree well. The 3D FE model captures all the natural frequencies for the three different closed form solutions discussed. For example in Fig. 4.5, the mode shapes for $n = 2$ (modes 4, 5 and 12 in Table 4.2) corresponding to different theories are shown. Along with the mode shape for the entire length the figure includes close-up to the top and bottom part of the shell for each mode. In Fig. 4.5a every cross section along the height experiences exactly the same deformation, as it is the case in the Rayleigh mode shapes (Fig. 4.3a). On the other hand, the Love mode shape (Fig. 4.3b) is shown in Fig. 4.5b where the circumferential waves rotate 90° from top cross section to bottom one. In Fig. 4.5c the top and bottom section have the same shape but now the axial half wave ($m = 1$) is clearly observed in the vibration mode. This was also the case for modes where $n = 3$, 4, 5 and 6. The first three modes in Table 4.2 represent rigid body modes of the model.

Table 4.2: Natural frequencies in Hz for the shell having free ends.

Mode	FE method			Rayleigh		Love		Gontkevich		
	f	*m*	*n*	*f*	*n*	*f*	*n*	*f*	*m*	*n*
1	0.0	-	-	-	-	-	-	-	-	-
2	0.0	-	-	-	-	-	-	-	-	-
3	0.0	-	-	-	-	-	-	-	-	-
4	1.63	-	2	1.63	2	-	-	-	-	-
5	1.65	-	2	-	-	1.65	2	-	-	-
6	4.63	-	3	4.62	3	-	-	-	-	-
7	4.64	-	3	-	-	4.64	3	-	-	-
8	7.73	1	3	-	-	-	-	7.94	1	3
9	8.88	-	4	8.86	4	-	-	-	-	-
10	8.89	-	4	-	-	8.88	4	-	-	-
11	9.63	1	4	-	-	-	-	9.68	1	4
12	12.96	1	2	-	-	-	-	13.51	1	2
13	13.27	2	4	-	-	-	-	13.47	2	4
14	14.37	-	5	14.33	5	-	-	-	-	-
15	14.38	-	5	-	-	14.35	5	-	-	-
16	14.63	1	5	-	-	-	-	14.62	1	5
17	15.88	2	5	-	-	-	-	15.93	2	5
18	17.28	2	3	-	-	-	-	17.79	2	3
19	19.16	3	5	-	-	-	-	19.32	3	5
20	20.84	3	4	-	-	-	-	21.25	3	4
21	21.11	-	6	21.02	6	-	-	-	-	-
22	21.12	-	6	-	-	21.05	6	-	-	-
23	21.25	1	6	-	-	-	-	21.19	1	6
24	21.77	2	6	-	-	-	-	21.73	2	6
25	23.15	3	6	-	-	-	-	23.16	3	6

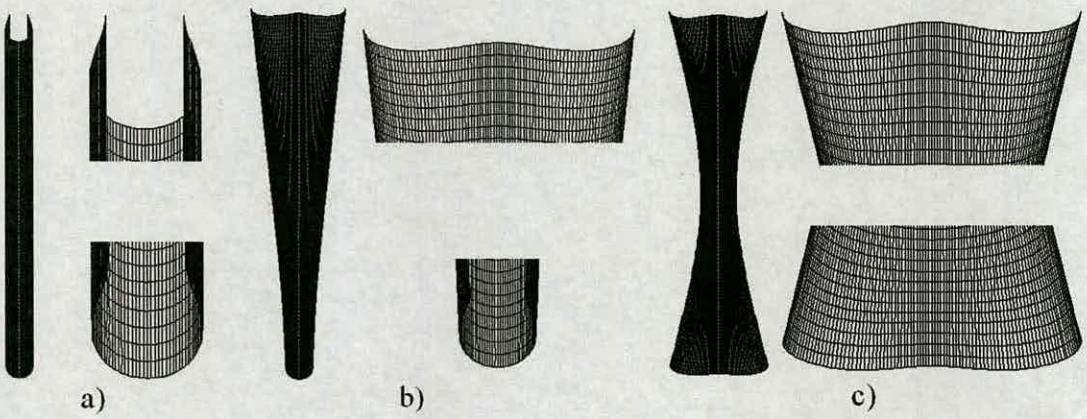

Figure 4.5: Mode shapes when $n = 2$ for the shell having free ends with a) Rayleigh, b) Love and c) $m = 1$ modes.

Clearly for the inextensional theory (Rayleigh and Love) as the circumferential waves increase the natural frequency increases (see Equations 4.15 and 4.17). However, this is not the case once the strain energy due to stretching is considered (this behaviour will be discussed in detail in the next section), where relatively more complex mode shapes are associated with lower frequencies. To observe this behaviour graphically a plot of the frequencies in Table 4.2 versus circumferential waves for the closed form solutions is shown in Fig. 4.6.

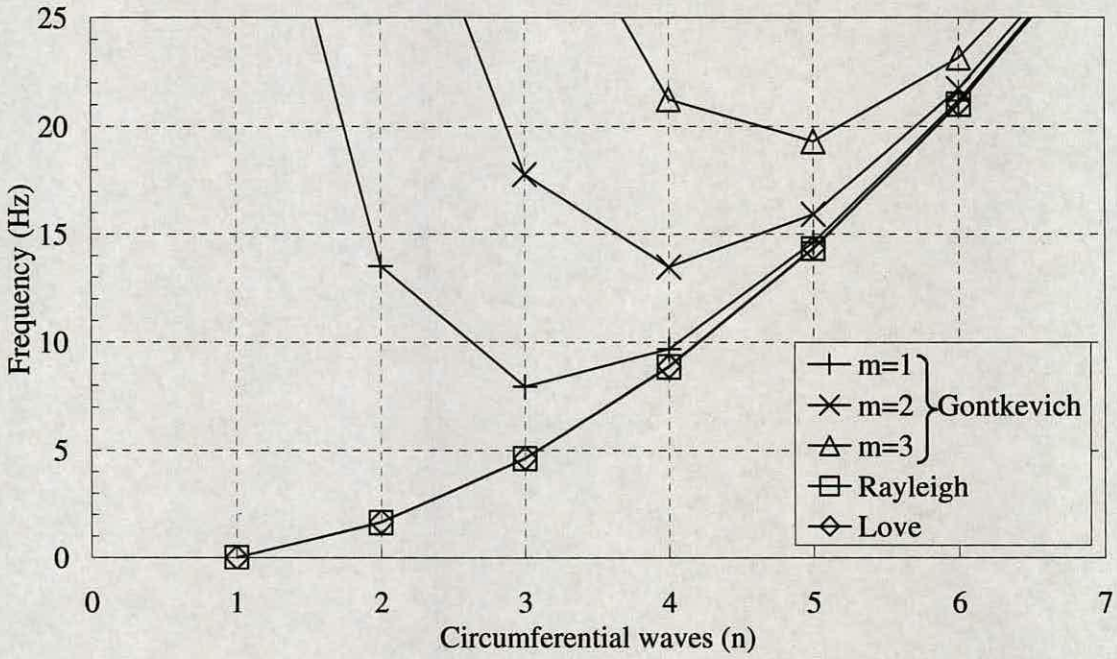

Figure 4.6: Lower natural frequencies for different theories for the shell having free ends.

4.7 SD-SD (Shear Diaphragm) boundary condition

The Shear Diaphragm condition has been called by different names in previous studies such as "freely supported" (Arnold and Warburton, 1949) to describe the boundary conditions

$$w = M_x = N_x = v = 0 \qquad \text{at} \qquad x = 0, L. \tag{4.19}$$

where M_x and N_x are the bending moment and the longitudinal membrane force respectively. By far this boundary condition has received the most attention. This is because the displacement functions of Equation 4.6 for infinite shells also exactly satisfy the Shear Diaphragm condition at both edges when

$$\lambda_m = m\pi R/L \qquad (m = 1,2,\ldots) \tag{4.20}$$

is selected.

The characteristic equation for the Donnell-Mushtari theory can be obtained by equating the determinant of the coefficient matrix of equation 4.7. The characteristic equation is of the form

$$\Omega^6 - K_2\Omega^4 + K_1\Omega^2 - K_0 = 0 \tag{4.21}$$

where

$$K_2 = 1+\frac{1}{2}(3-\nu)\left(n^2+\lambda_m^2\right)+k\left(n^2+\lambda_m^2\right)^2 \tag{4.22a}$$

$$K_1 = \frac{1}{2}(1-\nu)\left[(3+2\nu)\lambda_m^2+n^2+\left(n^2+\lambda_m^2\right)^2+\frac{(3-\nu)}{(1-\nu)}k\left(n^2+\lambda_m^2\right)^3\right] \tag{4.22b}$$

$$K_0 = \frac{1}{2}(1-\nu)\left[(1-\nu^2)\lambda_m^4+k\left(n^2+\lambda_m^2\right)^4\right] \tag{4.22c}$$

For each combination of n and λ_m in Equation 4.21, a finite cylindrical shell may vibrate in any of three different modes due to the three roots obtained in the nondimensional frequency parameter Ω^2. The modes are associated with radial, axial or circumferential motion and each of them having its own particular frequency. The lowest frequency is normally associated with radial motion.

From Equation 4.7 it is possible to obtain the ratios of amplitudes by choosing any two of the equations and discarding the third. The most convenient ratios to choose are *A/C* and *B/C*, which in the Donnell-Mushtari theory take the form:

$$\begin{bmatrix} -\lambda_m^2 - \frac{(1-\nu)}{2}n^2 + \Omega^2 & \frac{(1+\nu)}{2}\lambda_m n \\ \frac{(1+\nu)}{2}\lambda_m n & -\frac{(1-\nu)}{2}\lambda_m^2 - n^2 + \Omega^2 \end{bmatrix} \begin{bmatrix} A/C \\ B/C \end{bmatrix} = \begin{bmatrix} -\nu\lambda_m \\ n \end{bmatrix} \quad (4.23)$$

Inversion produces the ratios *A/C* and *B/C* for each of the three roots in Equation 4.21. These ratios will usually yield values less than unity, indicating primarily radial motion. This occurs for the lowest frequencies when $n \geq 2$ regardless of the axial half wave number m. This is not the case when the number of circumferential waves n is one or zero ($n = 1$ or $n = 0$) for the lowest natural frequencies. For the beam mode ($n = 1$) and for low axial half waves m the amplitude coefficients of the radial and circumferential displacement are approximately equal while the axial one is the smallest. In the case of the axisymmetric mode ($n = 0$) and low half waves m the amplitude coefficient of the axial displacement is greater than the radial while the circumferential one is zero (Leissa, 1973).

The same 3D FE model having free ends described in the previous section is modified to the SD-SD boundary conditions (Equation 4.19) and used here to extract its lowest natural frequencies. These results are compared in Table 4.3 with the Donnell-Mushtari theory and Gontkevich closed form solutions for SD-SD conditions.

Table 4.3: Natural frequencies in Hz for the shell having SD-SD end conditions.

Mode	FE method			Donnell-Mushtari			Gontkevich		
	f	m	n	f	m	n	f	m	n
1	5.38	1	3	5.89	1	3	5.38	1	3
2	5.91	1	2	6.12	1	2	5.94	1	2
3	9.04	1	4	9.61	1	4	9.02	1	4
4	10.90	2	4	11.39	2	4	10.89	2	4
5	11.67	2	3	11.93	2	3	11.66	2	3
6	14.44	1	5	14.99	1	5	14.39	1	5
7	15.03	2	5	15.57	2	5	14.98	2	5
8	16.44	3	4	16.83	3	4	16.47	3	4
9	17.15	3	5	17.63	3	5	17.11	3	5
10	17.22	1	1	17.46	1	1	17.22	1	1
11	21.15	1	6	21.66	1	6	21.06	1	6
12	21.36	2	6	21.92	2	6	21.32	2	6
13	21.64	4	5	22.01	4	5	21.57	4	5
14	-	-	-	22.22	2	2	22.04	2	2
15	22.26	3	6	22.76	3	6	22.17	3	6
16	23.92	3	3	24.07	3	3	23.88	3	3
17	24.20	4	6	24.70	4	6	24.15	4	6

The results agree well for the three different methods used. However, mode 14 evaluated using Donnell-Mushtari theory and Gontkevich closed form solutions is not present in the FE frequency extraction for this low frequency limit. For this mode (m = 2, n = 2) it is possible that the FE frequency extraction limit was below the frequency value of such mode, however this was not verified. The solution given by Donnell-Mushtari and Gontkevich assume sinusoidal motion and the mode shapes are clean n waves and m half waves. The natural frequencies slightly differ one from another but the number of waves n and half waves m can be distinguished and compared for the three methods. The lateral and cross sections of modes one to four in Table 4.3 are presented in Fig. 4.7. For these modes the circumferential wave number n and the axial half wave number m can easily be identified.

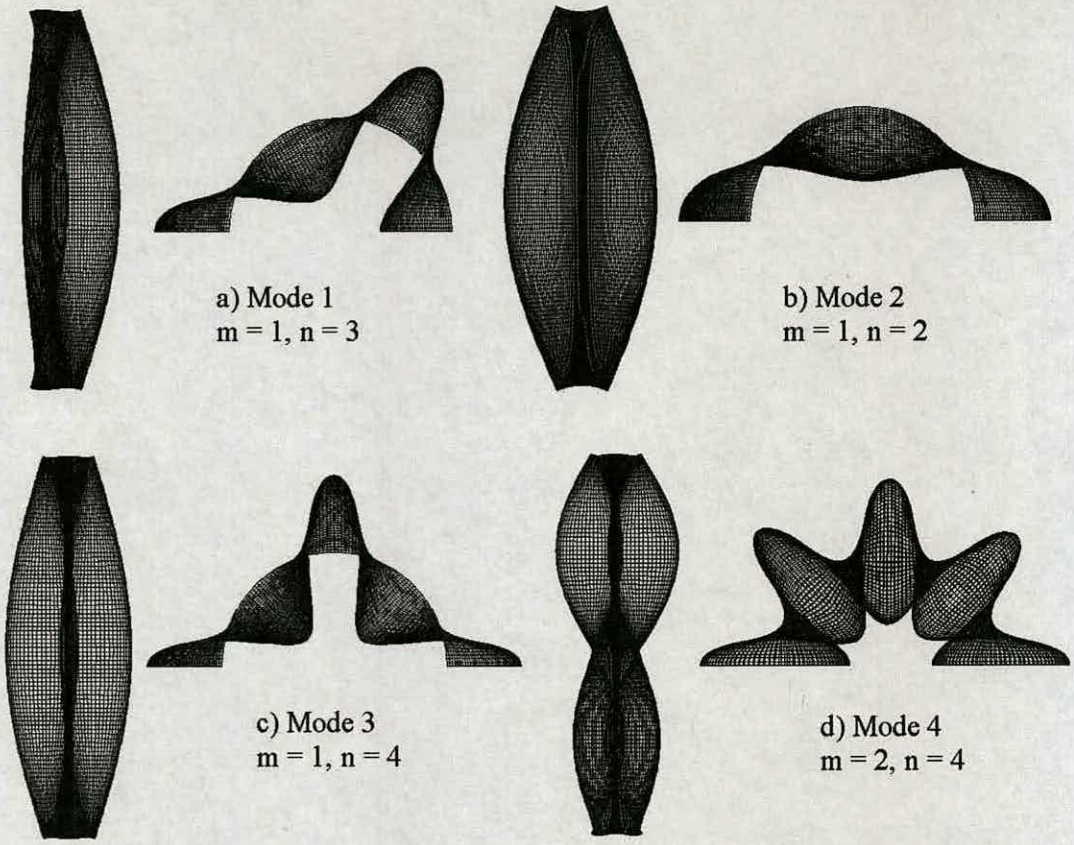

Figure 4.7: Lowest mode shapes for the shell having SD boundary conditions at both ends for a) $m = 1, n = 3$, b) $m = 1, n = 2$, c) $m = 1, n = 4$ and d) $m = 2, n = 4$.

To graphically observe the variation of frequencies with respect of n and m, these have been plotted in Fig. 4.8. It shows that for higher n values curves for all m values tend to the same curve (m = 1) In fact they tend to the Rayleigh's or Love's inextensional theory curve shown in Fig. 4.6. The figure also shows how relatively more complex modes are associated with lower frequencies similar to the Free-Free condition at both ends (see Fig. 4.6). For example, for m = 1 the lowest frequency occurs for n = 3 and not for n = 1. This behaviour is in contrast with other simpler systems such a beams or strings where as the mode shape becomes more complex the natural frequency increases. Arnold and Warburton (1949) investigated this behaviour by evaluating the total strain energy associated with different modes. They demonstrated that this is due to the strain energy distribution between stretching and bending. For example Fig. 4.9 shows the strain energy as a function of the circumferential wave number n for m = 1 and 2 based on the equations proposed by

the latter investigators. The plot shows how the stretching energy decreases with the increase in n, while the bending energy increases. Therefore the total strain energy first decreases with n and then increases as shown in Fig. 4.9. The figure also shows that the bending strain energy does not depend on the number of half axial waves m while the stretching energy does. The bending strain energy curve can be compared to the inextensional theory curves in Fig. 4.6, which only include bending energy.

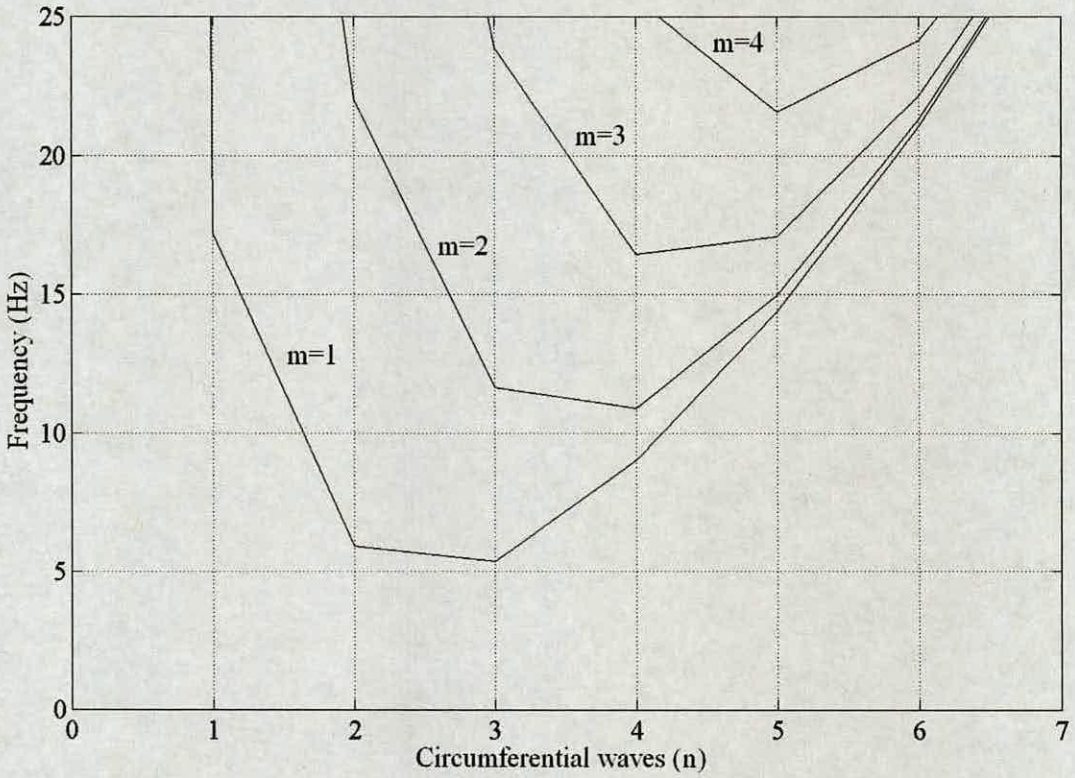

Figure 4.8: Lower natural frequencies for the shell having SD-SD ends with Gontkevich closed form solution.

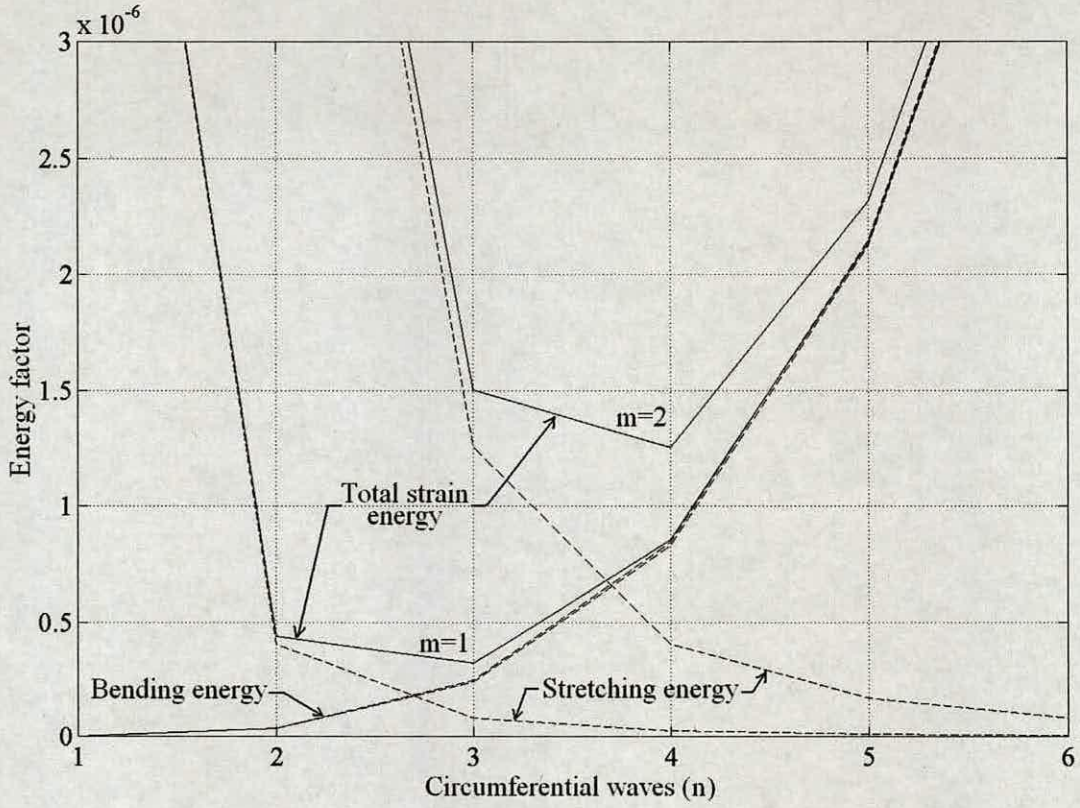

Figure 4.9: Strain energy distribution in cylindrical shell with SD-SD conditions.

4.7.1 The axisymmetric ($n = 0$) case

Axisymmetric motion has received particular attention from researchers because its behaviour differs from the beam ($n = 1$) or lobar ($n \geq 2$) modes. Substitution of $n = 0$ on Equation 4.7 produces the vanishing of the off-diagonal terms containing n and modification in the diagonal terms in the form:

$$\begin{bmatrix} -\lambda_m^2 + \Omega^2 & 0 & \nu\lambda_m \\ 0 & -\frac{(1-\nu)}{2}\lambda_m^2 + \Omega^2 & 0 \\ -\nu\lambda_m & 0 & 1 + k\left(\lambda_m^2\right)^2 - \Omega^2 \end{bmatrix} \begin{bmatrix} A \\ B \\ C \end{bmatrix} = \begin{bmatrix} 0 \\ 0 \\ 0 \end{bmatrix} \tag{4.24}$$

Setting the determinant of the coefficients matrix equal to zero it is possible to obtain the values for Ω^2 but now the solution is simpler. The second of the equations becomes uncoupled yielding a circumferential motion. The other two equations for axial and radial motion are coupled together and the Ω^2 roots can be determined from

the quadratic formula. Figure 4.10 shows the axisymmetric frequency parameter ($\Omega = \omega R(\rho(1-\nu^2)/E)^{1/2}$) versus axial wavelength parameter (L/mR) of the SD-SD shell presented above. The values have been calculated with the Donnell-Mushtari theory (Equation 4.24). The figure shows the uncoupled circumferential frequency parameter increases monotonically as the number of axial half waves increases. However, this is not the case for the coupled axial-radial parameters. For values of L/mR higher than π the lowest value from the axial-radial coupled equation is axial and this is reversed for values lower than π. From the coupled values (axial-radial) it is interesting to note that the radial parameter tend to $\Omega = 1$ until m is high enough to produce a significant rise in the frequency parameter (Leissa, 1973; Junger and Feit, 1986). This is known as the "ring frequency" (Scott, 1988) because it is independent of the axial half wave number m. The lowest frequency parameter in the axisymmetric case is due to circumferential motion for low m values ($L/mR > 2$) and radial for higher m values ($L/mR < 2$).

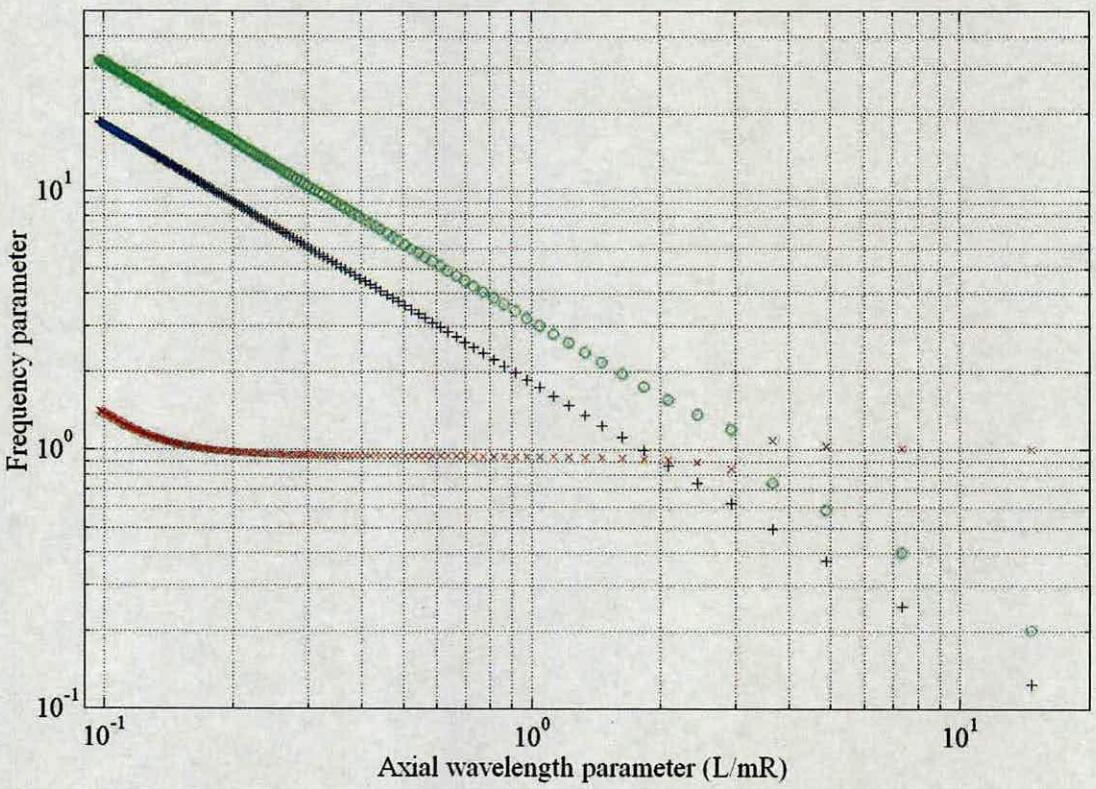

Figure 4.10: Axisymmetric ($n = 0$) frequency parameters (x = radial, o = axial and + = circumferential).

Another interesting feature in the axisymmetric mode is the behaviour of the amplitude ratios *A/C* and *B/C*. If $n = 0$ is substituted in Equation 4.23, the Donnell-Mushtari theory for the calculation of such ratios takes the form:

$$\begin{bmatrix} -\lambda_m^2 + \Omega^2 & 0 \\ 0 & -\frac{(1-\nu)}{2}\lambda_m^2 + \Omega^2 \end{bmatrix} \begin{bmatrix} A/C \\ B/C \end{bmatrix} = \begin{bmatrix} -\nu\lambda_m \\ 0 \end{bmatrix} \tag{4.25}$$

As discussed earlier the above equations can be solved to find the ratios *A/C* and *B/C*. This produces the *B/C* ratio being equal to zero indicating that there are not modal displacements in the circumferential direction for the axisymmetric case (see Equation 4.6). The coupled axisymmetric natural frequencies (axial-radial) for the SD-SD shell are presented graphically in Fig. 4.11 using the Donnell-Mushtari theory.

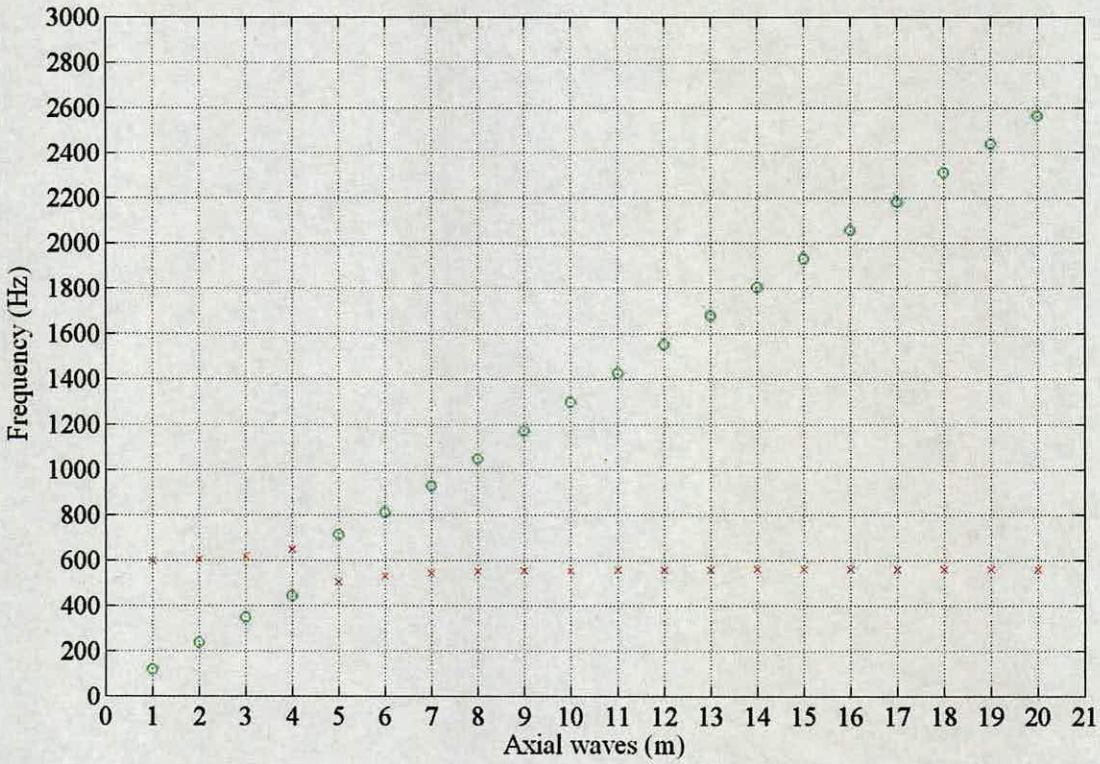

Figure 4.11: Axisymmetric ($n = 0$) natural frequencies for the SD-SD condition (x = radial and o = axial).

To compare the results from the Donnell-Mushtari theory and the Gontkevich closed form solution an axisymmetric FE model is constructed and analysed. The axisymmetric FE model has the same geometry as before (3 m diameter and 22 m long) and SD-SD boundary conditions with a total of 1835 elements and 1836 nodes. The elements used are SAX1, which are axisymmetric 2-node thin linear shell elements using three degrees of freedom per node (HKS, 2002). The results of the lowest axial-radial coupled frequencies are presented in Table 4.4 for the FE model, the Donnell-Mushtari theory and Gontkevich closed form solution having SD-SD boundary conditions. The results obtained from the FE frequency extraction follow the lower coupled values in Fig. 4.11. The first four modes are due to axial motion and the rest are due to radial. The results in the three cases agree well.

Table 4.4: Axisymmetric ($n = 0$) natural frequencies in Hz for the shell having SD-SD end conditions.

Mode	FE method f	Donnell-Mushtari f	Gontkevich f
1	120.49	120.41	120.41
2	238.81	238.62	238.62
3	350.71	350.35	350.35
4	445.24	444.63	444.63
5	504.68	503.96	503.96
6	531.58	531.00	531.00
7	543.60	543.17	543.18
8	549.80	549.46	549.43
9	553.43	553.15	553.14
10	555.75	555.53	555.51
11	557.34	557.16	557.13
12	558.48	558.33	558.30
13	559.32	559.20	559.17
14	559.97	559.87	559.83
15	560.49	560.40	560.35
16	560.90	560.83	560.77
17	561.23	561.18	561.11
18	561.52	561.48	561.39
19	561.76	561.73	561.62
20	561.96	561.95	561.82

4.8 Clamped-SD boundary condition

The Clamped-Shear Diaphragm boundary conditions are closest to the instrumented honking silo in this study, which is clamped at the bottom and has a conical thin roof at the top closely approximating the conditions of the SD edge. However, the model presented in this section is a simple shell with the boundary conditions mentioned above. The conditions at the edges for the clamped and SD end are:

$$u = v = w = \frac{\partial w}{\partial x} = 0 \qquad \text{at} \qquad x = 0 \tag{4.26a}$$

$$N_x = v = w = M_x = 0 \qquad \text{at} \qquad x = L \tag{4.26b}$$

respectively. In this case the Gontkevich closed form solution is used to compare with the 3D FE model. The FE model has been modified from the previous 3D model just in its boundary conditions and the results from the frequency extraction are listed in Table 4.5 together with the closed form solution proposed by Gontkevich. The results are in good agreement.

Table 4.5: Natural frequencies in Hz for the shell having Clamped-SD end conditions.

Mode	FE method			Gontkevich		
	f	*m*	*n*	*f*	*m*	*n*
1	6.26	1	3	6.34	1	3
2	8.86	1	2	9.15	1	2
3	9.23	1	4	9.23	1	4
4	11.88	2	4	11.96	2	4
5	14.07	2	3	14.34	2	3
6	14.49	1	5	14.45	1	5
7	15.35	2	5	15.33	2	5
8	17.97	3	5	18.01	3	5
9	18.34	3	4	18.53	3	4
10	21.18	1	6	21.08	1	6
11	21.53	2	6	21.44	2	6
12	22.60	3	6	22.54	3	6
13	23.01	4	5	23.11	4	5
14	24.66	1	1	25.94	1	1
15	24.90	4	6	24.87	4	6
16	26.77	2	2	27.55	2	2
17	27.20	3	3	27.69	3	3
18	28.17	4	4	28.47	4	4
19	28.78	5	6	28.79	5	6
20	29.16	1	7	28.98	1	7

Comparison between Table 4.3 (SD-SD condition) and Table 4.5 (Clamped-SD condition) shows an increase in frequencies due to the stiffer clamped end. The fundamental frequency in both cases occurs for the combination $m = 1$ and $n = 3$. The occurrence of this fundamental mode does not seem to be affected by the boundary conditions but by the *R/h* ratio. For a constant value in the axial wavelength parameter (*L/mR*), the fundamental frequency occurs at low *n* values if the *R/h* ratio is small in the SD-SD boundary condition. However, for higher *R/h* ratios the fundamental frequency occurs at greater *n* values (Leissa, 1973). This behaviour seems to prevail despite the inclusion of the clamped condition at one edge. The first eight mode shapes are shown in Fig. 4.12 for the Clamped-SD shell. The modes are comparable to those in Fig. 4.7 for the SD-SD shell; however, a small variation in shape at the bottom edge can be observed due to the clamped condition.

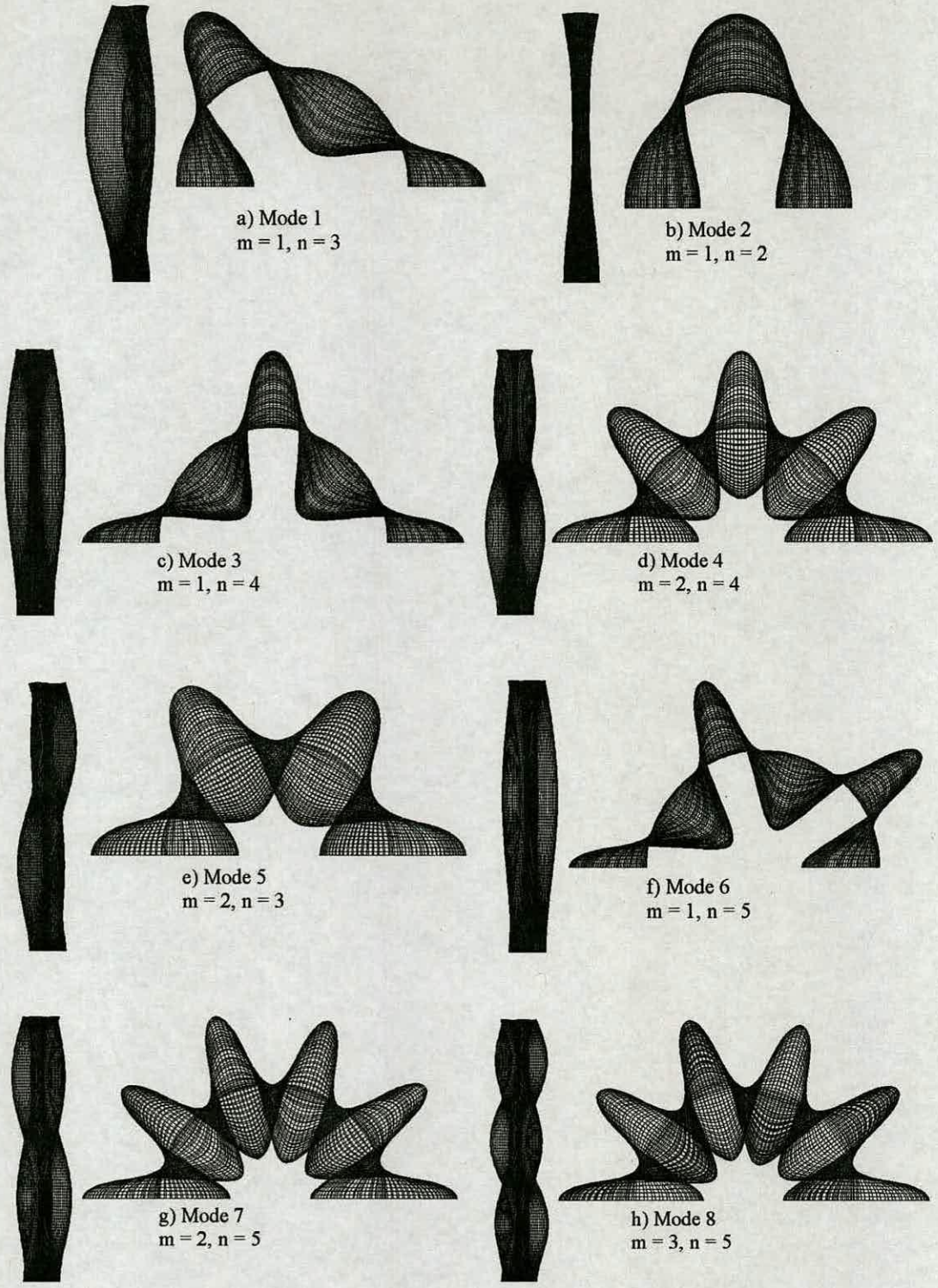

Figure 4.12: Lowest mode shapes for the shell having Clamped-SD boundary conditions.

The behaviour of the frequency variation versus the circumferential wave n is shown in Fig. 4.13 for different axial half waves m. Similar to curves of Figs. 4.6 and 4.8, the curves for different m values tend to the $m = 1$ curve or the inextensional theory curves. Again, relatively more complex modes are associated with lower frequencies due to stretching and bending strain energy distribution. Clearly, these modes are low compared with the honking fundamental frequency and its harmonics. Almost half of them in Table 4.5 are below the audible range. To investigate the behaviour at higher frequencies near the fundamental honking frequency (333 Hz) a natural frequency extraction using the Gontkevich closed form solution is presented in Fig. 4.14. The plot shows the variation in natural frequencies with the circumferential wave number n. Each curve represents different axial half wave number m. It is important to mention that only the lowest frequency of the three possible for each n and m combination has been plotted in Fig. 4.14. This gives the fundamental frequency response for each n and m combination regardless of the direction of vibration (radial, axial or circumferential). A dashed line has been drawn on the graph showing that a range of modes could be responsible for the vibration of the fundamental honking frequency at 333 Hz. In a similar way the higher honking harmonics could be caused by various n and m combinations without a clear pattern of occurrence. However, the influence of roof, hopper and thickness variation has not been included in the natural frequency behaviour of Fig. 4.14 and their inclusion could influence the free vibration characteristics. This is considered in the next Chapter.

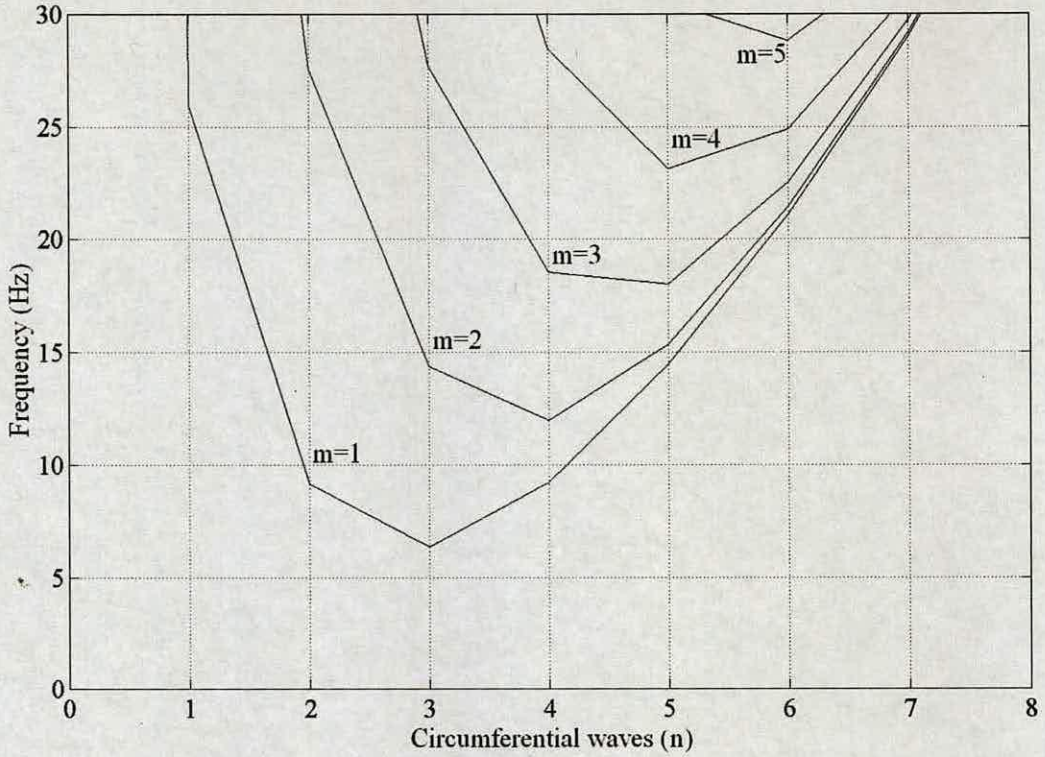

Figure 4.13: Lower natural frequencies for the shell having Clamped-SD end conditions with the Gontkevich closed form solution.

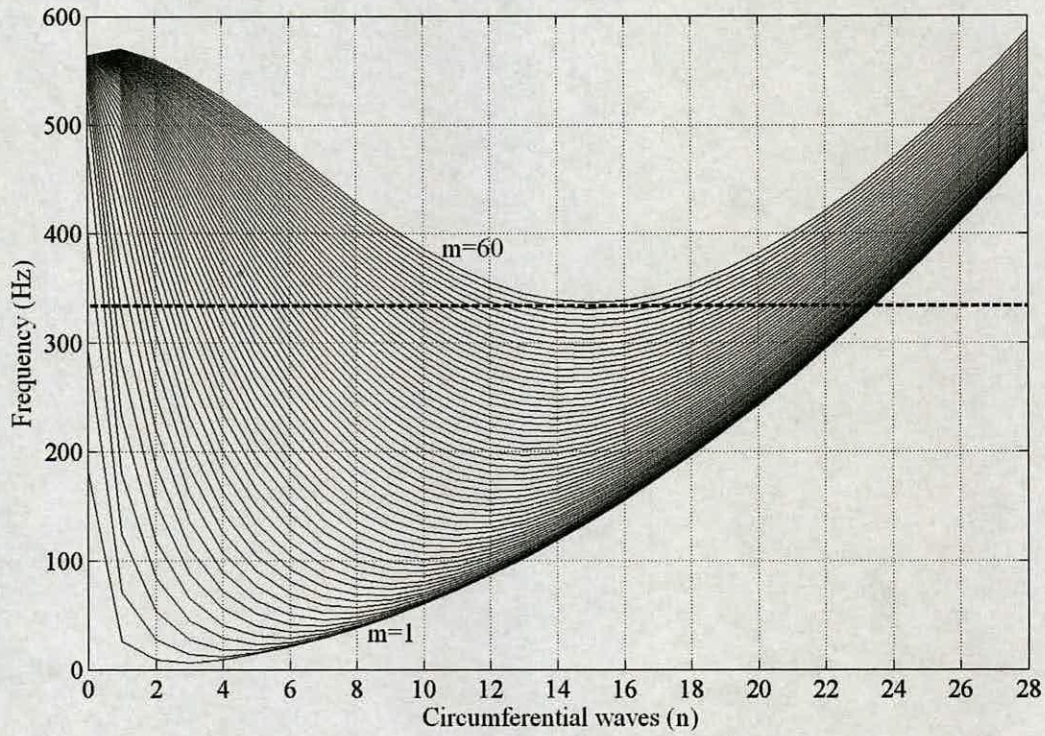

Figure 4.14: Natural frequencies for the shell having Clamped-SD end conditions (n = 0-28 and m = 1-60).

4.8.1 The axisymmetric ($n = 0$) case

The study of the axisymmetric case for the Clamped-SD shell is important in the honking problem due to the possible sources of excitation proposed to cause it. They have been proposed to occur in an axisymmetric way and will be described in detail in Chapter 6. The behaviour of the axisymmetric Clamped-SD shell is similar to that described for the SD-SD shell where the circumferential frequency uncouples from the other two and the axial and radial frequency remain coupled. This can be observed by assuming solution functions, which are generalizations of Equation 4.6 taking the form (Leissa, 1973)

$$\left.\begin{aligned} u &= Ae^{\lambda s}\cos(n\theta)\cos(\omega t) \\ v &= Be^{\lambda s}\sin(n\theta)\cos(\omega t) \\ w &= Ce^{\lambda s}\cos(n\theta)\cos(\omega t) \end{aligned}\right\} \tag{4.27}$$

where λ is an undetermined factor and the rest of the terms are similar to those discussed earlier. These equations preserve their periodic behaviour with respect to time t and circumferential angle θ, but the periodic variation with respect to x is generalized to an exponential form. Substitution of Equation 4.27 into the equation of motion Equation 4.3 for the Donnell-Mushtari theory leads to:

$$\begin{bmatrix} \lambda^2 - \frac{(1-\nu)}{2}n^2 + \Omega^2 & \frac{(1+\nu)}{2}\lambda n & \nu\lambda \\ -\frac{(1+\nu)}{2}\lambda n & \frac{(1-\nu)}{2}\lambda^2 - n^2 + \Omega^2 & -n \\ \nu\lambda & n & 1 + k\left(n^2 - \lambda^2\right)^2 - \Omega^2 \end{bmatrix} \begin{bmatrix} A \\ B \\ C \end{bmatrix} = \begin{bmatrix} 0 \\ 0 \\ 0 \end{bmatrix} \tag{4.28}$$

Substitution of $n = 0$ in Equation 4.28 produces

$$\begin{bmatrix} \lambda^2 + \Omega^2 & 0 & \nu\lambda \\ 0 & \frac{(1-\nu)}{2}\lambda^2 + \Omega^2 & 0 \\ \nu\lambda & 0 & 1 + k\left(-\lambda^2\right)^2 - \Omega^2 \end{bmatrix} \begin{bmatrix} A \\ B \\ C \end{bmatrix} = \begin{bmatrix} 0 \\ 0 \\ 0 \end{bmatrix} \tag{4.29}$$

Once again the circumferential frequency uncouples from the other two and it is again apparent that the amplitude coefficient B is zero.

The natural frequencies are calculated using the closed form solution proposed by Gontkevich. The results are compared with an axisymmetric model having the same characteristics as the one presented in the SD-SD axisymmetric case. However, the bottom boundary is modified to a clamped one. The axisymmetric frequency parameters ($\Omega = \omega R(\rho(1-\nu^2)/E)^{1/2}$) are plotted in Fig. 4.15 to observe its behaviour graphically.

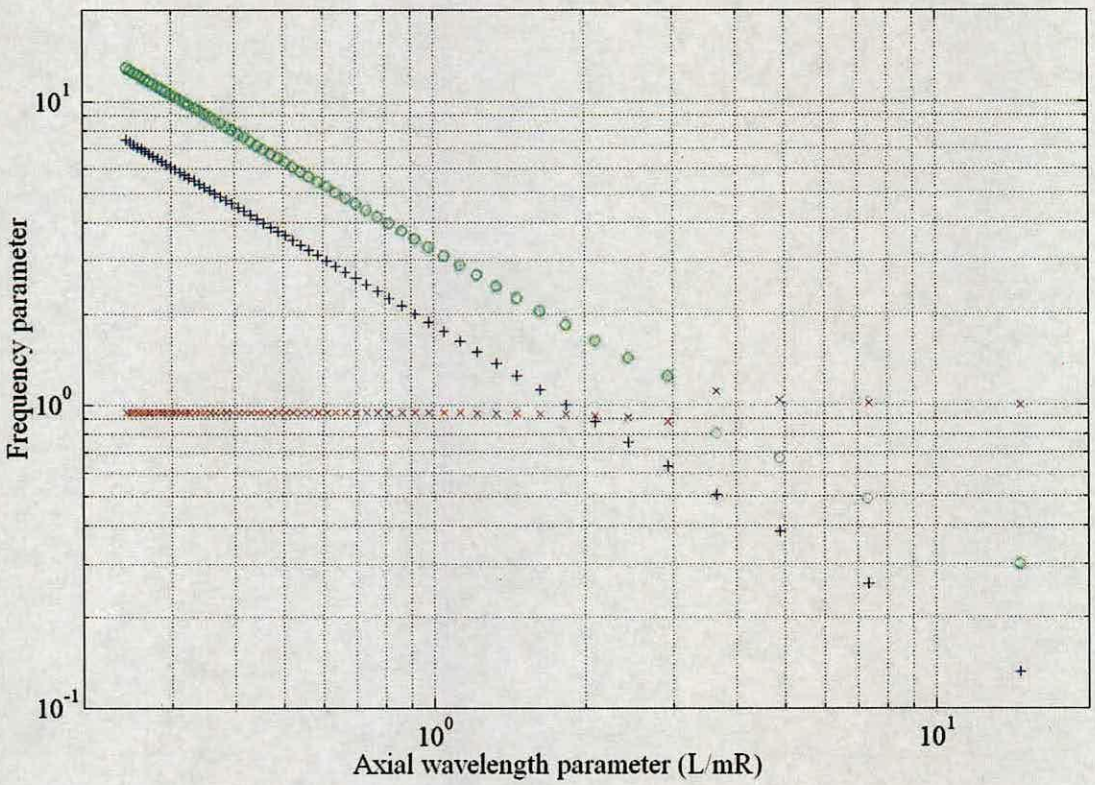

Figure 4.15: Axisymmetric ($n = 0$) frequency parameter (x = radial, o = axial and + = circumferential).

The Clamped-SD condition share with the SD-SD condition the alternation of the coupled axial-radial parameters at the same values of L/mR. For $L/mR > \pi$ the lowest value for the coupled equation is axial and for $L/mR < \pi$ the lowest value is radial. In the same way the lowest frequency parameter is radial or circumferential depending

on the axial wavelength parameter value. The ring frequency ($\Omega \approx 1$) can also be observed in this figure and it is not affected by the increment of stiffness due to the clamped end.

In the same way as the SD-SD axisymmetric case it is possible to obtain the amplitude ratios by choosing the first two equations in Equation 4.28 and discarding the third one. Subsequent substitution of $n = 0$ leads to the equation:

$$\begin{bmatrix} \lambda^2 + \Omega^2 & 0 \\ 0 & \frac{(1-\nu)}{2}\lambda^2 + \Omega^2 \end{bmatrix} \begin{bmatrix} A/C \\ B/C \end{bmatrix} = \begin{bmatrix} -\nu\lambda_m \\ 0 \end{bmatrix} \tag{4.30}$$

By inverting Equation 4.30 the ratios *A/C* and *B/C* can be found. As discussed earlier the modal displacement in the circumferential direction is zero. The coupled radial-axial natural frequencies in the axisymmetric case are presented in Fig. 4.16 calculated with the closed form solution proposed by Gontkevich.

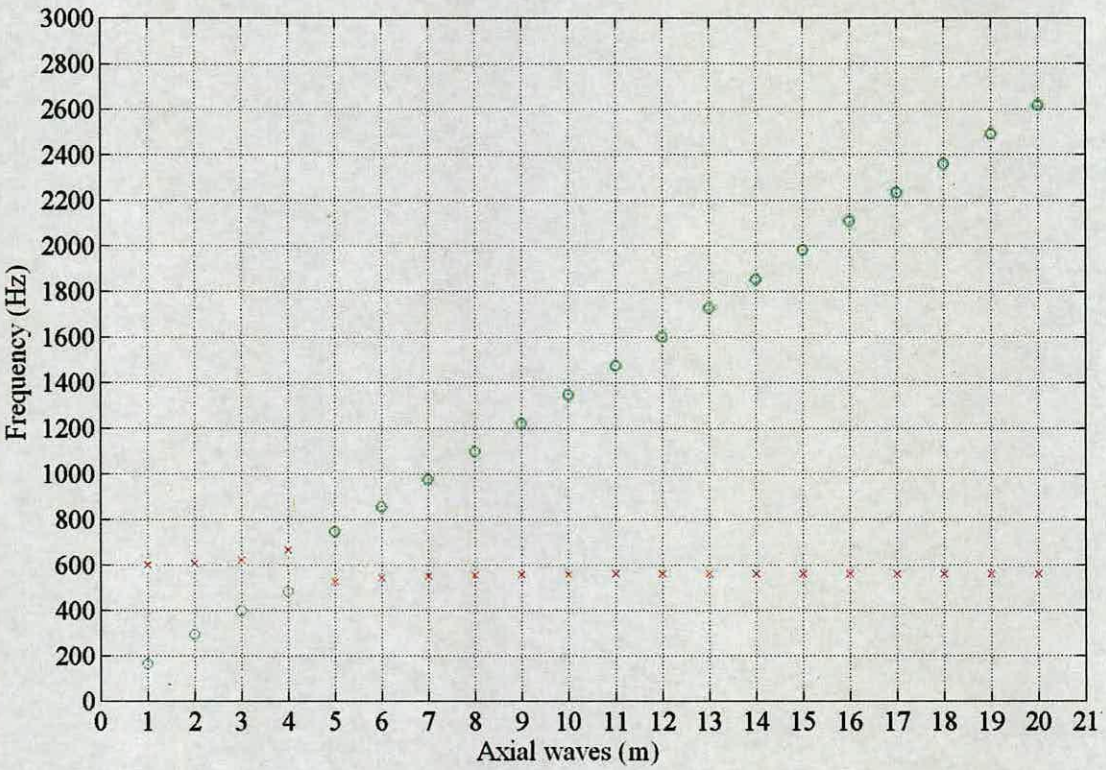

Figure 4.16: Axisymmetric ($n = 0$) natural frequencies for the Clamped-SD condition (x = radial and o = axial).

The lowest coupled values in Fig. 4.16 are presented in Table 4.6 for the Gontkevich closed form solution and the FE axisymmetric model. The FE axisymmetric model has the same characteristics as the one presented for the SD-SD condition, except the boundary conditions at the bottom are modified to clamped. The first mode in Table 4.6 is not calculated by the closed form solution. This is because the first mode due to the beam function with Clamped-SD boundary condition corresponds to half wave, while the first mode extracted from the FE model represents a quarter wave. It possible to calculate the first mode applying the Clamped-Free boundary condition with the Gontkevich closed form solution, which considers the deformation of such mode as quarter wave. Its value was obtained as $f = 66.17$ Hz. Here it is important to note that the beam functions satisfy only approximately the free edge boundary condition of the shell (Leissa, 1973). The results in Table 4.6 again are in good agreement.

Table 4.6: Axisymmetric ($n = 0$) natural frequencies in Hz for the shell having Clamped-SD end conditions.

Mode	FE method f	Gontkevich f
1	60.34	-
2	180.04	181.93
3	295.88	293.97
4	401.03	400.78
5	479.66	482.93
6	520.64	525.21
7	538.42	542.52
8	546.95	550.42
9	551.67	554.59
10	554.58	557.12
11	556.50	558.75
12	557.86	559.88
13	558.85	560.68
14	559.59	561.27
15	560.18	561.72
16	560.64	562.07
17	561.02	562.35
18	561.33	562.57
19	561.59	562.74
20	561.82	562.89

It is interesting to mention that the lowest four FE frequency values in Table 4.6, which correspond to mainly axial motion (see Fig. 4.16), can be calculated with the equation of longitudinal vibration of uniform bars (Bishop and Johnson, 1956):

$$f = \frac{r}{4L}\sqrt{\frac{E}{\rho}} \qquad \text{for} \qquad r = 1,3,5,7,... \tag{4.31}$$

where E, ρ and L are the Young's modulus, mass density and length of the bar respectively. Substitution of the shell values in Equation 4.31 gives the natural frequencies in Table 4.7. The first two modes are in good agreement with those correspondent modes in Table 4.6, however, the third and fourth modes in Table 4.7 are higher than those correspondent modes in Table 4.6. While the natural frequencies calculated with Equation 4.31 follow a linear behaviour, the FE natural frequencies extraction follows the coupled behaviour of the axisymmetric case in the cylindrical thin shell theory.

Table 4.7: Longitudinal natural frequencies with Equation 4.31.

r	f
1	60.34
3	181.02
5	301.71
7	422.39

As was shown in Chapter 3, the frequencies with the highest energy corresponding to small oscillations during non-honking periods are predominantly below 600 Hz in the axial direction (see Fig 3.20b, 3.21b, 3.22b and 3.23b). However, clean peaks cannot be observed at any particular frequency. It is interesting to note that the lowest axisymmetric natural frequencies obtained from the FE frequency extraction shown in Table 4.6 are axial and below 600 Hz, see Fig. 4.16. Additionally the possible sources of excitation (pulsating flow and slip-stick) previously suggested as the cause for honking and described in Chapter 2 occur in an axisymmetric way. These similarities suggest that the axisymmetric behaviour of the structure is an

important factor to consider in the more detailed frequency analysis with a refined model. This is considered in Chapter 5.

4.9 Conclusions

The theory of free vibration characteristics of thin cylindrical shells has been reviewed in this Chapter. Their characteristics are complex compared to other simpler systems such as beams or strings. Different FE models were constructed and validated with exact theories and closed form solutions available in literature. Mode shapes and natural frequencies were presented for shells with different boundary conditions. Of particular interest are shells with Clamped-SD conditions, which closely represents the boundary conditions in the real honking silo. The following conclusions can be drawn from the results:

- *3D FE model with Clamped-SD boundary conditions.* In this case the lowest natural frequencies are below the audible range. Moreover they are too low when compared with the honking frequencies evaluated in Chapter 3. A frequency calculation of higher modes near the honking fundamental frequency shows that several modes could be responsible for honking.

- *Axisymmetric FE model with Clamped-SD boundary conditions.* Comparison of axisymmetric natural frequencies with the spectra of measured response indicates that the structure vibrates predominantly in axisymmetric modes.

Chapter 5

Free vibration characteristics of the silo structure

5.1 Introduction

Finite element shell models were validated with analytical theories in Chapter 4. However, the instrumented honking silo in this study is not a simple cylindrical shell. Its geometry also includes a roof, hopper and thickness variation along the height. In this Chapter these implementations are included in the 3D and the axisymmetric models and their effects on the free vibration characteristics of the silo structure analysed. Additionally for the axisymmetric silo model the influence of bulk solid is discussed. The free vibration characteristics are investigated on the silo-fill system once the mass and stiffness of the bulk solid are included for different fill levels in the model. Parametric studies are also conducted for the axisymmetric silo model. These include examining the influence of hopper angle and shell height variation on the free vibration characteristics. Free vibration characteristics of models with different silo height to diameter ratios are also examined. In the last section a frequency extraction of higher frequencies in the axisymmetric model is conducted. The intention is to look for a possible harmonic pattern, which is a characteristic of the honking behaviour.

5.2 The 3D silo model

5.2.1 Implementations to the 3D shell model

The 3D shell model for the Clamped-SD boundary conditions is modified in this section to transform it as closely as possible to the real honking silo structure. The frequency extraction of the simple shell conducted in Chapter 4 shows that the lowest frequencies are below an audible range and far away from the honking fundamental frequency. Inclusion of the roof at the top, hopper at the bottom and thickness variation along the barrel height would influence the natural frequencies of the shell model. The roof and hopper are modelled with the same S4R5 shell elements as the barrel. An additional of 1344 shell elements on the roof and 960 shell elements on the hopper complement the 3D silo model. The total number of elements and nodes in the 3D silo model are 10752 and 10961 respectively. The thickness variation is included for different sets of elements to represent the variations shown in Fig. 3.1. Details of the FE model for the roof and hopper are shown in Figs. 5.1 and 5.2 respectively. Once again only half silo is included in the model.

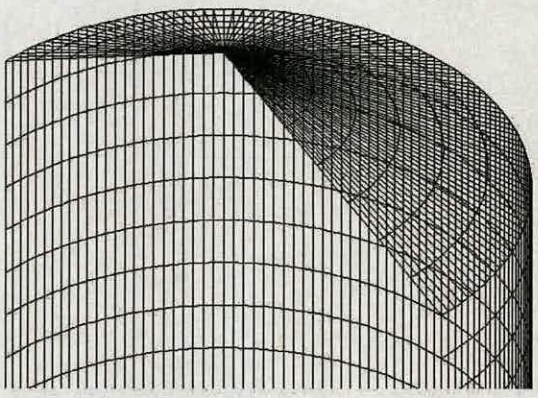

Figure 5.1: Roof detail.

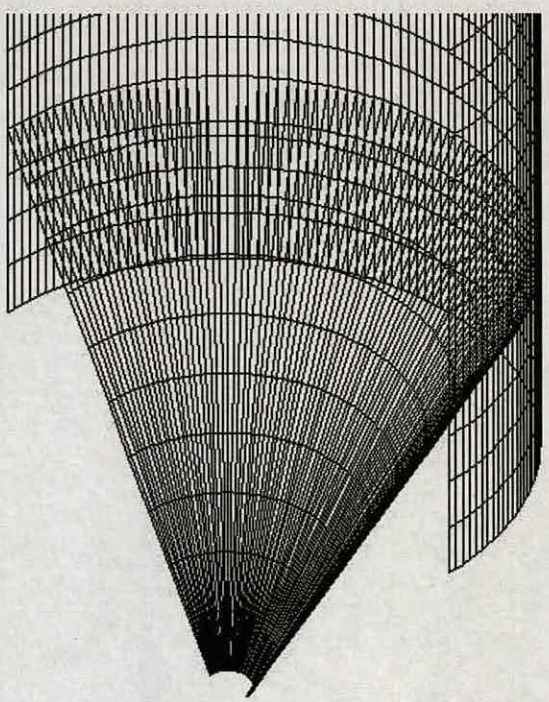

Figure 5.2: Hopper detail.

The clamped boundary conditions at the bottom part of the model are preserved while the roof substitutes the SD boundary conditions at the top. As discussed in the last Chapter for the shell model symmetry boundary conditions are now also applied along the roof and the hopper.

5.2.2 Free vibration characteristics

To assess the impact of the implementations above on the lowest natural frequencies, the first twenty modes are extracted from the 3D silo model. These are compared with the modes of the 3D shell and the Gontkevich closed form solution shown in Table 4.5. Table 5.1 shows the comparison of the results.

Table 5.1: Natural frequencies in Hz for the shell having Clamped-SD end conditions.

Mode	FE shell			Gontkevich			FE Silo		
	f	m	n	f	m	n	f	m	n
1	6.26	1	3	6.34	1	3	5.97	1	3
2	8.86	1	2	9.15	1	2	9.00	1	2
3	9.23	1	4	9.23	1	4	7.97	1	4
4	11.88	2	4	11.96	2	4	11.72	2	4
5	14.07	2	3	14.34	2	3	14.10	2	3
6	14.49	1	5	14.45	1	5	11.61	1	5
7	15.35	2	5	15.33	2	5	14.73	2	5
8	17.97	3	5	18.01	3	5	17.80	3	5
9	18.34	3	4	18.53	3	4	18.49	3	4
10	21.18	1	6	21.08	1	6	16.36	1	6
11	21.53	2	6	21.44	2	6	18.88	2	6
12	22.60	3	6	22.54	3	6	22.22	3	6
13	23.01	4	5	23.11	4	5	23.32	4	5
14	24.66	1	1	25.94	1	1	-	-	-
15	24.90	4	6	24.87	4	6	25.09	4	6
16	26.77	2	2	27.55	2	2	26.19	2	2
17	27.20	3	3	27.69	3	3	27.19	3	3
18	28.17	4	4	28.47	4	4	-	-	-
19	28.78	5	6	28.79	5	6	-	-	-
20	29.16	1	7	28.98	1	7	22.23	1	7

Clearly, thickness variation and inclusion of hopper and roof do not change significantly the lower natural frequencies of the simple shell, although the frequency results for the FE silo do not follow the same order of frequencies as those for the FE shell and the Gontkevich closed form solution. For some cases the frequencies differ by around 3 to 6 Hz (modes 6, 10, 11 and 20). However, the majority of the modes are still present in this low range frequency extraction once roof, hopper and thickness variations have been included. Inclusion of these variations resulted in modes 14,18 and 19 not appearing in these lowest frequencies. Instead, the modes due to the combinations $(m, n) = (0, 1)$, $(m, n) = (2, 7)$ and $(m, n) = (3, 7)$ appeared with the frequencies 7.00 Hz, 23.81 Hz and 27.64 Hz respectively. Due to the inclusion of the roof in the 3D silo instead of restricting the nodes at the top in the radial direction in the 3D shell the lowest mode for the beam modes ($m = 0$, $n = 1$) appears in the frequency extraction. None of these lowest modes were associated

with the roof or the hopper. In general, the results indicate that the vibration characteristics of the silo structure in the lower frequency region are similar to a simple cylindrical shell. It is also important to note that the first eleven results from the FE silo in Table 5.1 are below the audible range. Figure 5.3 shows the first eight mode shapes of the 3D silo model and these modes are seen to be similar to those in Fig. 4.12.

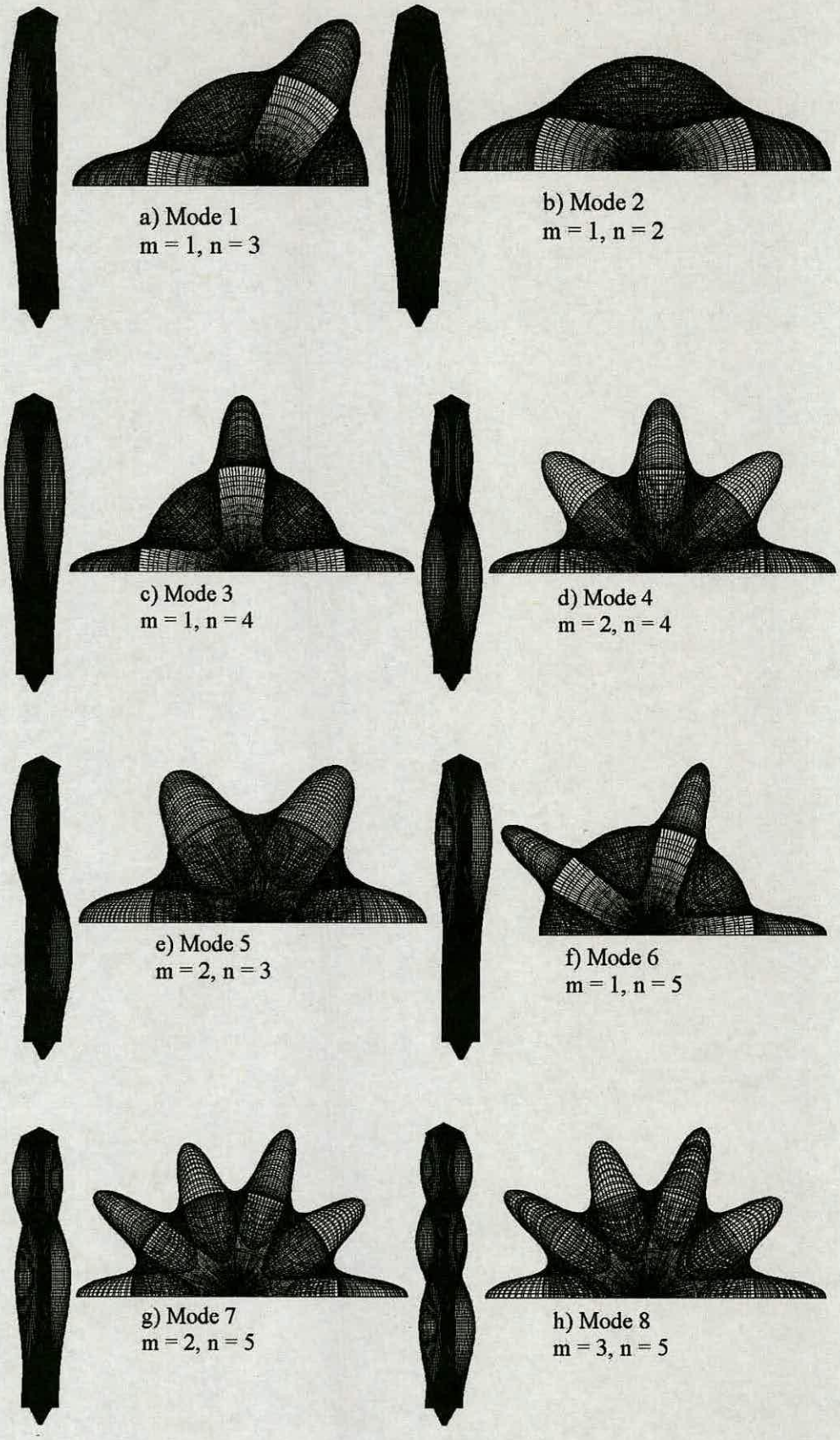

Figure 5.3: Lowest mode shapes for the 3D silo model.

5.3 The axisymmetric silo model

5.3.1 Implementations to the axisymmetric shell model

As it was discussed in Chapter 4, since the excitations are expected to be axisymmetric, the axisymmetric free vibration characteristics of the structure are important. The influence of the inclusion of hopper, roof and thickness variation on the natural frequencies of the axisymmetric shell model is discussed. Further the influence of the stored solid on the natural frequencies is considered in subsequent sections. Frequency spectra in Chapter 3 for different fill levels (90% and 60% silo capacity) showed that the fill level does not influence the honking frequencies. However, an understanding of the free vibration characteristics including the fill is important.

5.3.2 Influence of geometric implementations on the free vibrations

In this section the influence on the natural frequencies of different features such as roof, hopper and thickness variation in an axisymmetric silo model is considered. To study this influence, different axisymmetric models are analysed. The analysis is conducted using the same SAX1 axisymmetric shell elements described in Chapter 4 for the SD-SD and Clamped-SD axisymmetric models. The roof comprises 142 axisymmetric shell elements and 142 nodes while the hopper comprises 235 elements and the same number of nodes. Not all the models analysed in this section include the roof and the hopper. The following list describes the models considered:

- Model ASILO includes all the silo features – the hopper, the roof and thickness variation along the height. The model is clamped at the base.

- Model AHOPPER comprises a cylindrical shell of constant thickness (5.3 mm) and includes the hopper. The SD boundary condition is preserved at the top and the base is clamped.

- Model AROOF comprises a cylindrical shell of constant thickness and includes the roof (but not the hopper). Again it is clamped at the base.

- Model ATHICK comprises cylindrical shell with the thickness variation of the barrel included (as shown in Fig. 3.1). The hopper and the roof are not included in the model. The Clamped-SD boundary condition is applied at the base and top respectively.

- Model ASHELL is the simple cylindrical shell described in Chapter 4 with constant thickness having the Clamped-SD boundary conditions at the bottom and top respectively.

None of the above models include the particulate fill inside the silo at this stage. The axisymmetric models are shown in Fig. 5.4.

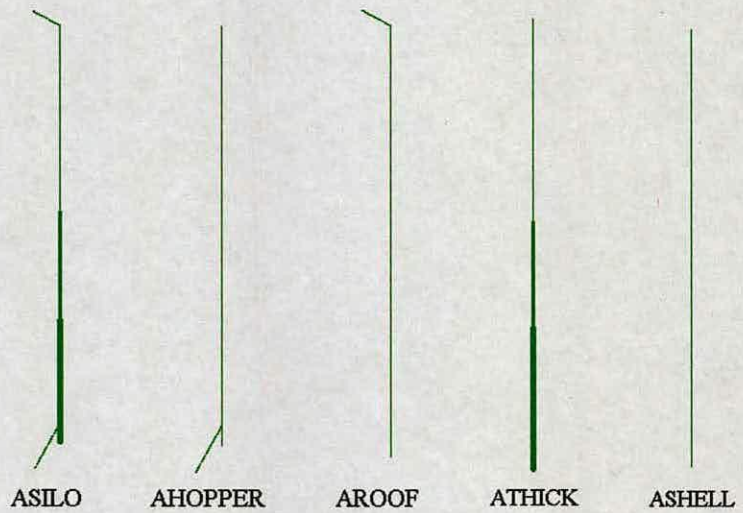

Figure 5.4: Axisymmetric models with different geometric implementations.

Table 5.2 shows the first twenty natural frequencies for the five models. The modes and natural frequencies of the models are arranged in the Table to show how each implementation affects the natural frequencies. The natural frequencies calculated for the axisymmetric simple shell with the Gontkevich closed form solution discussed earlier are also included in the last column of Table 5.2.

Table 5.2: Natural frequencies in Hz due to implementations in the axisymmetric FE model.

Mode	ASILO f	AHOPPER f	AROOF f	ATHICK f	ASHELL f	Gontkevich f
1	64.73	60.34	57.67	68.16	60.34	-
2	123.93	-	130.83	-	-	-
3	180.81	179.47	185.71	176.41	180.04	181.93
4	293.13	272.29	296.62	297.67	295.88	293.97
5	321.61	302.48	-	-	-	-
6	332.82	-	341.93	-	-	-
7	376.33	-	391.77	-	-	-
8	398.64	402.52	403.07	397.02	401.03	400.78
9	429.50	-	454.58	-	-	-
10	479.76	479.97	479.61	483.30	479.66	482.93
11	486.09	-	516.64	-	-	-
12	519.28	520.52	522.37	519.63	520.64	525.21
13	535.18	537.20	-	-	-	-
14	537.23	-	-	-	-	-
15	540.09	539.45	538.48	538.51	538.42	542.52
16	547.05	547.00	546.94	546.89	546.95	550.42
17	551.83	551.67	551.65	551.83	551.67	554.59
18	554.50	554.56	554.56	554.51	554.58	557.12
19	556.50	556.49	556.49	556.52	556.50	558.75
20	557.87	557.85	557.84	557.88	557.86	559.88

Table 5.2 shows that some frequencies appear in a particular model but are absent in others. A graphical representation shows that these can be attributed the specific features included in the model. The first eight modes of Table 5.2 are shown in Figs. 5.5 to 5.9 for different axisymmetric FE models. Two figures are shown for each mode. The one on the left side comprises the deformed and undeformed shape of the model in black and green colours respectively. The one on the right is again the deformed shape but now a colour code representing the modal displacement has been applied. Red colour represents the maximum modal displacement and the blue one represents the minimum. The only model that has all the eight modes is the ASILO model and the others have fewer corresponding modes. It is interesting to note how the different implementations affect modes 1, 3, 4 and 8, which appear in all the FE models. For example it is clear from the maximum modal displacement at the top that mode 1 in Figs. 5.6, 5.8 and 5.9 is due to the stretching of the shell, although

Figs. 5.5 and 5.7 give the impression of this being a mode due to roof deformation. The maximum modal displacement occurs at the roof for mode 1 but once the shell stretches the roof moves with it. Mode 3 appears to be modified by the inclusion of the roof. In Figs. 5.6, 5.8 and 5.9 the maximum modal displacement is in the shell for this mode while in Figs. 5.5 and 5.7 the maximum modal displacement seems to be in the roof. However, in models without the roof (Figs. 5.6, 5.8 and 5.9) its maximum modal displacement is at the top and it is possible that due to this deformation the roof deforms as shown in mode 3 of Figs. 5.5 and 5.7. Modes 4 and 8 preserve the same deformation on the shell and therefore easy to compare. The shape of the shell is not affected by the deformations of the roof or hopper when these are included in the models (e.g. modes 4 and 8 in Fig. 5.5, 5.6 and 5.7). The inclusion of the roof and the hopper introduces additional modes associated with these additions. For example mode 2, 6 and 7 are associated with the roof and mode 5 with the hopper as shown in Figs. 5.5, 5.6 and 5.7.

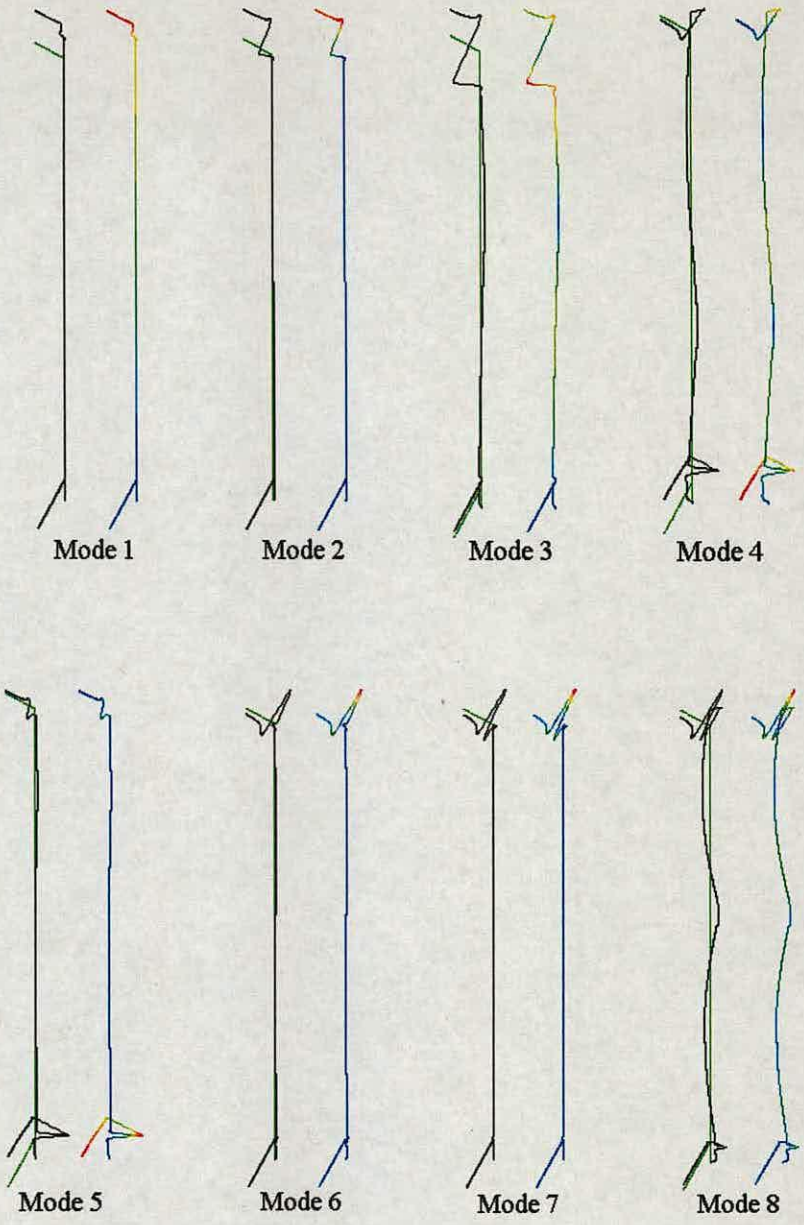

Figure 5.5: Lowest axisymmetric modes in Table 5.2 for the ASILO model. The colour coding used for the second diagram of each mode represents modal displacement amplitudes with red indicating the maximum value followed by yellow, green and blue.

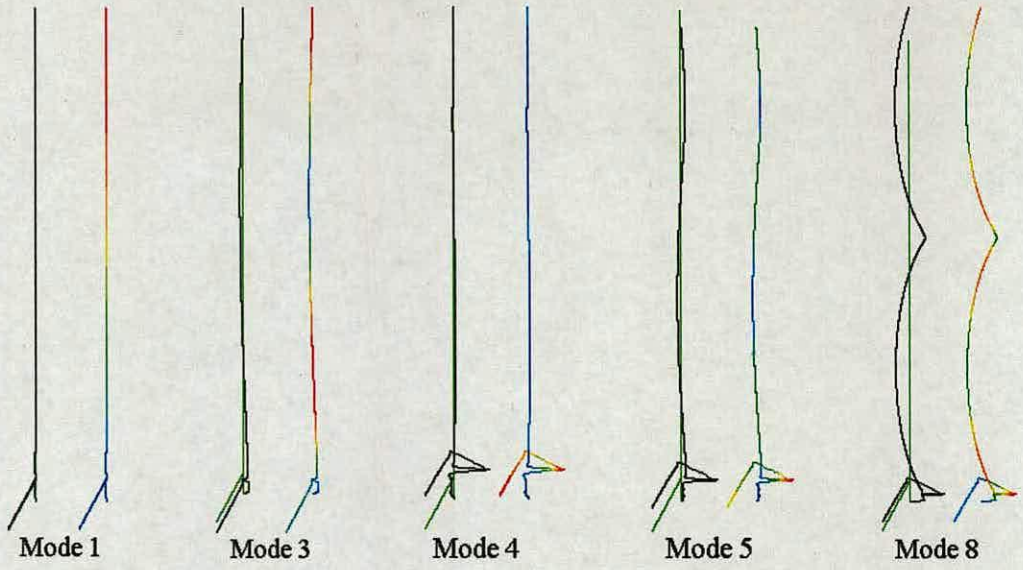

Figure 5.6: Lowest axisymmetric modes in Table 5.2 for the AHOPPER model.

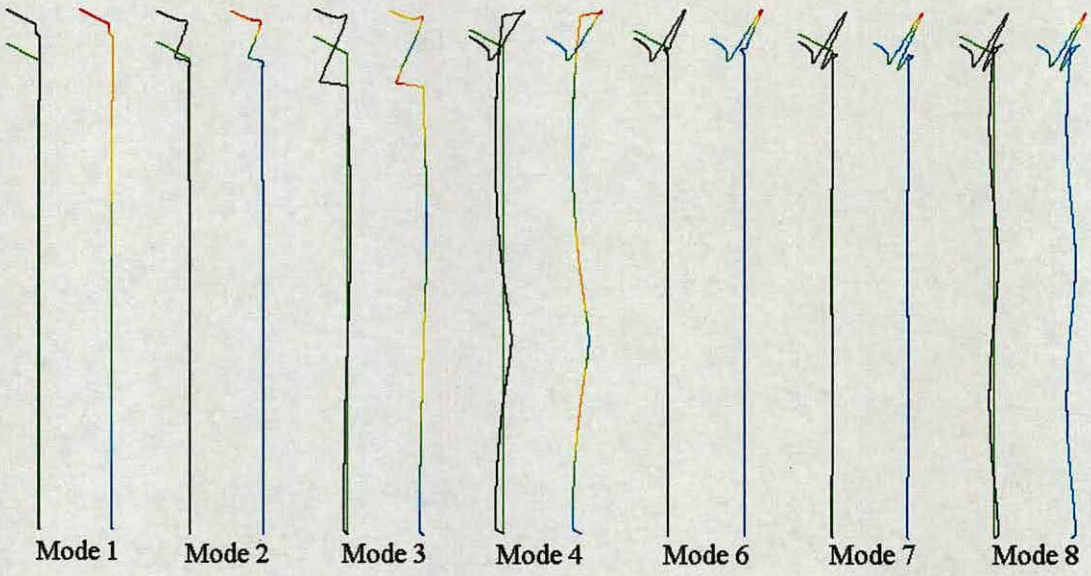

Figure 5.7: Lowest axisymmetric modes in Table 5.2 for the AROOF model.

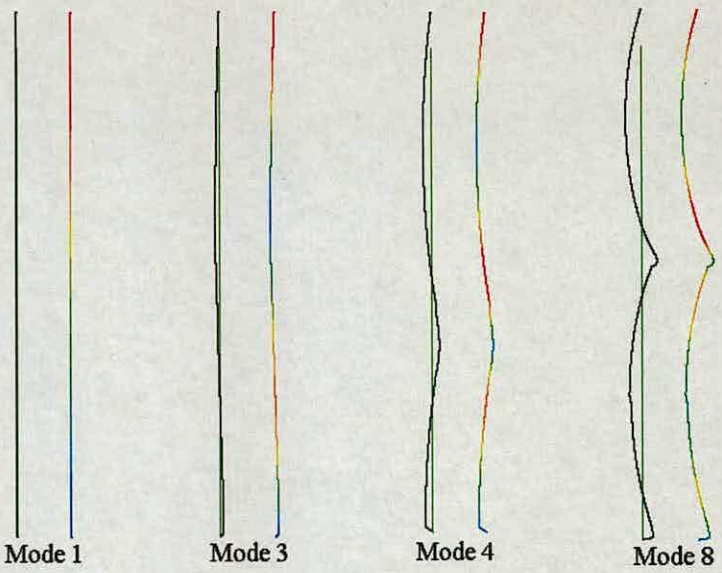

Figure 5.8: Lowest axisymmetric modes in Table 5.2 for the ATHICK model.

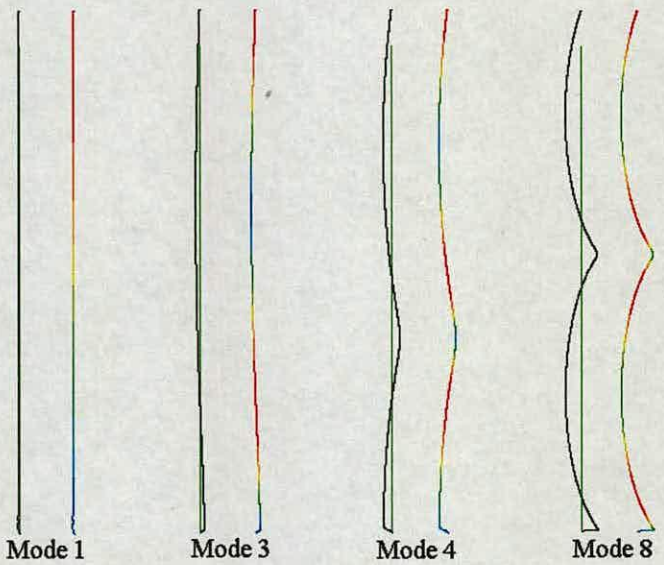

Figure 5.9: Lowest axisymmetric modes in Table 5.2 for the ASHELL model.

Comparing models ASHELL (simple shell) and ATHICK (simple shell with thickness variation) it can be noted that the inclusion of variable thickness modifies the frequencies of different modes in Table 5.2 but does not introduce new modes. The models AHOPPER and AROOF, when compared with model ASHELL, create

new modes and slightly modify the frequency of the existing modes. The ASILO model includes all the effects and the natural frequencies due to each of these changes. It is interesting to note that modes 5 and 6 are close to the honking fundamental frequency of the silo wall in the instrumented honking silo (f_h = 333 Hz). However, mode 5 is primarily due to the hopper vibration and mode 6 is due to the roof. The vibration in mode 5 (Figs. 5.5 and 5.6) produces a maximum modal displacement in the hopper and at the transition between shell and hopper while in mode 6 (Figs. 5.5 and 5.7) the maximum modal displacement occurs in the roof with a smaller value in the cylindrical shell. Modes 15 to 20 appear in all models, indicating that these modes are due to the cylindrical shell. In fact they tend to the "ring frequency" which comprises predominantly of radial motion.

The axisymmetric behaviour of thin cylindrical shells for the Clamped-SD boundary conditions was described in Chapter 4. In this axisymmetric behaviour the axial and radial motion are coupled together. From Fig. 4.16 it is easy to distinguish the axial frequencies from the radial ones. For the lowest frequency values in the coupled motion of Fig. 4.16 the first four frequencies are axial and the following frequencies are radial which have a fairly constant value ($\approx$ 570 Hz). These distinctions are not so apparent when roof and hopper are included. To compare the modes of ASILO (with roof and hopper) and ASHELL (only cylindrical shell) models modal displacements in the radial and axial directions are plotted along the height of the cylindrical shell. Modes 4, 10, 12 and 17 are selected from Table 5.2 for the two models mentioned above. Mode 4 is expected to vibrate predominantly in the axial direction while modes 10 and 12 are the modes near the transition from axial to radial and mode 17 should vibrate predominantly in the radial direction. The results are shown in Figs. 5.10 and 5.11. The plots show the modal displacements in the radial and axial direction versus the normalized height of the silo barrel including the skirt. The modes are normalised so that the maximum modal displacement is unity irrespective of the direction. The results of the ASHELL model in Fig. 5.10 show that the maximum modal displacement occurs in the axial direction for modes 4 and 10. However, the motion changes to predominantly radial for modes 12 and 17. For the same modes in the ASILO model in Fig. 5.11 the maximum value (unity) does not

occur in the shell except for mode 17 (Fig. 5.11d). For mode 4 in Fig. 5.11a the maximum axial modal displacements are higher than the radial along the height of the shell. However, the influence of the hopper is seen in the form of a sharp peak on the left hand side of the plot. The maximum modal displacements in the radial and axial direction are almost the same for mode 10 (Fig. 5.11b). For modes 12 and 17 the radial maximum modal displacements are higher than the axial ones and Figs. 5.10d and 5.11d can be seen to be almost identical. The modal participation factors confirm the behaviour shown in Figs. 5.10 and 5.11. The participation factors are higher in the axial direction than those in the radial direction for modes 4 and 10 in Fig. 5.10. The participation factors for modes 12 and 17 are higher in the radial direction than those in the axial one. For the ASILO model (Fig. 5.11) a similar behaviour was observed, however, the participation factor for mode 10 is slightly higher in the radial direction than that in the axial one.

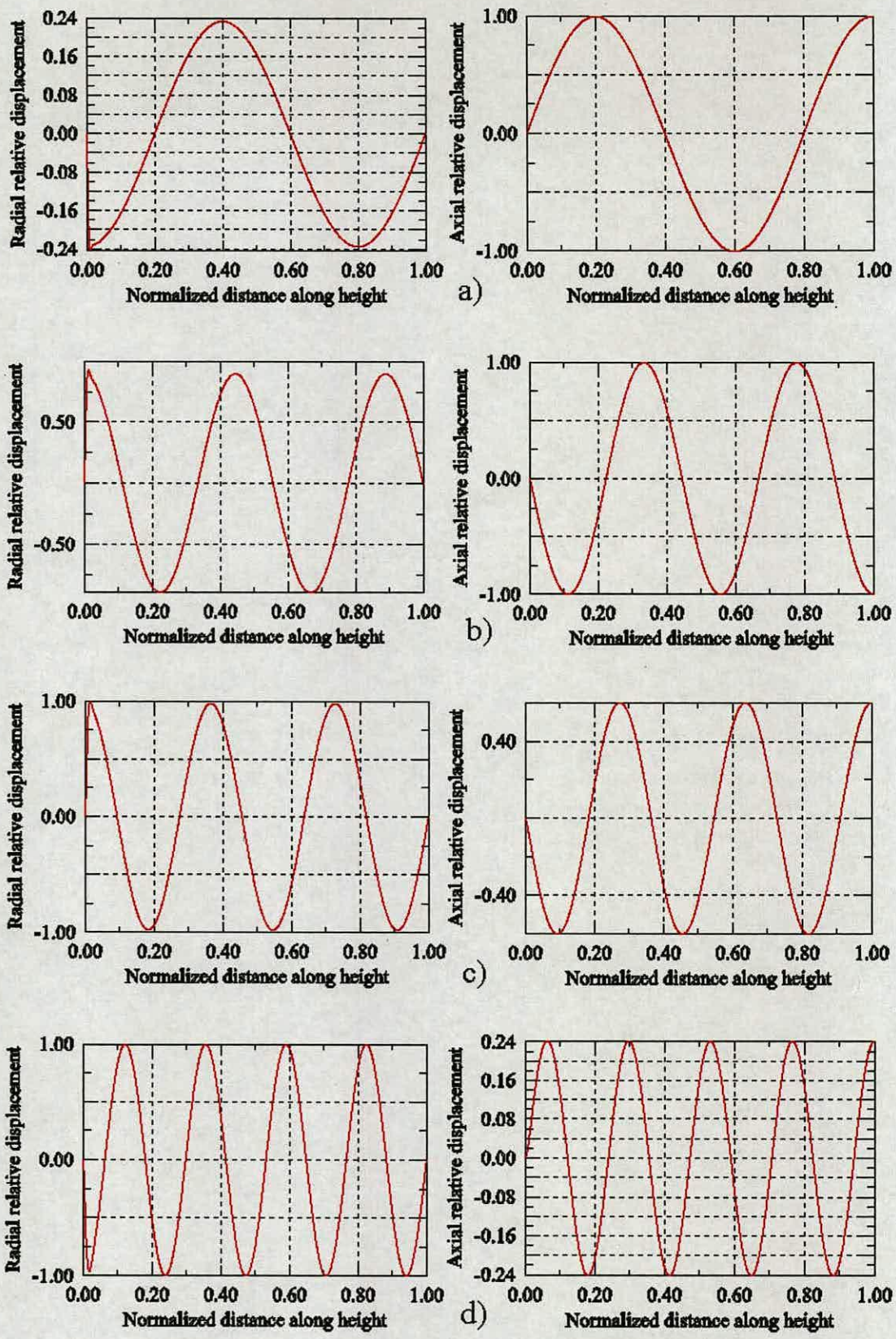

Figure 5.10: Radial and axial relative displacement in ASHELL model in Table 5.2 for modes a) 4, b) 10, c) 12 and d) 17.

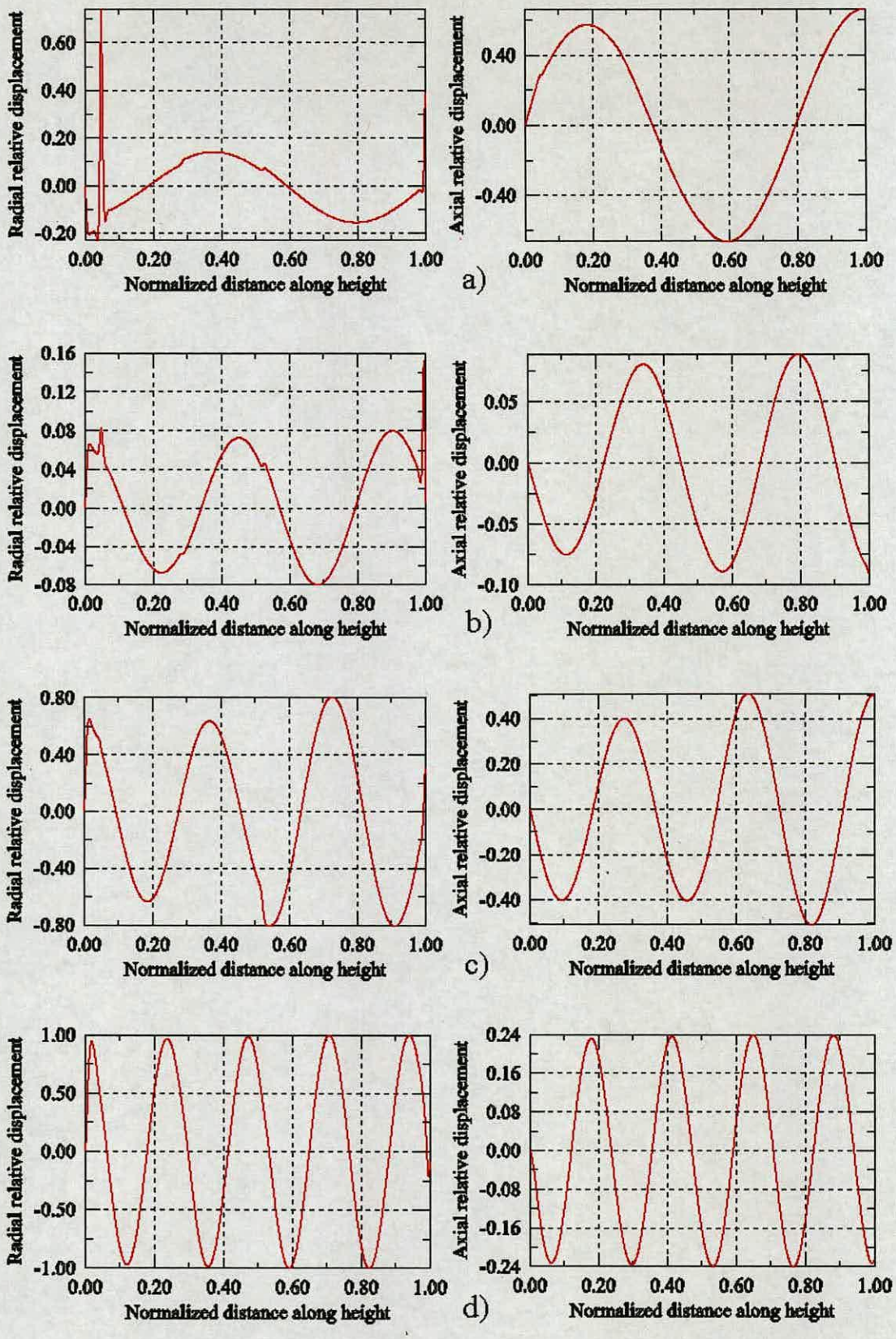

Figure 5.11: Radial and axial relative displacement in ASILO model in Table 5.2 for modes a) 4, b) 10, c) 12 and d) 17.

5.3.3 Bulk solid influence

In addition to the geometric implementations described in the previous section, the role of the bulk solid in the free vibration characteristics of the silo-fill system needs to be examined. As was mentioned in Chapter 3, the silo has been reported to honk when filled in the range of 100% to 50% of its capacity. Moreover the honking frequencies do not change with changes in the fill level in this range. Honking does not occur in the silo structure when it is filled below 50% of its capacity. In order to investigate the influence of the bulk solid on the natural frequencies of the silo-fill system, two additional axisymmetric models are considered. In these two models, the influence of the material height inside the silo is investigated. The analysis is conducted for two models in which the silo is considered to be filled up to 90% and 55% of its capacity (fill range in which the silo is known to honk). The influence of solid stiffness and mass on the free vibration characteristics of the silo-fill system is examined for these two cases. The axisymmetric ASILO model described earlier is used to model the silo structure, while the bulk solid material is modelled with axisymmetric solid elements. The axisymmetric solid elements used are CAX4, which is a 4-node bilinear element using two degrees of freedom per node (HKS, 2002). A total of 72,600 solid elements, 1815 rows and 40 columns, and 74,416 nodes complement the model at 90% silo capacity. The total number of elements and nodes modelling the stored solid at 55% silo capacity are 46,280 (1157 rows and 40 columns) and 47,478 respectively for the model. The models are shown in Fig. 5.12 (including the ASILO discussed earlier). The bulk material properties were determined following the procedures described by Masroor et al. (1987), for the determination of Young's modulus (E) and Poisson's ratio (v), and Akroyd (1958), for the determination of minimum and maximum density ($\rho_{MIN} - \rho_{MAX}$). A summary of these properties is listed in Table 5.3. It is important to note the difference between the Young's moduli of the structure (aluminium) and PET pellets, where the latter is significantly smaller. It is recognised that the Young's modulus of the bulk solid varies proportionally with the normal vertical stress within the solid and thus varies along the height. However, this variation is less critical in tall silos as the normal vertical stress is close to the value at infinite depth along most of the fill

height (see Chapter 1). Therefore the Young's modulus was assumed to be constant along the silo height. The maximum density value has also been assumed due to the highly packed condition of the bulk solid. The silo-fill interaction is complex in real silos, however, here it has been assumed that solid and silo are bonded. To achieve this, a pinned multi-point constrain is applied on the edge to model the silo-fill interaction. This interaction provides a pinned joint between the contact nodes (HKS, 2002).

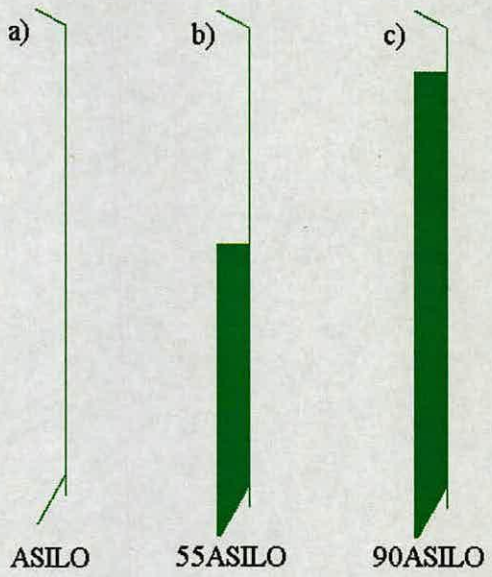

Figure 5.12: Axisymmetric models including the stored solid, a) empty, b) 55% silo capacity and c) 90% silo capacity.

Table 5.3: Properties of PET pellets stored in the honking silo.

E =	6.95×10^6 Pa
ν =	0.25
ρ_{MIN} =	770 kg/m³
ρ_{MAX} =	890 kg/m³

The natural frequencies of the first twenty modes of the ASILO, 55ASILO and 90ASILO models (Fig. 5.12) are presented in Table 5.4. The lowest natural frequencies are reduced significantly by the inclusion of the bulk material. Further, for the 55ASILO and 90ASILO models, all frequencies of Table 5.4 correspond to

the vibration modes associated with the motion of the fill solid and not to the silo structure. Moreover these natural frequencies are much lower than the honking fundamental frequency. As would be expected the frequencies corresponding to the 55ASILO and 90ASILO models are significantly different.

Table 5.4: Natural frequencies in Hz in the axisymmetric models including the bulk material influence at different heights.

Mode	ASILO f	55ASILO f	90ASILO f
1	64.73	11.43	8.55
2	123.93	14.62	13.30
3	180.81	16.54	14.70
4	293.13	18.73	15.83
5	321.61	21.15	17.05
6	332.82	23.60	18.38
7	376.33	26.01	19.81
8	398.64	26.56	21.29
9	429.50	28.34	22.79
10	479.76	30.40	24.09
11	486.09	31.02	24.43
12	519.28	32.33	25.80
13	535.18	32.49	27.22
14	537.23	33.13	28.58
15	540.09	33.86	29.59
16	547.05	34.12	29.90
17	551.83	34.89	31.12
18	554.50	35.74	31.31
19	556.50	36.31	32.21
20	557.87	37.23	32.29

The lowest modes for the 55ASILO and 90ASILO models are shown in Figs. 5.13 and 5.14 respectively. These can be compared with the mode shapes of the ASILO model shown in Fig. 5.5. The maximum modal displacement in red colour occurs in the solid while in most of the modes the minimum modal displacement in blue colour occurs in the silo structure. The lowest mode shapes in Figs. 5.13 and 5.14 are similar and clearly dissimilar to those presented in Fig. 5.5 for the ASILO model. Thus if honking were due to the silo-fill system acting together and responding to

excitations in some of its natural modes the honking frequencies would be expected to change with the fill level. This is not so from the observations in Chapter 3.

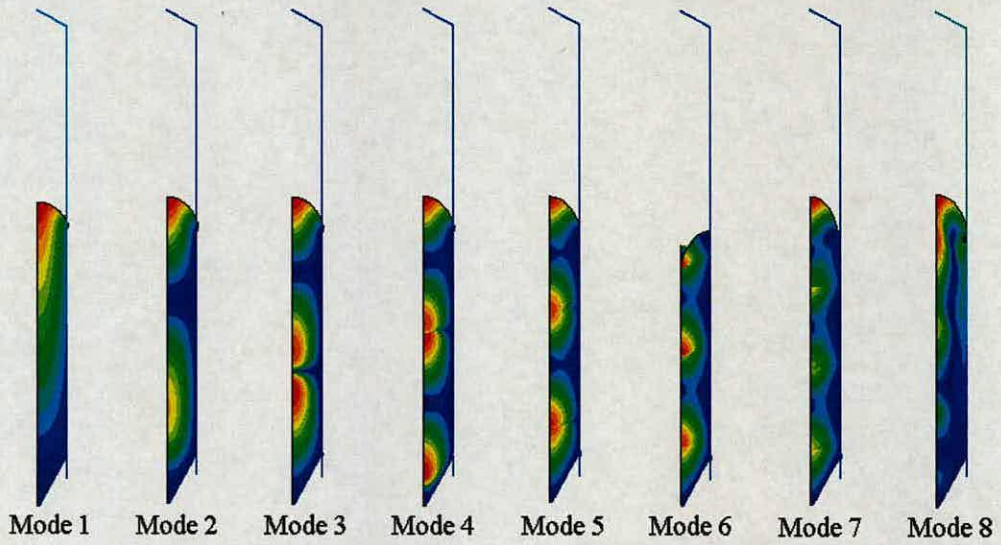

Figure 5.13: Axisymmetric mode shapes for the 55ASILO model.

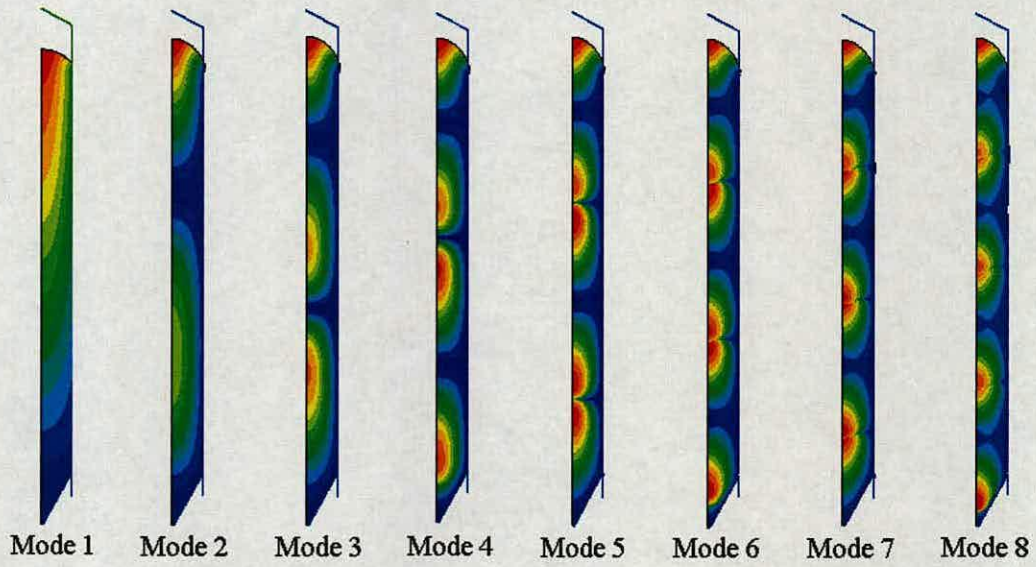

Figure 5.14: Axisymmetric mode shapes for the 90ASILO model.

The reduction in the natural frequencies is expected due to the mass of the stored material. A second series of analyses is conducted in which the influence of the stiffness of the solid is included but the mass is practically eliminated. This is achieved in the axisymmetric FE model by giving an extremely low value to the bulk

solid density. The results of the analysis are presented in Table 5.5. The natural frequencies are almost the same for the three models. A very small increment can be seen in the 55ASILO and 90ASILO models due to the stiffness of the solid. These models also show that fill height does not influence significantly the free vibration characteristics of the system when the mass of the stored solid is ignored.

Table 5.5: Natural frequencies in Hz in the axisymmetric models excluding the mass of the bulk material.

Mode	ASILO f	55ASILO f	90ASILO f
1	64.73	64.98	65.09
2	123.93	123.99	124.03
3	180.81	181.12	181.85
4	293.13	295.24	296.00
5	321.61	332.42	332.43
6	332.82	337.61	337.80
7	376.33	376.44	376.48
8	398.64	400.77	402.55
9	429.50	429.54	429.59
10	479.76	480.73	481.17
11	486.09	488.17	490.16
12	519.28	522.44	526.02
13	535.18	538.23	538.77
14	537.23	542.78	546.16
15	540.09	550.08	554.59
16	547.05	555.07	559.64
17	551.83	557.78	561.57
18	554.50	559.25	563.10
19	556.50	560.30	563.96
20	557.87	561.09	564.76

The lowest modes for the 55ASILO and 90ASILO models for analyses that exclude the mass of the stored material are shown in Figs. 5.15 and 5.16 respectively. The mode shapes in these figures are similar to those shown in Fig. 5.5 for the ASILO model, only modes 5 and 6 switch position. However, the difference in frequency between these two modes is small and the switch does not affect them, see Table 5.5. Now the modes associated with the roof are 2, 5 and 7 and the one associated with the hopper is mode 6. For modes 1, 3, 4 and 8, which are the modes associated with

the shell vibration, the stored solid has higher relative deformation than that in modes 2, 5 and 7 that are the modes associated with the roof. In these modes (2, 5 and 7) the stored solid barely deforms while it reaches its maximum relative displacement in the mode associated with the hopper (mode 6), but all these relative displacements are due to the modal displacement of the shell.

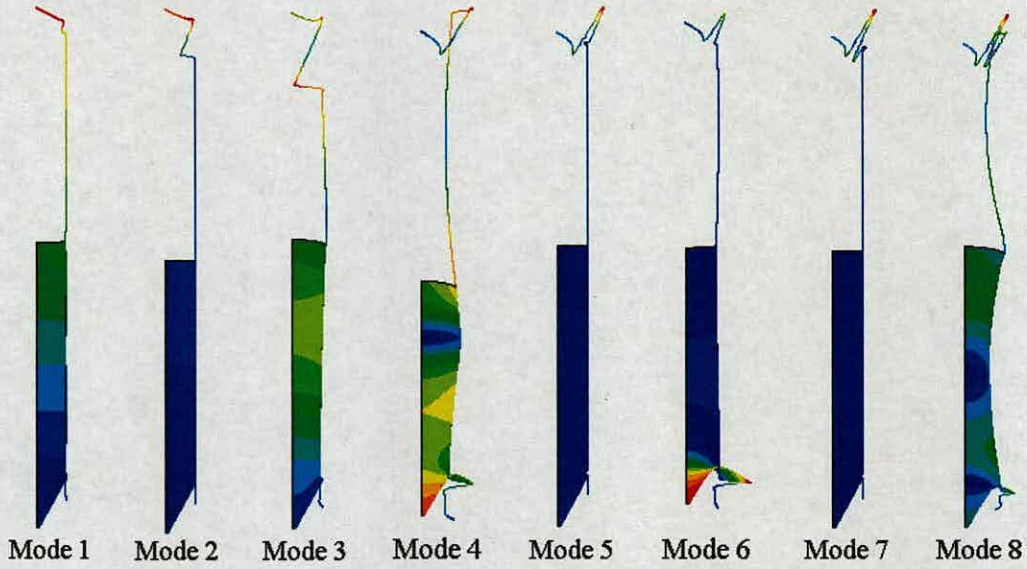

Figure 5.15: Axisymmetric mode shapes for the 55ASILO model excluding mass of stored material.

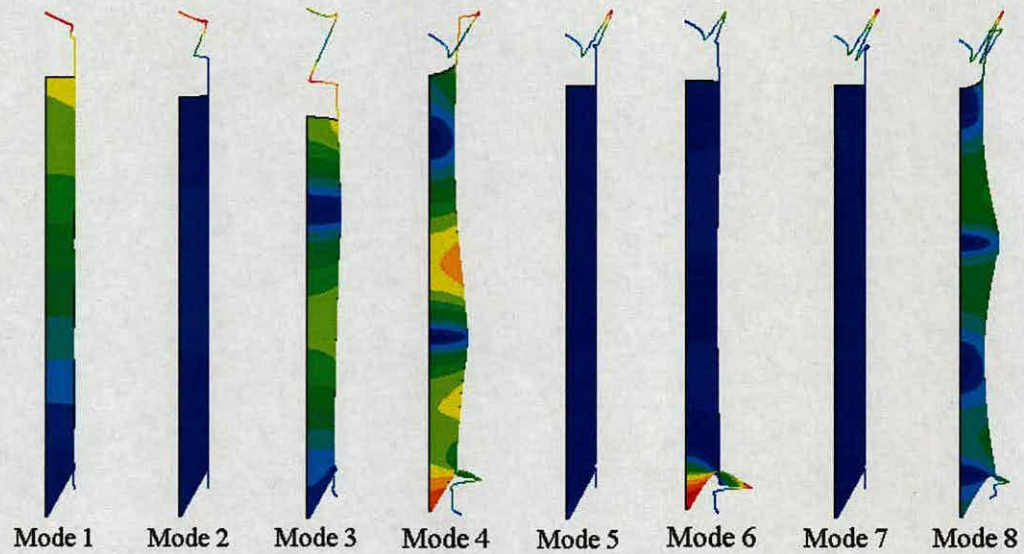

Figure 5.16: Axisymmetric mode shapes for the 90ASILO model excluding mass of stored material.

The results suggest that the stiffness introduced by the stored material has only a small influence on the natural frequencies of the silo. This is apparently due to the low Young's modulus of the stored solid in comparison to the silo structure. It is, however, clear that the mass of the fill material combined with the silo wall significantly reduces the natural frequencies and these frequencies change with the fill height. This indicates that during honking vibrations at high frequency the stored solid is uncoupled from the shell or particles do not remain attached to the silo wall. Thus while the fill has an important role to play in exciting the structure to honk, its role is relatively less important during honking.

5.4 Parametric study on the axisymmetric silo model

A frequency extraction varying different geometric parameters is conducted in this section using the ASILO model. Based on the results obtained in the previous section, the bulk solid is not included in the parametric study. The parameters whose variation is examined are the hopper angle and the silo aspect ratio, i.e. height to diameter ratio (L/D). Examining the variation in free vibration characteristics with hopper angle is considered to be important because it is apparent that the dynamic excitation is in the lower part of the silo, which includes the hopper and the barrel. Moreover, mode 6 in the frequency extraction shown in Table 5.5 is due to the hopper vibration (Fig. 5.16) and its frequency is close to the fundamental honking frequency.

5.4.1 Hopper angle variation

Different models are constructed varying the half hopper angle β (see Fig. 1.1) from 90° to 10° at 10° intervals. The 90° model is a flat-bottomed silo while the 10° is a silo with a very steep discharge cone. The motivation is to investigate the natural frequency variation of the silo structure with variation in the hopper angle. Particular attention is paid to those modes due to the hopper vibration. Table 5.6 shows the natural frequencies for seven different models. Every frequency value has a superscript representing the part or parts in the silo where the maximum modal displacement occurs. The superscripts S, R and H indicate the shell, roof and hopper

respectively. Multiple superscripts indicate that the maximum modal displacement occurs in these parts simultaneously. Of particular interest are modes in which large modal displacement occur at the transition of the hopper and the shell (see mode 6 in Fig. 5.16), which has a frequency close to the fundamental honking frequency. Further importance of such modes will be discussed in Chapter 7. These modes have been highlighted in Table 5.6. The highlighted values represent modes in which the modal displacement at the transition is significant. Red, yellow and blue indicate significant modal displacement in decreasing order at the transition. Red indicates that the modal displacement at the transition is the largest. Table 5.6 shows that the natural frequencies associated with the shell and roof do not change significantly with the hopper angle variation. The mode number varies but the frequency remains close and the mode shape similar. For example mode 1 for $\beta = 10^\circ - 70^\circ$ is associated with the shell and the natural frequency differs only slightly with change in hopper angle. Similarly mode 16 for $\beta = 70^\circ$ is associated with the roof. However, when $\beta = 60^\circ$ the mode associated with the roof is 14 and the shell also has large modal displacements. Similar roof mode can be found for $\beta = 50^\circ$ in mode 13 and for $\beta = 10^\circ - 40^\circ$ in mode 11. For larger β values more modes are associated with the hopper. However, when β is large the modal displacements at the transition are not significant for the first twenty modes. For example for $\beta = 50^\circ - 90^\circ$ the modal displacement at the transition is never maximum even when the mode is associated with the hopper. However, when $\beta = 10^\circ - 40^\circ$ the maximum modal displacement occurs at the transition for modes 5 ($\beta = 20^\circ - 40^\circ$) and 13 ($\beta = 10^\circ$). Mode 5 has a natural frequency close to the fundamental honking frequency. The hopper half angle variation between the range $\beta = 20^\circ - 40^\circ$ does not significantly influence the free vibration characteristic of the structure, except in higher modes for $\beta = 20^\circ$ where the maximum modal displacement is in both hopper and shell. It is interesting to note that the majority of the natural frequencies shown in Table 5.6 where significant modal displacement is observed at the transition are modes due to the hopper. The 90° and the 80° models are not included in the Table because the modal displacement at the transition is not significant ($\beta = 90^\circ$) or is relatively small ($\beta = 80^\circ$).

Table 5.6: Natural frequencies in Hz with hopper half angle variation (S = shell, R = roof, H = hopper and the displacement at transition is small, medium and maximum).

Mode	$\beta = 70^\circ$	$\beta = 60^\circ$	$\beta = 50^\circ$	$\beta = 40^\circ$	$\beta = 30^\circ$	$\beta = 20^\circ$	$\beta = 10^\circ$
1	64.74^{S}	64.74^{S}	64.73^{S}	64.73^{S}	64.73^{S}	64.72^{S}	64.70^{S}
2	123.95^{R}	123.94^{R}	123.94^{R}	123.93^{R}	123.96^{R}	123.91^{R}	123.89^{R}
3	126.62^{H}	$179.57^{H,S}$	180.96^{S}	180.92^{S}	180.81^{S}	180.58^{S}	178.59^{S}
4	181.12^{S}	$182.44^{H,S}$	$231.99^{H,S}$	$276.55^{H,S}$	$293.13^{H,S}$	$290.27^{H,S}$	215.74^{H}
5	260.98^{H}	298.15^{S}	298.41^{S}	$300.48^{S,H}$	$321.61^{S,H}$	$325.23^{S,H}$	300.30^{S}
6	297.91^{S}	332.72^{R}	332.72^{R}	332.73^{R}	332.82^{R}	332.97^{R}	332.72^{R}
7	300.47^{H}	355.72^{H}	376.25^{R}	376.26^{R}	376.33^{R}	376.41^{R}	376.24^{R}
8	332.72^{R}	376.24^{R}	$397.37^{R,S}$	$397.64^{R,S}$	$398.64^{R,S}$	$400.06^{R,S}$	$396.57^{R,S}$
9	353.72^{H}	$396.74^{H,S}$	429.48^{R}	429.48^{R}	429.50^{R}	429.52^{R}	429.43^{R}
10	376.25^{R}	$399.01^{H,S}$	433.06^{H}	479.58^{R}	479.76^{R}	480.02^{R}	$465.77^{H,S}$
11	397.27^{S}	429.48^{R}	476.12^{H}	485.82^{R}	486.09^{R}	486.44^{R}	482.05^{R}
12	405.03^{H}	453.19^{H}	479.83^{R}	492.32^{H}	$519.28^{R,S}$	$519.49^{R,S}$	$492.81^{R,S,H}$
13	429.48^{R}	$479.66^{S,R}$	486.03^{R}	$519.24^{R,S}$	535.18^{H}	537.05^{R}	$521.10^{S,R}$
14	469.75^{H}	$485.97^{S,R}$	$519.14^{R,H,S}$	533.51^{H}	$537.23^{R,H}$	540.02^{R}	537.35^{R}
15	$479.79^{S,R}$	505.45^{H}	527.55^{H}	537.20^{R}	540.09^{R}	$546.98^{R,S}$	540.29^{R}
16	486.12^{R}	519.50^{S}	$537.14^{R,S}$	540.11^{R}	$547.05^{R,S}$	$551.63^{H,S}$	$547.21^{R,S}$
17	519.31^{S}	537.08^{R}	$540.10^{R,S}$	$547.07^{R,S}$	551.83^{S}	$553.91^{H,S}$	551.99^{S}
18	527.50^{H}	540.05^{R}	$547.08^{R,S}$	551.86^{S}	554.50^{S}	$555.01^{H,S}$	554.59^{S}
19	537.18^{R}	$547.03^{S,R}$	551.86^{S}	554.51^{S}	556.50^{S}	$556.67^{H,S}$	556.57^{S}
20	540.14^{R}	551.78^{S}	554.51^{S}	556.51^{S}	557.87^{S}	$557.96^{S,H}$	557.92^{S}

The axisymmetric mode associated with relative large displacements in the transition and hopper is close to the fundamental honking frequency. To investigate if this behaviour repeats in other honking silos presented in Chapter 3 a similar frequency extraction with a hopper angle variation is conducted for the four cases (Fig. 3.26). For simplicity, only the results for Case1 and Case3 are presented in Table 5.7 and Table 5.8 respectively. The results for the remaining two cases are similar to those presented in Tables 5.6 to Table 5.8.

Table 5.7: Natural frequencies in Hz with hopper half angle variation in Case1 (S = shell, R = roof, H = hopper and the displacement at transition is small, medium and maximum).

Mode	$\beta = 70^\circ$	$\beta = 60^\circ$	$\beta = 50^\circ$	$\beta = 40^\circ$	$\beta = 30^\circ$	$\beta = 20^\circ$	$\beta = 10^\circ$
1	68.26^{S}	68.26^{S}	68.24^{S}	68.20^{S}	68.12^{S}	67.96^{S}	67.41^{S}
2	97.23^{R}	97.80^{R}	97.81^{R}	97.77^{R}	97.68^{R}	93.48^{R}	96.67^{R}
3	104.55^{H}	145.83^{H}	175.48^{H}	183.08^{H}	$183.26^{H,S}$	$179.29^{H,S}$	154.41^{H}
4	194.05^{S}	196.64^{S}	$208.96^{H,S}$	$236.35^{H,S}$	253.30^{R}	253.35^{R}	220.28^{H}
5	219.46^{H}	253.74^{R}	253.76^{R}	253.83^{R}	$259.30^{S,H,R}$	$262.01^{H,R,S}$	253.80^{R}
6	250.07^{H}	287.35^{R}	287.39^{R}	287.47^{R}	287.65^{R}	287.77^{R}	287.42^{R}
7	253.74^{R}	299.97^{H}	$321.18^{R,S}$	324.93^{R}	327.84^{R}	328.26^{R}	$317.57^{R,H,S}$
8	287.33^{R}	$318.70^{R,S,H}$	329.64^{R}	330.65^{R}	$337.40^{R,S}$	$346.16^{S,R}$	329.12^{R}
9	291.95^{H}	329.27^{R}	367.78^{H}	369.87^{R}	369.94^{R}	370.06^{R}	369.66^{R}
10	$317.91^{R,H,S}$	334.28^{H}	369.84^{R}	411.79^{R}	412.45^{R}	412.93^{R}	$397.56^{H,R,S}$
11	329.13^{R}	369.82^{R}	401.87^{H}	$417.37^{R,H}$	418.50^{R}	419.59^{R}	414.53^{R}
12	332.18^{H}	376.90^{H}	411.64^{R}	418.95^{H}	$450.78^{R,S}$	$450.78^{R,S}$	$434.52^{S,H}$
13	269.82^{R}	$410.81^{R,H}$	417.30^{R}	$450.42^{H,S}$	454.66^{H}	461.86^{R}	$452.03^{R,S}$
14	377.78^{H}	$415.99^{R,H}$	442.61^{H}	452.12^{H}	461.87^{R}	$467.07^{R,S}$	461.85^{R}
15	410.89^{R}	$418.91^{H,R}$	$450.61^{R,S}$	461.87^{R}	$467.14^{R,S}$	$471.97^{H,S}$	$467.02^{R,S}$
16	416.67^{R}	$450.55^{R,S}$	461.87^{R}	$467.19^{R,S}$	$472.19^{S,R}$	473.42^{H}	$472.33^{S,R}$
17	425.87^{H}	461.85^{R}	$467.22^{R,S}$	$472.21^{S,R}$	475.59^{S}	$475.88^{H,S}$	475.78^{S}
18	$450.51^{R,S}$	462.41^{H}	$472.19^{S,R}$	475.58^{S}	477.69^{S}	477.81^{S}	477.77^{S}
19	461.87^{R}	$467.33^{R,S}$	$475.50^{S,H}$	477.68^{S}	478.82^{S}	478.84^{S}	478.80^{S}
20	$467.23^{R,S}$	$472.31^{S,R}$	$477.61^{S,H}$	478.81^{S}	479.57^{S}	479.62^{S}	479.60^{S}

Table 5.8: Natural frequencies in Hz with hopper half angle variation in Case3 (S = shell, R = roof, H = hopper and the displacement at transition is small, medium and maximum).

Mode	$\beta = 70^\circ$	$\beta = 60^\circ$	$\beta = 50^\circ$	$\beta = 40^\circ$	$\beta = 30^\circ$	$\beta = 20^\circ$	$\beta = 10^\circ$
1	56.79^{S}	56.79^{S}	56.79^{S}	56.79^{S}	56.79^{S}	56.79^{S}	56.79^{S}
2	76.66^{R}	76.69^{R}	76.69^{R}	76.69^{R}	76.69^{R}	76.69^{R}	76.68^{R}
3	85.91^{H}	122.39^{H}	156.61^{H}	172.48^{S}	172.46^{S}	172.40^{S}	160.42^{H}
4	172.55^{S}	172.55^{S}	172.56^{S}	$187.98^{S,H}$	190.67^{R}	190.67^{R}	173.20^{S}
5	184.17^{H}	190.67^{R}	190.67^{R}	190.67^{R}	216.03^{R}	216.02^{R}	190.67^{R}
6	190.67^{R}	216.03^{R}	216.03^{R}	216.03^{R}	$227.51^{S,H}$	$237.29^{S,H}$	216.03^{R}
7	207.83^{H}	247.36^{R}	247.36^{R}	247.36^{R}	247.36^{R}	247.36^{R}	247.36^{R}
8	216.03^{R}	252.96^{H}	277.57^{R}	277.56^{R}	277.56^{R}	277.57^{R}	277.55^{R}
9	240.74^{H}	277.57^{R}	$285.57^{R,S}$	$285.55^{R,S}$	$285.49^{R,S}$	$285.53^{R,S}$	$285.45^{R,S}$
10	247.36^{R}	278.74^{H}	310.16^{H}	313.09^{R}	313.09^{R}	313.09^{R}	313.09^{R}
11	270.44^{H}	$285.61^{R,S}$	313.10^{R}	348.81^{R}	348.84^{R}	348.82^{R}	317.27^{S}
12	277.58^{R}	313.06^{R}	335.88^{H}	354.08^{H}	$355.86^{R,S}$	$355.75^{R,S}$	348.81^{R}
13	$285.63^{R,S}$	313.32^{H}	348.82^{R}	$356.00^{H,R,S}$	385.99^{H}	387.57^{R}	$355.67^{R,S}$
14	306.55^{H}	342.72^{H}	$355.66^{R,S}$	374.76^{H}	387.60^{R}	$390.85^{R,S}$	$382.83^{H,S}$
15	313.10^{R}	348.84^{R}	368.58^{H}	$386.92^{R,H}$	$390.95^{R,S}$	$399.61^{S,R}$	387.56^{R}
16	340.89^{H}	$355.73^{R,S}$	$378.99^{H,S}$	388.20^{R}	$399.76^{S,R}$	403.52^{H}	$390.83^{R,S}$
17	348.84^{R}	$375.79^{H,S}$	387.72^{R}	$391.62^{R,S}$	404.51^{S}	$404.66^{H,S}$	399.63^{S}
18	$355.71^{H,S}$	$383.37^{H,S}$	$391.29^{R,S}$	$399.97^{S,R}$	406.68^{S}	$406.70^{S,H}$	404.43^{S}
19	$375.54^{S,H}$	387.75^{R}	$399.86^{H,S}$	404.59^{S}	408.27^{S}	408.27^{S}	406.62^{S}
20	386.17^{H}	$391.37^{R/S}$	403.21^{H}	406.72^{S}	408.95^{H}	409.16^{S}	408.24^{S}

The variation of free vibration characteristics for Case1 and Case3 is similar to that shown in Table 5.6. For higher β angles the maximum modal displacement does not occur at the transition. However, for $\beta < 40^\circ$ a mode related with the hopper with maximum modal displacement at the transition occurs. When $\beta = 40^\circ$ for Case1 and Case3 the mode associated with the hopper and maximum modal displacement at transition has a frequency that is significantly different from the fundamental honking frequencies. This is similar to Table 5.6. Again for $\beta = 20^\circ$ - 30° the maximum modal displacement at the transition occurs for a mode associated with the hopper. Moreover the natural frequency for these particular modes is close to the correspondent honking fundamental frequencies for these silos (f_h = 292 Hz in Case1 and f_h = 246 Hz in Case3). It appears that the natural frequency associated with this hopper mode and relative maximum displacement at transition is inversely proportional to the silo diameter. This is in line with the observations for each honking silo.

5.4.2 Shell height variation

Axisymmetric models are constructed for four different aspect ratios and a frequency extraction conducted for each case. The aspect ratios considered are *L/D* = 7.33, 6, 4 and 2. The diameter is kept constant while the shell height is varied to obtain the desired ratio. All models include skirt, hopper and roof and dimensions of these are kept constant. As was shown in previous sections the thickness variation along the height slightly modifies the natural frequencies and is therefore not included in this frequency extraction. The lowest twenty frequencies are shown in Table 5.9. The *L/D* = 7.33 is the ASILO model discussed previously without the thickness variation. As expected the lowest natural frequencies (axial) increase as the *L/D* ratio decrease. The natural frequencies in each model tend to the ring frequency (570 Hz for a 3 m diameter shell).

Table 5.9: Natural frequencies in Hz with shell height variation (*S* = shell, *R* = roof, *H* = hopper and the displacement at transition is maximum).

Mode	*L/D* = 7.33 *f*	*L/D* = 6 *f*	*L/D* = 4 *f*	*L/D* = 2 *f*
1	58.68^{S}	70.93^{S}	100.32^{S}	126.39^{R}
2	131.80^{R}	135.20^{R}	145.33^{R}	229.91^{S}
3	185.38^{S}	223.12^{S}	$300.04^{S,R}$	$309.66^{S,H}$
4	$291.91^{H,S}$	$304.92^{S,H}$	331.60^{R}	335.02^{R}
5	$312.25^{S,H}$	334.61^{R}	337.56^{R}	379.37^{R}
6	334.94^{R}	360.78^{R}	379.57^{R}	431.56^{R}
7	378.77^{R}	379.97^{R}	431.50^{R}	484.85^{R}
8	$404.12^{R,S}$	431.44^{R}	481.98^{R}	$522.74^{R,S}$
9	431.80^{R}	$467.13^{R,S}$	490.35^{R}	535.26^{H}
10	479.42^{R}	485.83^{R}	534.67^{H}	541.79^{R}
11	486.89^{R}	$521.17^{R,S}$	$537.41^{R,H}$	554.34^{S}
12	$521.02^{R,S}$	535.01^{H}	542.22^{R}	559.39^{S}
13	534.92^{H}	539.71^{R}	$551.13^{S,R}$	561.33^{S}
14	$538.10^{R,S}$	542.76^{R}	555.95^{S}	562.34^{S}
15	541.80^{H}	$549.65^{R,S}$	558.41^{S}	563.01^{S}
16	$547.29^{H,S}$	553.86^{S}	559.86^{S}	563.62^{S}
17	551.79^{S}	556.38^{S}	560.80^{S}	564.29^{S}
18	554.62^{S}	558.02^{S}	561.45^{S}	565.12^{S}
19	556.52^{S}	559.15^{S}	561.93^{S}	566.11^{S}
20	557.86^{S}	559.98^{S}	562.30^{S}	567.08^{S}

The lowest frequency modes for each model in Table 5.9 are shown in Figs. 5.17 - 5.20. Modes in Fig. 5.17 can be compared with those in Fig. 5.5. They have practically the same mode shape as their correspondent mode. The number of modes due to axial vibration of the shell tends to reduce from amongst the lower modes as the *L/D* ratio reduces. On the other hand more modes due to the roof appear in the first twenty modes as the *L/D* ratio reduces. The hopper mode shape with a maximum modal displacement at the transition discussed earlier also appears in all the four models. For *L/D* = 7.33 it is mode 5, for *L/D* = 6 it is mode 4 and for *L/D* = 4 and 2 it is mode 3. The natural frequencies correspondents to these modes are marked in red in Table 5.9. The mode fairly preserves the same shape for the four models and the natural frequency varies only slightly (Table 5.9, range between 300 Hz – 312 Hz). The height variation neither affects the occurrence of the hopper modes nor modifies its natural frequencies. This behaviour matches the honking behaviour reported in Chapter 3, where the instrumented silo in study and the silo in Case 2 both have the same diameter (3 m) and the same hopper angle but different height, see Fig. 3.1 and Fig. 3.26. However, they both have been reported to honk at a fundamental frequency of 333 Hz.

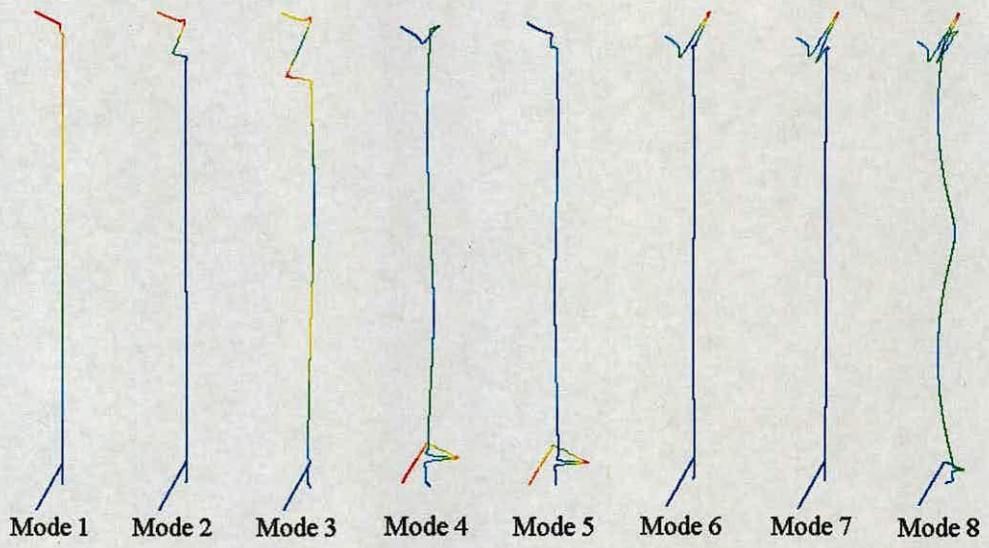

Figure 5.17: Lowest axisymmetric modes in Table 5.9 for the *L/D* = 7.33 model.

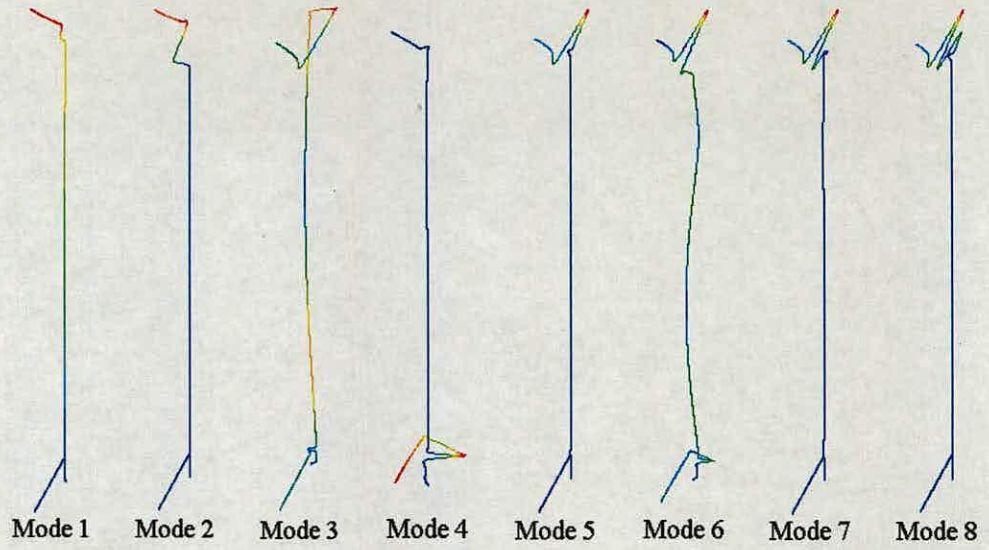

Figure 5.18: Lowest axisymmetric modes in Table 5.9 for the *L/D* = 6 model.

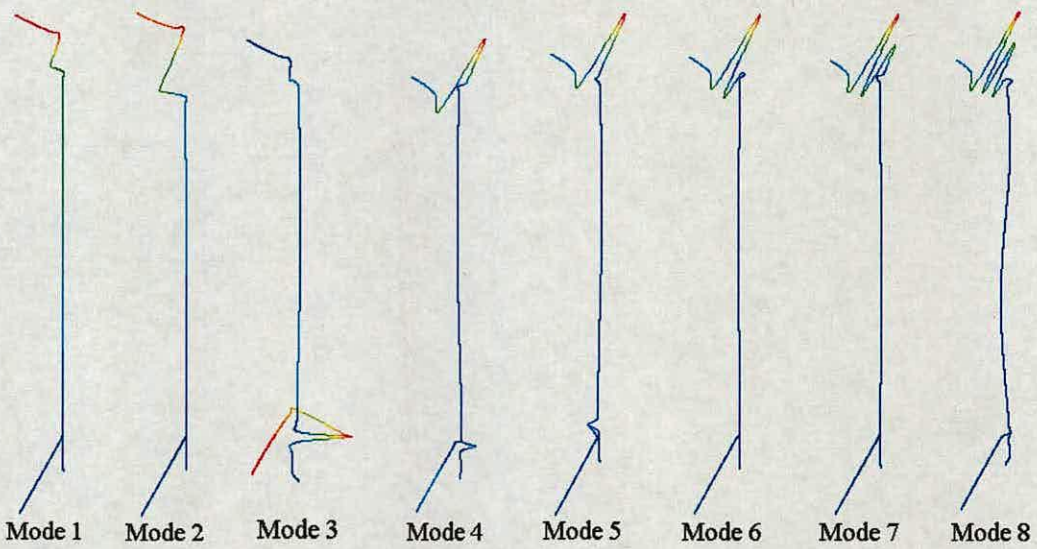

Figure 5.19: Lowest axisymmetric modes in Table 5.9 for the *L/D* = 4 model.

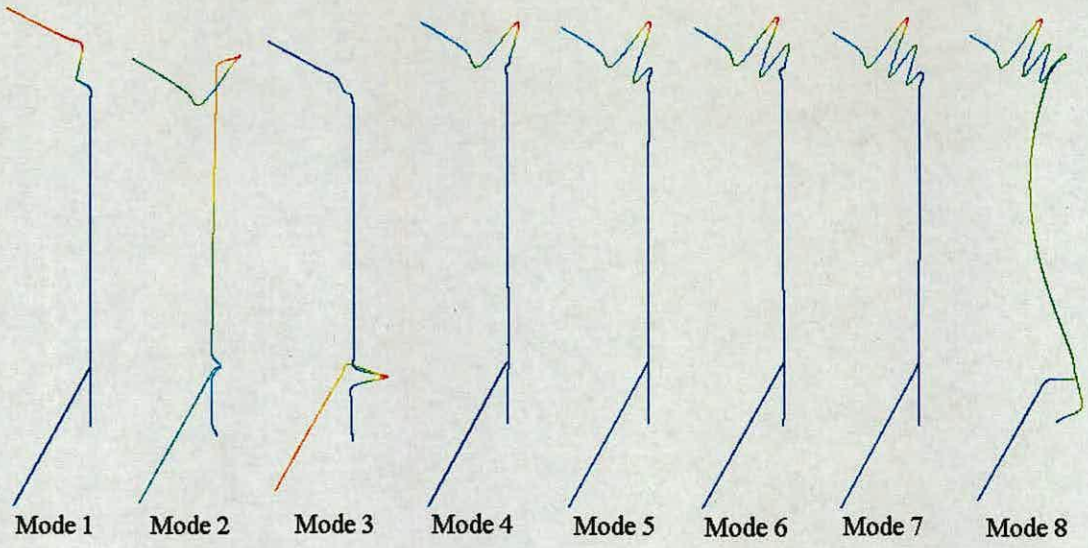

Figure 5.20: Lowest axisymmetric modes in Table 5.9 for the $L/D = 2$ model.

5.5 Higher harmonics in the axisymmetric silo model

Another characteristic of the instrumented honking silo analysed in Chapter 3 is its harmonic response. To examine this behaviour in the axisymmetric ASILO model a frequency extraction is conducted in which all frequencies up to 2000 Hz were obtained. Since higher modes need a finer mesh for accurate extraction the mesh of the ASILO model was refined and the total number of elements and nodes increased to 13255 and 13256 respectively. A plot showing the curve followed by the axisymmetric natural frequencies is shown in Fig. 5.21. The curve is similar to the lower coupled curve shown in Fig. 4.16 for the axisymmetric shell having Clamped-SD boundary conditions. However, Fig. 5.21 now includes the modes due to the hopper and roof. For the first modes on the curve a quick rise in frequency is observed. As was demonstrated earlier, these modes are linked to axial vibration or are due to the hopper and roof. The radial modes tend to the frequency value of the ring frequency ($\approx$ 570 Hz for a 3 m diameter shell) and then start to increase as the m number increases.

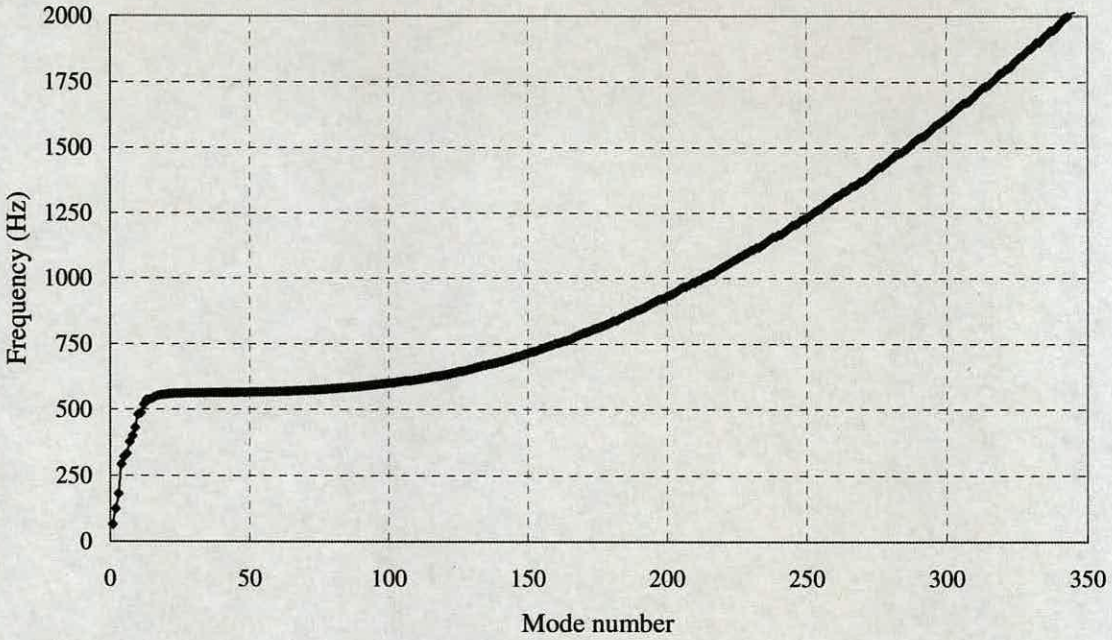

Figure 5.21: Natural frequency curve for the ASILO model.

The plot gives a large range of frequencies but does not help in identifying the modes responsible for harmonic response observed during honking. To identify these an inspection of the modes close to the higher harmonics of the hopper mode frequency is conducted. The hopper mode frequency is considered as 321 Hz, which is the frequency in mode 5 in Table 5.2 and Fig. 5.5. The higher harmonics are just integer values of this frequency. For example the second harmonic is f_2 = 642 Hz, the third one is f_3 = 963 Hz, etc. The modes at high frequencies are complex with a high number of axial half waves along the shell. A harmonic pattern is difficult to observe due to this complexity. However, some modes close to the higher harmonics show similarities in their mode shapes. These modes are shown in Fig. 5.22. The difference in percentage from the calculated harmonic to the value shown in Fig. 5.22 is less than 1% except for Fig. 5.22c, which is 1.8%. All these modes have a high number of axial half waves along the height and roof. The maximum modal displacement in all of them occurs in the hopper.

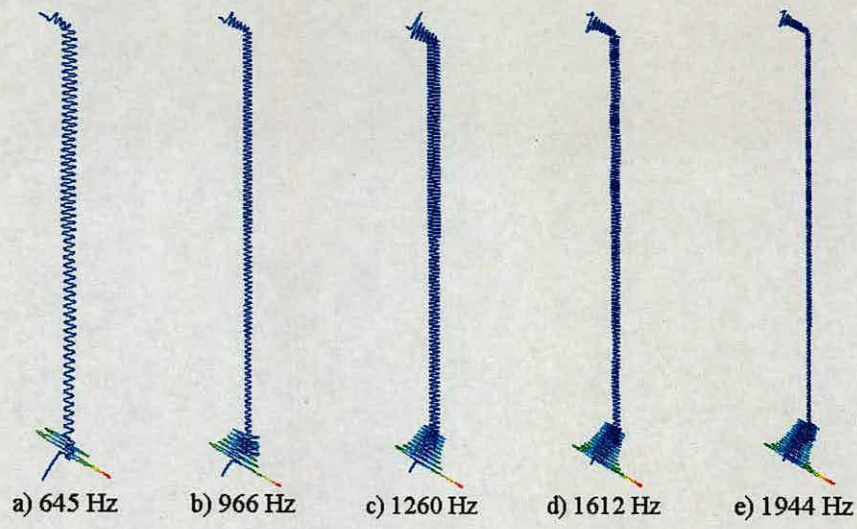

Figure 5.22: Mode shapes of approximate integer multiples (close to a) second, b) third, c) fourth, d) fifth and e) sixth harmonic) of the hopper mode frequency.

A magnification of the modal displacement of the hopper for each mode in Fig. 5.22 is shown in Fig. 5.23. The number of waves along the hopper increases as the natural frequency increases. For the second harmonic two waves are observed in the deformed hopper. Strikingly the number of waves increases by three for each subsequent mode. However, the reason why these modes are excited is not apparent.

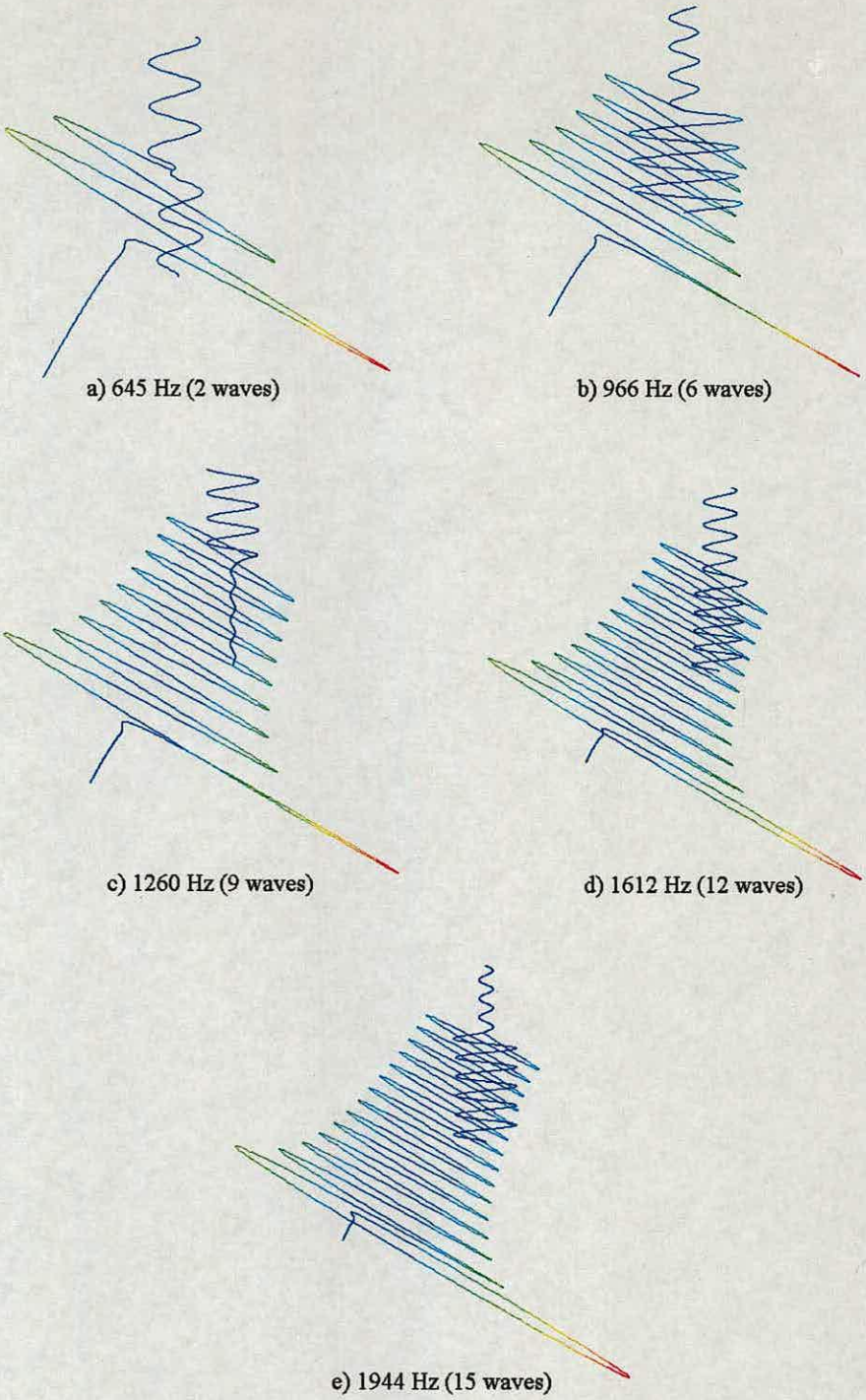

Figure 5.23: Magnification of the modal displacement of the hopper close to a) second, b) third, c) fourth, d) fifth and e) sixth harmonic.

5.6 Honking fundamental frequency

An examination of the frequency associated with the hopper showed that its ratio with the ring frequency was more or less constant. Consider Equation 4.8. Isolating the frequency f_h in the left hand side leads to:

$$f_h = \frac{\Omega}{2R}\sqrt{\frac{E}{\rho(1-\nu^2)\pi^2}} \tag{5.1}$$

In the above equation the frequency parameter Ω is generally unknown. However for the ring frequency it is a fairly constant value (slightly less than unity) until the number of axial half waves m is significantly (see Leissa, 1973). If the frequency from the hopper mode is divided by the ring frequency for cases considered in Chapter 3 (Fig. 3.26) then the frequency parameter for this particular mode can be obtained. The ring frequency values considered are obtained from the FE natural frequency extraction and are f_r = 570, 490, 420 Hz for the instrumented honking silo in this study, the silo in Case1 (Fig. 3.26a) and the silo in Case3 (Fig. 3.26c) respectively. These values were also verified with the Gontkevich closed form solution for three different cylinders having the same diameter as the axisymmetric silo models. The correspondent natural frequencies for the hopper mode in Table 5.6 to Table 5.8 are divided by their correspondent ring frequency, giving the values Ω = 321.61/570 = 0.56, Ω = 259.60/490 = 0.53 and Ω = 227.51/420 = 0.54. The closeness of these frequency parameters confirms that the hopper mode frequency is proportional to the ring frequency. If these parameters are multiplied by the radical in Equation 5.1, a factor close to a thousand is obtained (1003, 950 and 970 for the instrumented honking silo in this study, the silo in Case1 (Fig. 3.26a) and the silo in Case3 (Fig. 3.26c) respectively). This factor was mentioned in Chapter 3 as a honking characteristic linked to the silo diameter. As the hopper mode also varies with the silo diameter, it appears to be a rational explanation for the occurrence of the honking fundamental frequency. In this way, substitution of Ω = 0.55 in Equation 5.1 gives an approximate value for the honking fundamental frequency. It is

important to mention that the only information available is for aluminium honking silos, so that the thousand-factor is limited to this material.

5.7 Conclusions

Free vibration analyses were conducted for different FE models. These models included the roof, hopper and thickness variation existent in the instrumented honking silo in this study. The following conclusions can be drawn:

- *3D silo model.* In the 3D model the results indicate that the vibration characteristics of the silo structure in the low frequency range are similar to a simple cylindrical shell. The lowest 3D modes are below the audible range.

- *Geometric implementations in the axisymmetric model.* The inclusion of roof and hopper adds new modes to the already calculated modes due to the simple shell while thickness variation slightly modifies the natural frequencies but not the mode shapes.

- *Bulk solid influence in the axisymmetric model.* The natural frequencies are drastically reduced once the mass and stiffness of the solid are included. The lower modes are associated with the vibration of the stored solid and not to the silo structure. The natural frequencies change with height when the silo-fill system acts together. When the mass influence of the stored solid is eliminated from the model and only the stiffness of the bulk solid included the natural frequencies increase slightly in comparison to the empty silo. This is apparently due to the low Young's modulus of the stored solid in comparison to the silo structure. The fill height does not influence the free vibration characteristics once the mass of the silo-fill system is ignored. This indicates that during honking vibrations at high frequency the stored solid is uncoupled from the shell.

- *Hopper angle variation in the axisymmetric model.* The frequencies associated with the hopper modes are diameter dependent. They are inversely

proportional to the diameter. Moreover, for half hopper angle of 30° and 20° the hopper mode with a maximum modal displacement at the transition between hopper and shell is close to the correspondent fundamental honking frequency in all the cases studied. These are the hopper angles that the real honking silos discussed in Chapter 3 have.

- *Shell height variation in the axisymmetric model.* The modes due to shell vary in frequency once the height is varied. The natural frequency of the hopper mode with a maximum modal displacement at the transition is not affected by the height variation. It preserves the same mode shape and the frequency changes slightly. This matches the honking observations where silos are of different height but have the same diameter and have the same honking fundamental frequency.

- *Harmonic response in the axisymmetric model.* Apparently the harmonic response is also due to the vibration of the hopper. The number of waves in the hopper for frequencies close to the higher harmonics observed in the acceleration spectra obtained from measurements increases in steps of three. This behaviour is also in line with the hopper angle and shell height variations where the hopper modes match different features observed in the honking behaviour.

- *Honking fundamental frequency.* A frequency parameter (Ω) to calculate the honking fundamental frequency is proposed. The selection of this parameter is based on the conclusions drawn from the occurrence of the hopper mode with a maximum modal displacement at the transition.

Chapter 6

Sources of excitation

6.1 Introduction

This Chapter is divided in two main sections to consider two different sources of excitation that have been proposed previously for honking: slip-stick and pulsating flow. Previous research (Ooi et al., 1999; Roberts, 1993; Roberts and Wensrich, 2002; Shinohara et al., 1968; Bransby et al., 1973, 1975; Michalowski, 1984, 1987; Purutyan et al., 1994a, 1994b; Buick et al., 2003, 2005) has shown that both these phenomena occur in a fairly periodic manner during discharge. The periodicity, magnitude and location of these are important.

For examining slip-stick a laboratory study is conducted. Two types of polymer granulates are considered: PET pellets that are known to honk and polypropylene pellets that are not. The terms "honking pellets" and "non-honking pellets" have been used in the past, however, they must be carefully considered. It is true at least in the silos where the pellets were stored, so that other factors, such as the differences in silo geometry, may influence whether honking occurs or not. The measurements are performed using the Jenike shear tester on two commonly used wall materials: stainless steel and aluminium. The shearing response in particle-wall interaction is examined. The effects of stress level, sample size and rate of shearing are also investigated. The study shows considerable slip-stick fluctuations for one solid but

not the other, and reveals the influence of stress level and sample size on the slip-stick response. Existing literature is used to examine pulsating flow. It is believed that pulsations occur in almost all silos during discharge. However, the maximum exerted loads due to the pulses have been reported to occur at two different locations of the silo structure: the silo wall and the silo hopper. Excitations on both these are discussed.

6.2 Slip-stick

6.2.1 Test description

Two different pellets were tested – PET and polypropylene. Industrial experience suggests that PET pellets honk while polypropylene pellets do not. It is important to note that the evidence of a particular kind of pellets producing honking or not in a particular silo is largely anecdotal. There is no conclusive scientific evidence to suggest that polypropylene pellets will not generate honks in any silo with any geometry and/or physical characteristics. Similarly not all silos storing PET pellets are known to honk. The aim of the tests is to examine the particle-wall interaction. The PET pellets considered are in the shape of flattened cylinder with an elliptic cross-section. The typical cross-section of these pellets is 4x1.5–2 mm with 4 mm height (Fig. 6.1a) and the density is in the range 770–890 kg/m^3. The polypropylene pellets were shaped like squat cylinders with 5 mm diameter and height varying between 1.5–4 mm (Fig. 6.1b). The density range for these pellets is 550–620 kg/m^3. Two different plate materials were considered: aluminium and stainless steel. The aluminium plate has a thickness of 6.1mm with a surface average roughness Ra of 0.88 μm. The stainless steel plate is 4 mm thick with Ra of 0.5 μm. Particles and wall materials are typically those used in the industry.

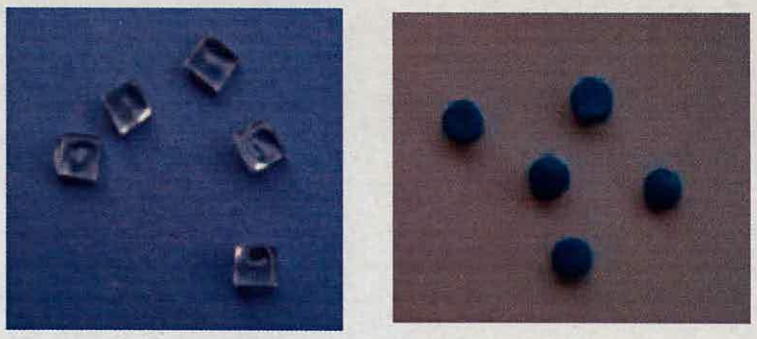

Figure 6.1: Pellets tested: a) PET and b) Polypropylene.

The shear response measurements were performed using a Jenike shear tester (IChE, 1989). Most tests were conducted using a shear cell of 143 mm diameter, which is larger than the standard Jenike cell. Shear cell diameters of 95 mm (standard Jenike cell) and 63 mm were also used to study the effect of sample size. To investigate the particles-wall interaction, a shear plane is created between the pellets and the wall sample plate (Fig. 6.2). In these tests the shear cell is placed over the plate and filled with pellets. Once the sample is levelled, a cover is placed on top of the pellets and a vertical force applied to the cover via a load hanger. Shearing is initiated by applying a horizontal load to the bracket under displacement control (IChE, 1989). The horizontal force was measured using a bending type load cell. The horizontal displacement was measured using a LVDT transducer measuring the displacement of the shear cell.

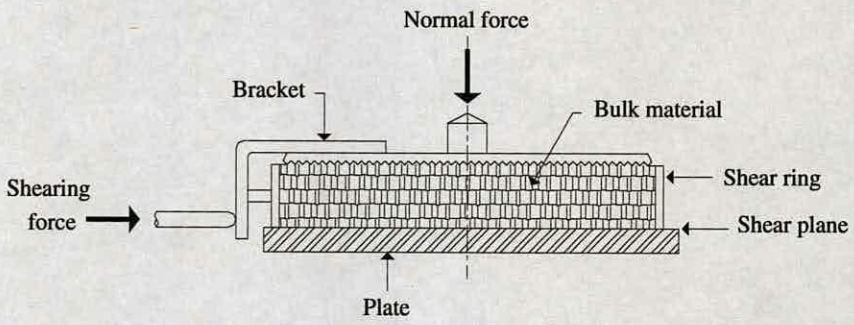

Figure 6.2: Jenike shear test for particle-wall interaction.

From the normal and shear loads applied, the mean normal and shear stress acting on the horizontal plane are evaluated. For each test with a mean normal stress, the test data is presented as a plot of the average shear stress with the shear displacement given by the movement of the shear cell.

6.2.2 Effect of stress level and wall material

Figure 6.3 shows the shearing response of PET pellets on the aluminium plate for four different normal stress levels and a nominal shear rate of 1 mm/min. The test data was recorded at 4 readings per second. The stress levels were chosen to reflect the real conditions in the honking aluminium silo with the PET pellets. The pressure calculations due to the stored material can be found in Appendix C. Considerable slip-stick response, illustrated by fluctuating shear stress, was observed between the PET pellets and the aluminium plate. The magnitude of these fluctuations increases with increasing normal stress level, indicating that slip-stick fluctuations would be larger with higher stresses towards the lower end of a silo. The pellets stick against the aluminium plate until a certain magnitude of shear stress is reached. After this a sudden slip occurs, bringing the shear stress down to a lower value. This behaviour is repeated periodically. The same normal stress levels were used with the polypropylene pellets on the aluminium plate and they were sheared at the same rate. The results are shown in Fig. 6.4. It can be seen that slip-stick fluctuations are almost absent in this case for all stress levels. It is also interesting to note that for polypropylene pellets, the shear stress increases to a peak value before softening gradually to a lower ultimate shear stress at large shearing displacement.

The stainless steel plate was used to perform the same tests with the two pellets. Figure 6.5 shows the shear response between PET pellets and stainless steel plate. It can be seen that slip-stick response is present for stainless steel as well. The corresponding results for polypropylene pellets are shown in Fig. 6.6 which show that polypropylene does not exhibit slip-stick against the stainless steel plate either.

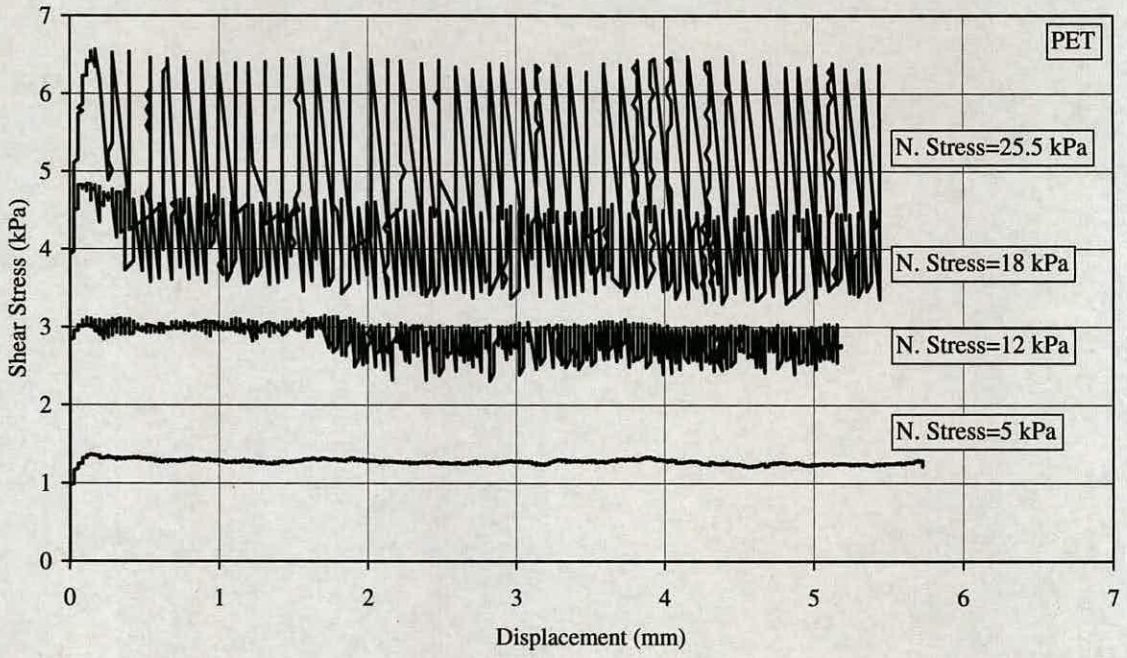

Figure 6.3: Shearing response for PET on aluminium plate.

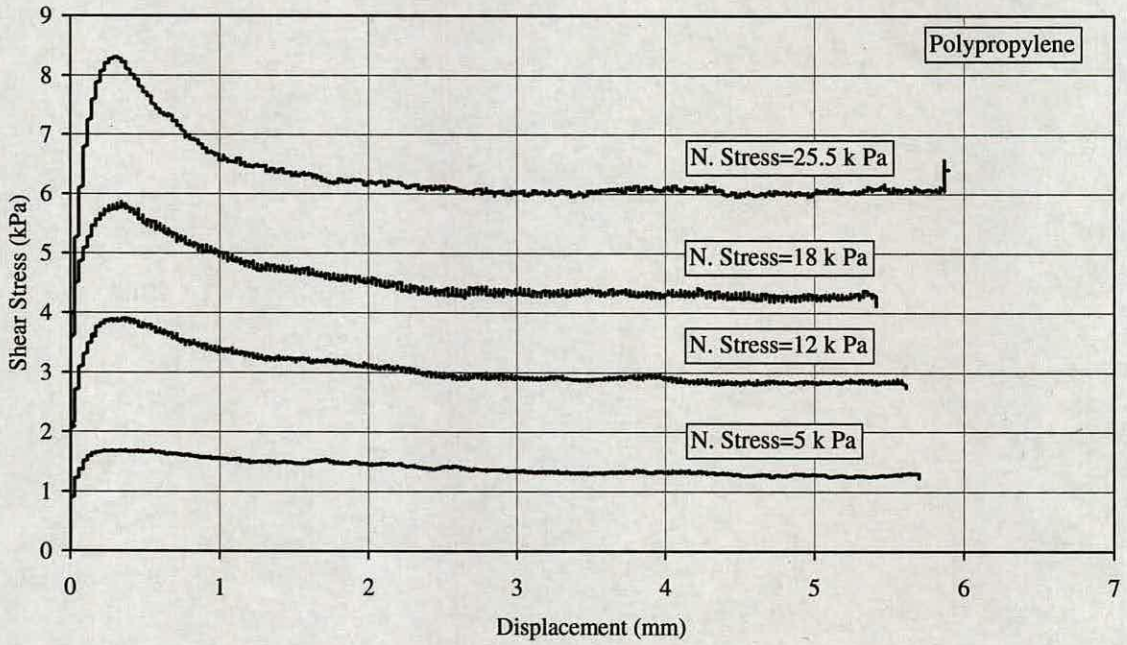

Figure 6.4: Shearing response for polypropylene on aluminium plate.

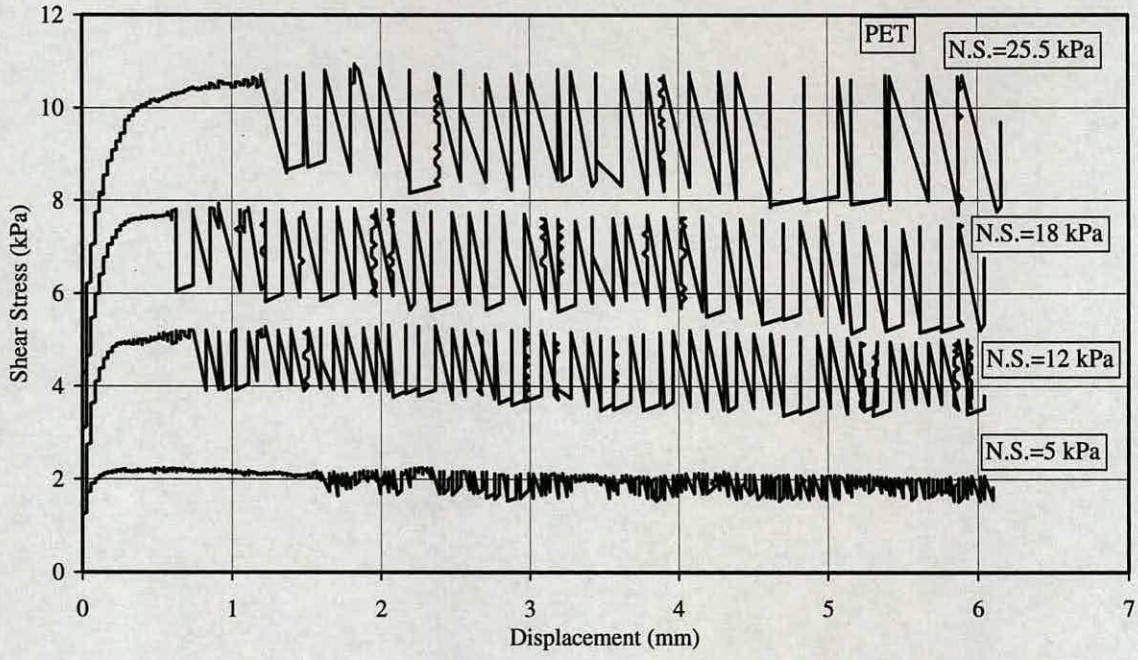

Figure 6.5: Shearing response for PET on stainless steel plate.

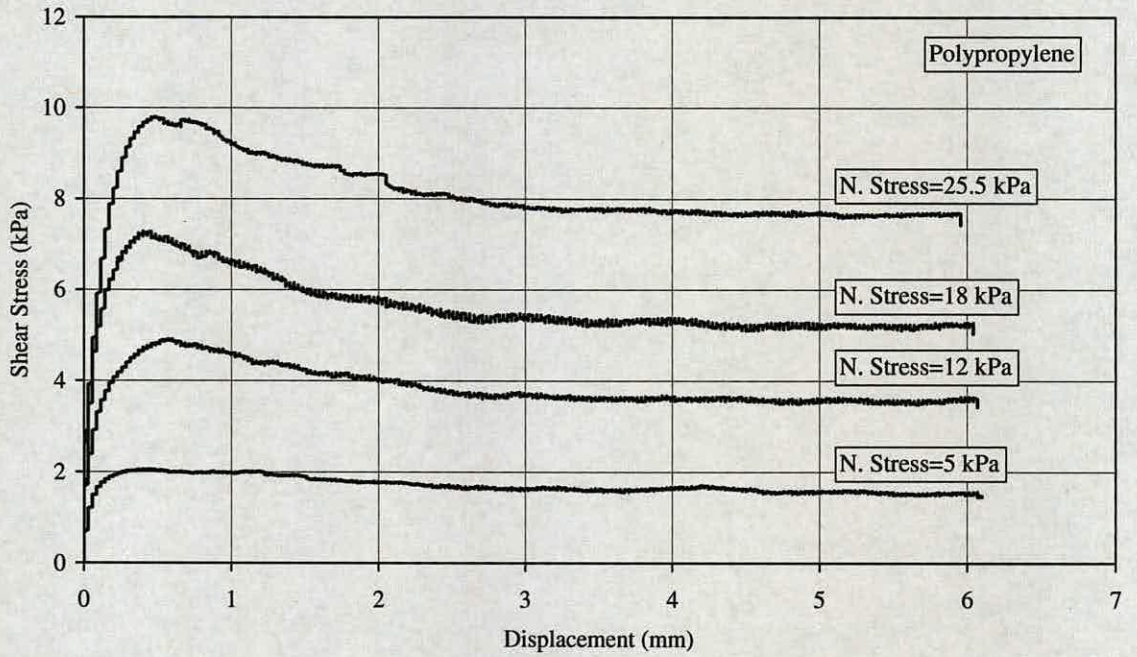

Figure 6.6: Shearing response for polypropylene on stainless steel plate.

It is worthwhile noting the key differences in the shearing behaviour of PET against the two wall plate materials by comparing Figs. 6.3 and 6.5. The overall coefficient of wall friction for the stainless steel plate is obviously larger than that for the aluminium plate. This is despite the aluminium plate having a larger average surface roughness Ra. The shear stress in each of the stainless steel tests is seen to reach a stable maximum before the slip-stick sets in. On the other hand with the aluminium plate slip-stick sets in at a very early stage. In addition, it can be seen that while there is negligible shear stress fluctuation at the lowest stress level tested (5 kPa) for the aluminium plate, a significant fluctuation is observed at this low stress level with the stainless steel plate. Figure 6.7 shows the averaged shear stress fluctuations for PET pellets on aluminium and steel plate. At the highest stress level tested, the magnitude of the shear stress fluctuation is slightly larger with stainless steel (see Fig. 6.7).

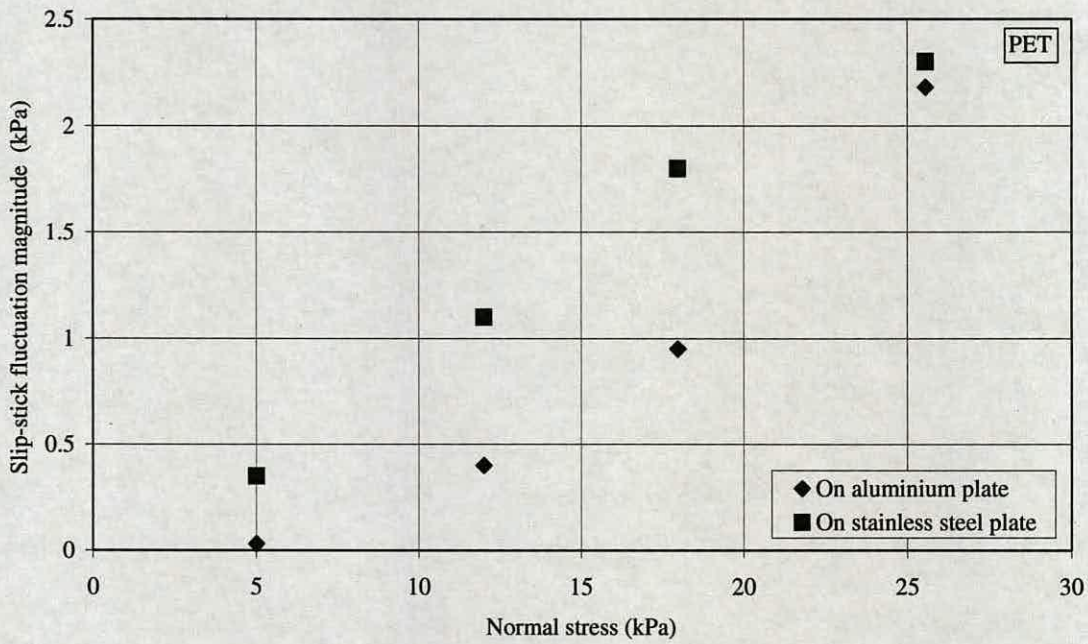

Figure 6.7: Magnitude of shear stress fluctuations.

The coefficient of wall friction can be evaluated by dividing the limiting shear stress by the normal stress, assuming no adhesion. The maximum and minimum shear stress averaged values in the slip-stick phase of each shear test can be determined from the test data. Dividing these values by the normal stress in each test give the

maximum and the minimum wall friction coefficients. Figure 6.8 shows how these wall friction coefficients vary with normal stress level for PET interaction with both aluminium and stainless steel wall materials. For the PET-aluminium combination, the maximum wall friction coefficient remains essentially constant with stress level at a value of 0.25. However the minimum wall friction coefficient, for this combination, reduces significantly with increasing normal stress, with the minimum coefficient dropping from a value of 0.25 at 5 kPa to 0.17 at 25 kPa. For the PET–stainless steel combination, both maximum and minimum wall friction coefficients show a small reduction with increasing normal stress, with the maximum coefficient in the range 0.43-0.45 and the minimum coefficient in the range 0.32-0.38. Comparing the two wall materials, the result indicates that slip-stick is very strongly stress dependent in the PET-aluminium case with the phenomenon almost disappearing below a stress level of 5 kPa and the magnitude of stress fluctuation increasing strongly with stress level. For the PET-stainless steel case, when the shear stress fluctuation is normalised with the normal stress level as depicted here, the magnitude of "normalised" stress fluctuation appears to remain relatively constant with changing stress level.

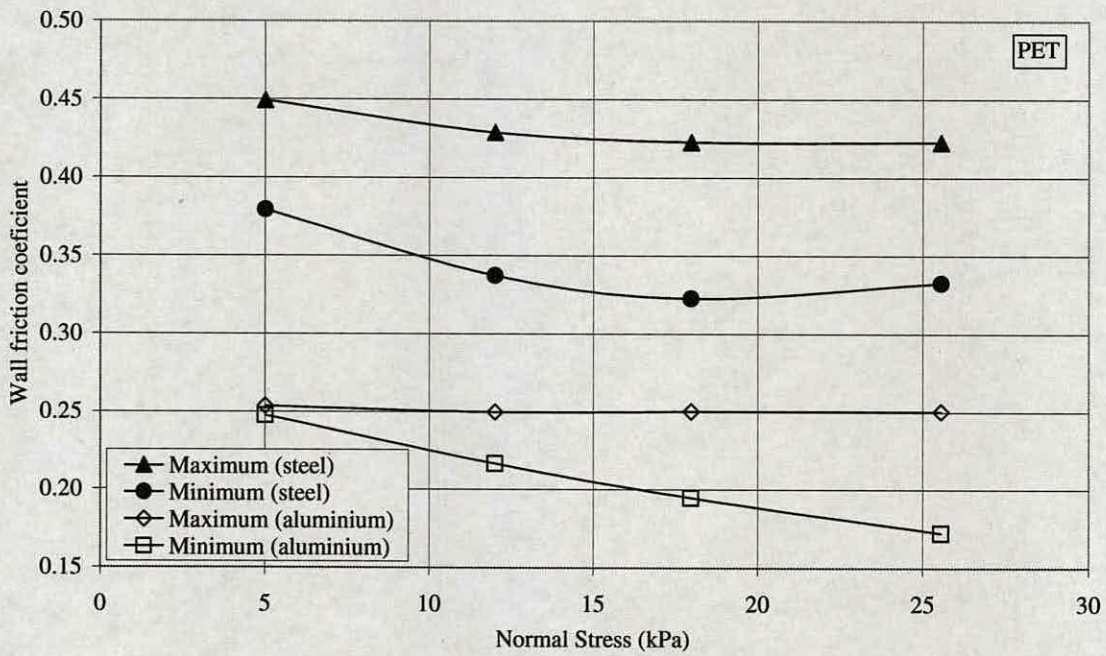

Figure 6.8: PET wall friction coeficient with aluminium and stainless steel.

6.2.3 Temporal variation of slip-stick

Figure 6.9 shows the shear stress response of the PET pellets on the aluminium and stainless steel plates as a function of time for 25.5 kPa normal stress. Once again these graphs are for a nominal shear rate of 1mm/min with a sampling rate of 4 readings per second. The results show stick phases of the order of 5.5 and 8.3 seconds when the particles are practically stationary for the aluminium and stainless steel plates respectively, followed by a sudden slip phase in a fraction of a second in both cases. These results show that slip-stick frequency for stainless steel and aluminium are significantly different for the same normal stress level. During each stick phase, there are typically over 20 readings for the aluminium test and over 30 readings for the stainless steel test, so the behaviour during the stick phase is well observed. However the slip phase typically occurs over one or two readings, so the minimum shear stress in each cycle cannot be recorded at great accuracy.

Figure 6.10 shows the temporal variation of slip-stick for different normal stress levels for the PET-aluminium combination. The graph shows that not only the shear stress level reduces with normal stress but also the stick period. These results show that the periodicity of the pulse axial load due to slip-stick will vary along the silo height. For instance, the silo shown in Fig. 3.1 at 90% capacity would exert varying normal stresses on the silo wall (see Appendix C). If slip-stick were occurring during discharge, the silo wall would be excited axially at a lower pulse frequency in the lower region (maximum stress level) and at a higher pulse frequency in the upper region (minimum stress level). This variation is not reflected in the measured response along the height on the silo wall where a honk occurs at the same interval of time at different positions along the silo height (see Fig. 3.13 and 3.15) and different positions have similar frequency content. The period of the sudden slip phase has not been calculated for the different normal stress plots in Fig. 6.10 because, as it has been shown in previous studies (Nasuno et al., 1998), the stiffness of the load cell influences the frequency content of the slip-stick response observed in a laboratory test. Therefore a comparison of the slip periods in Fig. 6.10 with the period observed in Figs. 3.17, 3.18 and 3.19 could lead to a misinterpretation of results.

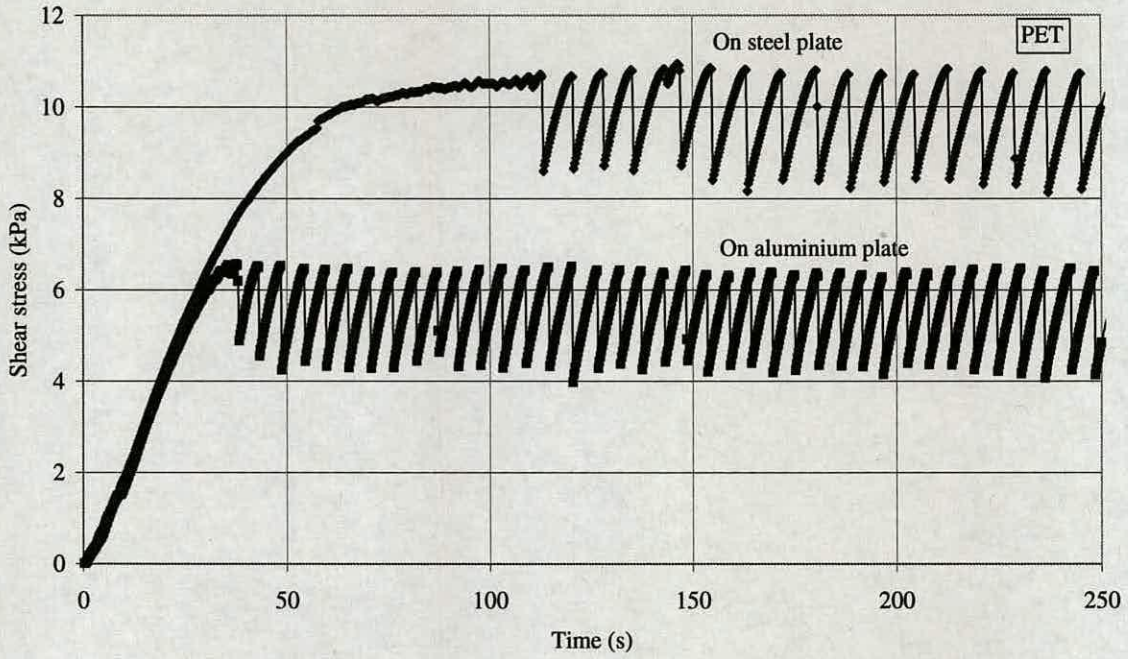

Figure 6.9: Shearing response as function of time for steel and aluminium plate.

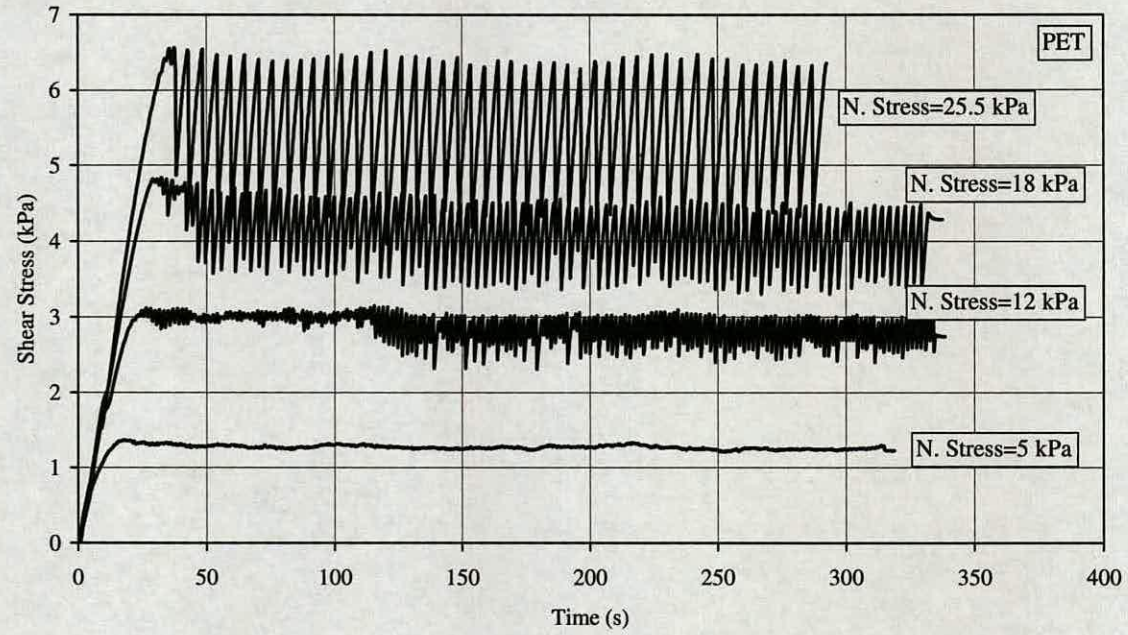

Figure 6.10: Shearing response as function of time on aluminium plate.

6.2.4 Effect of sample size

All the tests described above were conducted using the large shear cell with 143 mm diameter. To examine the influence of sample size, two other cell sizes were used – a standard Jenike cell at 95 mm diameter and a small cell at 63 mm diameter. Figure 6.11 shows the results for the three sample sizes for the PET–aluminium combination at a normal stress of 25.5 kPa. Significant slip-stick fluctuations are observed only for the large shear cell with no slip-stick occurring in the standard and small cells. The three tests all reach essentially the same maximum limiting shear stress, thus the maximum wall friction coefficient is independent of sample size. This finding on sample size effect, which does not appear to have been reported in published literature, may explain why reporting of slip-stick in particulate solids has been not totally consistent. In a typical silo design situation, it is generally accepted that the standard Jenike shear cell with a diameter $D_J = 95$ mm is adequate for capturing the shearing behaviour of PET pellets with maximum particle linear dimension of the order of $d = 4$ mm ($D_J/d = 24$). In this study it is clearly demonstrated that this is not the case for observing slip-stick.

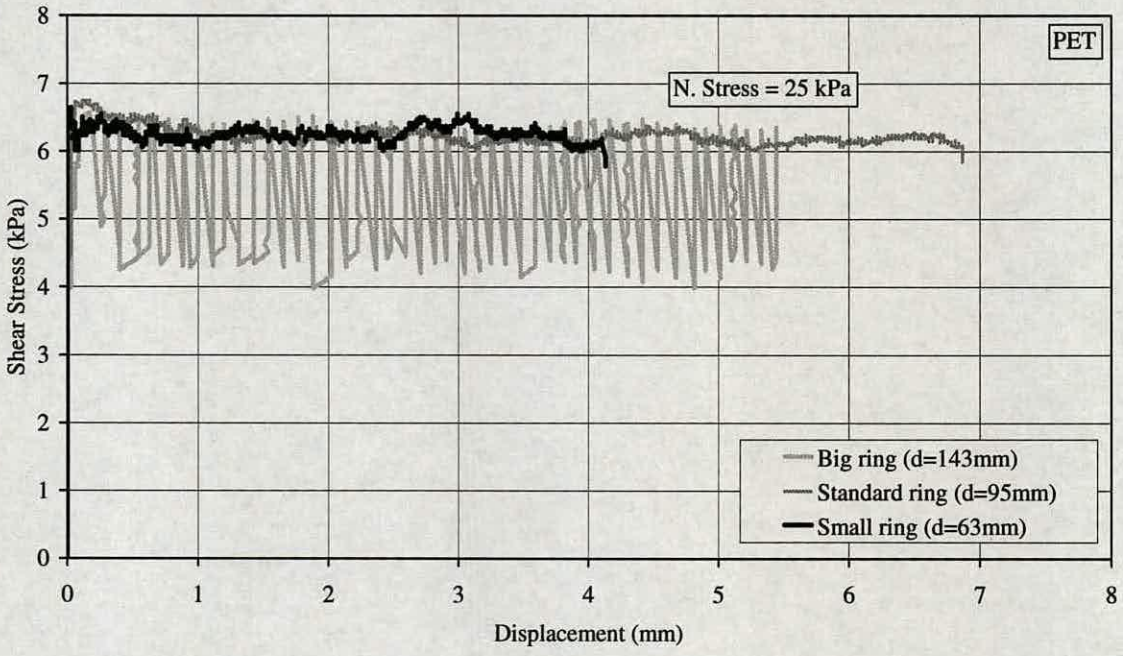

Figure 6.11: Effect of sample size on PET-aluminium shearing response.

The normal stress level was increased from 25.5 kPa to 55 kPa to further investigate the sample size effect. The results are shown in Fig. 6.12 for the standard and small shear cells. At this much higher normal stress level, regular slip-stick response appears in the standard cell sample, but are still largely absent in the small cell sample. The magnitude of shear stress fluctuations in the standard cell sample is about 3 kPa. The maximum wall friction coefficient reduces slightly from the value observed for the 0–25 kPa stress range (see Fig. 6.8), but this could be simply experimental scatter. A further increase of normal stress level to 126 kPa was attempted in the small cell and at this very large stress level, significant slip-stick fluctuations did occur (see Fig. 6.13).

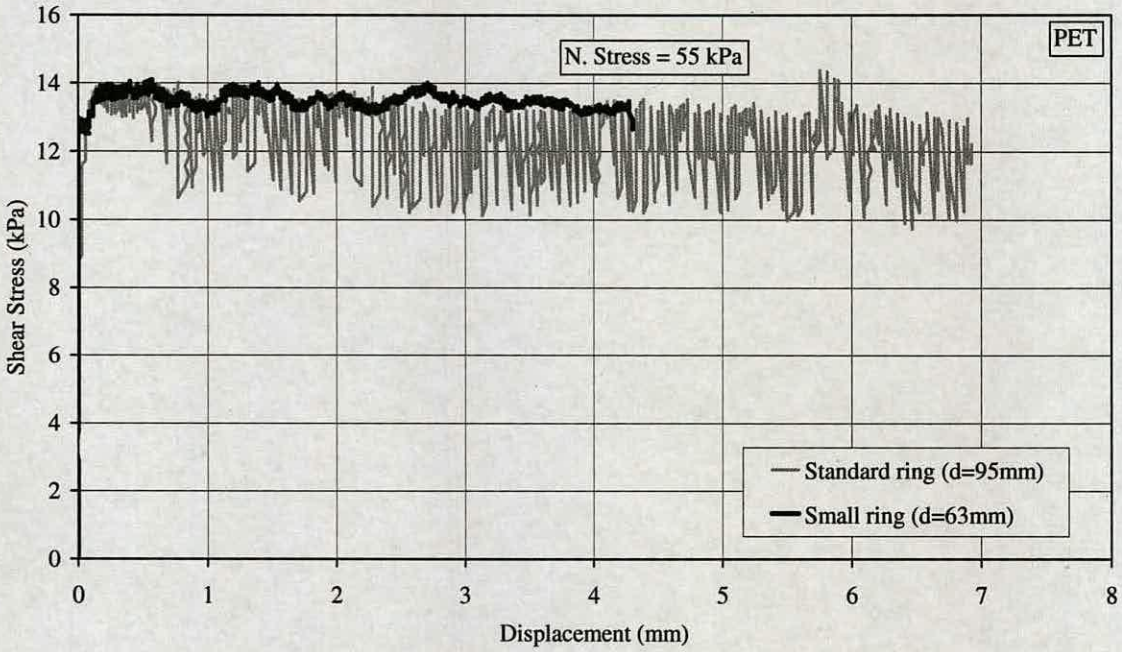

Figure 6.12: Effect of sample size on PET-aluminium response at 55 kPa normal stress level.

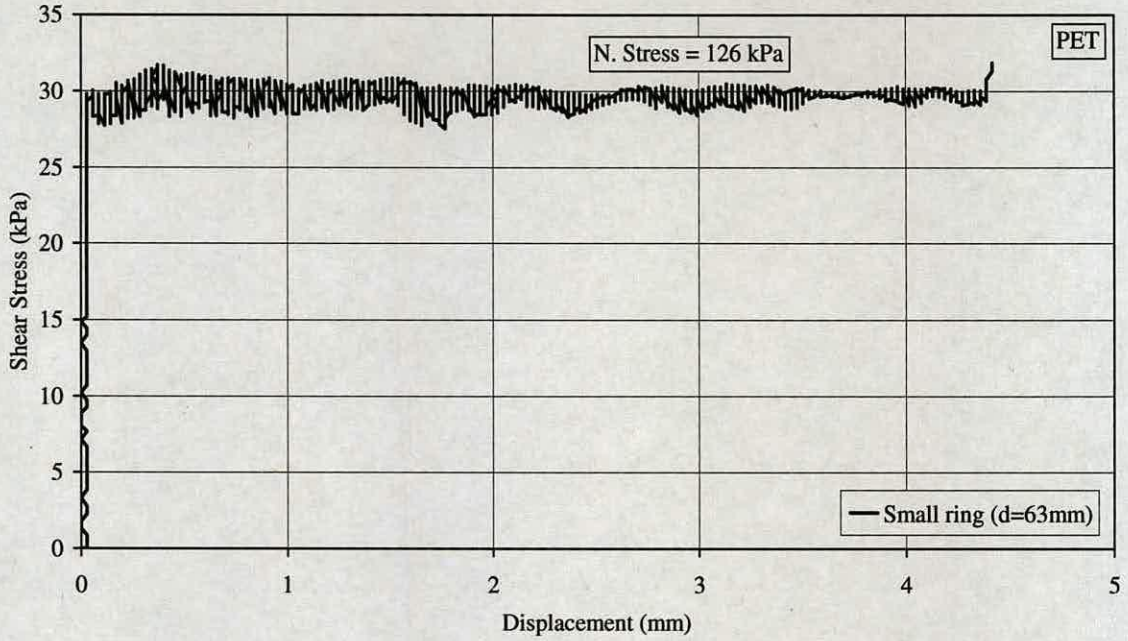

Figure 6.13: Effect of sample size on PET-aluminium response at 126 kPa normal stress level.

This slip-stick dependency on sample size and stress level cannot yet be readily explained. It is known that in a direct shear test, the shear stress during testing is far from uniform and shear failure is expected to propagate from the edges towards the centre of the sample (Sanad et al., 2000). The widely used interpretation of direct shear test of plotting the average shear stress, as is done here, is probably overly simple. It is possible that the boundary effects of the shear cell and the non-uniform stress distribution at the shearing plane have a role to play in the sample size effect reported here.

The same sample size tests were carried out for the polypropylene pellets. The response was very similar in all three sample sizes, with no slip-stick response observed for any of the cell sizes (see Fig. 6.14).

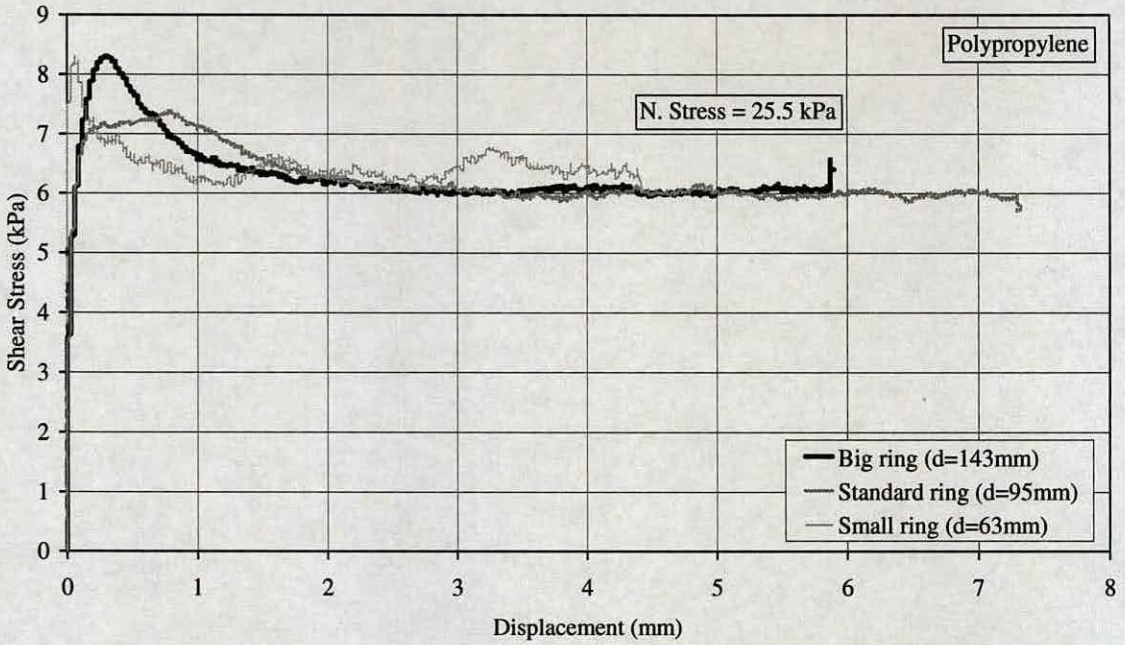

Figure 6.14: Effect of sample size on polypropylene-aluminium shearing response.

6.3 Pulsating flow

Pulsating flow was mentioned in Chapter 2 as a possible source of excitation for quaking in silos. Previous publications (Roberts and Wensrich, 2002; Tejchman, 1998) have considered silo honking as a variation of the silo quaking phenomenon. It is believed that pulsations in the flow occur in almost all silos. Normally they are not noticed as they do not result in observable vibrations and are not seen as a major concern in industrial plants. However, the pulsations can sometimes exert loads of significant amplitudes on the silo and its supporting structure. Whether they result in observable structural vibrations or not will depend on the structural characteristics of the silo or its supporting structure and on the severity of pulses. Pulsating flow is difficult to predict and is generally due to a combination of factors such as density changes due to dilation of the bulk material and the frictional behaviour between pellets and silo wall and pellets. Different theories about the position where the maximum influence of the pulses is exerted have previously been published (Roberts, 1993; Roberts and Wensrich, 2002; Shinohara et al., 1968). The parts mainly excited by the pulses are the silo wall and the silo hopper.

6.3.1 The plane of shock

The high frequency components of the flow pulsations have been proposed as a possible source of excitation for honking by Roberts and Wensrich (2002) who consider honking as a variation of the silo quaking problem. However, the periodic small oscillations and honks in Figs. 3.17, 3.18 and 3.19 and their spectral analyses suggest that a transient excitation is exerted periodically on the silo structure making it vibrate in its natural frequencies and not higher frequency components of the flow pulsations matching higher natural frequencies of the silo structure. The pulsating flow was described for tall mass-flow silos by Roberts and Wensrich (2002) as follows: above a critical level H_{sh} (see Fig. 6.15), above the transition, the velocity profile is fairly uniform while below this level the material converges due to the hopper and the velocity profile loses its uniformity. Dilation occurs due to the pressure developed in the hopper region causing a reduction in the support given by the vertical pressure in the barrel. This causes a sudden drop of the material generating a pulse load. This phenomenon is repeated periodically. The assumption of a plane of shock created within the stored material during mass flow discharge has been suggested to produce a sudden increment on the lateral wall pressure of the silo structure (Roberts, 1993; Roberts and Wensrich, 2002). In these studies a single shock plane is assumed while it is recognized that several shock planes may exist. The stored material above the shock plane is considered to produce pulse loads periodically due to slip-stick motion. These shocks are generated by density and wall friction variations. As is shown in Fig. 6.15 the plane of shock is assumed to occur at certain height ($H_{sh} \approx 1D$ - $2D$, where D is the silo diameter) above the transition. Expressions to calculate the maximum increment in the average vertical pressure and in the lateral wall pressure due to the shock loads are also proposed in the above studies. The calculation of these values can be found in Appendix E.

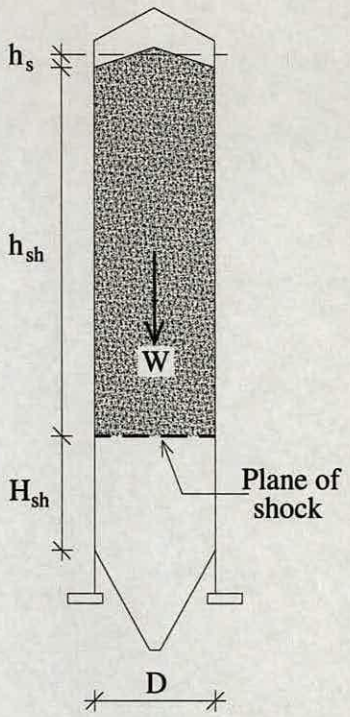

Figure 6.15: Dynamic load model proposed by Roberts (1993).

Roberts and Wensrich (2002) also proposed an expression for the prediction of the period in pulsating flows in which the material weight above the plane of shock is included. It has the form:

$$T = \left(t_0 + \frac{v_p}{a} \right) + \sqrt{\frac{v_p}{a}\left(2t_0 + \frac{v_p}{a} \right)}, \tag{6.1}$$

where

$$a = \frac{\Delta p_{v0}}{\gamma (h_{sh} + h_s)} \tag{6.2}$$

$$v_p = \frac{Q}{\rho_{MAX} A_c} \tag{6.3}$$

$$t_0 = \frac{\Delta \varepsilon_y}{v_p}. \tag{6.4}$$

In these equations a is the acceleration of upper mass during pulse motion, v_p the average velocity of bulk solid in the cylinder during discharge, Q the discharge rate, t_0 the time for motion of upper mass to be initiated, γ is the bulk unit weight, h_{sh} is the head of material above plane of shock, h_s is the effective surcharge head, A_c is the cross section area of the barrel, Δp_{v0} is the maximum increment in the average vertical pressure due to the shock load and $\Delta\varepsilon_y$ is the dynamic displacement of consolidated mass in the vertical direction. Calculations using Equations 6.1 to 6.4 can be found in Appendix E. The dynamic displacement of consolidated mass ($\Delta\varepsilon_y$) is difficult to calculate because it is dependent on the particle size, void ratio and properties of the boundary surface. In Appendix D, $\Delta\varepsilon_y$ has been calculated from recent investigations (Buick et al., 2004) of granular particles on a model silo, where the same PET pellets stored in the honking silo of Fig. 3.1 were used. It is important to note that the void ratio will depend on the degree of consolidation in the bulk material, which was significantly lower in the model silo in comparison to the silo of Fig. 3.1. Also the material of the model silo and the real one are different and therefore the dynamic displacement parameter should be considered as an approximate value. From the calculations in Appendices D and E the values $\Delta\varepsilon_y$ = 1.75 mm, t_0 = 0.25 s, v_p = 0.01 m/s, a = 4.81 m/s² and a period T = 0.28 s are obtained. This calculated period of pulsations is close to the range of 0.15-0.2 s observed in Figs 3.17, 3.18 and 3.19.

6.3.2 Velocity discontinuities

The creation of dynamic arches, rupture surfaces and fracture planes within the bulk material due to velocity discontinuities during mass flow discharge at the silo hopper has been reported to occur in a cyclic manner (Shinohara et al., 1968; Bransby et al., 1973, 1975; Michalowski, 1984, 1987; Purutyan et al., 1994b). For instance, it has been suggested that the dynamic arch theory is an oversimplification of the complex interaction and propagation of rupture surfaces in the hopper (Perry et al., 1976). The dynamic arch concept has been suggested as a hemispherical surface of initial acceleration of the bulk material during discharge. It has been suggested that the formation and collapse of the dynamic arch takes place periodically during silo discharge (Shinohara et al., 1968). Rupture surfaces are defined as zones of density

changes (dilation) caused as a result of shear in the stored material (Bransby et al., 1973, 1975; Michalowski, 1984). It is worth noting that rupture surfaces are accompanied by cyclic peak stresses on the walls of the hopper just below the transition (Bransby et al., 1973, 1975). An independent study (Kmita, 1985), in which the normal pressures of a mass flow silo were measured on the walls, shows pressure changes during discharge with considerable amplitudes. These variations in normal pressure were recognised as pulses by the investigator. Also in the same study, the normal pressure amplitudes during the pulses were considerable higher on the hopper than on the silo wall for the same period of time. It has been suggested that fracture planes are the result of velocity changes in a relatively small region causing periodic vibrations or thumps (Purutyan et al., 1994b). Model tests conducted by Purutyan et al. (1994b) showed that for the case where the hopper angle was close to the critical hopper angle for mass flow pulsations were observed during emptying. However, when the hopper angle was steeper than the critical angle for mass flow, no significant vibrations were observed. The vibration period and amplitude of pulses were reported to be a function of the discharge rate. The same study also showed that vibrations were sensitive to the stresses in the stored solid at the transition between cylinder and hopper. The stresses need to be high at the transition to observe vibrations, even when the hopper angle is close to the critical hopper angle for mass flow. It is worth noting that the honking silo shown in Fig. 3.1 has a hopper angle ($\beta = 30^{\circ}$) close to the critical one for the stored PET pellets tested in this Chapter. The wall friction angle can be calculated from Equation 1.1 taking the maximum wall friction coefficient (aluminium) in Fig. 6.8. This gives a wall friction angle of $\varphi_w = 14^{\circ}$, which together with the hopper half angle $\beta = 30^{\circ}$ in Fig. 1.3a shows that the silo hopper is close to the borderline of mass flow condition. Dean (2003) reported a similar behaviour where a honking silo was close to the critical hopper angle to achieve mass flow for the material stored. Moreover, it was also reported that another silo, similar in geometry and storing the same bulk material as the latter, does not honk. This last silo has a hopper angle well within the mass flow limits.

Shinohara et al. (1968) proposed an equation for the pulse frequency calculation of the dynamic arch. However, the bulk material parameters involved in the calculation are difficult to determine without a detailed experimental investigation of the bulk properties. Firewicz (Roberts, 1993) proposed an improved equation to that proposed by Shinohara et al. (1968) for the calculation of the pulse frequency f_p due to formation and collapse of dynamic arches:

$$f_p = \frac{1}{\sqrt{3}} \sqrt{\frac{gO_l}{k_h}} \frac{1}{T_p} \left(\frac{1-\varepsilon_0}{1-\varepsilon_i} \right), \tag{6.5}$$

where ε_0 is the void fraction at outlet, ε_i is the void fraction at dynamic arch, O_l is the outlet diameter of the hopper, $k_h = \tan \Theta$, Θ is the internal angle of the hopper and T_p is the thickness of falling layer. Again, some parameters in Equation 6.5 are difficult to evaluate, but some assumptions can be made to roughly calculate the pulse frequency. The assumption of loose and packed void ratios for the bulk material due to its minimum and maximum density is valid if it is considered that the particles at the outlet will be in a loose form while in the dynamic arch they will be tightly packed. Following the procedure described in Juarez-Badillo and Rico-Rodriguez (1996) to determine the density of the solids (excluding the voids), ρ_s = 1265 kg/m^3 was obtained. Then the void fraction for PET pellets can be calculated giving the values ε_0 = 1 - (770 kg/m^3/1265 kg/m^3) = 0.391 for loose particles and ε_i = 1 – (890 kg/m^3/1265 kg/m^3) = 0.296 for packed particles. Further assuming $T_p = O_l$ = 0.25 m, Equation 6.5 gives a frequency f_p = 2.4 Hz and a period T = 0.42 s. Even though the period T is higher than the observed for the occurrence of small oscillations and honks (0.15-0.20 s) in Chapter 3, it can still be considered, taking into account the considerations made, to be in line with the periodic behaviour observed in the acceleration measurements.

6.4 Conclusions

Two possible sources of excitation for honking have been investigated in this Chapter. The first of these (slip-stick) has been experimentally studied while the

other (pulsating flow) has been reviewed from previous published work. The following conclusions can be drawn:

- *Slip-stick.* The experimental study shows that slip-stick, represented by shear stress fluctuations, is absent when the polypropylene pellets are sheared on either aluminium or stainless steel plates. On the other hand, shear stress fluctuations are observed with the PET pellets for both wall materials. The magnitude of these fluctuations increases with the normal stress level, indicating that in a silo, these fluctuations would be larger towards the lower end where the stresses are higher and that the magnitude of the fluctuations would reduce with decreasing fill level. This matches common industrial observations that silo honking occurs at high fill levels with high stress levels (Buick et al. 2005; Tejchman, 1999, Hupkes, 2003), and that honking stops when the fill level drops below a certain height in an industrial silo. Slip-stick is fairly periodic like the small oscillations and honks observed in Figs. 3.17, 3.18 and 3.19, however, the slip-stick period changes with normal pressure. Silo honking has also been reported to commonly occur at higher outflow rates (Tejchman, 1999), however, studies suggest that the magnitudes of slip-stick fluctuation reduces when shearing rate increases (Buick et al., 2005; Budny, 1979; Nasuno et al., 1998). If slip-stick were causing the vibration responses observed in Chapter 3 (small oscillations and honks), its excitation would be in the form of an axial pulse load along the silo wall.

- *Pulsating flow – Plane of shock.* Pulsating flow is generally recognised to be due to density changes (dilation) of the bulk material and the frictional behaviour between the bulk material and the silo wall. Investigators in previous studies assumed that a plane of shock is created within the stored material during mass flow discharge producing a sudden increment in the lateral wall pressure acting on the silo structure. An expression for the prediction of the period in the pulsating flows has been used. The values obtained with this expression are in line with the range of periods observed in the acceleration measurements for small oscillations and honks in Chapter 3.

However, the parameters involved in the calculation of these periods are difficult to determine without a detailed experimental investigation. They mainly depend on bulk solid properties during flow and the calculated values should be considered as approximate values. The excitation due to this kind of pulse load would be on a small region of the silo wall in the radial direction.

- *Pulsating flow – Velocity discontinuities.* Different interpretations of velocity discontinuities (dynamic arch, rupture surfaces and fracture planes) phenomena were reviewed for the case of periodic pulses on the silo hopper. Experimental studies have shown that pressure amplitudes during these pulses were considerable higher on the hopper walls than on the silo walls. Also experimental studies found that flow pulsations due to velocity discontinuities are sensitive to the stress in the stored solid at the transition between the cylinder and the hopper. This also matches observations in Chapter 3 and previously reported studies where honking occurs at high fill levels with high stress levels (Buick et al. 2005; Tejchman, 1999, Hupkes, 2003), and stops when the fill level drops below a certain height in an industrial silo. Flow pulsations also depend on the hopper angle, which needs to be close to the critical value for mass flow in order to observe the pulses. The silo shown in Fig. 3.1 has a hopper angle ($\beta = 30^{\circ}$) which is close to the critical value for the stored PET pellets tested. The excitation due to this kind of pulse load would be normal to the silo hopper.

Chapter 7

Transient dynamic response of the silo structure

7.1 Introduction

In Chapter 3 it was concluded that honking cannot be due to a steady state harmonic response of the excitation source. This conclusion is further supported by the excitation sources studied in Chapter 6, where they occur periodically as transient excitations. The transient dynamic response of the silo structure subjected to pulse loads at different locations is considered in this Chapter. The different sources of excitations discussed in Chapter 6 form the basis for the location of the pulse loads. As discussed these locations are on the silo wall and silo hopper, which are the most likely regions to be excited by particulate solids during discharge. The aim is to determine whether vibration characteristics similar to those observed during honking can be simulated by the pulse loads. As the excitations considered are axisymmetric, the axisymmetric finite element model is used for all simulations.

7.2 Pulse load considerations and the dynamic model

7.2.1 Pulse load considerations

The honking phenomenon was characterised in Chapter 3 using acoustic and acceleration measurements. These measurements show honks with different

acceleration amplitudes, however, the fundamental honking frequency and its integer multiples do not change for different honks. The load amplitude will influence the acceleration amplitude of the wall vibrations but it will not change the frequency content. Therefore dynamic loading in the form of a rectangular pulse load with unit amplitude is employed. The pulse loads are applied in different regions of the silo structure, based on the excitation proposed for honking in Chapter 6, to examine if the excited modes correspond to the frequencies evaluated from field measurements presented in Chapter 3.

7.2.2 The dynamic model

The axisymmetric silo model analysed in this section is the same empty ASILO model presented in Chapter 5, Section 5.5. The mode superposition method is applied to evaluate the transient dynamic response of the silo structure. The natural frequencies of the silo structure are extracted up to 2000 Hz (≈ 345 modes). These modes are combined to produce the total deformation of the structure at any instant of time. This mode superposition procedure provides time history analysis of linear systems. A time step Δt = 2E-4 s is used. This represents a Nyquist frequency of 2500 Hz. In all cases the rectangular pulse load is applied for duration of 4E-3 s ($20\Delta t$) and the total time of analysis is t_T = 0.2048 s allowing the structure to vibrate in its natural frequencies during application and after removal of the load. Since damping (normally 2% for steel and aluminium) has only a small influence on the response frequencies excited, the model is assumed to be undamped. Once the transient dynamic response of the silo structure is obtained, a Fourier analysis of the silo wall acceleration at different heights is conducted to examine its frequency content. The MATLAB (Math Works Inc., 1999) code can be found in Appendix A.

7.3 Axisymmetric excitation of the silo wall

7.3.1 Axial pulse load

One of the sources of excitation previously proposed for honking is slip-stick between particles and silo wall (Ooi et al., 1999). This behaviour was also

investigated by laboratory tests in Chapter 6 for the particles stored in the instrumented honking silo. This investigation shows that the slip-stick behaviour is strongly influenced by the normal pressure on the silo wall. Slip-stick is less evident when the normal pressure is reduced. These observations are consistent with the honking behaviour, which does not occur when the fill level is low (low normal pressure). Figure 6.10 shows the shear stress response of PET pellets on an aluminium plate as a function of time for different normal stresses. The laboratory test plot shows a stick phase of the PET pellets against the aluminium plate that reaches a high shear stress value and then suddenly drops. This cycle is repeated continually during shearing. In a silo the sudden drop (slip) and then reattachment (stick) may be transmitted as axial forces along the wall. The stick phase may transmit axial forces while the slip phase may represent a release of these forces. This excitation is simulated in the axisymmetric FE model as a simple axial pulse load along the silo wall. The pulse load is applied along two different heights of the silo wall to represent different fill levels (see Fig. 7.1): one representing 90% silo capacity (90FL model) and the other representing at 55% silo capacity (55FL model), both within the fill level range that is known to produce honking in this structure.

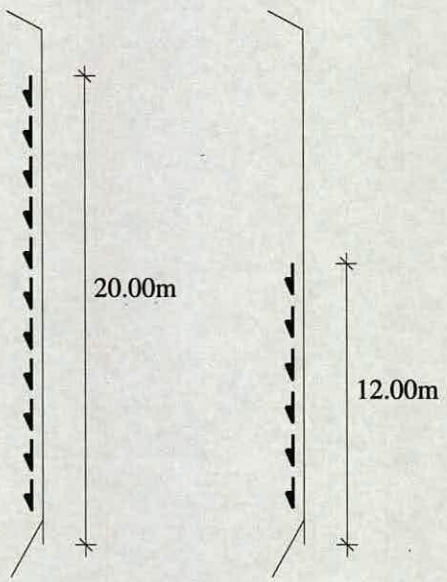

Figure 7.1: Schematic representation of the axial pulse load at a) 90% and b) 55% silo capacity.

A Fourier analysis of the dynamic response to these axial pulses is conducted and the results are shown in Figs. 7.2 to 7.5. The positions selected for the analysis are at ≈ 11.95 m (P6) and ≈ 19.90 m (P10) of the silo height. Figures 7.2 and 7.3 show the spectra for the 90FL model at P6 and P10 respectively. It is clear that this sort of excitation will excite the natural frequencies of the silo. The majority of the frequencies seen in the spectra are the natural frequencies of the axisymmetric ASHELL model (without roof and hopper). For example in Fig. 7.2a, radial spectrum at P6, the frequencies at ≈ 64 Hz, ≈ 180 Hz, ≈ 400 Hz, ≈ 620 Hz, ≈ 740 Hz and ≈ 1000 Hz are excited by the axial load. Similarly in Fig. 7.3a, radial spectrum at P10, the same frequencies are observed, however, the peaks at ≈ 64 Hz and ≈ 180 Hz have lower energy than those observed in Fig. 7.2a. All these frequencies can be seen in Fig. 4.15. The axial spectra, Figs. 7.2b and 7.3b, show clear peaks at ≈ 64 Hz, ≈ 125 Hz and ≈ 180 Hz that are the lowest axial axisymmetric frequencies except ≈ 125 Hz in Fig. 7.2b which is due to the roof vibration. The energy in the axial spectra is at least twenty times higher than that in the radial spectra for the maximum values in these two positions analysed. The frequencies excited for the 55FL model are similar to those for the 90FL model. However, frequencies beyond 1000 Hz are observed in the radial spectra, see Figs. 7.4a and 7.5a. The energy again is clearly higher for the axial spectra than that in the radial spectra for the maximum values. It is interesting to note that the peaks observed in the radial spectra are separated, in higher frequency values, at 120 Hz, which is the separation of the axial natural frequencies observed in the axisymmetric shell model (see Fig. 4.16). Fourier analyses at different positions than those analysed previously (P6 and P10) exhibit similar features in the frequency spectra to those in Figs. 7.2 to 7.5 in the axial and radial directions for the two models 90FL and 55FL. As one would expect the results show that an axial pulse excitation along the silo wall regardless of the height of application excites mainly frequencies associated with the cylindrical shell. The honking fundamental frequency or integer multiples of this frequency are not observed in the radial and axial dynamic response of the structure.

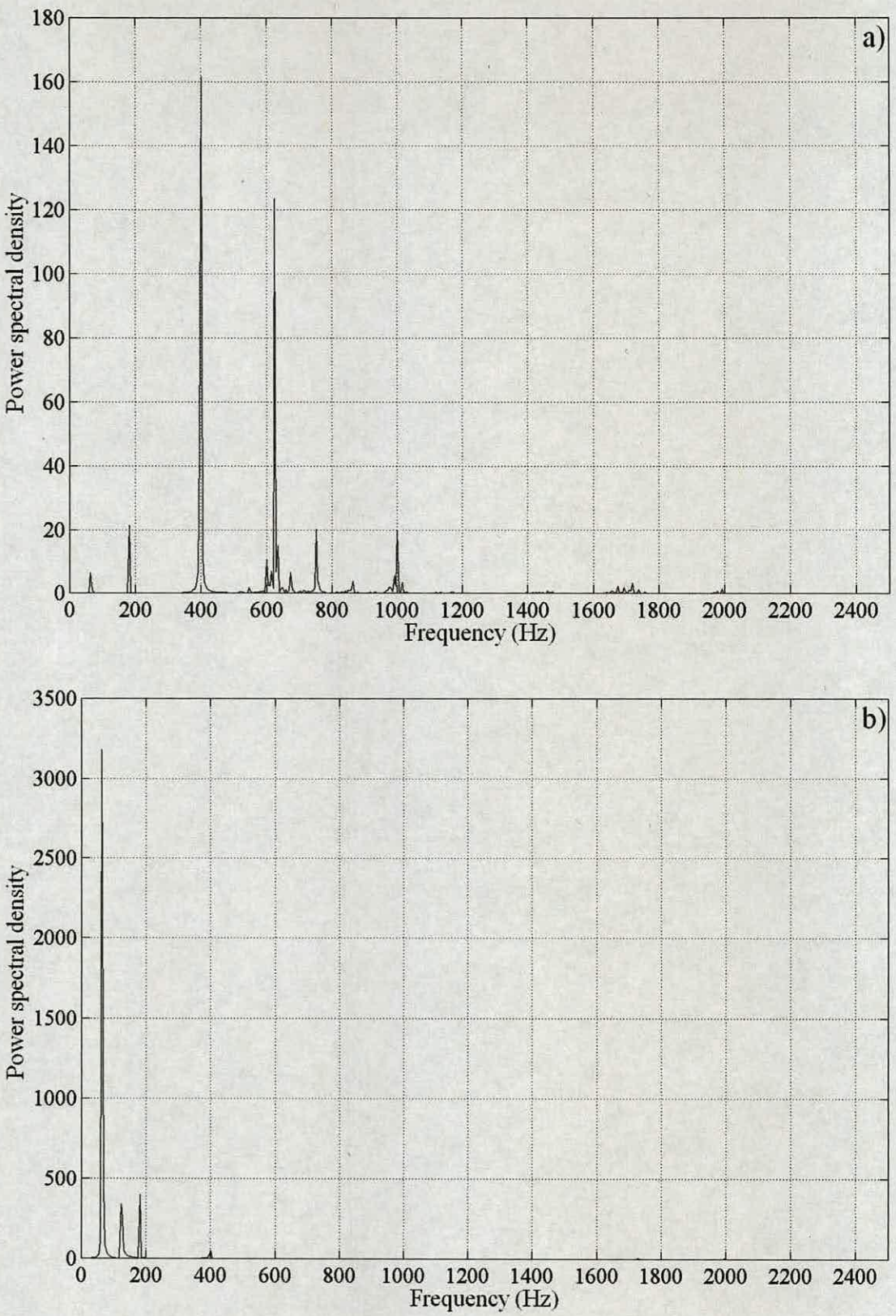

Figure 7.2: Frequency spectra of the silo dynamic response at ≈ 11.95 m (P6) in the a) radial and b) axial direction for an axial pulse load along the height when the silo capacity is 90%.

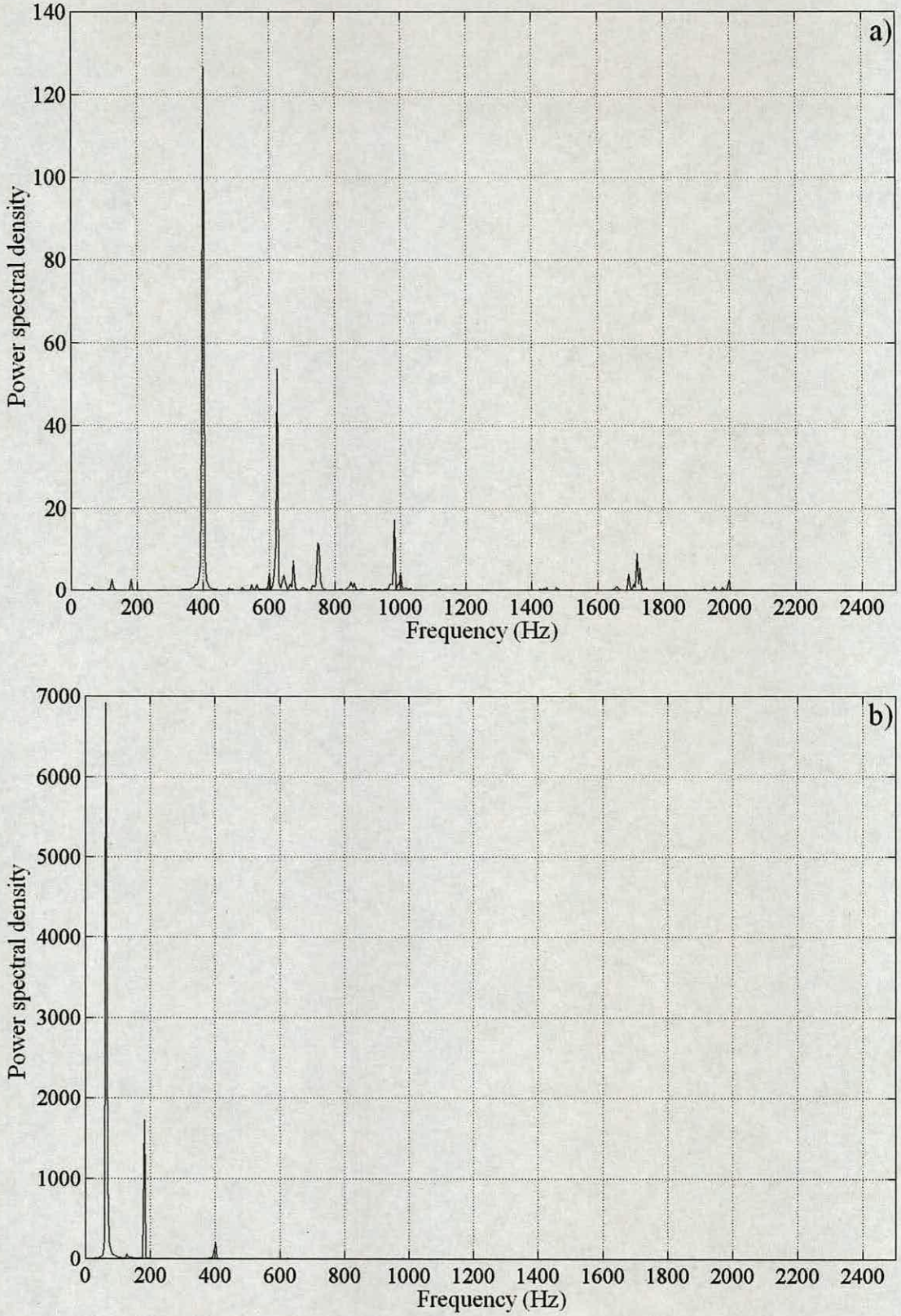

Figure 7.3: Frequency spectra of the silo dynamic response at ≈ 19.90 m (P10) in the a) radial and b) axial direction for an axial pulse load along the height when the silo capacity is 90%.

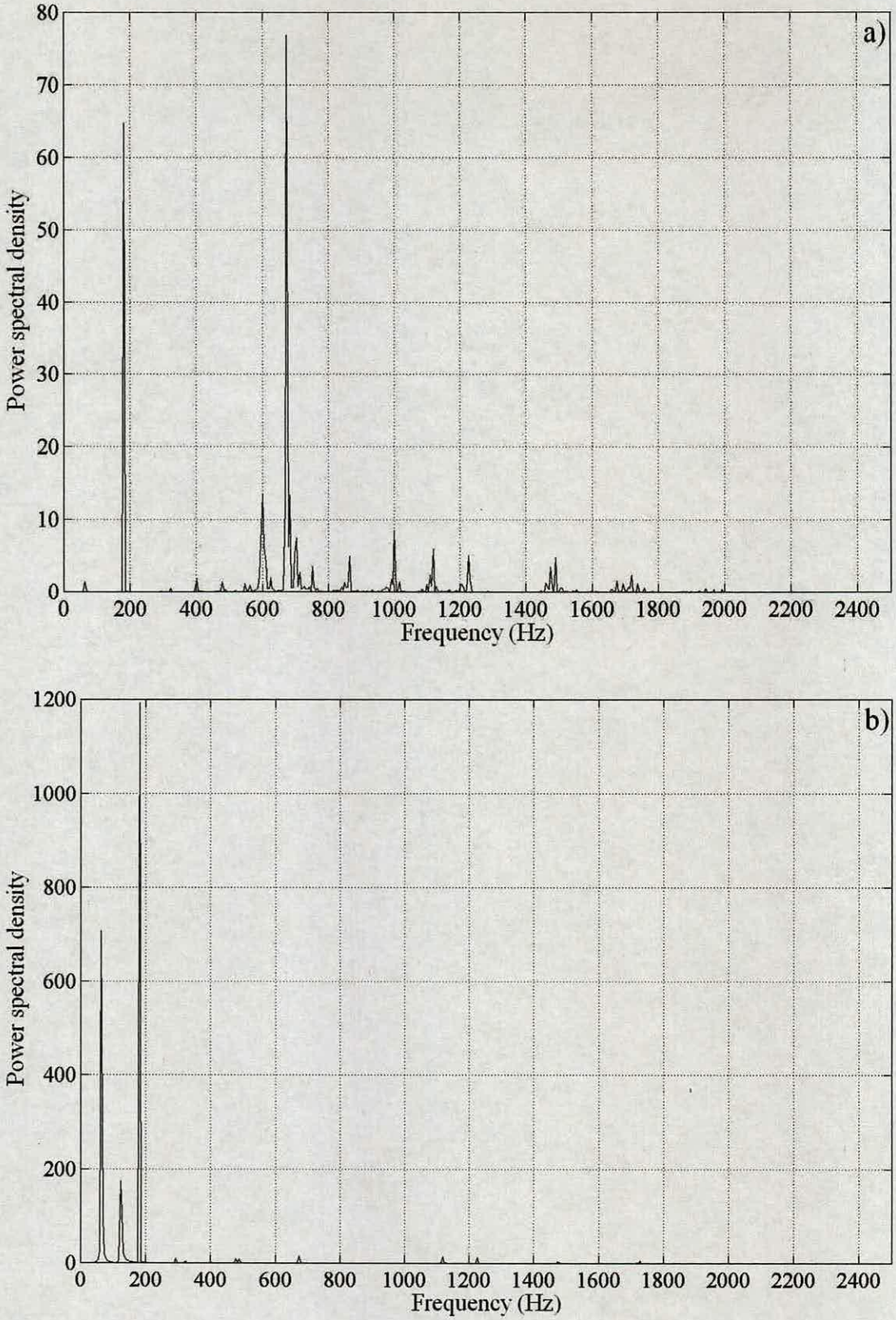

Figure 7.4: Frequency spectra of the silo dynamic response at ≈ 11.95 m (P6) in the a) radial and b) axial direction for an axial pulse load along the height when the silo capacity is 55%.

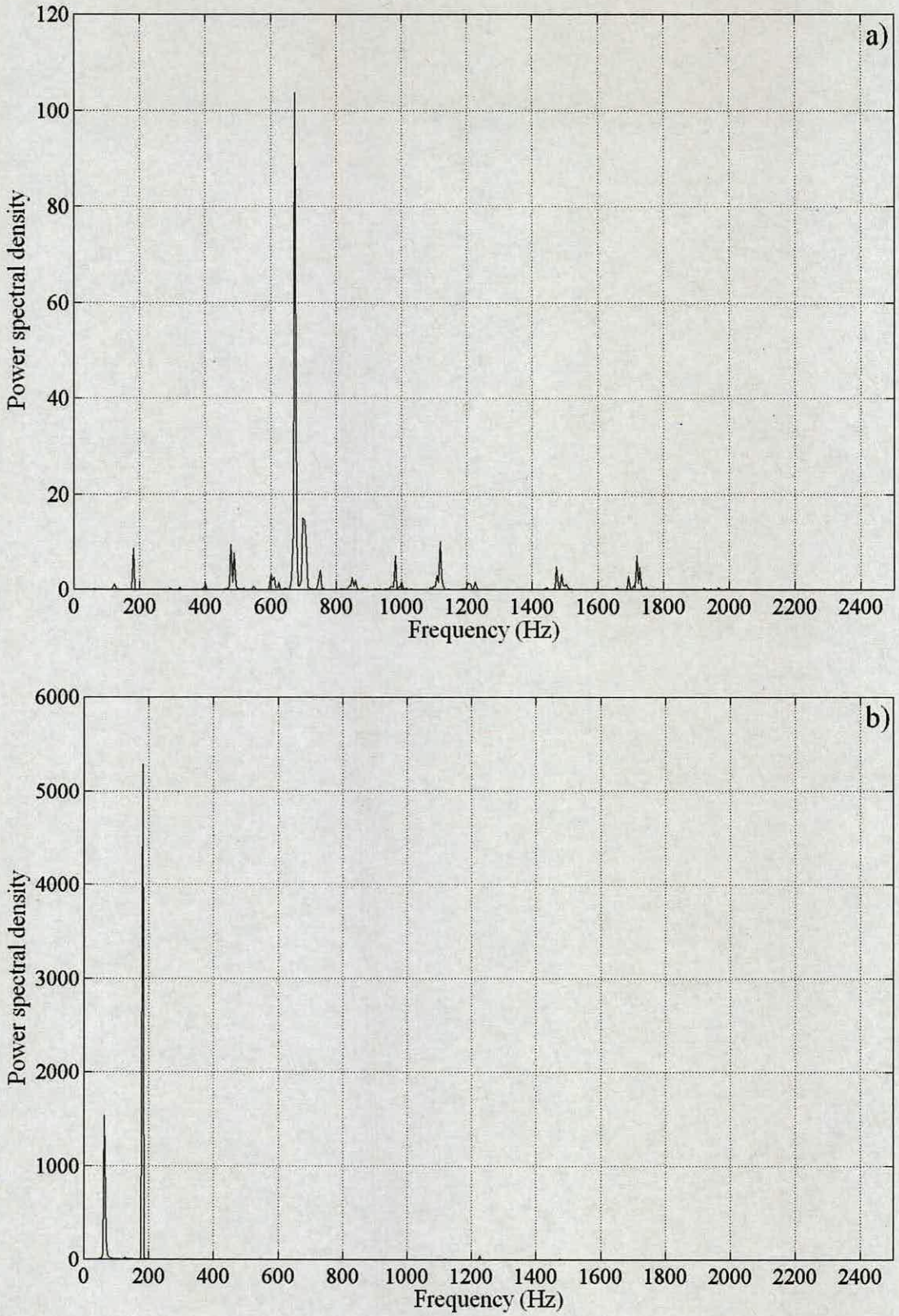

Figure 7.5: Frequency spectra of the silo dynamic response at ≈ 19.90 m (P10) in the a) radial and b) axial direction for an axial pulse load along the height when the silo capacity is 55%.

Some of the modes excited are easily identified from the displacement response at different instants of time and are presented in Fig.7.6. Again two figures are shown for each mode. The one on the left comprises the deformed and undeformed shape of the model in black and green colours respectively. The one on the right is again the deformed shape but now a colour code representing the modal displacement has been applied. Red colour represents the maximum displacement and blue represents the minimum. The modes identified are mode 1, 2 and 3 listed in Table 5.2 and shown in Fig. 5.5. Their frequencies can be compared with the axial spectra in Figs. 7.2 to 7.5 and mode shapes with Fig. 7.6 respectively.

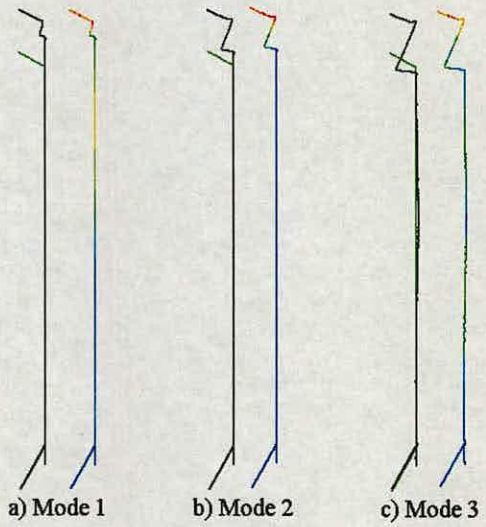

Figure 7.6: Structure deformation at three different instants of time where mode a) 1, b) 2 and c) 3 are identified.

7.3.2 Radial pulse load

The higher frequency components of the flow pulsations have been proposed as a possible source of excitation for honking by Roberts and Wensrich (2002) who consider it as a variation of the silo quaking problem. Even though, it has been shown in Chapters 3 that a harmonic load is not exciting the silo structure during honking, the dynamic load model presented in Roberts and Wensrich (2002) is considered in this section as a sudden pulse load. The dynamic load model considers a plane of shock within the material that is located at certain height ($H_{sh} \approx 1D$ to $2D$,

where *D* is the silo diameter) above transition. In the plane of shock, the average vertical pressure suddenly increases to a large value and the lateral wall pressure increases in the same way. The increment in the lateral wall pressure would impart sudden radial excitation to the barrel of the silo in the plane of shock location. This sudden increment in the lateral wall pressure is applied in the axisymmetric FE model as a pulse load along the circumference of the silo at three different locations *1D* (3.0 m), *1.5D* (4.5 m) and *2D* (6.0 m) above the transition. Figure 7.7 shows the schematic application of the circumferential pulse load for the three cases considered.

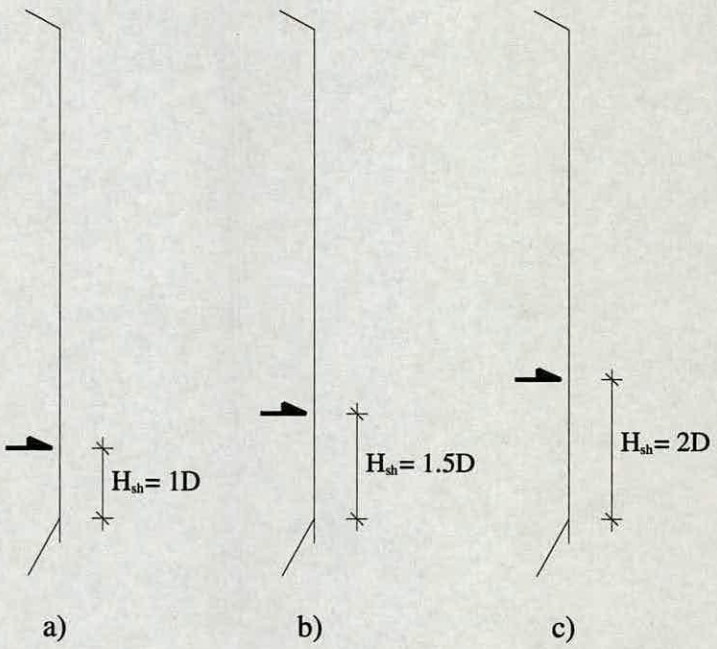

Figure 7.7: Schematic representation of the radial pulse load at a) H_{sh}=*1D*=3 m, b) H_{sh}=*1.5D*=4.5 m and c) H_{sh}=*2D*=6 m.

The analyses show that the frequency spectra of the response for the three excitations have the same features. Therefore, only the frequency spectra for the pulse load applied at *1.5D* are discussed here. The radial and axial frequency spectra at ≈ 11.95 m (P6) and ≈ 19.90 m (P10) above the silo base are presented in Figs. 7.8 and 7.9 respectively. The radial spectra (Figs. 7.8a and 7.9a) show clear peaks in the frequency range of 550 Hz to 650 Hz. As discussed in Chapter 4, the "ring

frequency" (Scott, 1988) of this structure is within this range. This frequency receives this name because the axisymmetric radial vibration is independent of the length of the shell until a considerably high value of axial half waves is reached (Leissa, 1973; Junger and Feit, 1986). The results indicate that a radial excitation along the circumference at a specific location will excite the radial frequencies near the "ring frequency" of the silo structure. This frequency is higher than the fundamental honking frequency (333 Hz) of the instrumented silo structure. The energy associated with axial vibrations is significantly smaller (Figs. 7.8b and 7.9b) and a wider range of frequencies are seen in the axial spectrum. The peaks with the highest energy are concentrated near the range mentioned above for radial response. One of the frequencies observed with a considerably energy in the axial spectra is the axial natural frequency of the axisymmetric model at $\approx$ 400 Hz. Some small peaks are also observed for frequencies at 65 Hz, 185 Hz and 300 Hz all of which are axial natural frequencies, see Figs. 7.8b and 7.9b. The location of the pulse radial load in the range of *1D* to *2D* does not affect the frequency response of the structure; similar spectra are obtained for the three locations of the load shown in Fig. 7.7. Again the fundamental honking frequency (333 Hz) or integer multiples of this frequency are not observed in the radial and axial spectra of the structure for the radial pulse loads applied.

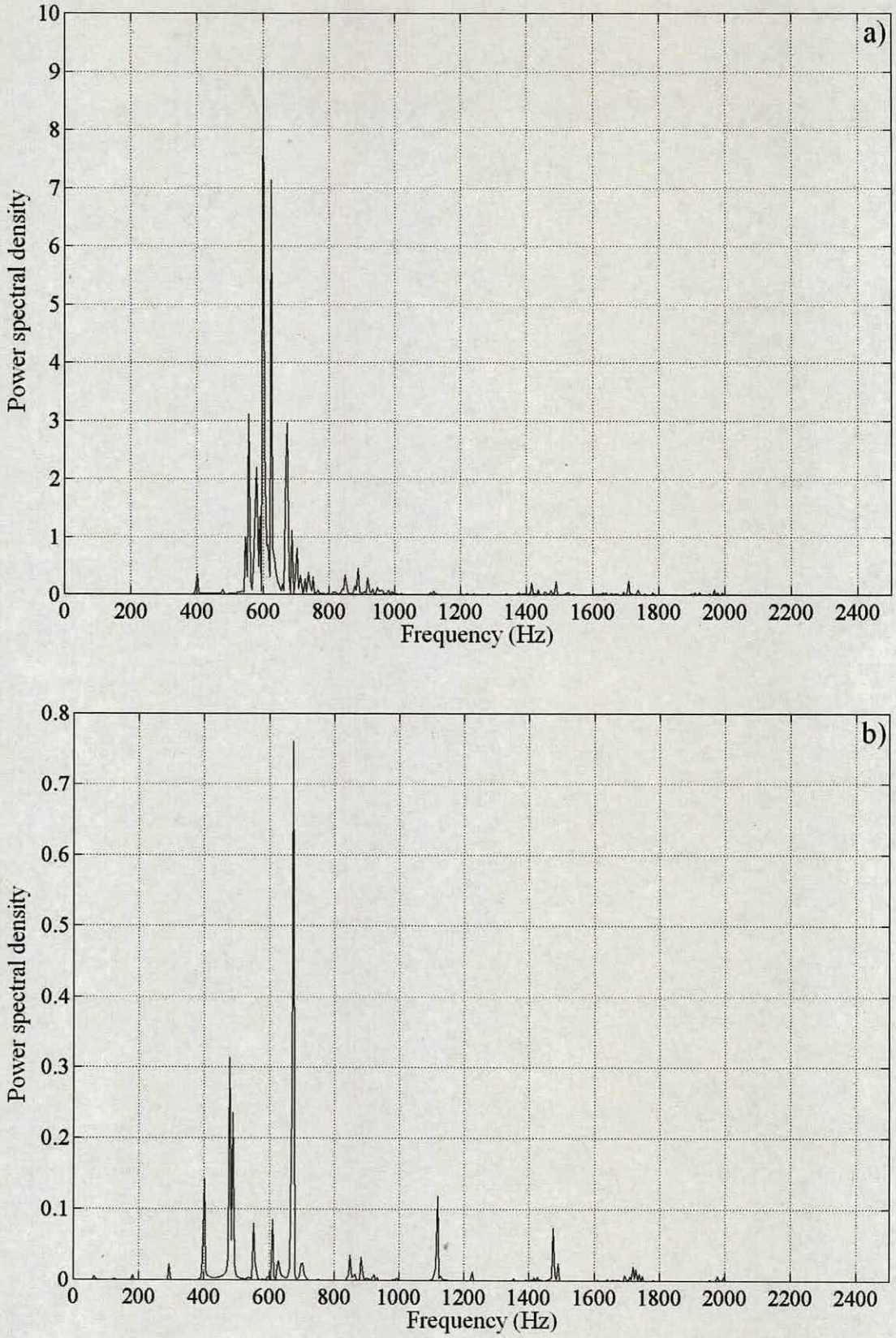

Figure 7.8: Frequency spectra of the silo dynamic response at ≈ 11.95 m (P6) in the a) radial and b) axial direction for a radial pulse load at *1.5D* above transition.

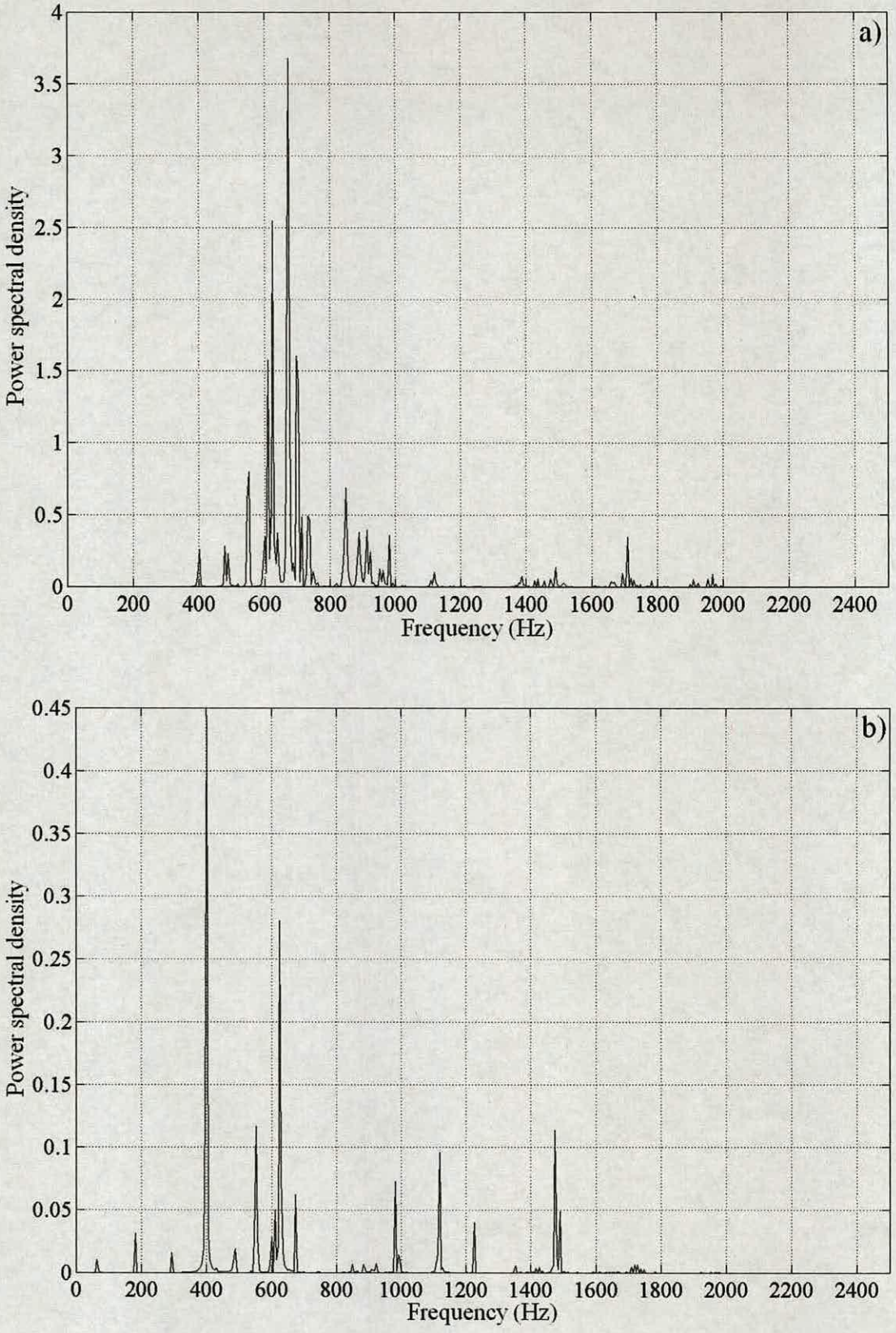

Figure 7.9: Frequency spectra of the silo dynamic response at ≈ 19.90 m (P10) in the a) radial and b) axial direction for a radial pulse load at *1.5D* above transition.

The identification of modes from the displacement response was not as easy as it was for the structural response due to the axial load along the shell. A particular instant of time is selected from the total period of vibration of the structure and its deformation shown in Fig. 7.10. The deformation of the structure is complex. A high number of waves are observed along the silo height. However, a clear mode cannot be identified as this deformation is expected to be the summation of different modes near the "ring frequency". Again the two figures shown for each mode follow the colour codes discussed earlier.

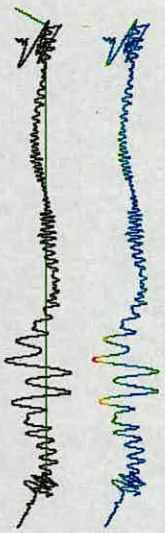

Figure 7.10: Structure deformation at a particular instant of time for a radial load at *1.5D*.

7.4 Axisymmetric excitation of the hopper

7.4.1 Normal pulse load

Frequency response due to pulse loads representing two different sources of excitation was considered in the previous section. These excitations act on the silo barrel. In this section a different source of excitation is proposed and considered: velocity discontinuities occurring close the transition. Due to these velocity discontinuities, fracture planes would be created periodically in the transition zone, which are accompanied by sudden increments in normal pressure on the silo hopper.

This behaviour of the material and some of its features were reviewed in Chapter 6. For the dynamic analysis, a pulse load is applied normal to the silo hopper of the axisymmetric ASILO model. A schematic representation of the normal pulse load applied on the silo hopper is shown in Fig. 7.11.

Figure 7.11: Schematic representation of the normal excitation pulse load on hopper.

The frequency spectra in the radial and axial direction of vibration at ≈ 11.95 m (P6) and ≈ 19.90 m (P10) above the silo base are presented in Figs. 7.12 and 7.13 respectively. The radial spectra for both figures (Figs. 7.12a and 7.13a) show that a wide range of frequencies are excited. It is interesting to observe that some of the peaks representing higher frequencies are integer multiples of a fundamental frequency i.e. the spectra show peaks at ≈ 320 Hz, ≈ 650 Hz and ≈ 940 Hz. It may be recalled that during honking frequency 333 Hz and its second (666 Hz) and third (999 Hz) harmonics were observed. Some of the excited frequencies due to normal loads on the hopper appear fairly close to those observed during honking. The radial spectra also show peaks at frequencies beyond 1000 Hz that are close to the integer multiples of a fundamental. Thus the response observed from the radial spectra due to normal excitation of the hopper closely matches the honking behaviour. In the axial spectra (Fig. 7.12b and 7.13b) frequencies at ≈ 295 Hz and ≈ 320 Hz are always

observed at different locations together with low power frequencies separated at ≈ 120 Hz. This again seems to be the separation of the axial natural frequencies of the simple shell, see Fig. 4.16. The energy for the maximum frequency values is almost the same for the radial and axial spectra. The frequency spectra, in the radial and axial direction, are typical for a number of heights investigated in the axisymmetric ASILO model. These results show that a pulse load normal to the silo hopper excites a frequency close to the fundamental honking frequency of the instrumented silo structure and frequencies close to the second and third integer value of that fundamental one.

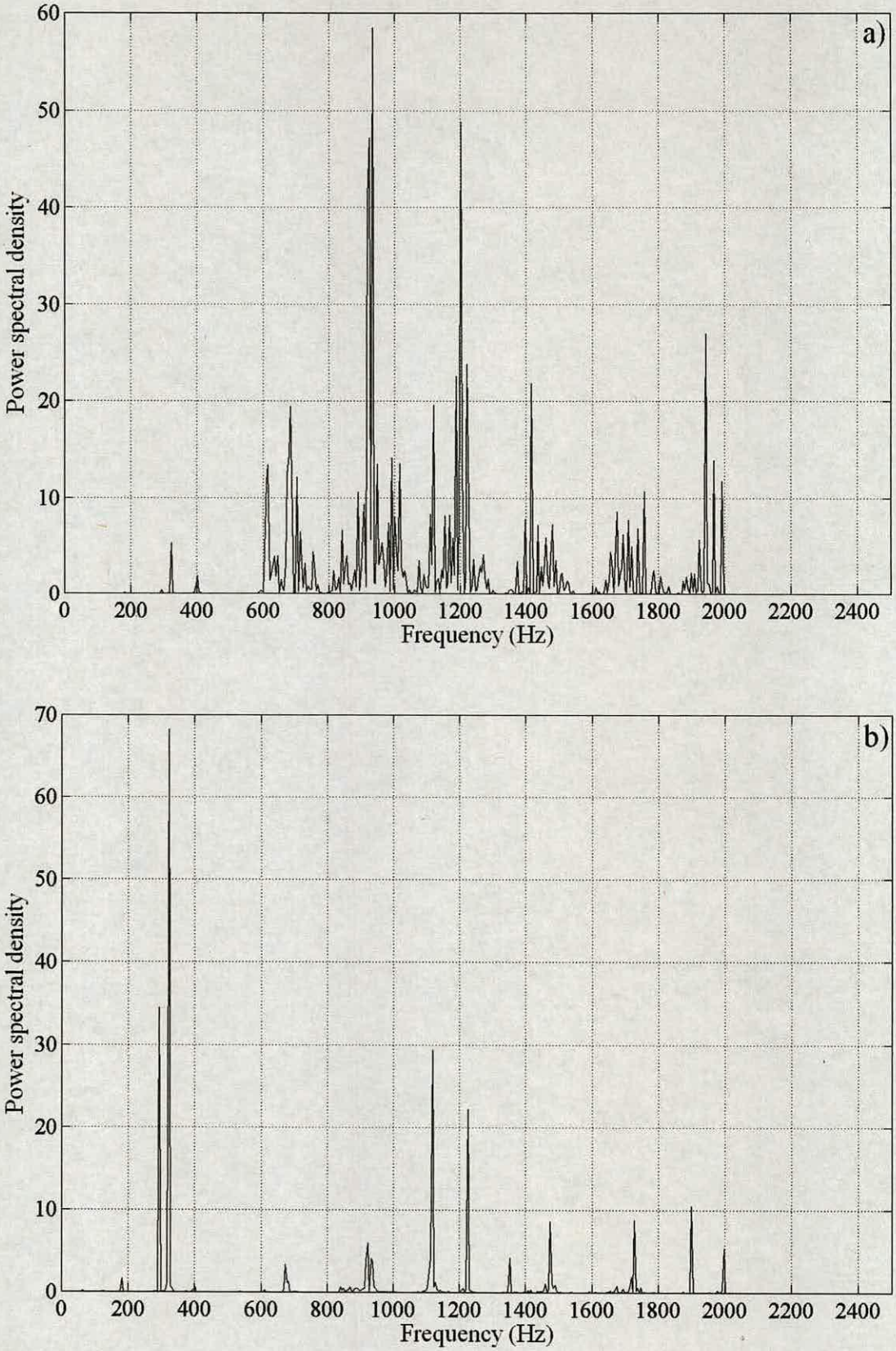

Figure 7.12: Frequency spectra of the silo dynamic response at ≈ 11.95 m (P6) in the a) radial and b) axial direction for a normal pulse load applied on hopper.

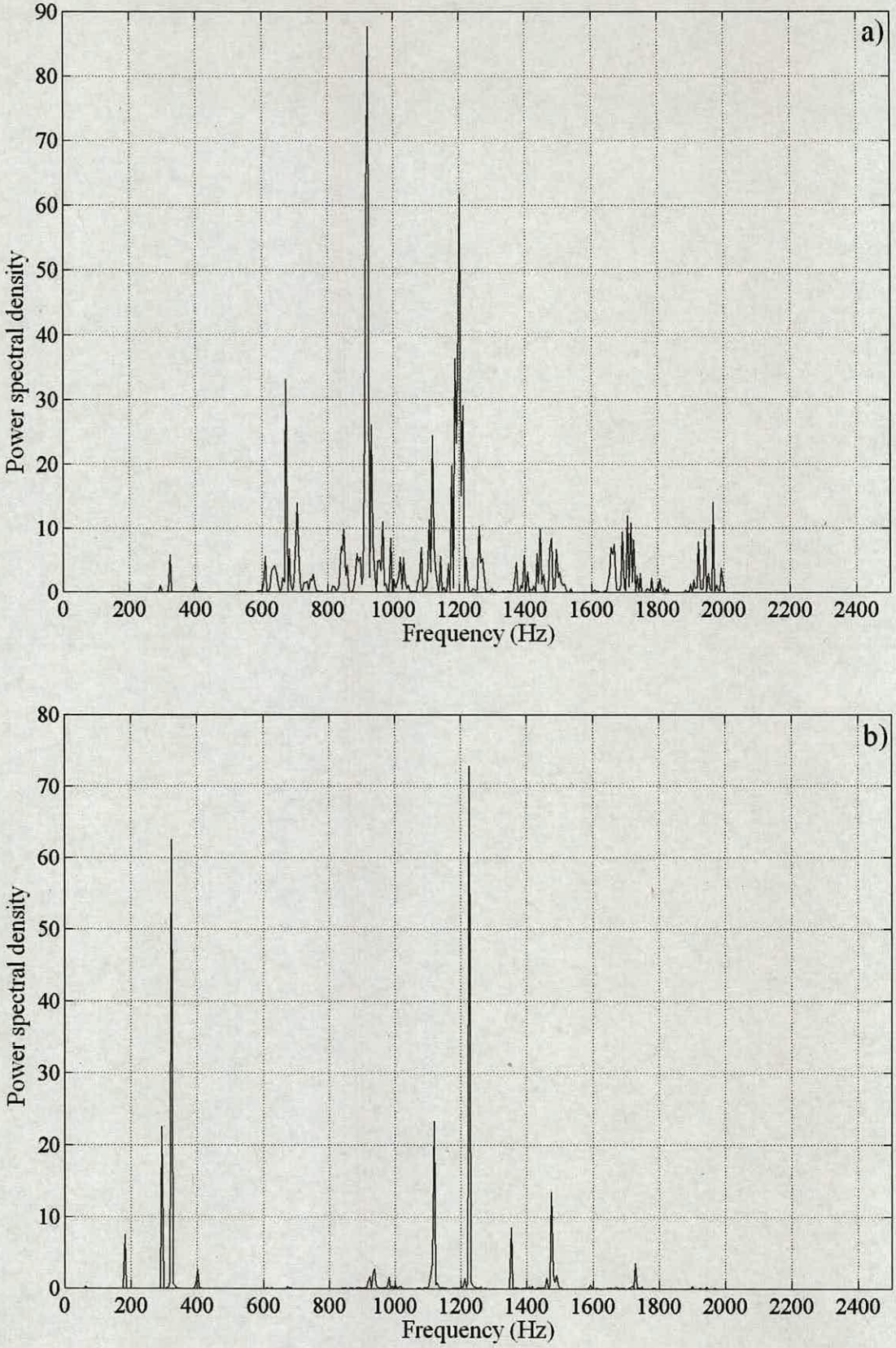

Figure 7.13: Frequency spectra of the silo dynamic response at ≈ 19.90 m (P10) in the a) radial and b) axial direction for a normal pulse load applied on hopper.

A particular instant of time is selected from the total period of vibration of the structure and its deformation shown in Fig. 7.14. This deformed shape appears to have contributions from modes corresponding to frequencies at ≈ 320 Hz, ≈ 650 Hz and ≈ 940 Hz.

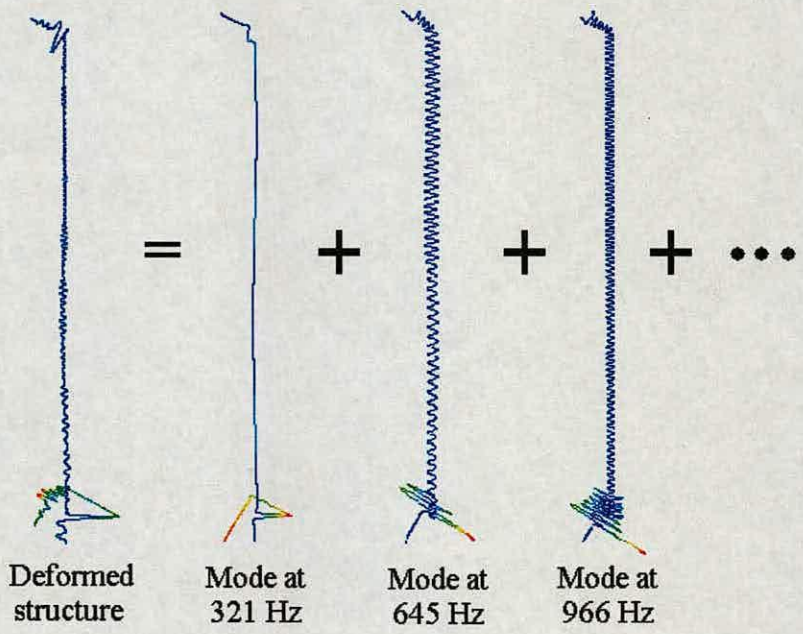

Figure 7.14: Assumed modal contribution for the structure deformation at a particular instant of time.

7.4.2 Axial and radial pulse load

To further examine the response due to normal pulse load on the hopper this load is divided into axial and radial components (see Fig. 7.15). The objective of this is to investigate if just one of the load components is sufficient for generating the spectral response similar to that observed during honking.

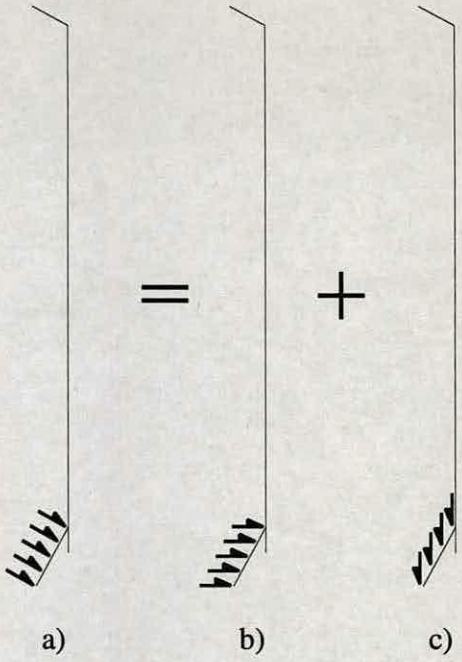

Figure 7.15: Schematic representation of the a) normal, b) radial and c) axial excitation pulse load on hopper.

The results of the axial pulse load on the silo hopper are presented in Fig. 7.16 and 7.17. Figures 7.16 and Fig. 7.17 show the radial and axial frequency spectra at ≈ 11.95 m (P6) and ≈ 19.90 m (P10) respectively. These are the same heights as those considered for the normal pulse load. The radial spectra show similar features as those observed for the normal pulse load on the silo hopper. However, the higher frequency components seem to have less energy. For example in Fig. 7.16a and 7.17a the peaks beyond 1200 Hz are barely observed. Peaks at 320 Hz are also observed in the axial spectra (Fig. 7.16b and 7.17b). These axial spectra also show peaks at ≈ 295 Hz and in a smaller extent at ≈ 180 Hz, which are axial frequencies of the silo structure. Frequencies greater than 500 Hz have clearly reduced their energy content with respect to other peaks to those in Figs. 7.12b and 7.13b. However, the maximum energy values in the axial spectra have increased, they are now more than four times greater than those in the radial spectra. Different heights along the silo wall were also investigated and the behaviour is similar.

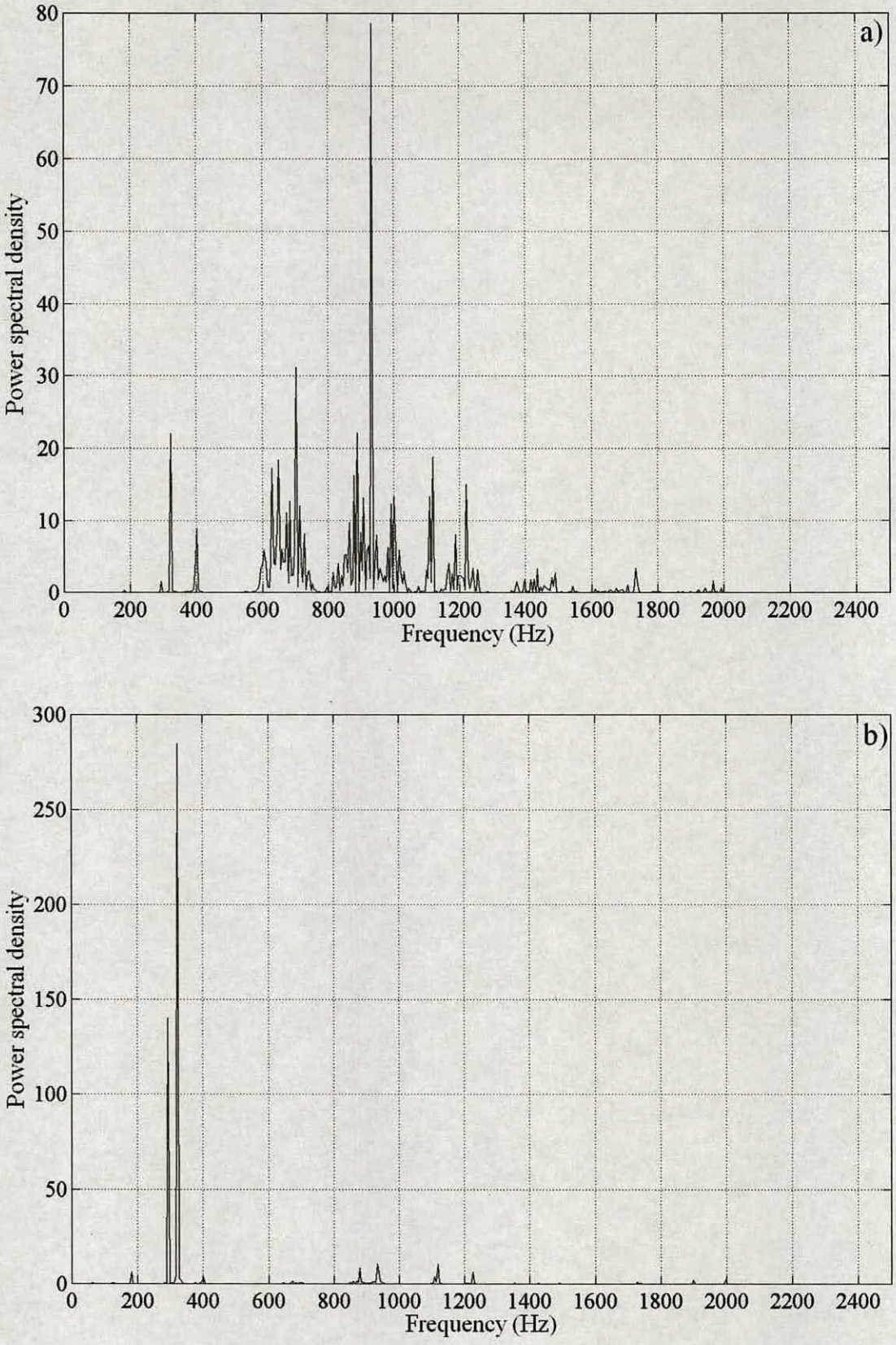

Figure 7.16: Frequency spectra of the silo dynamic response at ≈ 11.95 m (P6) in the a) radial and b) axial direction for an axial pulse load applied on hopper.

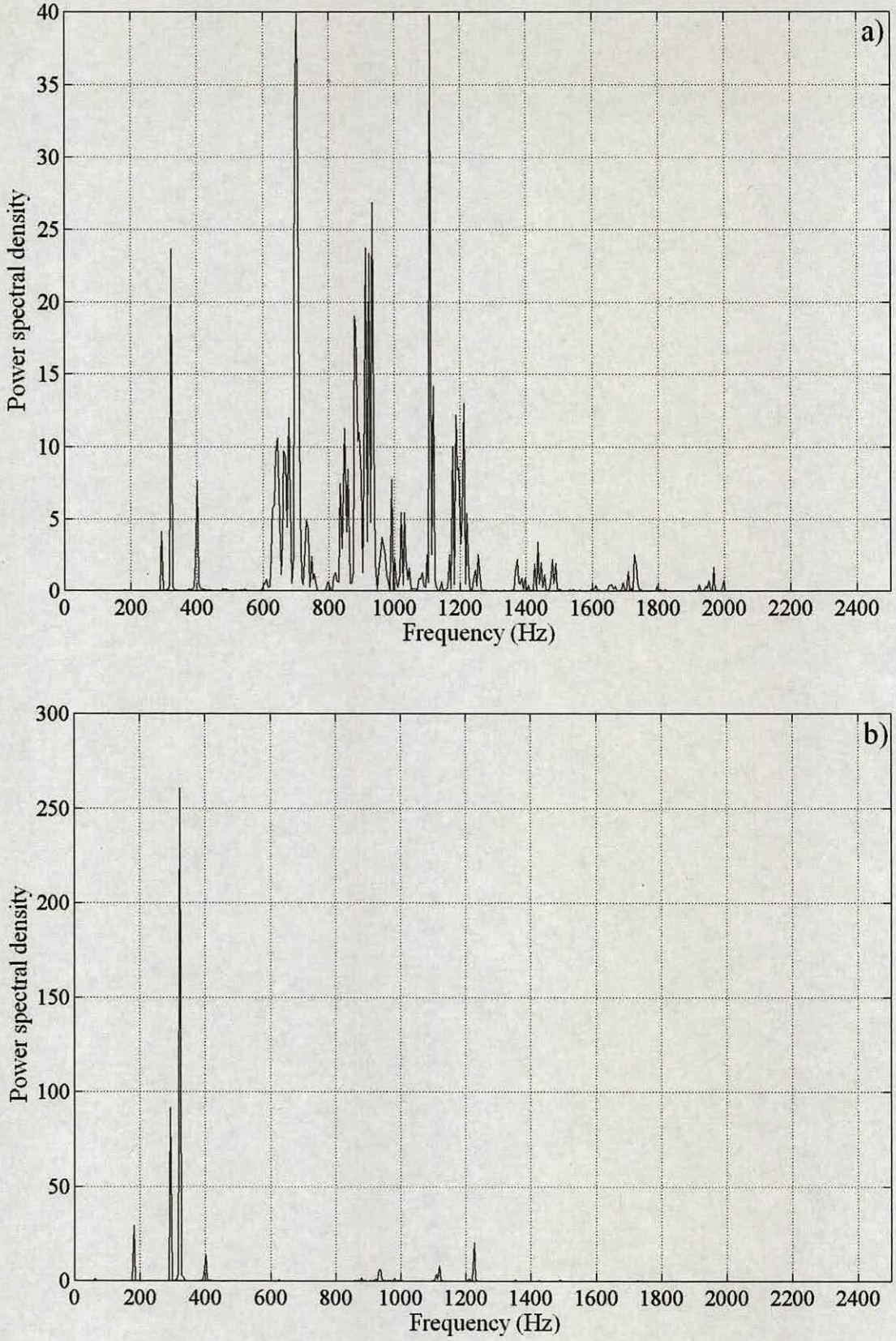

Figure 7.17: Frequency spectra of the silo dynamic response at ≈ 19.90 m (P10) in the a) radial and b) axial direction for an axial pulse load applied on hopper.

The silo hopper was excited by the radial component of the pulse. Figure 7.18 and 7.19 show the radial and axial frequency spectra at ≈ 11.95 m (P6) and ≈ 19.90 m (P10) heights above the silo base respectively. The radial spectra (Figs. 7.18a and 7.19a) show sharp peaks at integer values of the fundamental one for frequencies greater than 600 Hz. However, the fundamental frequency (≈ 320 Hz) is not observed in either of the radial spectra. The two axial spectra (Figs. 7.18b and 7.19b) show a similar behaviour, where frequencies below 600 Hz are not seen. Now the maximum energy values are greater in the radial spectra than those in the axial one. A number of heights analysed along the silo wall show similar features. These results show that the radial excitation on the hopper does not excite the honking fundamental frequency but harmonics above the "ring frequency" of the structure (≈ 570 Hz). This behaviour is similar to one of the features identified for the radial spectra of the acceleration measurements in Chapter 3, where often the fundamental honking frequency is absent but not the second or higher harmonics. The axial frequency spectrum of Fig. 7.18b shows peaks at the second (≈ 640 Hz) and third harmonic (≈ 960 Hz) at ≈ 11.95 m (P6) from the silo base. This behaviour is also in line with the honking behaviour where the honking fundamental frequency and its harmonics are also observed in the axial direction.

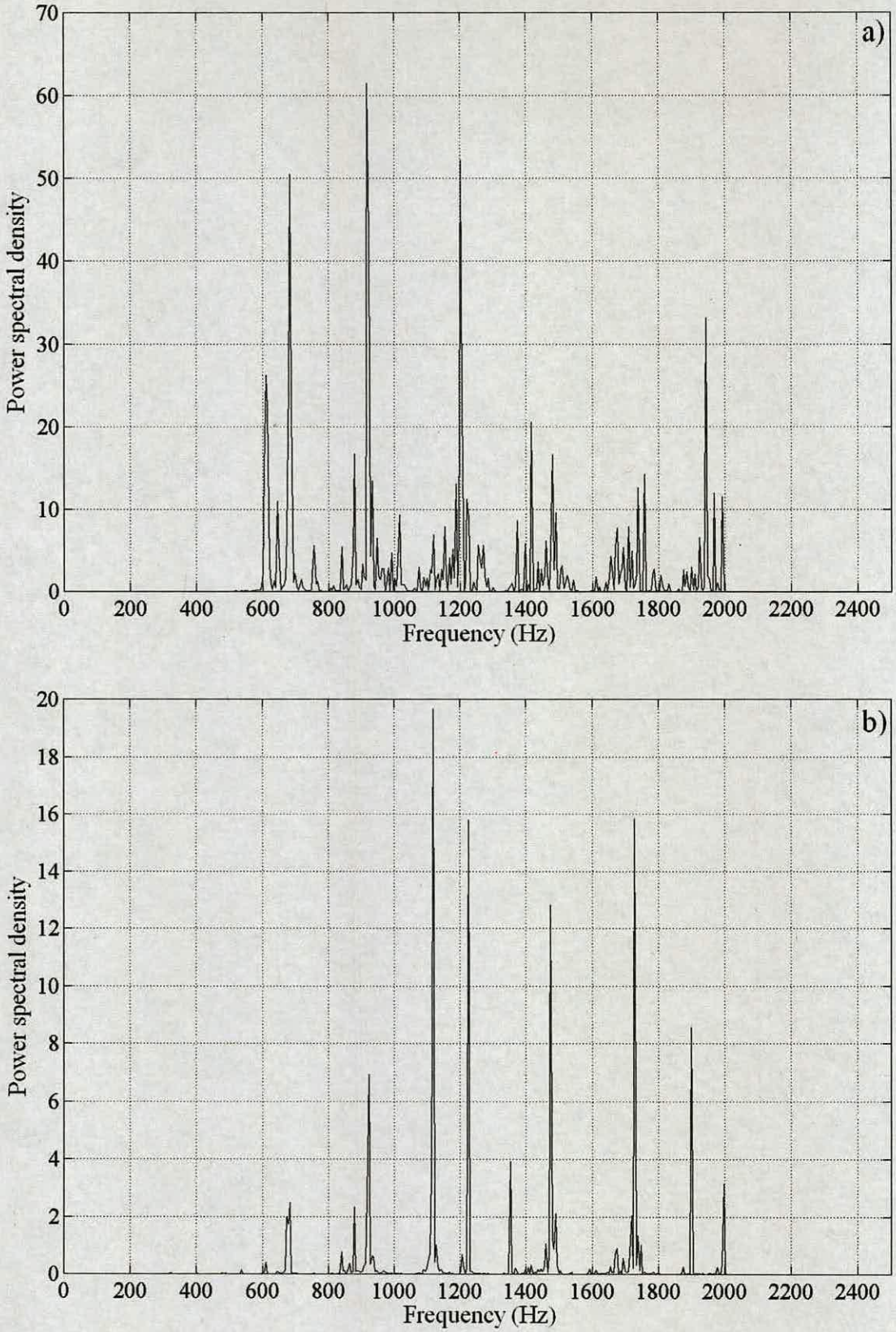

Figure 7.18: Frequency spectra of the silo dynamic response at ≈ 11.95 m (P6) in the a) radial and b) axial direction for a radial pulse load applied on hopper.

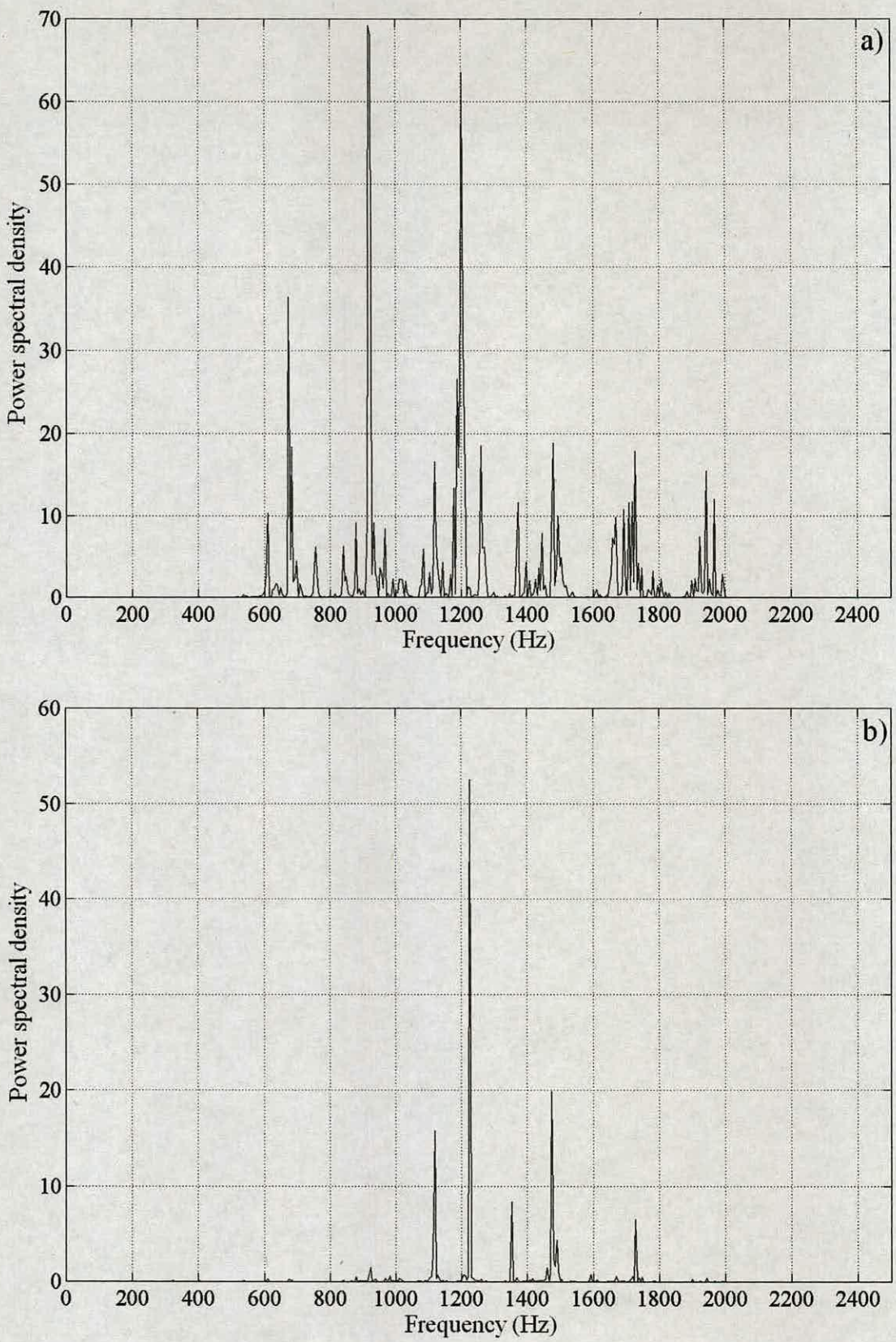

Figure 7.19: Frequency spectra of the silo dynamic response at ≈ 19.90 m (P10) in the a) radial and b) axial direction for a radial pulse load applied on hopper.

The results suggest that the axial pulse load on the silo hopper excites lower modes of the axisymmetric ASILO model, some of which are close to the honking fundamental frequency. On the other hand a radial pulse excites higher harmonics some of which are close to multiples of the fundamental honking frequency. This is also in line with the honking silo in Case4 (Fig. 3.26d) where the fundamental frequency is absent from the sound spectra (Fig. 3.27). The radial component in a steeper hopper (Case4) has higher influence on the normal pressure compared with those less steep hoppers (silo in Fig. 3.1). The results suggest that to excite the entire range of harmonics both radial and axial components are required. The two components will occur simultaneously due to the increment of normal pressure on the silo hopper. Clearly an exact agreement between the spectra of the acceleration measurements on the silo wall and the spectra of the FE axisymmetric model cannot be expected. The results in the numerical analysis are affected by the limitations in the numerical method and by the simplicity of the pulse load considerations, which is expected to increase in complexity in the real structure.

7.5 Conclusions

A numerical study of the transient dynamic response of a silo has been conducted in this Chapter. An axisymmetric FE model of the silo structure was used. Different pulse loads were applied to the silo barrel and hopper of the model. Fourier analyses of the acceleration response at different points along the silo height were conducted to obtain the frequency response due to the loads applied. The following conclusions can be drawn from the different pulse loads applied:

- *Axial pulse load along silo wall.* The axial spectra show that an axial pulse load applied along the silo wall will excite the axial natural frequencies of the silo structure. The height of the region where the axial pulse load is applied does not affect the frequency response of the structure. The frequency response due to an axial pulse load does not resemble that observed during honking.

- *Radial pulse load on silo wall.* A radial pulse load was applied at different heights on the silo wall. This kind of pulse load represents a sudden increase in the normal pressure at a plane of shock within the stored material. The radial spectra show sharp peaks near the "ring frequency" of the silo structure. This "ring frequency" is higher than the honking fundamental frequency of the structure, which is not seen in the spectra.

- *Pulse load on silo hopper.* An alternative pulse load on the silo hopper was applied simulating an increase in the normal pressure due to the occurrence of rupture surfaces in the transition zone of the silo structure. The normal pulse load applied on the silo hopper excited a range of frequencies which include those close to the honking fundamental frequency and its harmonics suggesting that the hopper excitation may be the source that leads to honking. The axial and radial components of the normal load on hopper seem to play different roles in the excitation mechanism. While the axial component seems to be enough to excite a frequency close to the fundamental honking frequency, the radial component is found to excite frequencies close to higher harmonics of the fundamental honking frequency. The results are consistent with the spectral analyses undertaken on the acceleration measurements of the instrumented honking silo in Chapter 3.

Chapter 8

Conclusions and recommendations

8.1 Conclusions

A summary by Chapter of the key conclusions from this study is as follows.

Chapter 2

- Honking is a loud annoying noise (> 100 dB) that emanates from silos during discharge. However, anecdotal evidence suggests that sometimes honking also occurs after a discharge period.

- Generally, honking is known to occur in tall cylindrical aluminium silos designed for mass flow and storing polymer granulates.

- Honking noise has been associated with vibrations of the silo wall and higher outflow rates.

Chapter 3

- Frequency spectra of acoustic and wall acceleration measurements of a honking silo show clear peaks at a fundamental frequency (333 Hz) and at

integer multiples of this fundamental frequency constituting a harmonic series.

- During honking the amplitudes of the radial wall acceleration were generally larger than acceleration amplitudes in the axial direction.

- The harmonic acceleration response of the wall during honking is independent of accelerometer position and fill level, indicating that the stored material does not participate in the honking response of the silo structure.

- Frequency spectra of the small oscillatory motions during non-honking periods also show a harmonic response (a fundamental frequency and integer multiples of the fundamental frequency), although there is no sound radiation. However, this harmonic response is not observed for periods where oscillatory motions are not apparent in the acceleration response in non-honking periods, indicating that a harmonic excitation is not present during the entire discharge process.

Chapter 4

- Analysis of a three dimensional cylindrical shell, with properties and boundary conditions resembling the instrumented honking silo, shows that the lowest natural frequencies are much lower than the frequencies responsible for honking.

- As the source of excitation is likely to be axisymmetric, axisymmetric vibration modes are of particular interest. Comparison of axisymmetric natural frequencies with the spectra of measured response indicates that the structure vibrates predominantly in axisymmetric modes.

Chapter 5

- The natural frequencies of the axisymmetric FE models constructed to investigate the influence of the fill drastically reduce once the mass and stiffness of the stored solid are considered in the analysis. The lower modes of the silo-fill system are associated with the vibration of the stored material and not to the silo structure. The system natural frequencies change with fill height.

- When only the stiffness of the stored material is considered (i.e. the mass of the stored solid ignored) in the silo-fill system the natural frequencies increase slightly in comparison to the empty silo. The fill height does not influence the free vibration characteristics.

- The frequencies associated with the hopper modes are diameter dependent. They are inversely proportional to the diameter. A hopper mode with a maximum modal displacement at the transition has a natural frequency close to the fundamental honking frequency for half hopper angles of 30° and 20°.

- The natural frequency and mode shape of the hopper mode with a maximum modal displacement at the transition is independent of shell height.

- The harmonic response observed in the acceleration spectra obtained from measurements appears to be associated with hopper mode, where the number of waves for higher hopper modes near integer multiples of the hopper mode frequency increases in steps of three.

Chapter 6

- Experimental studies show that PET pellets exhibit a slip-stick phenomenon when sheared against aluminium and steel plates. The magnitude of the shear stress fluctuations increases with the normal stress level, indicating that in a silo, these fluctuations would be larger towards the lower end where the

stresses are higher and the magnitude of fluctuations would reduce with decreasing fill level.

- From experimental studies previously reported, it was found that flow pulsations due to velocity discontinuities are sensitive to the stress in the stored solid at the transition. These flow pulsations also depend on the hopper angle, which needs to be close to the critical value for mass flow to generate these pulses.

Chapter 7

- Transient dynamic analysis of an axial pulse load applied along the silo wall shows that the frequencies excited are the axial natural frequencies of the silo structure. The frequency response due to this pulse load does not resemble that observed during honking.

- In a similar way, a radial pulse load was applied at different heights along the silo wall. These radial pulse loads excite frequencies close to the "ring frequency" of the silo structure. The honking fundamental frequency or its harmonics are not seen in the frequency response.

- The transient dynamic analysis of a pulse load applied normal to the hopper shows that it excites a range of frequencies which include those that are close to the honking fundamental frequencies and its harmonics.

Honking has been reported to occur in the form of short pulses. The occasional occurrence of honking after a discharge period also suggests that sudden pulse loads excite the silo structure and make it respond in some of its natural frequencies. These pulses (honks and smaller oscillatory motions) were observed in the wall acceleration measurements at a fairly regular period. The frequency response due to a pulse load applied normal to the silo hopper suggests that the hopper excitation may be the source that leads to honking. This indicates that, from the possible sources of excitation studied in this thesis, pulsating flow due to velocity discontinuities may be

the source responsible for honking and the observed periodic oscillatory motions. Pulsating flow is periodic and stress level dependent. This is supported by observations which show that honking occurs at high fill levels with high stress levels and stops when the fill level drops below a certain height. Available evidence also suggests that the hopper angle needs to be close to the critical value for mass flow in order to create pulses. This is the case for the instrumented honking silo in this study and other silos considered.

8.2 Recommendations

Stopping the impulse excitation of the hopper from exciting the cylindrical shell that is responsible for honking emission. This can be achieved by having a hopper that is structurally detached from the cylindrical section of the silo.

If pulsating flow due to velocity discontinuities near the transition is the cause of honking, then the following solutions could also be applied:

For existing silos it is possible to modify the hopper angle and/or the frictional behaviour between the hopper wall and the stored material to create a mass flow condition far away from the borderline limits to achieve mass flow (see Fig. 1.3). For example, a 20° half hopper angle will not eliminate the hopper mode. It would change the flow behaviour of the material in the instrumented silo of this study by bringing it to a flow condition well within the mass flow limits. The frictional behaviour can be modified by lining the hopper with a material whose wall friction angle with respect to the stored solid creates a flow condition well within the mass flow limits.

For future silo design it is recommended that borderline mass flow conditions should be avoided between the hopper angle and the hopper wall friction angle. To achieve this the design should be based on realistic wall friction tests. These tests should include variations that cause changes to frictional properties such as humidity and temperature. This can be achieved in well-controlled laboratory tests.

References

Akroyd, T.N.W. (1958) *Laboratory Testing in Soil Engineering*, Soil Mechanics Ltd London.

Arnold, R. N. and Warburton, G. B. (1949) "Flexural vibrations of the walls of thin cylindrical shells having freely supported ends" *Proceedings of the Royal Society of London, Series A, Mathematical and Physical Science*, Vol. 197, Issue 1049, 238-256.

Bishop R. E. D. and Johnson D. C. (1956) *Vibration analysis tables*, Cambridge University Press, Cambridge.

Bransby, P.L. and Blair-Fish, P.M. (1975) "Initial deformations during mass flow from a bunker: Observations and Idealizations" *Powder Technology*, **11**, 273-288.

Bransby, P.L., Blair-Fish, P.M. and Jame, R.G. (1973) "An investigation of the flow of granular materials" *Powder Technology*, **8**, 197-206.

Budny, T. J. (1979) "Stick-slip friction as a method of powder flow characterization" *Powder Technology*, **23**, 197-201.

Buick, J.M., Chavez-Sagarnaga, J., Zhong, Z., Ooi, Y., Pankaj, Campbell, D.M. and Greated, C.A. (2003) "Investigation of silo honking: slip-stick excitation and wall vibration" *16th ASCE Engineering Mechanics Conference*, Seattle, paper 625.

Buick, J.M., Chavez-Sagarnaga, J., Zhong, Z., Ooi, Y., Pankaj, Campbell, D.M. and Greated, C.A. (2005) "Investigation of silo honking: slip-stick excitation and wall vibration" *Journal of Engineering Mechanics ASCE*, **131**, 299-307.

Buick, J.M., Pankaj, Ooi, J.Y., Chavez-Sagarnaga, J., Pearce, A., Houghton, G. (2004) "Motion of granular particles on the wall of a model silo and the associated wall vibrations" *Journal of Physics D: Applied Physics*, **37**, 2751-2760.

Dean, P. (2003) Internal communication.

ENV 1991-4 (1995), Eurocode 1: Basis of design and actions on structures, Part 4: Actions in silos and tanks, CEN, Brussels.

Greenberg, M.D. (1998) *Advanced Engineering Mathematics*, Prentice-Hall, 2nd ed., New Jersey.

Gudehus, G. and Tejchman, J. (1992) "Silo music and silo quake" *Silos - Forschung und Praxis Tagung '92*, Karlsruhe, October, 1992, 103-110.

Hardow, B., Schulze, D. and Schwedes, J. (1998) "An experimental analysis of the 'silo quaking' phenomenon" *Proc.*, World Congress for Particle Technology, 11-19.

Harris, C.M. (Chief Editor) (1996) *Shock and vibration handbook*, McGraw-Hill, 4th ed., New York; London.

HKS (2002) "ABAQUS/Standard User's Manual", Rode Island, Version 6.3-1.

Hupkes, I.G. (2003) "Silophone – On the mistery of silo-honking" Master's Thesis, University of Twente, Holland.

IChE (1989) "*Standard shear testing technique for particulate solids using the Jenike shear cell*". Institute of Chemical Engineers/ European Federation of Chemical Engineering joint publication, Institute of Chemical Engineers , England.

Juarez-Badillo, E. y Rico-Rodriguez, A. (1996) *Mecanica de suelos, Tomo I, Fundamentos de la mecanica de suelos*, Limusa Noriega Editores, 3ª edicion, Mexico.

Junger, M.C. and Feit, D. (1986) "Sound, Structures, and Their Interaction" 2nd ed. (MIT, Cambridge, MA).

Kmita, J. (1985) "Silo as a system of self-induced vibration" *Journal of structural Engineering*, Vol. 3(1), 190-204.

Kraus, H. (1967) "Thin elastic shells", New York, John Wiley & Sons, Inc.

Leissa, A.W., (1973) "Vibration of shells" NASA SP-288, National Aeronautics and Space Administration, Washington, D.C.

Levison, B. and Munch-Andersen, J. (1994) "Shocks in coal silos" *Powder Handling and Processing*, **6** (4), 385-388.

Love, A.E.H. (1888) "The small free vibrations and deformation of a thin elastic shell" *Philosophical Transactions of the Royal Society of London. A*, Vol. 179, 491-546.

Masroor, S.A., Zachary, L.W. and Lohnes, R.A. (1987) "A test apparatus for determining elastic constants of bulk solids" *Proceedings of the 1987 SEM Spring Conference on Experimental Mechanics*, Houston, 553-558.

Math Works Inc. (1999) *Using MATLAB*, Massachusetts, Version 5.3.

Michalowski, R.L. (1984) " Flow of granular material through a plane hopper" *Powder Technology*, **39**, 29-40.

Michalowski, R.L. (1987) "Flow of granular media through a plane parallel/converging bunker" *Chemical Engineering Science*, Vol. 42(11), 2587-2596.

Muite, B.K., Quinn, S.F., Sundaresan, S. and Rao, K.K (2004) "Silo music and silo quake: granular flow-induced vibration" *Powder Tecnology*, **145**, 190-202.

Nasuno, S., Kudrolli, A., Bak, A. and Gollub, J.P. (1998) "Time-resolved studies of stick-slip friction in sheared granular layers", *Phys. Rev. E*, Vol. 58(2), 2161-2171.

Niedostatkiewicz, M. and Tejchman, J. (2003) "Experimental and theoretical studies on resonance dynamic effects during silo flow" *Powder Handling and Processing*, 15 (1), 36-42.

Ooi, J.Y., Zhong, Z. and Hardy, M.S.H. (1999) "Investigation of vibration and honking in DuPont silos" Confidential Technical Investigation Report, University of Edinburgh, 30 pp.

Perry, M.G., Rothwell, E. and Woodfin, W.T. (1976) "Model studies of mass-flow bunkers – II Velocity distributions in the discharge of solids from mass-flow bunkers" *Powder Technology*, **14**, 81-92.

Purutyan, H., Bengston, K.E. and Carson, J.W. (1994a) "Identifying and controlling silo vibration mechanisms: Part I" *Powder and Bulk Engineering*, November, 58-65.

Purutyan, H., Bengston, K.E. and Carson, J.W. (1994b) "Identifying and controlling silo vibration mechanisms: Part II" *Powder and Bulk Engineering*, December, 19-27.

Rao, S.S. (2004) *Mechanical Vibrations*, Pearson Prentice Hall, 4th Int. Ed., New Jersey.

Rayleigh, Lord (1888) "On the bending and vibration of thin elastic shells, especially of cylindrical form" *Proceedings of the Royal Society of London*, Vol. 45, 105-123.

Rayleigh, Lord (1945) *Theory of sound, Vol.1 & 2*, Dover Publications, 2nd ed. New York.

Roberts, A.W. (1993) "Mechanics of self excited dynamic loads in bins and silos" *Proc.* Int. Symp. Reliable Flow of Particulate Solids II, Oslo, 983-1004.

Roberts, A.W. and Wensrich, C.M. (2002) "Flow dynamics or 'quaking' in gravity discharge from silos" *Chemical Engineering Science*, **57**, 295-305.

Roberts, A.W. and Wiche, S.J. (1991) "Silo quaking – a pulsating load problem during discharge in bins and silos" *Proc.,* Bulk 2000 Conference, Institution of Mechanical Engineers, London, 7-12.

Rotter, J.M. (2001) *Guide for the economic design of circular metal silos*. Spon, London.

Sanad, A.M., Holst, J.M.F.G., Ooi, J.Y., Rotter, J.M., Masson, S., Martinez, J., Guines D. and Ragneau, E. (2000) "Comparison of direct shear test simulations from Britain and France" *Proc., Int. Conf. Powder and Bulk Solids Handling*, IMechE, London.

Schulze, D. (1998) "Silo Quaking" in *Silos – Fundamentals of theory, behaviour and design*, eds C.J. Brown and J. Nielsen, E & FN Spon, London, 171-182.

Scott, J.F.M (1988) "The free modes of propagation of an infinite fluid-loaded thin cylindrical shell", *Journal of Sound and Vibration*, Vol. 125(2), 241-280.

Sharma, C. B. (1979) "Vibration characteristics of thin circular cylinders" *Journal of Sound and Vibration*, Vol. 63(4), 581-592.

Sharma C. B. (1980) "An analytical vibration study of thin circular cylinders" *International conference on recent advances in structural dynamics*, Southampton, England, July 7-11, Vol. 1, 61-72.

Shinohara, K., Idemitsu, Y., Gotoh, K. and Tanaka, T. (1968) "Mechanism of gravity flow of particles from a hopper" Industrial and Engineering Chemistry Process Design and Development, Vol. 7(3), 378-383.

Soedel, W. (1980) "A new frequency formula for closed circular cylindrical shells for a large variety of boundary conditions" *Journal of Sound and Vibration*, Vol. 70(3), 309-317.

Tejchman, J. (1995) "Silo quake – experiments and a polar hypoplastic model" *European Symp: Storage and Flow of Particulate Solids (Janssen Centennial)*, March, Nurnberg, 151-162.

Tejchman, J. (1998) "Silo-quake – measurements, a numerical approach and a way for its suppression" *Thin-walled structures*, **31**, 137-158.

Tejchman, J. (1999) "Technical concept to prevent the silo honking" *Powder Technology*, **106**, 7-22.

Tejchman, J. and Gudehus, G. (1993) "Silo music and silo quake experiments and numerical Cosserat approach" *Powder Technology*, **76**, 201-202.

Thomson F. M. (1984) "Storage of particulate solids" *Handbook on Powder Science & Technology*, Chapter 9, Van Nostrand.

Zienkiewicz, O.C. and Taylor R.L. (1989) *The Finite Element Method, Vol. I, Basic formulation and linear problems*, McGraw Hill, 4th ed., London.

Appendix A

MATLAB codes

A.1 Acoustic and acceleration measurements analyses

This MATLAB code was used to analyse the acoustic and acceleration signals from the measurements conducted on the instrumented honking silo (Chapter 3).

```
clear;
%
%
% Data reading
%
%
fid=fopen('FILE NAME.dat');
a=fscanf(fid,'%f %f %f %f %f \n',[5 inf]);
fclose(fid);
time=a(1,:)*0.5;
mic=a(2,:)*122.0;
%axi=a(3,:)/0.000933;
%axi=-600+a(3,:)/0.000933;
axi=-500+a(3,:)/0.000933;
%tan=a(4,:)/0.000933;
%tan=-900+a(4,:)/0.000933;
tan=-900+a(4,:)/0.000933;
rad=-1*a(5,:)/0.000933;
%
%
% Figures for the entire discharge process
%
%
figure; plot(time,axi,'k',time,rad,'k',time,tan,'k'),grid on
%,a(1,:),mic,'k')
title('Acceleration measurements in a discharge period');
xlabel('Time (s)');
ylabel('Acceleration (m/s^2)');
```

```
figure; plot(time,mic,'k'),grid on
title('Sound pressure measurements in a discharge period');
xlabel('Time (s)');
ylabel('Pressure (Pa)');
figure; plot(time,axi,'g'),grid on
title('Axial acceleration measurements in a discharge period');
xlabel('Time (s)');
ylabel('Acceleration (m/s^2)');
figure; plot(time,rad,'r'),grid on
title('Radial acceleration measurements in a discharge period');
xlabel('Time (s)');
ylabel('Acceleration (m/s^2)');
figure; plot(time,tan,'b'),grid on
title('Circumferential acceleration measurements in a discharge
period');
xlabel('Time (s)');
ylabel('Acceleration (m/s^2)');
pause;
%
%
% Period of time to be anlysed
%
%
n=7500;
N=87500;
b(1,:)=a(1,n:n+N-1)*0.5;
b(2,:)=(a(2,n:n+N-1)/0.000933)*1.21*0.00008*343.0;
%b(3,:)=a(3,n:n+N-1)/0.000933;
%b(3,:)=-6000+a(3,n:n+N-1)/0.000933;
b(3,:)=-100+a(3,n:n+N-1)/0.000933;
%b(4,:)=a(4,n:n+N-1)/0.000933;
%b(4,:)=-11000+a(4,n:n+N-1)/0.000933;
b(4,:)=-150+a(4,n:n+N-1)/0.000933;
b(5,:)=a(5,n:n+N-1)/0.000933;
%
%
% Spectrograms
%
%
%specgram(b(3,:),256,12500);
%specgram(b(4,:),256,12500);
specgram(b(5,:),256,12500);
%
%
% Set of figures for the specific period of time
%
%
figure;
plot(b(1,:),b(3,:),'k',b(1,:),b(4,:),'k',b(1,:),b(5,:),'k'),grid on
title('Honk');
xlabel('Time (s)');
ylabel('Acceleration (m/s^2)');
figure; plot(b(1,:),b(2,:),'k'),grid on
title('Sound pressure');
xlabel('Time (s)');
ylabel('Pressure (Pa)');
pause;
figure; plot(b(1,:),b(3,:),'g'),grid on
title('Axial acceleration');
```

```
xlabel('Time (s)');
ylabel('Acceleration (m/s^2)');
pause;
figure; plot(b(1,:),b(4,:),'b'),grid on
title('Circumferential acceleration');
xlabel('Time (s)');
ylabel('Acceleration (m/s^2)');
pause;
figure; plot(b(1,:),b(5,:),'r'),grid on
title('Radial acceleration');
xlabel('Time (s)');
ylabel('Acceleration (m/s^2)');
pause;
%
%
% Fourier analyses
%
%
Bm=fft(b(2,:),N);
Ba=fft(b(3,:),N);
Bt=fft(b(4,:),N);
Br=fft(b(5,:),N);
% f = no. of samples per second *(0:N/2 -1) /N
f=(50000/4)*(0:((N/2)-1))/N;
PBBm=Bm.*conj(Bm)/N;
PBBa=Ba.*conj(Ba)/N;
PBBt=Bt.*conj(Bt)/N;
PBBr=Br.*conj(Br)/N;
%
%
% Frequency spectra figures
%
%
figure; plot(f,PBBm(1:N/2),'k'),grid on
title('Acoustic frequency spectrum');
xlabel('Frequency (Hz)');
ylabel('Power spectral density');
pause;
figure; plot(f,PBBa(1:N/2),'g'),grid on
title('Axial frequency spectrum');
xlabel('Frequency (Hz)');
ylabel('Power spectral density');
pause;
figure; plot(f,PBBt(1:N/2),'b'),grid on
title('Circumferential frequency spectrum');
xlabel('Frequency (Hz)');
ylabel('Power spectral density');
pause;
figure; plot(f,PBBr(1:N/2),'k'),grid on
title('Radial frequency spectrum');
xlabel('Frequency (Hz)');
ylabel('Power spectral density');
%
% Sound file
%
wavwrite(40*a(2,:),50000/4,16,'mp05r01.wav');
```

A.2 Gontkevich closed form solution

This MATLAB code was used to calculate the natural frequencies of finite shells with simple boundary conditions and validate the FE model in Chapter 4.

```
clear;
%
%
% Boundary conditions evaluated by this program
%
% Shear Diaphragm-Shear Diaphragm condition (1)
% Clamped-Shear Diaphragm condition (2)
% Free-Free condition (3)
%
%
% Definition of variables
%
% rho = Density
% E =   Young's modulus
% nu =  Poisson's ratio
% R =   Shell radius
% h =   Thickness
% L =   Length
%
%
% Boundary condition to be evaluated
%
bcond=1;
%
%
% Shear Diaphragm-Shear Diaphragm condition
%
if bcond==1;
rho=2800.0;
E=0.79e11;
nu=0.33;
R=1.5;
h=0.0053;
L=22.0;
%
%
% k value, see Equation 4.5
%
k=h^2/(12.*R^2);
%
%
% Programming for SD-SD condition, see Table 4.1
%
Delm(1)=1.0;
Delm(2)=1.0;
Delm(3)=1.0;
Delm(4)=1.0;
Delm(5)=1.0;
Epsm(1)=1.0*pi;
Epsm(2)=2.0*pi;
```

```
Epsm(3)=3.0*pi;
Epsm(4)=4.0*pi;
Epsm(5)=5.0*pi;

for m=6:1000;
    Delm(m)=1.0;
end
for m=6:1000;
    Epsm(m)=m*pi;
end
%
%
% See Equation 4.13 and Table 4.1
for m=1:1000;
    Mum(m)=Epsm(m)*R/L;
    Gamm(m)=-Delm(m);
end
%
%
% Axial half wave number "m" and circumferential wave number "n"
% This values vary according the modes to evaluate
%
for m=1:20;
   for n=0:0;
      if n==0
        AWLP=L/(m*R);
        KC(1)=1.0;
        %
        KC(2)=(-1.0)*(Mum(m)^2/Delm(m)+1.0+0.5*(1.0-
nu)*Delm(m)*Mum(m)^2+k*(2.0*(1.0-nu)*Delm(m)*Mum(m)^2+Mum(m)^4));
        %
        KC(3)=((Mum(m)^2)*(0.5*(1.0-
nu)*Delm(m)*Mum(m)^2+1.0)+0.5*(1.0-nu)*Delm(m)^2*Mum(m)^2-
nu^2*Gamm(m)^2*Mum(m)^2+k*((Mum(m)^2+0.5*(1.0-
nu)*Delm(m)^2*Mum(m)^2)*(Mum(m)^4)+(2.0*(1.0-
nu)*Delm(m)*Mum(m)^2)*(Mum(m)^2+Delm(m))))/Delm(m);
        %
        KC(4)=(-1.0)*((0.5*(1.0-nu)*Delm(m)*Mum(m)^4*(1.0-
Gamm(m)^2*nu^2)+k*((Mum(m)^2*(1.0-Gamm(m)^2*nu^2))*(2.0*(1.0-
nu)*Delm(m)*Mum(m)^2)+((Mum(m)^2)*(0.5*(1.0-
nu)*Delm(m)*Mum(m)^2))))/Delm(m));
        %
        OME=roots(KC);
        OME1=min(OME);
        OME2=sum(OME)-min(OME)-max(OME);
        OME3=max(OME);
        if L/(m*R)<=2.0
            OMEr=OME1;
            OMEa=OME3;
            OMEt=OME2;
         elseif 2.0<=L/(m*R)<=pi;
            OMEr=OME2;
            OMEa=OME3;
            OMEt=OME1;
         elseif L/(m*R)>=pi;
            OMEr=OME3;
            OMEa=OME2;
            OMEt=OME1;
         end
```

```
      else
        %KC(1)*OME^6-KC(2)*OME^4+KC(3)*OME^2-KC(4)=0
        KC(1)=1.0;
        %
        KC(2)=(-1.0)*(Mum(m)^2/Delm(m)+0.5*(3.0-
nu)*n^2+1.0+0.5*(1.0-nu)*Delm(m)*Mum(m)^2+k*(n^2+2.0*(1.0-
nu)*Delm(m)*Mum(m)^2+Mum(m)^4-
2.0*n^2*Mum(m)^2*Gamm(m)+n^4+2.0*n^2*Mum(m)^2*(1.0-
nu)*(Delm(m)+Gamm(m))));
        %
        KC(3)=((Mum(m)^2+0.5*(1.0-nu)*Delm(m)*n^2)*(n^2+0.5*(1.0-
nu)*Delm(m)*Mum(m)^2+1.0)+0.5*(1.0-nu)*Delm(m)^2*Mum(m)^2-
nu^2*Gamm(m)^2*Mum(m)^2-n^2*Mum(m)^2*((-
0.5*Delm(m)+nu*(Gamm(m)+0.5*Delm(m)))^2)+k*((Mum(m)^2+0.5*(3.0-
nu)*n^2*Delm(m)+0.5*(1.0-nu)*Delm(m)^2*Mum(m)^2)*(Mum(m)^4-
2.0*n^2*Mum(m)^2*Gamm(m)^2+n^4+2.0*n^2*Mum(m)^2*(1.0-
nu)*(Delm(m)+Gamm(m)))+(n^2+2.0*(1.0-
nu)*Delm(m)*Mum(m)^2)*(Mum(m)^2+0.5*(1.0-nu)*Delm(m)*n^2+Delm(m))-
2.0*n^2*Delm(m)*(n^2+Mum(m)^2*(2.0*(1.0-nu)*Delm(m)-
Gamm(m)*nu))))/Delm(m);
        %
        KC(4)=(-1.0)*((0.5*(1.0-nu)*Delm(m)*Mum(m)^4*(1.0-
Gamm(m)^2*nu^2)+k*((0.5*(1.0-nu)*Delm(m)*n^2+Mum(m)^2*(1.0-
Gamm(m)^2*nu^2))*(n^2+2.0*(1.0-
nu)*Delm(m)*Mum(m)^2)+((Mum(m)^2+0.5*(1.0-
nu)*Delm(m)*n^2)*(n^2+0.5*(1.0-nu)*Delm(m)*Mum(m)^2)-n^2*Mum(m)^2*(-
0.5*Delm(m)+nu*(Gamm(m)+0.5*Delm(m)))^2)*(Mum(m)^4-
2.0*n^2*Mum(m)^2*Gamm(m)+n^4+2.0*n^2*Mum(m)^2*(1.0-
nu)*(Delm(m)+Gamm(m)))-n^2*(Mum(m)^2*Delm(m)*Gamm(m)*(1.0-nu)*nu-
2.0*nu^2*Mum(m)^2*Gamm(m)^2+2.0*(Mum(m)^2+0.5*(1.0-
nu)*Delm(m)*n^2))*(n^2+Mum(m)^2*(2.0*Delm(m)*(1.0-nu)-
Gamm(m)*nu))))/Delm(m));
        %
        OME=roots(KC);
        OME1=min(OME);
        OME2=sum(OME)-min(OME)-max(OME);
        OME3=max(OME);
        A1(1,1)=-(Mum(m)^2)-((1.0-nu)/2.0)*n^2+OME1;
        A1(1,2)=((1.0+nu)/2.0)*Mum(m)*n;
        A1(2,1)=((1.0+nu)/2.0)*Mum(m)*n;
        A1(2,2)=(-(1.0-nu)/2.0)*Mum(m)^2-n^2+OME1;
        A2(1,1)=-(Mum(m)^2)-((1.0-nu)/2.0)*n^2+OME2;
        A2(1,2)=((1.0+nu)/2.0)*Mum(m)*n;
        A2(2,1)=((1.0+nu)/2.0)*Mum(m)*n;
        A2(2,2)=(-(1.0-nu)/2.0)*Mum(m)^2-n^2+OME2;
        A3(1,1)=-(Mum(m)^2)-((1.0-nu)/2.0)*n^2+OME3;
        A3(1,2)=((1.0+nu)/2.0)*Mum(m)*n;
        A3(2,1)=((1.0+nu)/2.0)*Mum(m)*n;
        A3(2,2)=(-(1.0-nu)/2.0)*Mum(m)^2-n^2+OME3;
        u(1,1)=-nu*Mum(m);
        u(2,1)=n;
        x1=abs(A1\u);
        x2=abs(A2\u);
        x3=abs(A3\u);
        if x1(1,1)<1.0 & x1(2,1)<1.0;
           OMEr=OME1;
        elseif x2(1,1)<1.0 & x2(2,1)<1.0;
           OMEr=OME2;
        elseif x3(1,1)<1.0 & x3(2,1)<1.0;
```

```
            OMEr=OME3;
         end
         if x1(1,1)>1.0 & x1(1,1)>x1(2,1);
            OMEa=OME1;
         elseif x2(1,1)>1.0 & x2(1,1)>x2(2,1);
            OMEa=OME2;
         elseif x3(1,1)>1.0 & x3(1,1)>x3(2,1);
           OMEa=OME3;
         end
         if OMEr==OME1 & OMEa==OME2;
            OMEt=OME3;
         elseif OMEr==OME1 & OMEa==OME3;
            OMEt=OME2;
         elseif OMEa==OME1 & OMEr==OME2;
            OMEt=OME3;
         elseif OMEa==OME1 & OMEr==OME3;
            OMEt=OME2;
         end
         if n==1
            OMEr=OME1;
            if L/(m*R)>2.0;
               OMEa=OME2;
               OMEt=OME3;
            else
               OMEa=OME3;
               OMEt=OME2;
            end
         end
       end
         freqr=sqrt((OMEr*E)/(rho*R^2*(1.0-nu^2)*4*pi^2));
         freqa=sqrt((OMEa*E)/(rho*R^2*(1.0-nu^2)*4*pi^2));
         freqt=sqrt((OMEt*E)/(rho*R^2*(1.0-nu^2)*4*pi^2));
         if n==0
            waveno=n;
            fr=freqr;
            fa=freqa;
            ft=freqt;
         else
            waveno=[waveno;n];
            fr=[fr;freqr];
            fa=[fa;freqa];
            ft=[ft;freqt];
         end
    end
%
%
% Plotting options for different graphs
%
plot(m,freqr,'Color','r','Marker','x'), grid on
title('Axisymmetric (n=0) frequencies');
xlabel('Axial waves (m)');
ylabel('Frequency (Hz)');
plot(m,freqa,'Color','g','Marker','o')
%plot(m,freqt,'Color','b','Marker','+')
%plot(AWLP,sqrt(OMEr),'Color','r','Marker','x'), grid on
%title('Axisymmetric (n=0) frequencies');
%xlabel('Axial waves (m)');
%ylabel('Frequency (Hz)');
%plot(AWLP,sqrt(OMEa),'Color','g','Marker','o')
```

```
%plot(AWLP,sqrt(OMEt),'Color','b','Marker','+')
%plot(waveno,fr,'k'), grid on
%title('Radial natural frequencies SD-SD');
%xlabel('Circumferential waves (n)');
%ylabel('Frequency (Hz)');
%plot(waveno,fa)
%title('Axial natural frequencies Shear Diaphragm - Shear
Diaphragm');
%xlabel('n Circumferential waves');
%ylabel('Frequency (Hz)');
%plot(waveno,ft)
%title('Circumferential natural frequencies Shear Diaphragm - Shear
Diaphragm');
%xlabel('n Circumferential waves');
%ylabel('Frequency (Hz)');
hold on
end
hold off
%
%
%
% Clamped-Shear Diaphragm condition
%
elseif bcond==2;
rho=2800.0;
E=0.79e11;
nu=0.33;
R=1.5;
h=0.0053;
L=16.25;
%
%
% k value, see Equation 4.5
%
k=h^2/(12.*R^2);
%
%
% Programming for Clamped-Shear Diaphragm condition, see Table 4.1
%
Delm(1)=0.723422;
Delm(2)=0.856926;
Delm(3)=0.902022;
Delm(4)=0.925136;
Delm(5)=0.939525;
Epsm(1)=3.92660;
Epsm(2)=7.06858;
Epsm(3)=10.2102;
Epsm(4)=13.3518;
Epsm(5)=16.4934;

for m=6:600;
    Delm(m)=1-(1.0/((m+0.25)*pi));
end
for m=6:600;
    Epsm(m)=((4.0*m+1)/4.0)*pi;
end
%
%
% See Equation 4.13 and Table 4.1
```

```
%
for m=1:600;
    Mum(m)=Epsm(m)*R/L;
    Gamm(m)=-Delm(m);
end
%
%
% Axial half wave number "m" and circumferential wave number "n"
% This values vary according the modes to evaluate
%
for m=1:100;
   for n=0:30;
      AWLP=L/(m*R);
      if n==0
        KC(1)=1.0;
        %
        KC(2)=(-1.0)*(Mum(m)^2/Delm(m)+1.0+0.5*(1.0-
nu)*Delm(m)*Mum(m)^2+k*(2.0*(1.0-nu)*Delm(m)*Mum(m)^2+Mum(m)^4));
        %
        KC(3)=((Mum(m)^2)*(0.5*(1.0-
nu)*Delm(m)*Mum(m)^2+1.0)+0.5*(1.0-nu)*Delm(m)^2*Mum(m)^2-
nu^2*Gamm(m)^2*Mum(m)^2+k*((Mum(m)^2+0.5*(1.0-
nu)*Delm(m)^2*Mum(m)^2)*(Mum(m)^4)+(2.0*(1.0-
nu)*Delm(m)*Mum(m)^2)*(Mum(m)^2+Delm(m))))/Delm(m);
        %
        KC(4)=(-1.0)*((0.5*(1.0-nu)*Delm(m)*Mum(m)^4*(1.0-
Gamm(m)^2*nu^2)+k*((Mum(m)^2*(1.0-Gamm(m)^2*nu^2))*(2.0*(1.0-
nu)*Delm(m)*Mum(m)^2)+((Mum(m)^2)*(0.5*(1.0-
nu)*Delm(m)*Mum(m)^2))))/Delm(m));
        %
        OME=roots(KC);
        OME1=min(OME);
        OME2=sum(OME)-min(OME)-max(OME);
        OME3=max(OME);
        if L/(m*R)<=2.0
            OMEr=OME1;
            OMEa=OME3;
            OMEt=OME2;
         elseif 2.0<=L/(m*R)<=pi;
            OMEr=OME2;
            OMEa=OME3;
            OMEt=OME1;
         elseif L/(m*R)>=pi;
            OMEr=OME3;
            OMEa=OME2;
            OMEt=OME1;
         end
      else
        KC(1)=1.0;
        %
        KC(2)=(-1.0)*(Mum(m)^2/Delm(m)+0.5*(3.0-
nu)*n^2+1.0+0.5*(1.0-nu)*Delm(m)*Mum(m)^2+k*(n^2+2.0*(1.0-
nu)*Delm(m)*Mum(m)^2+Mum(m)^4-
2.0*n^2*Mum(m)^2*Gamm(m)+n^4+2.0*n^2*Mum(m)^2*(1.0-
nu)*(Delm(m)+Gamm(m))));
        %
        KC(3)=((Mum(m)^2+0.5*(1.0-nu)*Delm(m)*n^2)*(n^2+0.5*(1.0-
nu)*Delm(m)*Mum(m)^2+1.0)+0.5*(1.0-nu)*Delm(m)^2*Mum(m)^2-
nu^2*Gamm(m)^2*Mum(m)^2-n^2*Mum(m)^2*((-
```

```
0.5*Delm(m)+nu*(Gamm(m)+0.5*Delm(m)))^2)+k*((Mum(m)^2+0.5*(3.0-
nu)*n^2*Delm(m)+0.5*(1.0-nu)*Delm(m)^2*Mum(m)^2)*(Mum(m)^4-
2.0*n^2*Mum(m)^2*Gamm(m)^2+n^4+2.0*n^2*Mum(m)^2*(1.0-
nu)*(Delm(m)+Gamm(m)))+(n^2+2.0*(1.0-
nu)*Delm(m)*Mum(m)^2)*(Mum(m)^2+0.5*(1.0-nu)*Delm(m)*n^2+Delm(m))-
2.0*n^2*Delm(m)*(n^2+Mum(m)^2*(2.0*(1.0-nu)*Delm(m)-
Gamm(m)*nu))))/Delm(m);
        %
        KC(4)=(-1.0)*((0.5*(1.0-nu)*Delm(m)*Mum(m)^4*(1.0-
Gamm(m)^2*nu^2)+k*((0.5*(1.0-nu)*Delm(m)*n^2+Mum(m)^2*(1.0-
Gamm(m)^2*nu^2))*(n^2+2.0*(1.0-
nu)*Delm(m)*Mum(m)^2)+((Mum(m)^2+0.5*(1.0-
nu)*Delm(m)*n^2)*(n^2+0.5*(1.0-nu)*Delm(m)*Mum(m)^2)-n^2*Mum(m)^2*(-
0.5*Delm(m)+nu*(Gamm(m)+0.5*Delm(m)))^2)*(Mum(m)^4-
2.0*n^2*Mum(m)^2*Gamm(m)+n^4+2.0*n^2*Mum(m)^2*(1.0-
nu)*(Delm(m)+Gamm(m)))-n^2*(Mum(m)^2*Delm(m)*Gamm(m)*(1.0-nu)*nu-
2.0*nu^2*Mum(m)^2*Gamm(m)^2+2.0*(Mum(m)^2+0.5*(1.0-
nu)*Delm(m)*n^2))*(n^2+Mum(m)^2*(2.0*Delm(m)*(1.0-nu)-
Gamm(m)*nu))))/Delm(m));
        %
        OME=roots(KC);
        OME1=min(OME);
        OME2=sum(OME)-min(OME)-max(OME);
        OME3=max(OME);
        OMEr=OME1;
        n=n;
        m=m;
        A1(1,1)=-(Mum(m)^2)-((1.0-nu)/2.0)*n^2+OME1;
        A1(1,2)=((1.0+nu)/2.0)*Mum(m)*n;
        A1(2,1)=((1.0+nu)/2.0)*Mum(m)*n;
        A1(2,2)=(-(1.0-nu)/2.0)*Mum(m)^2-n^2+OME1;
        A2(1,1)=-(Mum(m)^2)-((1.0-nu)/2.0)*n^2+OME2;
        A2(1,2)=((1.0+nu)/2.0)*Mum(m)*n;
        A2(2,1)=((1.0+nu)/2.0)*Mum(m)*n;
        A2(2,2)=(-(1.0-nu)/2.0)*Mum(m)^2-n^2+OME2;
        A3(1,1)=-(Mum(m)^2)-((1.0-nu)/2.0)*n^2+OME3;
        A3(1,2)=((1.0+nu)/2.0)*Mum(m)*n;
        A3(2,1)=((1.0+nu)/2.0)*Mum(m)*n;
        A3(2,2)=(-(1.0-nu)/2.0)*Mum(m)^2-n^2+OME3;
        u(1,1)=-nu*Mum(m);
        u(2,1)=n;
        x1=abs(A1\u);
        x2=abs(A2\u);
        x3=abs(A3\u);
        if x1(1,1)<1.0 & x1(2,1)<1.0;
           OMEr=OME1;
        elseif x2(1,1)<1.0 & x2(2,1)<1.0;
           OMEr=OME2;
        elseif x3(1,1)<1.0 & x3(2,1)<1.0;
           OMEr=OME3;
        end
        if x1(1,1)>1.0 & x1(1,1)>x1(2,1);
           OMEa=OME1;
        elseif x2(1,1)>1.0 & x2(1,1)>x2(2,1);
           OMEa=OME2;
        elseif x3(1,1)>1.0 & x3(1,1)>x3(2,1);
          OMEa=OME3;
        end
        if OMEr==OME1 & OMEa==OME2;
```

```
            OMEt=OME3;
         elseif OMEr==OME1 & OMEa==OME3;
            OMEt=OME2;
         elseif OMEa==OME1 & OMEr==OME2;
            OMEt=OME3;
         elseif OMEa==OME1 & OMEr==OME3;
            OMEt=OME2;
         end
         if n==1
            OMEr=OME1;
            if L/(m*R)>2.0;
               OMEa=OME2;
               OMEt=OME3;
            else
               OMEa=OME3;
               OMEt=OME2;
            end
         end
       end
         freqr=sqrt((OMEr*E)/(rho*R^2*(1.0-nu^2)*4*pi^2));
         freqa=sqrt((OMEa*E)/(rho*R^2*(1.0-nu^2)*4*pi^2));
         freqt=sqrt((OMEt*E)/(rho*R^2*(1.0-nu^2)*4*pi^2));
         if n==0
            waveno=n;
            fr=freqr;
            fa=freqa;
            ft=freqt;
            Or=OMEr;
            Oa=OMEa;
            Ot=OMEt;
         else
            waveno=[waveno;n];
            fr=[fr;freqr];
            fa=[fa;freqa];
            ft=[ft;freqt];
            Or=[Or;OMEr];
            Oa=[Oa;OMEa];
            Ot=[Ot;OMEt];
         end
    end
%
%
% Plotting options for different graphs
%
%plot(waveno,fr,'k'),grid on
%title('Radial natural frequencies Clamped-Shear Diaphragm');
%xlabel('Circumferential waves (n)');
%ylabel('Frequency (Hz)');
%plot(waveno,fa,'k')
%plot(waveno,ft,'k')
%plot(m,freqr,'Color','r','Marker','x'), grid on
%title('Beam (n=1) frequencies');
%xlabel('Axial waves (m)');
%ylabel('Frequency (Hz)');
%plot(m,freqa,'Color','g','Marker','o')
%plot(m,freqt,'Color','b','Marker','+')
plot(1/AWLP,sqrt(Or),'Color','k','Marker','x'), grid on
title('Variation of frequency parameters');
xlabel('Axial wavelenght parameter (L/mR)');
```

```
ylabel('Frequency parameter)');
%plot(AWLP,sqrt(OMEa),'Color','g','Marker','o')
%plot(AWLP,sqrt(OMEt),'Color','b','Marker','+')
%title('Axial natural frequencies Clamped - Shear Diaphragm');
%xlabel('n Circumferential waves');
%ylabel('Frequency (Hz)');
%title('Circumferential natural frequencies Clamped - Shear
Diaphragm');
%xlabel('n Circumferential waves');
%ylabel('Frequency (Hz)');
hold on
end
hold off
%
%
% Free-Free condition
%
elseif bcond==3;
rho=2800.0;
E=0.79e11;
nu=0.33;
R=1.5;
h=0.0053;
L=22.0;
%
%
% k value, see Equation 4.5
%
k=h^2/(12.*R^2);
%
%
% Programming for Free-Free condition, see Table 4.1
%
Delm(1)=2.211601;
Delm(2)=1.766169;
Delm(3)=1.545592;
Delm(4)=1.424419;
Delm(5)=1.347244;
Gamm(1)=-0.549879;
Gamm(2)=-0.744024;
Gamm(3)=-0.818051;
Gamm(4)=-0.858533;
Gamm(5)=-0.884249;
Epsm(1)=4.73004;
Epsm(2)=7.853204;
Epsm(3)=10.995608;
Epsm(4)=14.137166;
Epsm(5)=17.27876;

for m=6:80;
    Delm(m)=1+(6.0/((m+0.5)*pi));
end
for m=6:80;
    Gamm(m)=-1.0+(2.0/((m+0.5)*pi));
end
for m=6:80;
    Epsm(m)=((2.0*m+1.0)/2.0)*pi;
end
for m=1:80;
```

```
    Mum(m)=Epsm(m)*R/L;
end
%
%
% Axial half wave number "m" and circumferential wave number "n"
% This values vary according the modes to evaluate
%
for m=1:4;
   for n=0:7;
      if n==0
        KC(1)=1.0;
        %
        KC(2)=(-1.0)*(Mum(m)^2/Delm(m)+1.0+0.5*(1.0-
nu)*Delm(m)*Mum(m)^2+k*(2.0*(1.0-nu)*Delm(m)*Mum(m)^2+Mum(m)^4));
        %
        KC(3)=((Mum(m)^2)*(0.5*(1.0-
nu)*Delm(m)*Mum(m)^2+1.0)+0.5*(1.0-nu)*Delm(m)^2*Mum(m)^2-
nu^2*Gamm(m)^2*Mum(m)^2+k*((Mum(m)^2+0.5*(1.0-
nu)*Delm(m)^2*Mum(m)^2)*(Mum(m)^4)+(2.0*(1.0-
nu)*Delm(m)*Mum(m)^2)*(Mum(m)^2+Delm(m))))/Delm(m);
        %
        KC(4)=(-1.0)*((0.5*(1.0-nu)*Delm(m)*Mum(m)^4*(1.0-
Gamm(m)^2*nu^2)+k*((Mum(m)^2*(1.0-Gamm(m)^2*nu^2))*(2.0*(1.0-
nu)*Delm(m)*Mum(m)^2)+((Mum(m)^2)*(0.5*(1.0-
nu)*Delm(m)*Mum(m)^2))))/Delm(m));
        %
        OME=roots(KC);
        OME1=min(OME);
        OME2=sum(OME)-min(OME)-max(OME);
        OME3=max(OME);
         if L/(m*R)>2.3;
            OMEt=OME1;
            OMEa=OME2
            OMEr=OME3;
         else
            OMEr=OME1;
            OMEt=OME2
            OMEa=OME3;
         end
      else
        KC(1)=1.0;
        %
        KC(2)=(-1.0)*(Mum(m)^2/Delm(m)+0.5*(3.0-
nu)*n^2+1.0+0.5*(1.0-nu)*Delm(m)*Mum(m)^2+k*(n^2+2.0*(1.0-
nu)*Delm(m)*Mum(m)^2+Mum(m)^4-
2.0*n^2*Mum(m)^2*Gamm(m)+n^4+2.0*n^2*Mum(m)^2*(1.0-
nu)*(Delm(m)+Gamm(m))));
        %
        KC(3)=((Mum(m)^2+0.5*(1.0-nu)*Delm(m)*n^2)*(n^2+0.5*(1.0-
nu)*Delm(m)*Mum(m)^2+1.0)+0.5*(1.0-nu)*Delm(m)^2*Mum(m)^2-
nu^2*Gamm(m)^2*Mum(m)^2-n^2*Mum(m)^2*((-
0.5*Delm(m)+nu*(Gamm(m)+0.5*Delm(m)))^2)+k*((Mum(m)^2+0.5*(3.0-
nu)*n^2*Delm(m)+0.5*(1.0-nu)*Delm(m)^2*Mum(m)^2)*(Mum(m)^4-
2.0*n^2*Mum(m)^2*Gamm(m)^2+n^4+2.0*n^2*Mum(m)^2*(1.0-
nu)*(Delm(m)+Gamm(m)))+(n^2+2.0*(1.0-
nu)*Delm(m)*Mum(m)^2)*(Mum(m)^2+0.5*(1.0-nu)*Delm(m)*n^2+Delm(m))-
2.0*n^2*Delm(m)*(n^2+Mum(m)^2*(2.0*(1.0-nu)*Delm(m)-
Gamm(m)*nu))))/Delm(m);
        %
```

```
        KC(4)=(-1.0)*((0.5*(1.0-nu)*Delm(m)*Mum(m)^4*(1.0-
Gamm(m)^2*nu^2)+k*((0.5*(1.0-nu)*Delm(m)*n^2+Mum(m)^2*(1.0-
Gamm(m)^2*nu^2))*(n^2+2.0*(1.0-
nu)*Delm(m)*Mum(m)^2)+((Mum(m)^2+0.5*(1.0-
nu)*Delm(m)*n^2)*(n^2+0.5*(1.0-nu)*Delm(m)*Mum(m)^2)-n^2*Mum(m)^2*(-
0.5*Delm(m)+nu*(Gamm(m)+0.5*Delm(m)))^2)*(Mum(m)^4-
2.0*n^2*Mum(m)^2*Gamm(m)+n^4+2.0*n^2*Mum(m)^2*(1.0-
nu)*(Delm(m)+Gamm(m)))-n^2*(Mum(m)^2*Delm(m)*Gamm(m)*(1.0-nu)*nu-
2.0*nu^2*Mum(m)^2*Gamm(m)^2+2.0*(Mum(m)^2+0.5*(1.0-
nu)*Delm(m)*n^2))*(n^2+Mum(m)^2*(2.0*Delm(m)*(1.0-nu)-
Gamm(m)*nu))))/Delm(m));
        %
        OME=roots(KC);
        OME1=min(OME);
        OME2=sum(OME)-min(OME)-max(OME);
        OME3=max(OME);
        OMEr=OME1;
        A1(1,1)=-(Mum(m)^2)-((1.0-nu)/2.0)*n^2+OME1;
        A1(1,2)=((1.0+nu)/2.0)*Mum(m)*n;
        A1(2,1)=((1.0+nu)/2.0)*Mum(m)*n;
        A1(2,2)=(-(1.0-nu)/2.0)*Mum(m)^2-n^2+OME1;
        A2(1,1)=-(Mum(m)^2)-((1.0-nu)/2.0)*n^2+OME2;
        A2(1,2)=((1.0+nu)/2.0)*Mum(m)*n;
        A2(2,1)=((1.0+nu)/2.0)*Mum(m)*n;
        A2(2,2)=(-(1.0-nu)/2.0)*Mum(m)^2-n^2+OME2;
        A3(1,1)=-(Mum(m)^2)-((1.0-nu)/2.0)*n^2+OME3;
        A3(1,2)=((1.0+nu)/2.0)*Mum(m)*n;
        A3(2,1)=((1.0+nu)/2.0)*Mum(m)*n;
        A3(2,2)=(-(1.0-nu)/2.0)*Mum(m)^2-n^2+OME3;
        u(1,1)=-nu*Mum(m);
        u(2,1)=n;
        x1=abs(A1\u);
        x2=abs(A2\u);
        x3=abs(A3\u);
        if x1(1,1)<1.0 & x1(2,1)<1.0;
           OMEr=OME1;
        elseif x2(1,1)<1.0 & x2(2,1)<1.0;
           OMEr=OME2;
        elseif x3(1,1)<1.0 & x3(2,1)<1.0;
           OMEr=OME3;
        end
        if x1(1,1)>1.0 & x1(1,1)>x1(2,1);
           OMEa=OME1;
        elseif x2(1,1)>1.0 & x2(1,1)>x2(2,1);
           OMEa=OME2;
        elseif x3(1,1)>1.0 & x3(1,1)>x3(2,1);
          OMEa=OME3;
        end
        if OMEr==OME1 & OMEa==OME2;
           OMEt=OME3;
        elseif OMEr==OME1 & OMEa==OME3;
           OMEt=OME2;
        elseif OMEa==OME1 & OMEr==OME2;
           OMEt=OME3;
        elseif OMEa==OME1 & OMEr==OME3;
           OMEt=OME2;
        end
        if n==1
           OMEr=OME1;
```

```
            if L/(m*R)>2.0;
               OMEa=OME2;
               OMEt=OME3;
            else
               OMEa=OME3;
               OMEt=OME2;
            end
         end
      end
         freqr=sqrt((OMEr*E)/(rho*R^2*(1.0-nu^2)*4*pi^2));
         freqa=sqrt((OMEa*E)/(rho*R^2*(1.0-nu^2)*4*pi^2));
         freqt=sqrt((OMEt*E)/(rho*R^2*(1.0-nu^2)*4*pi^2));
         if n==0
            waveno=n;
            fr=freqr;
            fa=freqa;
            ft=freqt;
         else
            waveno=[waveno;n];
            fr=[fr;freqr];
            fa=[fa;freqa];
            ft=[ft;freqt];
         end
   end
%
%
% Plotting options for different graphs
%
plot(waveno,fr,'k'),grid on
%plot(waveno,frray,'g');
%plot(waveno,frlov,'r');
title('Radial natural frequencies Free-Free');
xlabel('Circumferential waves (n)');
ylabel('Frequency (Hz)');
%plot(waveno,fa)
%title('Axial natural frequencies Free-Free');
%xlabel('n Circumferential waves');
%ylabel('Frequency (Hz)');
%plot(waveno,ft)
%title('Circumferential natural frequencies Free-Free');
%xlabel('n Circumferential waves');
%ylabel('Frequency (Hz)');
hold on
end
hold off
end
```

A.3 Donnell-Mushtari theory

This MATLAB code was used to calculate the natural frequencies of finite shells with SD-SD boundary conditions and validate the FE model in Chapter 4.

```
clear;
%
bcond=1;
%
%
%Shear Diaphragm-Shear Diaphragm condition
%
if bcond==1;
rho=2800.0;
E=0.79e11;
nu=0.33;
R=1.5;
h=0.0053;
L=22.0;
%
%
% k value, see Equation 4.5
%
k=(h^2)/(12.0*R^2);
%
%
% Programming for SD-SD condition
%
Lamm(1)=(1.0*pi*R)/L;
Lamm(2)=(2.0*pi*R)/L;
Lamm(3)=(3.0*pi*R)/L;
Lamm(4)=(4.0*pi*R)/L;
Lamm(5)=(5.0*pi*R)/L;

for m=6:10000;
    Lamm(m)=(m*pi*R)/L;
end
%
%
% Axial half wave number "m" and circumferential wave number "n"
% This values vary according the modes to evaluate
%
for m=1:4;
   for n=0:7;
        if n==0
        OMEr=0.5*(1.0-nu)*Lamm(m)^2;
        else
        AXWLPA=L/(m*R);
        %KC(1)*OME^6-KC(2)*OME^4+KC(3)*OME^2-KC(4)=0
        KC(1)=1.0;
        %
        KC(2)=(-1.0)*(1.0+(1/2)*(3.0-
nu)*(n^2+Lamm(m)^2)+k*(n^2+Lamm(m)^2)^2);
        %
        KC(3)=((1/2)*(1.0-nu)*((3.0-
2.0*nu)*Lamm(m)^2+n^2+(n^2+Lamm(m)^2)^2+((3.0-nu)/(1.0-
nu))*k*(n^2+Lamm(m)^2)^3));
        %
        KC(4)=(-1.0)*((1/2)*(1.0-nu)*((1.0-
nu^2)*Lamm(m)^4+k*(n^2+Lamm(m)^2)^4));
        %
        OME=roots(KC);
        OMEr=min(OME);
        OME1=sqrt(OMEr);
```

```
        A1(1,1)=-(Lamm(m)^2)-((1.0-nu)/2.0)*n^2+OMEr;
        A1(1,2)=((1.0+nu)/2.0)*Lamm(m)*n;
        A1(2,1)=((1.0+nu)/2.0)*Lamm(m)*n;
        A1(2,2)=(-(1.0-nu)/2.0)*Lamm(m)^2-n^2+OMEr;
        u(1,1)=-nu*Lamm(m);
        u(2,1)=n;
        A1I=inv(A1);
        x1=abs(A1\u);
        UW=x1(1,1);
        VW=x1(2,1);
        freqr=sqrt((OMEr*E)/(rho*R^2*(1.0-nu^2)*4.0*pi^2));
        waveno=[waveno;n];
        fr=[fr;freqr];
    end
  end
plot(waveno,fr,'k'), grid on
title('Radial natural frequencies');
xlabel('Circumferential waves (n)');
ylabel('Frequency (Hz)');
%plot(waveno,fa)
%plot(waveno,ft)
hold on
end
hold off
end
```

A.4 Fourier analyses of the transient dynamic response of the silo

This MATLAB code was used to conduct Fourier analyses of the transient dynamic response of the silo structure in Chapter 7.

```
clear;
%
%
% Data reading
%
fid=fopen('FILE NAME.dat');
a=fscanf(fid,'%g %g',[2 inf]);
a = a';
fclose(fid);
displ=a(:,2);
%
%
% Acceleration plot
%
figure; plot(a(:,1),displ,'k'),grid on
title('Radial acceleration');
xlabel('Time(s)');
ylabel('Acceleration (m/s^2)');
pause;
```

```
%
%
% Points analysed
%
N = 1024;
y = a(:,2);
Y = fft(y,N);
Pyy = Y.* conj(Y) / N;
f = 5000*(0:N/2)/N;
%
%
% Frequency spectrum
%
figure; plot(f,Pyy(1:(N/2)+1)),grid on
title('Radial frequency analysis');
xlabel('Frequency (Hz)');
ylabel('Power spectral density');
```

Appendix B

ABAQUS input files

B.1 Input files for the FE models analysed

This appendix contains all the input files in ABAQUS (HKS, 2002) analysed in this study. Only the input files for the Clamped-SD boundary conditions are included, however, the rest of the boundary conditions can be achieved by modifying the boundary section in the input file.

B.1.1 3D Shell - Clamped-SD boundary conditions

```
*HEADING
 FREE VIBRATION ANALYSIS, LANCZOS EIGENSOLVER
 3D SHELL MODEL (1/2 SHELL), CLAMPED-SD CONDITION
*NODE
1,  1.0607,1.4,-1.0607
2,  1.0948,1.4,-1.0254
96, -1.0254,1.4,1.0948
97, -1.0607,1.4,1.0607
389, 1.0607,2.45,-1.0607
390, 1.0948,2.45,-1.0254
484, -1.0254,2.45,1.0948
485, -1.0607,2.45,1.0607
583, 1.0607,2.9,-1.0607
584, 1.0948,2.9,-1.0254
678, -1.0254,2.9,1.0948
679, -1.0607,2.9,1.0607
8537, 1.0607,23.4,-1.0607
8538, 1.0948,23.4,-1.0254
8632, -1.0254,23.4,1.0948
8633, -1.0607,23.4,1.0607
*NGEN,LINE=C,NSET=BOTT
2,96,1, ,0.,1.4,0.,0.,-1.,0.
```

```
*NGEN,LINE=C,NSET=CONE
390,484,1, ,0.,2.45,0.,0.,-1.,0.
*NGEN,LINE=C,NSET=MIDC
584,678,1, ,0.,2.90,0.,0.,-1.,0.
*NGEN,LINE=C,NSET=TOP
8538,8632,1, ,0.,23.40,0.,0.,-1.,0.
*NGEN,NSET=BND1
1,389,97
389,583,97
583,8537,97
*NFILL,NSET=BODY
BOTT,CONE,4,97
*NFILL,NSET=BODY
CONE,MIDC,2,97
*NFILL,NSET=BODY
MIDC,TOP,82,97
*NGEN,NSET=BND2
97,485,97
485,679,97
679,8633,97
*NSET,NSET=ALL
BND1,BND2,BODY
*****
*ELEMENT,TYPE=S4R5
 1, 1,2,99,98
*ELEMENT,TYPE=S4R5
 385, 389,390,487,486
*ELEMENT,TYPE=S4R5
 577, 583,584,681,680
*ELEMENT,TYPE=S4R5
 2401,2426,2427,2524,2523
*ELEMENT,TYPE=S4R5
 4417,4463,4464,4561,4560
*ELGEN,ELSET=BO
 1, 96,1,1,25,97,96
*ELGEN,ELSET=MI
 2401, 96,1,1,21,97,96
*ELGEN,ELSET=TO
 4417, 96,1,1,42,97,96
*SHELL SECTION,ELSET=BO,MATERIAL=MAT
 .0053
*SHELL SECTION,ELSET=MI,MATERIAL=MAT
 .0053
*SHELL SECTION,ELSET=TO,MATERIAL=MAT
 .0053
*TRANSFORM,TYPE=C,NSET=ALL
 0.,0.,0., 0.,1.,0.
*MATERIAL,NAME=MAT
*ELASTIC
 0.79E11,.33
*DENSITY
 2800.0
*RESTART, WRITE
*PREPRINT, ECHO=YES, MODEL=YES, HISTORY=YES
*STEP
*FREQUENCY, EIGENSOLVER=LANCZOS
 80,0.0
*BOUNDARY
```

```
BND1,YSYMM
BND2,YSYMM
TOP,1
TOP,2
TOP,4
TOP,6
BOTT,1
BOTT,2
BOTT,4
BOTT,5
BOTT,6
BOTT,3
BOT1,3
*EL PRINT,FREQUENCY=0
*NODE PRINT,FREQUENCY=0
*MODAL FILE
*END STEP
```

B.1.2 3D Silo – Clamped-SD boundary condition

```
*HEADING
 FREE VIBRATION ANALYSIS, LANCZOS EIGENSOLVER
 3D SILO MODEL (1/2 SILO), CLAMPED-SD CONDITION
*NODE
1,  1.0607,1.4,-1.0607
2,  1.0948,1.4,-1.0254
96, -1.0254,1.4,1.0948
97, -1.0607,1.4,1.0607
389, 1.0607,2.45,-1.0607
390, 1.0948,2.45,-1.0254
484, -1.0254,2.45,1.0948
485, -1.0607,2.45,1.0607
583, 1.0607,2.9,-1.0607
584, 1.0948,2.9,-1.0254
678, -1.0254,2.9,1.0948
679, -1.0607,2.9,1.0607
8537, 1.0607,23.4,-1.0607
8538, 1.0948,23.4,-1.0254
8632, -1.0254,23.4,1.0948
8633, -1.0607,23.4,1.0607
8634, 0.08839,0.,-0.08839
8635, 0.09123,0.,-0.08545
8729, -0.08545,0.,0.09123
8730, -0.08839,0.,0.08839
9507, 0.96343,2.205,-0.96343
9508, 0.99444,2.205,-0.93139
9602, -0.93139,2.205,0.99444
9603, -0.96343,2.205,0.96343
9604, 0.90913,23.514286,-0.90913
9605, 0.93839,23.514286,-0.8789
9699, -0.8789,23.514286,0.93839
9700, -0.90913,23.514286,0.90913
10089,0.15153,24.085714,-0.15153
10090,0.1564,24.085714,-0.14649
10184,-0.14649,24.085714,0.1564
10185,-0.15153,24.085714,0.15153
10865,0.00707,24.19467,-0.00707
```

```
10866,0.00730,24.19467,-0.00684
10960,-0.00684,24.19467,0.00730
10961,-0.00707,24.19467,0.00707
10962,0.,24.2,0.
*NGEN,LINE=C,NSET=BOTT
2,96,1, ,0.,1.4,0.,0.,-1.,0.
*NGEN,LINE=C,NSET=CONE
390,484,1, ,0.,2.45,0.,0.,-1.,0.
*NGEN,LINE=C,NSET=MIDCY
584,678,1, ,0.,2.90,0.,0.,-1.,0.
*NGEN,LINE=C,NSET=TOP
8538,8632,1, ,0.,23.4,0.,0.,-1.,0.
*NGEN,LINE=C,NSET=OUTL
8635,8729,1, ,0.,0.,0.,0.,-1.,0.
*NGEN,LINE=C,NSET=MIDCO
9508,9602,1, ,0.,2.205,0.,0.,-1.,0.
*NGEN,LINE=C,NSET=RBOT
9605,9699,1, ,0.,23.514286,0.,0.,-1.0,0.
*NGEN,LINE=C,NSET=RTOP1
10090,10184,1, ,0.,24.085714,0.,0.,-1.0,0.
*NGEN,LINE=C,NSET=RTOP2
10866,10960,1, ,0.,24.19467,0.,0.,-1.0,0.
*NGEN,NSET=BND1
1,389,97
389,583,97
583,8537,97
*NFILL,NSET=BODY
BOTT,CONE,4,97
*NFILL,NSET=BODY
CONE,MIDCY,2,97
*NFILL,NSET=BODY
MIDCY,TOP,82,97
*NFILL,NSET=COBO
OUTL,MIDCO,9,97
*NFILL,NSET=ROBO1
RBOT,RTOP1,5,97
*NFILL,NSET=ROBO2
RTOP1,RTOP2,8,97
*NGEN,NSET=BND2
97,485,97
485,679,97
679,8633,97
*NGEN,NSET=BND1C
8634,9507,97
*NGEN,NSET=BND2C
8730,9603,97
*NGEN,NSET=BND1R
9604,10089,97
*NGEN,NSET=BND2R
9700,10185,97
*NGEN,NSET=BND3R
10089,10865,97
*NGEN,NSET=BND4R
10185,10961,97
*NSET,NSET=ALL
BND1,BND2,BODY,COBO,ROBO1,ROBO2,BND1C,BND2C,
BND1R,BND2R,BND3R,BND4R
*NSET,NSET=BOT1
```

```
1,97
*NSET,NSET=TOPR1
10865,10961
*****
*ELEMENT,TYPE=S4R5
 1, 2,1,98,99
*ELEMENT,TYPE=S4R5
 385, 390,389,486,487
*ELEMENT,TYPE=S4R5
 577, 584,583,680,681
*ELEMENT,TYPE=S4R5
 2401,2427,2426,2523,2524
*ELEMENT,TYPE=S4R5
 4417,4464,4463,4560,4561
*ELEMENT,TYPE=S4R5
 8449,8635,8634,8731,8732
*ELEMENT,TYPE=S4R5
 9313,9508,9507,389,390
*ELEMENT,TYPE=S4R5
 9409,8538,8537,9604,9605
*ELEMENT,TYPE=S4R5
 9505,9605,9604,9701,9702
*ELGEN,ELSET=BO
 1, 96,1,1,25,97,96
*ELGEN,ELSET=MI
 2401, 96,1,1,21,97,96
*ELGEN,ELSET=TO
 4417, 96,1,1,42,97,96
*ELGEN,ELSET=CO1
 8449, 96,1,1,9,97,96
*ELGEN,ELSET=CO2
 9313, 96,1,1,1,9118,96
*ELGEN,ELSET=RO1
 9409, 96,1,1,1,1067,96
*ELGEN,ELSET=RO2
 9505, 96,1,1,13,97,96
*SHELL SECTION,ELSET=BO,MATERIAL=MAT
 .0062
*SHELL SECTION,ELSET=MI,MATERIAL=MAT
 .0053
*SHELL SECTION,ELSET=TO,MATERIAL=MAT
 .0040
*SHELL SECTION,ELSET=CO1,MATERIAL=MAT
 .0040
*SHELL SECTION,ELSET=CO2,MATERIAL=MAT
 .0040
*SHELL SECTION,ELSET=RO1,MATERIAL=MAT
 .0040
*SHELL SECTION,ELSET=RO2,MATERIAL=MAT
 .0040
*TRANSFORM,TYPE=C,NSET=ALL
 0.,0.,0., 0.,1.0,0.
*MATERIAL,NAME=MAT
*ELASTIC
 0.79E11,.33
*DENSITY
 2800.0
*RESTART, WRITE
```

```
*PREPRINT, ECHO=YES, MODEL=YES, HISTORY=YES
*STEP
*FREQUENCY,EIGENSOLVER=LANCZOS
 20,0.0
*BOUNDARY
 BND1,YSYMM
 BND2,YSYMM
 BND1C,YSYMM
 BND2C,YSYMM
 BND1R,YSYMM
 BND2R,YSYMM
 BND3R,YSYMM
 BND4R,YSYMM
 BOTT,1
 BOTT,2
 BOTT,4
 BOTT,5
 BOTT,6
 BOTT,3
 BOT1,3
*EL PRINT,FREQUENCY=0
*NODE PRINT,FREQUENCY=0
*MODAL FILE
*END STEP
```

B.1.3 Axisymmetric Shell - Clamped-SD boundary conditions

```
*HEADING
 FREE VIBRATION ANALYSIS, LANCZOS EIGENSOLVER
 AXISYMMETRIC SHELL, CLAMPED-SD CONDITION
*NODE
**1,   0.125,0.0
236, 1.5,2.45
670, 1.5,7.65
1108,1.5,12.9
1983,1.5,23.4
**2125,0.0,24.2
2126,1.5,1.4
2213,1.5,2.43807
**NGEN,NSET=HOPPER
**1,236,1
*NGEN,NSET=SHELL
236,670,1
*NGEN,NSET=SHELL
670,1108,1
*NGEN,NSET=SHELL
1108,1983,1
**NGEN,NSET=ROOF
**1983,2125,1
*NGEN,NSET=SKIRT
2126,2213,1
*NSET,NSET=ALL
SHELL,SKIRT
**ROOF,HOPPER,SKIRT
*****
**ELEMENT,TYPE=SAX1
** 1, 1,2
```

```
*ELEMENT,TYPE=SAX1
 236,236,237
*ELEMENT,TYPE=SAX1
 670,670,671
*ELEMENT,TYPE=SAX1
 1108,1108,1109
**ELEMENT,TYPE=SAX1
** 1983,1983,1984
*ELEMENT,TYPE=SAX1
 2125,2126,2127
*ELEMENT,TYPE=SAX1
 2212,2213,236
**ELGEN,ELSET=HOP
** 1, 1,1,1,235,1,1
*ELGEN,ELSET=SH6
 236, 1,1,1,434,1,1
*ELGEN,ELSET=SH5
 670, 1,1,1,438,1,1
*ELGEN,ELSET=SH4
 1108, 1,1,1,875,1,1
**ELGEN,ELSET=ROO
** 1983, 1,1,1,142,1,1
*ELGEN,ELSET=SKI
 2125, 1,1,1,87,1,1
*ELSET,ELSET=SKI
 2212
*SHELL SECTION,ELSET=SH6,MATERIAL=MAT
 .0053
*SHELL SECTION,ELSET=SH5,MATERIAL=MAT
 .0053
*SHELL SECTION,ELSET=SH4,MATERIAL=MAT
 .0053
**SHELL SECTION,ELSET=ROO,MATERIAL=MAT
** .0040
**SHELL SECTION,ELSET=HOP,MATERIAL=MAT
** .0040
*SHELL SECTION,ELSET=SKI,MATERIAL=MAT
 .0053
*MATERIAL,NAME=MAT
*ELASTIC
 0.79E11,.33
*DENSITY
 2800.0
*RESTART, WRITE
**PREPRINT, ECHO=YES, MODEL=YES, HISTORY=YES
*STEP
*FREQUENCY,EIGENSOLVER=LANCZOS
 20,0.0
*BOUNDARY
 1983,1
** 1983,2
** 1983,6
 2126,1
 2126,2
 2126,6
*EL PRINT,FREQUENCY=0
*NODE PRINT,FREQUENCY=0
*MODAL FILE
```

*END STEP

B.1.4 Axisymmetric Silo - Clamped-SD boundary conditions

```
*HEADING
 FREE VIBRATION, LANCZOS EIGENSOLVER
 AXISYMMETRIC SILO, CLAMPED-SD CONDITION
 0 TO  Hz
*NODE
1,  0.125,0.0
236, 1.5,2.45
670, 1.5,7.65
1108,1.5,12.9
1983,1.5,23.4
2125,0.0,24.2
2126,1.5,1.4
2213,1.5,2.43807
*NGEN,NSET=HOPPER
1,236,1
*NGEN,NSET=SHELL
236,670,1
*NGEN,NSET=SHELL
670,1108,1
*NGEN,NSET=SHELL
1108,1983,1
*NGEN,NSET=ROOF
1983,2125,1
*NGEN,NSET=SKIRT
2126,2213,1
*NSET,NSET=ALL
SHELL,SKIRT,HOPPER,ROOF
*****
*ELEMENT,TYPE=SAX1
 1, 1,2
*ELEMENT,TYPE=SAX1
 236,236,237
*ELEMENT,TYPE=SAX1
 670,670,671
*ELEMENT,TYPE=SAX1
 1108,1108,1109
*ELEMENT,TYPE=SAX1
 1983,1983,1984
*ELEMENT,TYPE=SAX1
 2125,2126,2127
*ELEMENT,TYPE=SAX1
 2212,2213,236
*ELGEN,ELSET=HOP
 1, 1,1,1,235,1,1
*ELGEN,ELSET=SH6
 236, 1,1,1,434,1,1
*ELGEN,ELSET=SH5
 670, 1,1,1,438,1,1
*ELGEN,ELSET=SH4
 1108, 1,1,1,875,1,1
*ELGEN,ELSET=ROO
 1983, 1,1,1,142,1,1
*ELGEN,ELSET=SKI
```

```
2125, 1,1,1,87,1,1
*ELSET,ELSET=SKI
 2212
*SHELL SECTION,ELSET=SH6,MATERIAL=MAT
 .0062
*SHELL SECTION,ELSET=SH5,MATERIAL=MAT
 .0053
*SHELL SECTION,ELSET=SH4,MATERIAL=MAT
 .0040
*SHELL SECTION,ELSET=ROO,MATERIAL=MAT
 .0040
*SHELL SECTION,ELSET=HOP,MATERIAL=MAT
 .0040
*SHELL SECTION,ELSET=SKI,MATERIAL=MAT
 .0062
*MATERIAL,NAME=MAT
*ELASTIC
 0.79E11,.33
*DENSITY
 2800.0
*RESTART, WRITE
**PREPRINT, ECHO=YES, MODEL=YES, HISTORY=YES
*STEP
*FREQUENCY,EIGENSOLVER=LANCZOS
 20,0.0
*BOUNDARY
** 1983,1
** 1983,2
** 1983,6
 2126,1
 2126,2
 2126,6
*EL PRINT,FREQUENCY=0
*NODE PRINT,FREQUENCY=0
*MODAL FILE
*END STEP
```

B.1.5 Axisymmetric Silo - Silo-Fill System (90% Capacity)

```
*HEADING
 FREE VIBRATION, LANCZOS EIGENSOLVER
 AXISYMMETRIC SILO - SILO-FILL SYSTEM (90%)
 CLAMPED-SD CONDITION
*NODE
1,  0.125,0.0
236, 1.5,2.45
670, 1.5,7.65
1108,1.5,12.9
1983,1.5,23.4
2125,0.0,24.2
2126,1.5,1.4
2213,1.5,2.43807
10001,0.0,0.0
10236,0.0,2.45
10670,0.0,7.65
11108,0.0,12.9
11816,0.0,21.396
```

```
82641,0.123,0.0
82876,1.4969,2.45
83310,1.4969,7.65
83748,1.4969,12.9
84456,1.4969,21.396
*NGEN,NSET=HOPPER
1,236,1
*NGEN,NSET=SHELL
236,670,1
*NGEN,NSET=SHELL
670,1108,1
*NGEN,NSET=SHELL
1108,1983,1
*NGEN,NSET=ROOF
1983,2125,1
*NGEN,NSET=SKIRT
2126,2213,1
*NSET,NSET=ALLSH
SHELL,ROOF,HOPPER,SKIRT
*NGEN,NSET=SOLSIMA
10001,10236,1
*NGEN,NSET=SOLSIMB
10236,10670,1
*NGEN,NSET=SOLSIMC
10670,11108,1
*NGEN,NSET=SOLSIMD
11108,11816,1
*NGEN,NSET=SOLSHA
82641,82876,1
*NGEN,NSET=SOLSHB
82876,83310,1
*NGEN,NSET=SOLSHC
83310,83748,1
*NGEN,NSET=SOLSHD
83748,84456,1
*NFILL,NSET=SOLIDA
SOLSIMA,SOLSHA,40,1816
*NFILL,NSET=SOLIDB
SOLSIMB,SOLSHB,40,1816
*NFILL,NSET=SOLIDC
SOLSIMC,SOLSHC,40,1816
*NFILL,NSET=SOLIDD
SOLSIMD,SOLSHD,40,1816
*NSET,NSET=SOLSH
SOLSHA,SOLSHB,SOLSHC,SOLSHD
*NSET,NSET=SHSOL,GENERATE
1,1816,1
*MPC
PIN,SOLSH,SHSOL
*****
*ELEMENT,TYPE=SAX1
 1, 1,2
*ELEMENT,TYPE=SAX1
 236,236,237
*ELEMENT,TYPE=SAX1
 670,670,671
*ELEMENT,TYPE=SAX1
 1108,1108,1109
```

```
*ELEMENT,TYPE=SAX1
 1983,1983,1984
*ELEMENT,TYPE=SAX1
 2125,2126,2127
*ELEMENT,TYPE=SAX1
 2212,2213,236
*ELEMENT,TYPE=CAX4
 10001,10001,11817,11818,10002
*ELGEN,ELSET=HOP
 1, 1,1,1,235,1,1
*ELGEN,ELSET=SH6
 236, 1,1,1,434,1,1
*ELGEN,ELSET=SH5
 670, 1,1,1,438,1,1
*ELGEN,ELSET=SH4
 1108, 1,1,1,875,1,1
*ELGEN,ELSET=ROO
 1983, 1,1,1,142,1,1
*ELGEN,ELSET=SKI
 2125, 1,1,1,87,1,1
*ELSET,ELSET=SKI
 2212
*ELGEN,ELSET=SOL
 10001,40,1816,1,1815,1,40
*SHELL SECTION,ELSET=SH6,MATERIAL=SHMAT
 .0062
*SHELL SECTION,ELSET=SH5,MATERIAL=SHMAT
 .0053
*SHELL SECTION,ELSET=SH4,MATERIAL=SHMAT
 .0040
*SHELL SECTION,ELSET=ROO,MATERIAL=SHMAT
 .0040
*SHELL SECTION,ELSET=HOP,MATERIAL=SHMAT
 .0040
*SHELL SECTION,ELSET=SKI,MATERIAL=SHMAT
 .0062
*SOLID SECTION,ELSET=SOL,MATERIAL=SOLMAT
*MATERIAL,NAME=SHMAT
*ELASTIC
 0.79E11,.33
*DENSITY
 2800.0
*MATERIAL,NAME=SOLMAT
*ELASTIC
 0.695E7,.25
*DENSITY
 890.0
*RESTART, WRITE
*PREPRINT, ECHO=YES, MODEL=YES, HISTORY=YES
*STEP
*FREQUENCY,EIGENSOLVER=LANCZOS
 25,0.0
*BOUNDARY
 2126,1
 2126,2
 2126,6
*EL PRINT,FREQUENCY=0
*NODE PRINT,FREQUENCY=0
```

```
*MODAL FILE
*END STEP
```

B.1.6 Axisymmetric Silo - Transient Modal Dynamic Analysis

```
*HEADING
 TRANSIENT MODAL DYNAMIC ANALYSIS, LANCZOS EIGENSOLVER
 AXISYMMETRIC SILO, CLAMPED-SD CONDITION
*NODE
1,   0.125,0.0
1406, 1.5,2.45
4006, 1.5,7.65
6631, 1.5,12.9
11881,1.5,23.4
12731,0.0,24.2
12732,1.5,1.4
13256,1.5,2.448
*NGEN,NSET=HOPPER
1,1406,1
*NGEN,NSET=SHELL
1406,4006,1
*NGEN,NSET=SHELL
4006,6631,1
*NGEN,NSET=SHELL
6631,11881,1
*NGEN,NSET=ROOF
11881,12731,1
*NGEN,NSET=SKIRT
12732,13256,1
*NSET,NSET=ALL
SHELL,ROOF,HOPPER,SKIRT
*****
*ELEMENT,TYPE=SAX1
 1, 1,2
*ELEMENT,TYPE=SAX1
 1406,1406,1407
*ELEMENT,TYPE=SAX1
 4006,4006,4007
*ELEMENT,TYPE=SAX1
 6631,6631,6632
*ELEMENT,TYPE=SAX1
 11881,11881,11882
*ELEMENT,TYPE=SAX1
 12731,12732,12733
*ELEMENT,TYPE=SAX1
 13255,13256,1406
*ELGEN,ELSET=HOP
 1, 1,1,1,1405,1,1
*ELGEN,ELSET=SH6
 1406, 1,1,1,2600,1,1
*ELGEN,ELSET=SH5
 4006, 1,1,1,2625,1,1
*ELGEN,ELSET=SH4
 6631, 1,1,1,5250,1,1
*ELGEN,ELSET=ROO
 11881, 1,1,1,850,1,1
*ELGEN,ELSET=SKI
```

```
 12731, 1,1,1,524,1,1
*ELSET,ELSET=SKI
 13255
*SHELL SECTION,ELSET=SH6,MATERIAL=MAT
 .0062
*SHELL SECTION,ELSET=SH5,MATERIAL=MAT
 .0053
*SHELL SECTION,ELSET=SH4,MATERIAL=MAT
 .0040
*SHELL SECTION,ELSET=ROO,MATERIAL=MAT
 .0040
*SHELL SECTION,ELSET=HOP,MATERIAL=MAT
 .0040
*SHELL SECTION,ELSET=SKI,MATERIAL=MAT
 .0062
*MATERIAL,NAME=MAT
*ELASTIC
 0.79E11,.33
*DENSITY
 2800.0
*AMPLITUDE, NAME=DILOAD
0.0,0.0,0.0,1.0,4.0E-3,1.0,4.0E-3,0.0
*RESTART, WRITE
**PREPRINT, ECHO=YES, MODEL=YES, HISTORY=YES
*STEP
*FREQUENCY,EIGENSOLVER=LANCZOS
 350,0.0,2000.0
*BOUNDARY
 12732,1
 12732,2
 12732,6
*EL PRINT,FREQUENCY=0
*NODE PRINT,FREQUENCY=0
*MODAL FILE
*END STEP
*STEP,INC=1100
*MODAL DYNAMIC
 2.0E-4,0.2048
*CLOAD, AMPLITUDE=DILOAD
 HOPPER,2,-0.5
 HOPPER,1,0.866
*OUTPUT,FIELD
*NODE OUTPUT
 U
 V
 A
*NODE PRINT,GLOBAL=NO
 RF
*END STEP
```

Appendix C

Pressures on silo wall

C.1 Pressures on silo wall

A spreadsheet was developed to evaluate and plot normal and frictional pressure distribution on the wall of a silo structure. The spreadsheet is included in this Appendix.

SILO STRUCTURES

Title .- ***Symmetrical loading (Shell 22 m. at 90% of capacity)***

Reference Codes

(1) ENV 1991-4 (1995) **Eurocode 1: Basis of design and actions on structures**
Part 4: Actions in silos and tanks

I) Silo data

1.- Barrel

Reliability Class =	3		
Solid height Hb =	19.00		m
Silo height =	22.00		m
Silo iameter D =	3.00		m
Slope of the roof =	28.07	°	
Material description.-	Aluminium		
Category of wall surface .-			D1
Filling eccentricity	0.00		m
Discharge eccentricity	0.00		m
Max. eccentricity	0.00		m

II) Solid data

1.- Type of bulk solid .- PET pellets

2.- Physical properties of solid

γl =	7.6		kN/m³	Lower bulk weight
γu =	8.7		kN/m³	Upper bulk weight
φr =	0.00	°		Angle of repose
φil =	0.00	°		Lower effective angle of internal friction
φiu =	0.00	°		Upper effective angle of internal friction
Kl =	0.33			Lower lateral pressure ratio
Ku =	0.33			Upper lateral pressure ratio
φwl =	14.00	°		Lower wall friction angle
φwu =	14.00	°		Upper wall friction angle

III) Load Magnifier "C"

Filling

Ch =	1.00
Cw =	1.00

Discharge

Ch =	1.35
Cw =	1.10

IV) Values of properties to be used for different wall loading assessments

Load Case	μ	K	φi
Max. Normal Pressure	Lower	Upper	Lower
Max. Frictional Traction	Upper	Upper	Lower

V) Loads Calculations

1.- Wall friction coefficient

μl =	Tan(φwl) =	0.249	
μu =	Tan(φwu) =	0.249	

2.- Silo capacity (Rating the silo)

hcon =	Tan(φr)(R) =	0.00	m
Vsilo =	(Pi)(R²)(h+hcon/3) =	134.30	m³
Cap r =	(Vsilo)(γl) =	1014.53	kN

3.- Silo capacity (For load determination)

Cap l =	(Vsilo)(γu) =	1172.60	kN

4.- Equivalent surface

Vcon =	(Pi)(R²)(hcon)/3 =	0.00	m³
ho =	(Vcon)/(Pi)(R²) =	0.000	m
hc =	h + ho =	19.00	m

5.- Wall pressure at infinite depth (Normal pressure case)

Pho =	(γu)(R)/(μl)(2) =	26.26	kN/m²

6.- Wall pressure at infinite depth (Frictional traction case)

Pho =	(γu)(R)/(μu)(2) =	26.26	kN/m²

7.- Vertical stress in solid at infinite depth

Pvo =	(γu)(R)/(Ku)(μu)(2) =	79.11	kN/m²

8.- Janssen reference depth

zo =	(R)/(Ku)(μl)(2) =	9.06	m	(Normal pressure)
zo =	(R)/(Ku)(μu)(2) =	9.06	m	(Frictional traction)

11.- Wall pressure calculations

a) Normal pressure acting on the wall (Normal Pressure case)

Filling

Phf = (pho)(1-e^(-z/zo))

Discharge

Phe = (pho)(1-e^(-z/zo))

b) Normal pressure coexistent with maximum vertical force on the wall (Frictional traction case)

Filling

Phf = (pho)(1-e^(-z/zo))

Pwf = (μ)(Phf)

Discharge

Phe = (pho)(1-e^(-z/zo))

Pwe = (μ)(Phe)

12.- Pressures acting on the wall (kN/m²)

	Normal Pressure and Frictional Traction Case			
z (m)	Filling Phf	Filling Pwf	Discharge Phe	Discharge Pwe
0.00	0.00	0.00	0.00	0.00
0.26	0.75	0.19	1.01	0.21
0.53	1.48	0.37	2.00	0.41
0.79	2.19	0.55	2.95	0.60
1.05	2.87	0.72	3.88	0.79
1.28	3.45	0.86	4.65	0.95
1.50	4.01	1.00	5.41	1.10
1.75	4.61	1.15	6.23	1.27
2.00	5.20	1.30	7.02	1.43
2.25	5.78	1.44	7.80	1.58
2.50	6.33	1.58	8.55	1.74
2.75	6.88	1.71	9.28	1.89
3.00	7.40	1.85	9.99	2.03
3.25	7.92	1.97	10.69	2.17
3.50	8.42	2.10	11.36	2.31
3.75	8.90	2.22	12.02	2.44
4.00	9.37	2.34	12.65	2.57
4.25	9.83	2.45	13.28	2.70
4.50	10.28	2.56	13.88	2.82
4.75	10.72	2.67	14.47	2.94
5.00	11.14	2.78	15.04	3.05
5.25	11.55	2.88	15.59	3.17
5.50	11.95	2.98	16.13	3.28
5.75	12.34	3.08	16.66	3.38
6.00	12.72	3.17	17.17	3.49
6.25	13.09	3.26	17.67	3.59
6.50	13.45	3.35	18.15	3.69
6.75	13.80	3.44	18.62	3.78
7.00	14.13	3.52	19.08	3.88
7.25	14.46	3.61	19.53	3.97
7.50	14.79	3.69	19.96	4.06
7.75	15.10	3.76	20.38	4.14
8.00	15.40	3.84	20.79	4.22
8.25	15.70	3.91	21.19	4.31
8.50	15.99	3.99	21.58	4.38
8.75	16.26	4.06	21.96	4.46
9.00	16.54	4.12	22.32	4.54
9.25	16.80	4.19	22.68	4.61
9.50	17.06	4.25	23.03	4.68
9.75	17.31	4.32	23.37	4.75
10.00	17.55	4.38	23.70	4.81
10.25	17.79	4.44	24.02	4.88
10.50	18.02	4.49	24.33	4.94
10.75	18.25	4.55	24.63	5.00
11.00	18.46	4.60	24.93	5.06
11.25	18.68	4.66	25.21	5.12
11.50	18.88	4.71	25.49	5.18
11.75	19.08	4.76	25.76	5.23

12.00	19.28	4.81	26.03	5.29
12.25	19.47	4.85	26.28	5.34
12.50	19.65	4.90	26.53	5.39
12.75	19.83	4.95	26.78	5.44
13.00	20.01	4.99	27.01	5.49
13.25	20.18	5.03	27.24	5.53
13.50	20.34	5.07	27.46	5.58
13.75	20.51	5.11	27.68	5.62
14.00	20.66	5.15	27.89	5.67
14.25	20.81	5.19	28.10	5.71
14.50	20.96	5.23	28.30	5.75
14.75	21.11	5.26	28.49	5.79
15.00	21.25	5.30	28.68	5.83
15.25	21.38	5.33	28.87	5.86
15.50	21.52	5.36	29.05	5.90
15.75	21.65	5.40	29.22	5.94
16.00	21.77	5.43	29.39	5.97
16.25	21.89	5.46	29.56	6.00
16.50	22.01	5.49	29.72	6.04
16.75	22.13	5.52	29.87	6.07
17.00	22.24	5.55	30.03	6.10
17.25	22.35	5.57	30.17	6.13
17.50	22.46	5.60	30.32	6.16
17.75	22.56	5.63	30.46	6.19
18.00	22.66	5.65	30.59	6.22
18.25	22.76	5.67	30.73	6.24
18.50	22.85	5.70	30.85	6.27
18.75	22.95	5.72	30.98	6.29
19.00	23.04	5.74	31.10	6.32

Fig. C1: Normal Pressures on silo wall

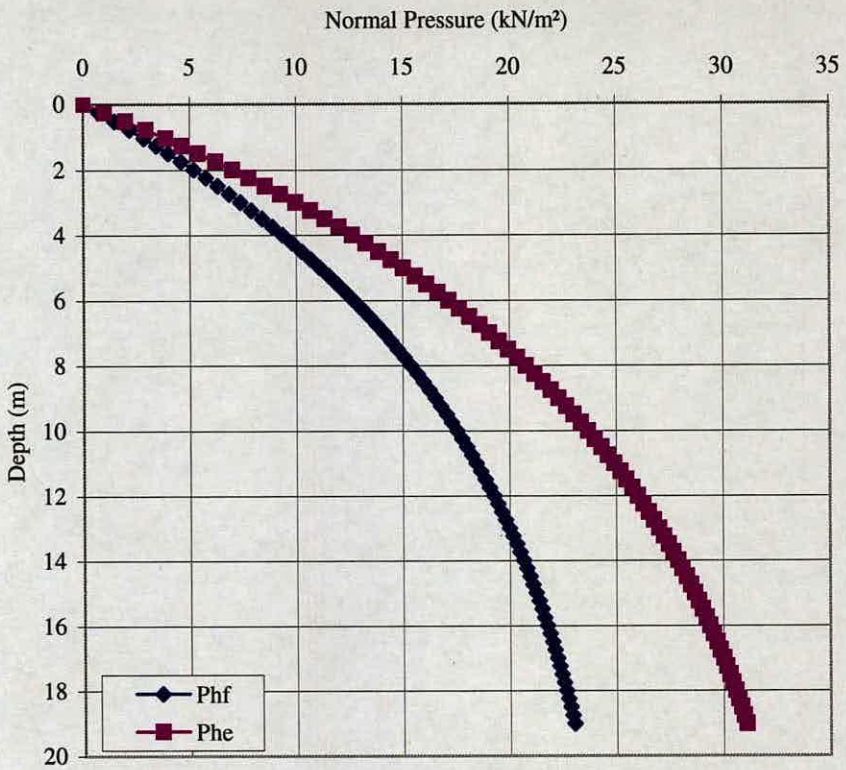

Fig. C2: Frictional Traction on silo wall

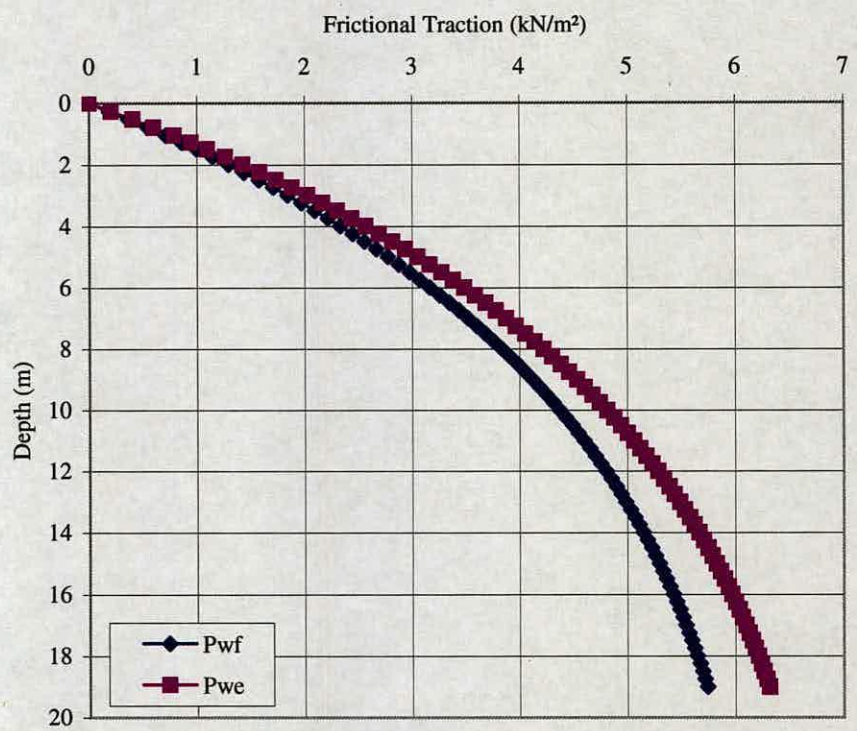

Appendix D

Dynamic displacement of consolidated mass

D.1 Dynamic displacement calculation

A spreadsheet was developed to evaluate the dynamic displacement of consolidated mass. This parameter is used in Section 6.3.1 and Appendix E.

Calculation of dynamic displacement from Fig. 5 data (Buick et al., 2004)

$\Delta t =$ 0.12

Time (s)	Velocity (mm/s)	Displacement (mm)	Dynamic displacement (mm)
tn	*V*	*Δt*V*	Σ of displacements
0.12	-0.005777	0.000693	
0.24	-7.911781	0.949414	
0.36	-4.396477	0.527577	1.957074
0.48	-4.000694	0.480083	
0.60	0.004947	0.000594	
0.72	0.009715	0.001166	
0.84	-4.357127	0.522855	
0.96	-4.462371	0.535485	1.574921
1.08	-4.304847	0.516582	
1.20	-0.000081	0.000010	
1.32	-0.000057	0.000007	
1.44	-2.627255	0.315271	
1.56	-5.838687	0.700642	1.564296
1.68	-4.569854	0.548382	
1.80	-0.001123	0.000135	
1.92	0.000236	0.000028	
2.04	-4.188223	0.502587	
2.16	-6.457404	0.774888	1.277475
2.28	0.001267	0.000152	
2.40	-0.106654	0.012799	
2.52	-0.140740	0.016889	
2.64	-0.002036	0.000244	
2.76	-7.205874	0.864705	
2.88	-5.645125	0.677415	1.682366
3.00	-0.863366	0.103604	
3.12	-0.305354	0.036642	
3.24	-0.001097	0.000132	
3.36	-3.254257	0.390511	
3.48	-4.644168	0.557300	
3.60	-4.083713	0.490046	1.934238
3.72	-3.962405	0.475489	
3.84	-0.174104	0.020893	
3.96	-0.002671	0.000320	
4.08	-0.002125	0.000255	
4.20	-3.685427	0.442251	
4.32	-4.029782	0.483574	1.155498
4.44	-1.913938	0.229673	
4.56	-0.003319	0.000398	
4.68	0.000918	0.000110	
4.80	-2.141365	0.256964	
4.92	-5.918228	0.710187	
5.04	-5.230494	0.627659	1.989573
5.16	-3.289689	0.394763	
5.28	0.002576	0.000309	
5.40	0.002694	0.000323	
5.52	-3.629579	0.435550	
5.64	-4.923679	0.590841	1.482551
5.76	-3.801337	0.456160	

5.88	0.001746	0.000210	
6.00	-4.364613	0.523754	
6.12	-4.640087	0.556810	1.438751
6.24	-2.984894	0.358187	
6.36	0.000742	0.000089	
6.48	-0.301100	0.036132	
6.60	-3.762651	0.451518	
6.72	-4.514860	0.541783	1.461090
6.84	-3.089629	0.370755	
6.96	-0.507512	0.060901	
7.08	0.000276	0.000033	
7.20	-4.123394	0.494807	
7.32	-4.535509	0.544261	
7.44	-4.518502	0.542220	1.873955
7.56	-2.438887	0.292666	
7.68	0.002039	0.000245	
7.80	0.002657	0.000319	
7.92	-7.922229	0.950667	
8.04	-7.361246	0.883350	3.210588
8.16	-7.565640	0.907877	
8.28	-3.905788	0.468695	
8.40	-0.034722	0.004167	
8.52	0.000099	0.000012	
8.64	-8.125330	0.975040	
8.76	-4.423803	0.530856	
8.88	-5.156887	0.618826	2.684248
9.00	-3.827512	0.459301	
9.12	-0.835203	0.100224	
9.24	-0.000596	0.000072	
9.36	-0.002342	0.000281	
9.48	-0.001012	0.000121	
9.60	-6.748402	0.809808	
9.72	-4.996308	0.599557	
9.84	-3.259839	0.391181	2.279531
9.96	-3.991539	0.478985	
10.08	0.001552	0.000186	
10.20	-0.105457	0.012655	
10.32	-4.409550	0.529146	
10.44	-5.000049	0.600006	1.351156
10.56	-1.744580	0.209350	
10.68	0.001685	0.000202	
10.80	-0.000243	0.000029	
10.92	-4.789573	0.574749	
11.04	-4.221463	0.506576	
11.16	-0.484010	0.058081	1.481495
11.28	-2.850745	0.342089	
11.40	-0.003483	0.000418	
11.52	-3.223231	0.386788	
11.64	-4.672474	0.560697	1.241930
11.76	-2.453710	0.294445	
11.88	0.000297	0.000036	
12.00	-4.593041	0.551165	
12.12	-8.286333	0.994360	1.818366
12.24	-2.273675	0.272841	

12.36	-0.003652	0.000438	
12.48	-0.002266	0.000272	
12.60	-4.172400	0.500688	
12.72	-5.093448	0.611214	1.595009
12.84	-4.025897	0.483108	
12.96	0.000319	0.000038	
	Average dynamic displacement (mm)		1.752706

Appendix E

Plane of shock – dynamic model

E.1 Dynamic model

A spreadsheet was developed to evaluate the maximum increment in the average vertical pressure and the pulse period based on the dynamic model of the plane of shock assumptions. The maximum flow rate for mass flow is also included in the spreadsheet.

Calculations for the plane of shock dynamic model

Silo geometry

D =	3.00	m	D	Diameter
R =	1.50	m	R	Radius
L =	22.00	m	H	Barrel height (including skirt)
sk =	1.00	m	sk	Skirt
Hb =	21.00	m	Hb	Barrel height
Ol =	0.25	m	Ol	Outlet diameter

Material properties and parameters to calculate the maximum rate for mass flow (Rotter, 2001)

SC%=	90		SC%	Approx silo capacity (%)
E =	6950000	N/m²	E	Young's modulus
ν =	0.25		ν	Poisson's ratio
ρmin =	770	kg/m³	ρmin	Minimum density
ρmax =	890	kg/m³	ρmax	Maximum density
μ =	0.226		μ	Wall friction coefficient
K =	0.332		K	Lateral pressure ratio
dp =	0.004	m	dp	Mean particle diameter
ks =	2.4		ks	Particle shape constant
				1.6 For nearly spherical particles
				2.4 For nearly angular particles

φi = ArcSin(1-(K/1.1)) φi Internal friction angle
φi = 44.28 °

βo = 45°-(φi/2)
βo = 22.86 ° βo Angle to calculate Gf
If βo < 30°, then β = 30°

Gf = 0.75(1-0.08*Cosβ)/((Sinβ)^(1/2))
Gf = 0.9872 Gf Parameter

Parameters to calculate the maximum increment in the
average vertical pressure (Roberts, 1993; Roberts and Wensrich, 2002)

kd =	1		kd	Dynamic load factor
m =	1		m	Parameter due to silo geometry
				0 For rectangular silo
				1 For circular silo

Re =D/(2(1+m))
Re = 0.75 m Re Effective radius

Hs =Tanφi*R
Hs = 1.46 m Hs Actual surcharge head

hs =Hs/(m+2)
hs = 0.49 m hs Effective surcharge head
Hsh = 3.00 1 D Hsh Location of shock plane

hsh =SC%*Hb-Hsh

hsh =	15.90	m	hsh	Head (height of material above shock plane)
Δey =	0.00175	m	Δey	Dynamic displacement of consolidated mass in the vertical direction, see Appendix D

Flow rate for mass flow (maximum), see Rotter (2001)

Q = 0.6*9.81*ρmin*Gf*((Ol-ks*dp)^2.5/g^(1/2))

Q =	0.0404769	Tonne/sec
Q =	160.62504	Ton/h
Q =	0.0446181	Ton/sec

Average vertical pressure (maximum increment), see Roberts and Wensrich (2002)

Δpvo =kd*9.81*ρmax*((1-e^(-μKh/Re))*(Re/μK-hs)+hs)

Δpvo =	70354.466	N/m²

Pulse period, see Roberts and Wensrich (2002)

a =	4.82	m/sec²	See Equation 6.2
vp =	0.01	m/sec	See Equation 6.3
to =	0.25	sec	See Equation 6.4
T =	0.28	sec	See Equation 6.1
f =	3.63	Hz	

Appendix F

Publications

Investigation of silo honking: slip-stick excitation and wall vibration

J. M. Buick[1], J. Chavez-Sagarnaga[1], Z. Zhong[1], J. Y. Ooi[1], Pankaj[1], D.M. Campbell[2] and C.A. Greated[2]
(1) Institute for Infrastructure & Environment, University of Edinburgh, Edinburgh EH9 3JN, U.K.
(2) School of Physics, University of Edinburgh, Edinburgh EH9 3JZ, UK.

The phenomenon of silo honking, a loud, acoustic emission from a silo during discharge is investigated. Simultaneous measurements of the three components of the acceleration of a full scale silo wall and the acoustic emission are presented. The results indicate a fundamental frequency of 330 Hz which characterizes the silo/particle combination. Results of laboratory investigations into the interaction of particulate solids with the silo walls and also internally with other particles are also presented. The observed slip-stick behaviour is a possible excitation mechanism for silo honking and is examined for a range of different particles and wall materials.

1 Introduction

Huge quantities of bulk materials in the form of granular solids are handled each year throughout the world. During emptying from thin-walled metal silos very loud intermittent honking sounds can be generated. This honking noise contains much higher frequencies and differs radically in nature from the periodic thumping or banging which can be heard in some silos during discharge. Honking of silos has been a fairly common industrial problem and has been known to exist in silos with differing dimensions, construction materials and fills in a variety of locations world wide. As noise pollution becomes increasingly unacceptable, silo honking has become an issue that needs to be urgently addressed. Honking with sound pressure levels in excess of 100-110dB can cause long term hearing damage if hearing protection is not worn. In recent years, the dynamic effects during silo discharge have been studied to a limited extent and various descriptive terms such as silo vibration, silo quaking, silo music or silo shocks have been used (Tejchman and Gudehus, 1993; Roberts, 1993). A recent study (Tejchman, 1999) examined the displacement and acceleration response of the walls of a honking silo, but did not consider the causes of honking. Several sources of the dynamic excitations in silos have been proposed (Gudehus and Tejchman, 1992; Roberts, 1993; Schulze, 1998). These include slip-stick behaviour between stored solids and silo walls, internal slip-stick behaviour within the stored solids, alternating flow patterns during flow, collapsing arches and solid dilation during flow.

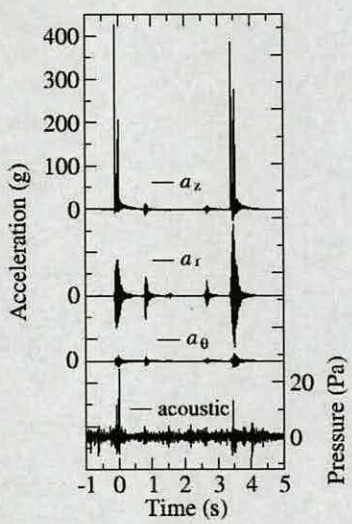

Figure 1: Accelerometer and microphone measurements

2 Silo Honking: Field Measurements

Measurements were obtained during honking from a full scale industrial honking silo in Scotland. The cylindrical part of the silo has a diameter of 3 m and is 21 m tall, it is constructed from horizontal aluminium strips which have three thickness of 4.0 mm, 5.2 mm and 6.2 mm from top to bottom. The conical hopper has a half angle to the vertical of 30° and was designed to ensure the PET pellets inside the silo undergo mass flow. The silo was instrumented using a triaxial accelerometer consisting of three PCB 303A02 accelerometers which were calibrated between 1 and 10 kHz. Outwith this range they had a maximum error of ± 10% up to 20 kHz; an Audio-Technica microphone ATM33a which had an approximately flat frequency response between 200 Hz and 2 kHz and a variation of no more than 5dB between 40Hz and 200 Hz and between 2kHz and 20 kHz; and a CEL-254 digital impulse sound level meter with a measurement range of 35-135 dB and a frequency range of 10 Hz to 25 kHz, which was calibrated with a CEL-282 acoustic calibrator. The combination of the triaxial accelerometer and the microphone enabled simultaneous measurements of the acoustic emission and the three components of the silo wall vibration in the axial, z; radial, r; and circumferential, θ, directions.

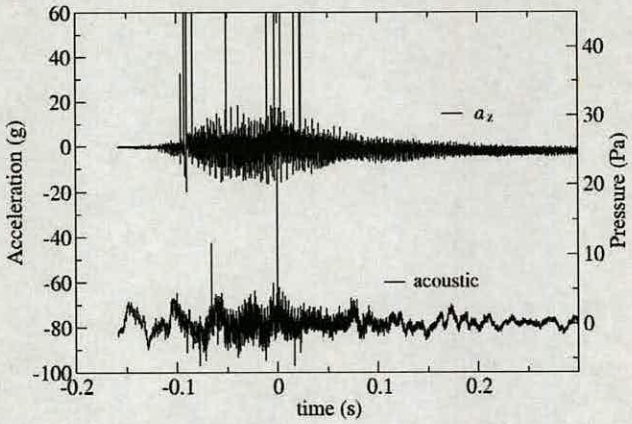

Figure 2: The axial acceleration and the acoustic signal

Figure 1 shows the acceleration measurements obtained from the triaxial accelerometer attached to the silo wall at a height z = 17.7m above the hopper transition. Also shown in figure 1 is the acoustical emission measured by the microphone at the base of the silo. The measurements presented in figure 1 correspond to one discharge cycle of the silo during which the silo was heard to honk 5 times, Honk1 at $t \sim 0.0$, Honk2 at $t \sim 0.8$, Honk3 at $t \sim 1.5$, Honk4 at $t \sim 2.6$ and Honk5 at $t \sim 3.5$ s. At these times the acceleration plots in figure 1 show corresponding wall accelerations of varying magnitudes which can be associated with the acoustic emissions. It is not, however, possible to detect the individual honks from a visual display of the pressure readings obtained from the microphone, however these can be observed if the low frequency noise is removed from the signal using a digital filter. Figure 2 shows a magnification of the axial acceleration and the acoustic signal around Honk1. The axial component of the acceleration, a_z, shows accelerations of over 400 g, which is comparable with the magnitude of acceleration measured elsewhere (Tejchman 1999), however figure 2 indicates that these high accelerations are intermittent impulses and are not oscillatory. Figure 2 shows that the typical acceleration amplitude of oscillatory response is up to 20 g.

Frequency analysis of the acceleration and pressure measurements was also performed and is shown in figure 3. The spectrum for each acceleration component shows the same harmonic series as was obtained for the acoustic signal indicating a direct correlation between the two. The figure indicates that there were significant acceleration at frequencies up to 10 kHz for the radial and circumferential components, at frequencies up to 20 kHz for the axial acceleration and up to 6 kHz for the acoustic signal. Each spectrum shows a harmonic series of peaks at a fundamental acoustic frequency of approximately 330 Hz and further peaks at frequencies corresponding to integer multiples of the fundamental acoustic frequency. This behaviour was observed in all measurements and the fundamental acoustic frequency was found to be independent of fill height and position of the accelerometers in further measurements.

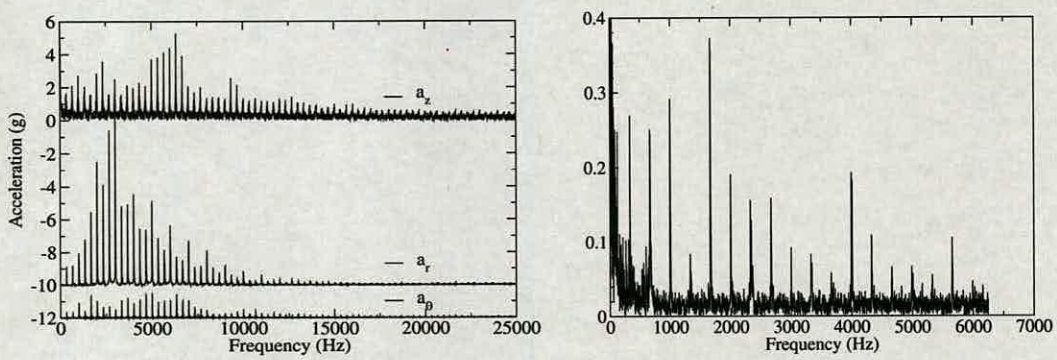

Figure 3: Frequency spectrum for the three components of the wall acceleration and the acoustic signal.

3 Wall Excitations: A Laboratory Study

In this section possible excitation mechanisms for the silo walls during discharge are considered. There are a number of possible excitation mechanisms which could potentially be responsible for exciting the silo

walls: a) Slip-stick behaviour between pellets and silo walls; b) Internal slip-stick behaviour within the pellets; c) Changing pattern of flow during discharge; and d) Dilation of the bulk solid during flow.
Three different particles were used in the laboratory measurements. Results are presented for PET pellets which were know to produce honking and blue polypropylene pellets which have not been reported to exhibiting honking. Aluminium plates were used with the same grade and thickness as used in silo constructions. Stainless steel plates were also used for comparison.

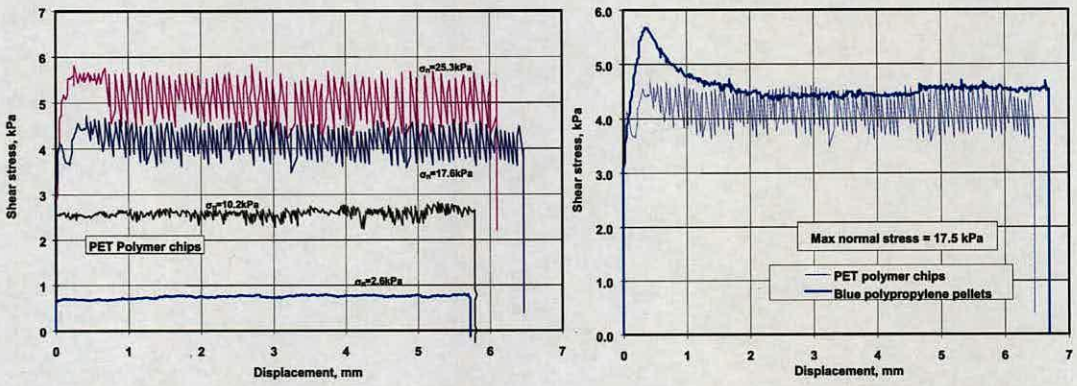

Figure 4: Shearing response of PET and blue polypropylene pellets on an aluminium wall for a nominal shear rate of 1mm/min.

Using Janssen theory (Janssen, 1895), it is possible to calculate the normal wall pressure on a silo wall. For the silo from which the acceleration measurements were obtained this was found to increase to just over 30 kPa near the transition. The testing of the mechanical behaviour of the pellets was therefore conducted with the stress level between 0-30 kPa. Wall friction tests were conducted using a Jenike shear tester (IChE, 1989) with a non-standard, large shear cell of 143 mm in diameter. In each test, the shear ring was positioned on top of the plate and then carefully filled with the pellets. After levelling the surface of the pellets, a shear lid was placed on top and a normal load was applied before the shearing was initiated. The results are presented in figure 4 for the PET pellets at four different normal stress levels and for both the PET and blue polypropylene particles for a normal stress level of 17.5 kPa.

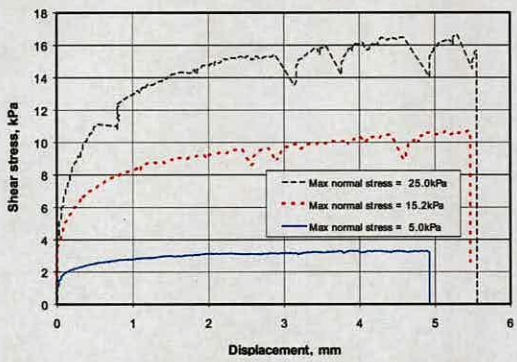

Figure 5: Inter-particle shearing response for the PET pellets.

The results show the shearing response of the PET pellets on the aluminium plate for the four normal stress levels and a shear rate of 1 mm/min. After the initial period when the shear stress increased towards shear failure, there was considerable slip-stick response. The pellets appeared to stick against the aluminium plate until the shear stress reached a certain magnitude, and then a sudden slip occurred, bringing the shear stress down to a lower value before building up again. The shear stress fluctuated between the peaks and the troughs as the pellets slip-stick continually during shearing against the aluminium plate. The slip-stick response is also noted to be very much stress level dependent, with considerably larger fluctuations at larger normal stress, and very little fluctuations at very low stress levels. Since the stress level in the real silo is partly governed by the height of fill, this indicates that the slip-stick phenomena at the walls may become significant only when the horizontal stress reaches around 10-15 kPa, which equates to z = 11-13 m in the instrumented silo. Similar results were also obtained for a second type of PET pellets, however, the blue polypropylene did not exhibit this slip-stick behaviour. Slip-stick motion was also observed between the PET pellets and a stainless steel wall sample but with a reduced magnitude.

Jenike direct shear tests were conducted to explore the internal stress-strain response of the honking PET pellets. The testing procedure involved setting up a sample of the pellets within two split rings, which were then sheared relative to one another under a certain normal stress. Figure 5 shows the results of three tests under normal stresses of 5.0, 15.2 and 25.0 kPa respectively. At higher stress levels, say above 10-15 kPa, the pellets exhibit some slip-stick phenomena, but these do not take place on a regular basis. The results indicate that internal slip-stick is probably not significant in this bulk solid and is certainly less than the wall slip-stick.

4 Conclusions

The phenomenon of silo honking has been investigated using a two-pronged approach. Full scale measurements have been obtained from a honking silo to evaluate the honking process and laboratory measurements were performed to investigate the excitation mechanism which is responsible for generating the honks. The full scale measurements provided simultaneous measurements of the three components of the wall acceleration during honking as well an acoustic recording of the honk. The most striking feature of the measurements was the constant value of the fundamental frequency of both the acoustic and wall acceleration measurements. This was found to be approximately 330 Hz and was totally repeatable and appeared to be independent of the position of the accelerometer, the fill level and other external factors such as temperature and humidity and acts as a signature of the silo/particle combination. Higher harmonics of 330 Hz were also observed. The laboratory measurements concentrated on investigating the slip-stick behaviour which can occur between the fill particles and the silo wall and internally between particles. The measurements were performed at wall pressures typical of those found at different height in a realistic silo. The two pellets which were known to exhibit honking in an aluminium silo displayed a slip-stick motion against a aluminium wall plate, while the third pellet which was thought not to exhibit honking showed no slip-stick behaviour. The amplitude of the fluctuations in the slip-stick motion was seen to increase with increased normal wall pressure. Internal slip-stick between the pellets in the silo was also considered. These showed some slip-stick properties but this was not considered significant when compared to the particle-wall slip-stick motion.

5 Acknowledgements

We would like to thank Mark Astin, Tim Bell, John Carson, Ron Dailey, Paul Dean, Paul, Michael Duerr, Karl Jacob, Paul Mayer, Colin Milton, Peter Moon, and John Thorman for many useful discussions throughout the course of the work. The authors would like to acknowledge the financial and practical assistance of Braby silos; Dow Chemical Company; DuPont; DuPont Teijin Films; Eastman Chemical Company; Jansens & Dieperink; Jenike & Johanson Inc.; and Waeschle and the financial support of EPSRC UK (grant no. GR/R44263) and an ORS Award (Chavez-Sagarnaga).

References

1. IChE (1989) "*Standard shear testing technique for particulate solids using the Jenike shear cell*". IChE/EFChE joint publication, IChE, England.
2. Janssen, H.A. (1895) "Versuche uber Getreidedruck in Silozellen" *Zeitschrift des Vereines Deutscher Ingenieure*, **39**, 1045-1049.
3. Roberts, A.W. (1993) "Mechanics of self excited dynamic loads in bins and silos" *Proc.* Int. Symp. Reliable Flow of Particulate Solids II, Oslo, 983-1004.
4. Schulze, D. (1998) "Silo Quaking" in *Silos - Fundamentals of theory, behaviour and design*, eds C.J. Brown and J. Nielsen, E & FN Spon, London, 171-182.
5. Tejchman, J. and Gudehus, G. (1993) "Silo music and silo quake experiments and a numerical Cosserat approach" *Powder Technology*, **76**, 201-212.
6. Tejchman, J. (1999) "Technical concept to prevent silo honking" *Powder Technology,* **106**, 7-22.

Investigation of Silo Honking: Slip-Stick Excitation and Wall Vibration

J. M. Buick[1]; J. Chavez-Sagarnaga[2]; Z. Zhong[3]; J. Y. Ooi[4]; Pankaj[5]; D. M. Campbell[6]; and C. A. Greated[7]

Abstract: Silo honking is an acoustical emission with a fundamental frequency of several hundred Hertz and an intensity often greater than 100 dB. It occurs when a silo is discharging and is similar to the "honk" of a lorry horn. The high amplitude of the honk makes it a significant noise pollution issue for workers at the site and for neighboring businesses and residents. This paper considers some possible excitation mechanisms that may be responsible for honking and presents measurements obtained from a full scale honking silo detailing the acoustic emissions and the associated vibration of the silo walls. Experimental results are presented which are comprised of simultaneous measurements of the three components of the wall vibrations and the acoustic pressure. The wall vibrations have an initial impulse response with a high amplitude $O(100g)$ and subsequent oscillatory accelerations with amplitude $O(10g)$. The frequency spectra of the acceleration and acoustic pressure measurements comprises a sharp peak at the fundamental acoustic frequency and a harmonic series of peaks at integer multiples of the fundamental frequency. It is shown that the honking is not generated by a resonance inside the silo, as in a flute or organ pipe; the sound is generated by the silo walls acting as large speakers. The interaction between the wall and the sliding pellets is considered as a possible excitation mechanism for the acoustic emissions. Laboratory friction measurements are presented using pellets from the honking silo and a wall sample. The results of these measurements show that the particles exhibit a slip-stick behavior when sheared against the wall material. This slip-stick behavior is characterized under different conditions for pellets that are known to produce honking. Particles that have not been observed to honk were also tested and did not produce slip-stick motion at the wall.

DOI: 10.1061/(ASCE)0733-9399(2005)131:3(299)

CE Database subject headings: Acoustics; Noise; Vibration; Slip; Silos; Particle motion; Particulate media.

Introduction

Huge quantities of bulk materials in the form of granular solids are handled each year throughout the world. During emptying from storage structures, many of these granular solids, such as plastic pellets (Tejchman 1999), corn (Roberts and Wiche 1991), coal (Levison and Munch-Andersen 1994), and rape seeds (Tejchman and Gudehus 1993) induce significant vibrations and dynamic loads on the storage systems. In addition to these dynamic loads, some granular solids, such as PET pellets, nylon pellets, and PVC powder, emit very loud intermittent honking sounds during discharge from thin-walled metal silos. This honking noise contains much higher frequencies and differs radically in nature from the periodic thumping or banging which can be heard in some silos during discharge. Honking of silos has been a fairly common industrial problem and has been known to exist in thin-walled metal silos with differing dimensions and fills in a variety of locations worldwide. As noise pollution becomes increasingly unacceptable, silo honking has become an issue that needs to be addressed. Honking with sound pressure levels in excess of 100–110 dB can cause long term hearing damage if hearing protection is not worn. The intermittent nature of silo honking can cause an unexpected distraction and create further hazards. The noise can also create problems for the local population residing close to industrial plants and in some cases, has been known to cause curtailment of normal silo operations (fill levels and operating hours).

In recent years, the dynamic effects during silo discharge have been studied to a limited extent and various descriptive terms such as silo vibration, silo quaking, silo music, or silo shocks have been used (Roberts and Wiche 1991; Gudehus and Tejchman 1992; Roberts 1993; Tejchman 1995; Schulze 1998b). However, all these studies predominantly focused on the additional dynamic loads induced on the silo structure during flow and did not address, to any significant extent, the acoustic effects of the vibra-

[1]Research Fellow, Institute for Infrastructure & Environment, School of Engineering & Electronics, Univ. of Edinburgh, Edinburgh EH9 3JN, U.K.; Lecturer, Physics and Electronics, School of Biological, Biomedical and Molecular Sciences, The Univ. of New England, Armidale, NSW 2351, Australia.

[2]PhD Student, Institute for Infrastructure & Environment, School of Engineering & Electronics, Univ. of Edinburgh, Edinburgh EH9 3JN, U.K.

[3]Research Fellow, Institute for Infrastructure & Environment, School of Engineering & Electronics, Univ. of Edinburgh, Edinburgh EH9 3JN, U.K.

[4]Reader, Institute for Infrastructure & Environment, School of Engineering & Electronics, Univ. of Edinburgh, Edinburgh EH9 3JN, U.K.

[5]Senior Lecturer, Institute for Infrastructure & Environment, School of Engineering & Electronics, Univ. of Edinburgh, Edinburgh EH9 3JN, U.K.

[6]Professor, School of Physics, Univ. of Edinburgh, Edinburgh EH9 3JZ, U.K.

[7]Professor, School of Physics, Univ. of Edinburgh, Edinburgh EH9 3JZ, U.K.

Note. Associate Editor: Eric N. Landis. Discussion open until August 1, 2005. Separate discussions must be submitted for individual papers. To extend the closing date by one month, a written request must be filed with the ASCE Managing Editor. The manuscript for this paper was submitted for review and possible publication on November 7, 2003; approved on August 31, 2004. This paper is part of the ***Journal of Engineering Mechanics***, Vol. 131, No. 3, March 1, 2005. ©ASCE, ISSN 0733-9399/2005/3-299–307/$25.00.

tions. Indeed a significant number of these studies were on concrete structures rather than on thin-walled metal silos in which honking occurs. A recent study (Tejchman 1999) examined the displacement and acceleration response of the walls of a honking silo, but did not consider the causes of honking. The two main solutions proposed to date are the installation of waffle sheets (rough wall plates) or a central discharge tube. These silo modifications can be expensive to implement, interfere considerably with the industrial processes, are not well accepted by the industry due their complexity and, since they have been developed for specific silos without a comprehensive understanding of the phenomenon, they may not work in all situations. Moreover, waffle sheets change the flow pattern and introduce additional nonuniform loading on the silo walls that can have serious implications on the structural integrity of thin-walled metal silos. Several sources of the dynamic excitations in silos have been proposed (Gudehus and Tejchman 1992; Roberts 1993; Schulze 1998b; Tejchman 1999). These include slip-stick behavior between stored solids and silo walls, internal slip-stick behavior within the stored solids, alternating flow patterns during flow, collapsing arches, and solid dilation during flow.

In this paper the honking phenomenon is studied. The aim is to establish the physical process that leads to the honking acoustic emission and investigate the mechanism through which this is achieved. Measurements of wall vibration and acoustic pressure during honking of a full scale silo were made and carefully analyzed. The focus is to investigate whether the honking can be produced by the motion of the silo wall that is observed to vibrate during honking. It is also of interest to consider the mechanism through which the wall vibrations are initiated. Several possible sources of excitation are discussed. Laboratory material tests were conducted to investigate whether slip-stick behaviors between the stored solid and the wall and within the solid are probable sources of excitation responsible for the wall vibrations which lead to silo honking.

Silo Honking: Field Measurements

Silo Properties

Measurements were obtained during honking from a full-scale cylindrical aluminum silo with diameter of 3 m and height of 21 m above the cone section. The silo is constructed from horizontal aluminum strips which have three thicknesses: 4.0, 5.2, and 6.2 mm from top to bottom. The cone half angle to the vertical is 30° and the silo is designed such that the PET pellets inside the silo undergo mass flow.

Instrumentation

The silo was instrumented using a triaxial accelerometer consisting of three PCB 303A02 accelerometers that were calibrated between 1 and 10 kHz. With this range they had a maximum error of ±10% up to 20 kHz. For acoustic recording an Audio-Technica microphone ATM33a with an approximately flat frequency response between 200 Hz and 2 kHz and a variation of no more than 5 dB between 40 and 200 Hz and between 2 and 20 kHz, and a CEL-254 digital impulse sound level meter with a measurement range of 35–135 dB and a frequency range of 10 Hz to 25 kHz, that was calibrated with a CEL-282 acoustic calibrator, were used. The combination of the triaxial accelerometer and the microphone enabled simultaneous measurements of

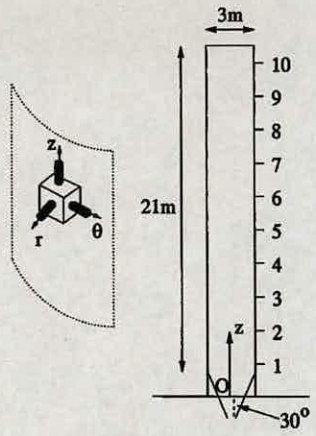

Fig. 1. Coordinate system for the triaxial acceleration measurements and the key dimensions of the silo

the acoustic emission and the three components of the silo wall vibration in the axial, z, radial, r, and circumferential, θ, directions (Fig. 1). Measurements were obtained with the triaxial accelerometer at 10 different heights on the silo. Access to these positions was obtained by scaffolding that was erected at the back of the silo. The position of the accelerometer at each level is described by its axial coordinate, z (see Fig. 1). The origin of the axial coordinate was the roof level of a single story building that contained the cone section. This is 105 cm below the transition between the cylindrical section and the hopper. The key silo dimensions are also indicated in Fig. 1. The accelerometers were placed vertically above each other. Sound pressure measurements were also taken at different heights to characterize the acoustical emissions. Acoustic records were obtained using the microphone at the base of the silo.

Results

Wall Acceleration and Acoustic Pressure Measurements

Fig. 2 shows the acceleration measurements obtained from the triaxial accelerometer attached to the silo wall at a height z

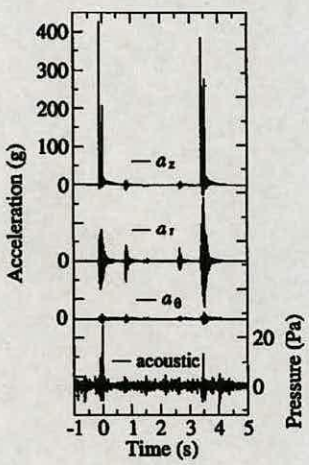

Fig. 2. Three components of the acceleration measured 17.7 m from the foot of the silo and the acoustical signal measured at the silo base

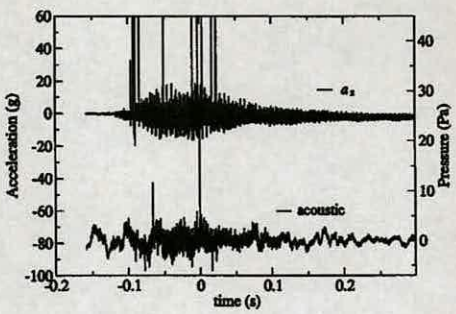

Fig. 3. Axial acceleration and the acoustic signal during the initial honk

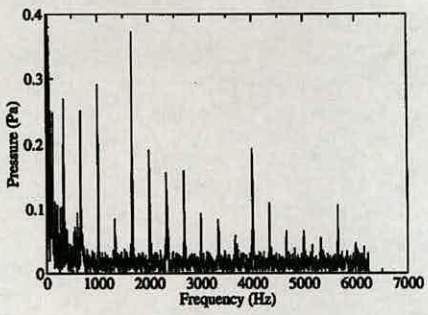

Fig. 4. Frequency spectrum of the acoustic signal

=17.7 m. The three acceleration components are plotted on the same scale, but the zero axis for each component has been shifted to improve clarity. Also shown in Fig. 2 is the acoustical emission measured by the microphone at the base of the silo. Each signal was captured at a sampling frequency of 12.5 kHz. The data acquisition was performed within *Matlab* and was triggered when one of the signals exceeded a preset threshold. The signals were, however, continuously sampled, enabling the signal just prior to triggering to be recovered from the system's buffer. This enabled the full honking event to be captured including the buildup before the system is triggered (negative time in Fig. 2). The measurements presented in Fig. 2 correspond to one discharge cycle of the silo during which the silo was heard to honk 5 times, Honk 1 at $t\sim0.0$, Honk 2 at $t\sim0.8$, Honk 3 at $t\sim1.5$, Honk 4 at $t\sim2.6$, and Honk 5 at $t\sim3.5$ s. At these times the acceleration plots in Fig. 2 show corresponding wall accelerations of varying magnitudes that can be associated with the acoustic emissions. It is not, however, possible to detect the individual honks from a visual display of the pressure readings obtained from the microphone; this will be discussed in more detail later.

Fig. 3 shows a magnification of the axial acceleration and the acoustic signal around Honk 1. The axial component of the acceleration, a_z, shows peak accelerations of over $400g$ which is in line with the magnitude of acceleration measured elsewhere (Tejchman 1999), however, Fig. 3 indicates that these accelerations are nonoscillatory, intermittent impulsive responses. In fact, Fig. 3 shows that typical acceleration amplitudes of the oscillatory response are typically in the range of $10g-20g$. Fig. 3 also shows high acceleration peaks that correspond to the large acceleration values observed in Fig. 2. These typically correspond to only a single point in the sampled record and so last for no longer than 50 μs. Such peaks could not be responsible for creating an acoustical emission at an audible frequency. In each case the peaks correspond to an acceleration in the positive direction, towards the top of the silo. In some of the measurements, acceleration peaks with a similar magnitude were also observed in the radial component of acceleration, always in the outward direction. We also note an impulsive response in the microphone signal in Fig. 3. Considering only the oscillatory components of the measured accelerations and ignoring the impulsive responses, the results show that for each honk the wall vibrates rapidly within an envelope. The shape of the envelope is similar for each honk and for each component: it builds up rapidly over a few hundredths of a second before decaying more gradually over several tenths of a second. The amplitude of the envelope varies between different honks. The amplitude of the circumferential accelerations is always the smallest and is generally about an order of magnitude smaller than the other components (see the radial and circumferential components in Fig. 2). The radial and axial components are generally similar with the radial component slightly larger than the axial component, however, the relative strengths of these two components varied with the position at which the accelerometer was placed suggesting that the silo is oscillating in a nodal manner.

Fig. 2 highlights a number of features of the silo honking which were typical of a large number of measurements obtained at different heights on the silo wall. Throughout the measurement period the fill level in the silo was maintained between 85 and 100%. Typically sound pressure measurements at the base of the silo were in the range 100–110 dB (this measurement corresponds to the loudest single honk during any discharge cycle). Within this variation no noticeable trend was observed due to the position of the accelerometers (other than the variations discussed above which were attributed to the nodal nature of the oscillations) or the fill level. It is, however, known that honking is not a problem when the fill level is less than about half full, the enforced operating conditions for the silo to prevent honking occurring. Sound pressure measurements were also obtained at different positions on the scaffolding. Again, the variations observed in the sound pressure level at different heights were no more than the general variation between honks.

Acoustic Signal

It is clear from Fig. 2 that the acoustic honks can be observed in the wall acceleration records as regions of high acceleration. Although it is not possible to detect the individual honks from a visual inspection of the microphone recording, they are clearly audible when playing back the signal through a speaker. The reason for this is the high level of background noise that was present at the plant and was measured between 85 and 90 dB. During discharge the level was higher due to the additional noise of the particulate solids falling through the silo. In Fig. 3, however, a difference in the acoustic signal can be observed. Before $t=-0.1$ s and after $t\sim0.15$ s the signal is varying slowly in time with a period of a few hundredths of a second corresponding to the low frequency background noise with a frequency of the order of tens of hertz. Between these times the signal is varying between positive and negative pressures with a period which is too small to determine on the scale of Fig. 3: this corresponds to the high frequency honking. This can be seen in more detail by considering the frequency spectrum of the acoustic signal which is shown in Fig. 4. The spectrum shows a series of harmonic peaks with the fundamental acoustic frequency at approximately 333 Hz and the higher harmonics at integer multiples of this frequency. In general the larger peaks correspond to frequencies up to about

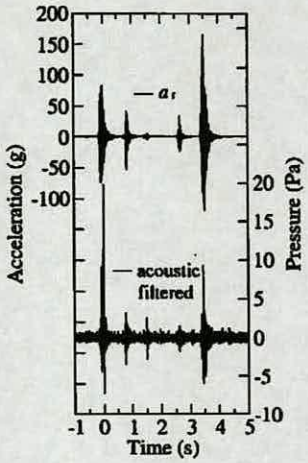

Fig. 5. Filtered acoustic signal and the radial component of the wall acceleration

4,000 Hz; above 6,000 Hz the peaks are not significantly larger than the background. At frequencies below 150 Hz the spectrum shows the background noise which is present and can be ignored in this study. The value of the spectrum is off the scale of the graph that was selected to highlight the harmonic nature of the spectrum above these frequencies.

Filtering the Acoustic Signal

It is possible to remove a significant proportion of the noise from the acoustic signal by passing it through a high-pass filter. This was done using a fifth order Butterworth filter with a cutoff frequency of 250 Hz, selected to be sufficiently lower than the measured fundamental acoustic frequency. The result of this filtering action is demonstrated in Fig. 5 that shows the filtered acoustic signal and the radial component of the wall vibration for comparison. The individual honks can now be observed from the filtered acoustic signal; for example, at $t \sim 2.2$ s the acoustic signal in Fig. 2 shows what might be interpreted as a honk, however, Fig. 5 makes it clear that there is no honk occurring at this time.

Spectral Analysis of the Wall Accelerations

Frequency analysis of the acceleration measurements was also performed and is shown in Fig. 6. The spectrum for each component shows the same harmonic series as was obtained for the acoustic signal (Fig. 4). The figure indicates that there were significant accelerations at frequencies up to 10 kHz for the radial

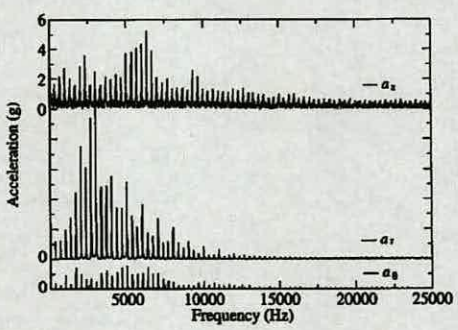

Fig. 6. Frequency spectrum for the three components of the wall acceleration

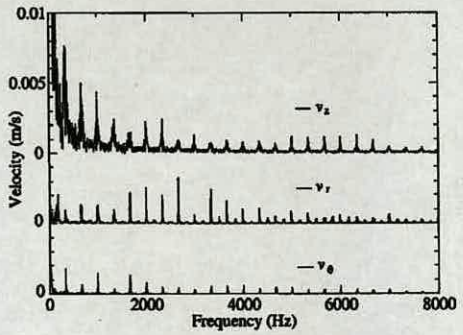

Fig. 7. Velocity spectrum calculated by integrating the acceleration spectra

and circumferential components and at frequencies up to 20 kHz for the axial acceleration. In Fig. 6 each component has been measured from a separate honking event with a sampling rate of 50 kHz to prevent aliasing. Spectra obtained from the simultaneous measurement of the three components shown in Fig. 2 showed the same features as Fig. 6 except that there was some aliasing in the spectrum for the axial component due to the lower sampling rate.

Velocity Spectra

The wall acceleration spectra in Fig. 6 and the spectrum of the acoustical signal in Fig. 4 all show a harmonic series with a fundamental frequency of 333 Hz. There are, however, a number of differences. In particular, the series of peaks is observed at higher frequencies in the wall acceleration spectra and the largest peaks occur at a higher frequency. Consider a silo wall that is vibrating in a manner described by the spectra in Fig. 6. The acceleration can be considered as the superposition of a number of sinusoidal oscillations

$$a = \sum_n a_n \cos(n\omega_0 t)$$

where n=integer and $\omega_0 = 2\pi f_0$=fundamental angular frequency with f_0=333 Hz. Integrating this we see that the amplitude of each component is reduced by a factor of $n\omega_0$. The velocity spectrum in Fig. 7 is calculated by integrating the acceleration signal in Fourier space, that is by dividing through by the angular frequency. The axial and circumferential components were found from the spectra in Fig. 6 while the radial component was found from the spectra for the radial acceleration of Honk 1 in Fig. 2. This means that this velocity spectrum can be compared to the acoustic spectrum in Fig. 4 since the two measurements were obtained simultaneously. Some effect of aliasing can be seen in the spectrum for the radial component in Fig. 7 as the small peaks are approximately equidistant to the harmonic peaks.

Comparison of the Radial Velocity and the Acoustic Pressure Measurements

For a progressive acoustic wave the velocity with which an air molecule oscillates is related to the variation in pressure by (Kinsler et al. 1982)

$$\frac{p'}{p_0} = \frac{v}{c}$$

where the pressure is given by $p = p_0 + p'$ where p_0=ambient pressure, p' and v=the acoustic pressure and velocity variation due to

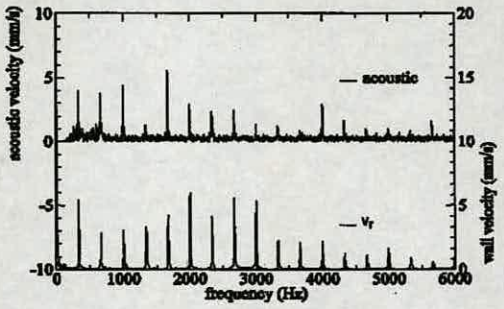

Fig. 8. Acoustic velocity spectrum calculated from the microphone pressure reading and the radial wall velocity spectrum, v_r, calculated by integrating the radial acceleration spectra

the sound wave, respectively, and c=speed of sound. A comparison of the radial velocity spectrum of the silo wall vibrations, v_r, and the acoustic velocity spectrum measured close to the wall is shown in Fig. 8. The two spectra have the same basic features. For example, in both spectra the majority of the largest peaks are for frequencies less than 4 kHz. Comparing the magnitudes of the spectra we also observe good agreement between the spectra. Therefore there is both qualitative and quantitative agreement between the acoustic spectra and the radial velocity spectra, suggesting that the honking is produced by the horizontal oscillations of the silo wall acting as a large loud speaker. Clearly we would not expect an exact agreement between the velocity measured at a single point on the structure and the pressure measurement from a microphone which, although close to the wall, corresponds to the combined emission from the whole structure. The sound pressure level (SPL) is given by

$$\text{SPL} = 20 \log\left(\frac{p'}{p_f}\right)$$

where p_f is taken to be 2×10^{-5} Pa which is the pressure of a 1,000 Hz pure tone that is barely audible to a person with unimpaired hearing. Now a typical acoustical velocity of 0.004 m/s corresponds to an acoustical pressure variation p'=0.4 Pa which has a SPL=86 dB. Since this corresponds to a single component of the overall honk this is broadly in line with the overall measurement of 100–110 dB for the sound pressure level. We note also that the results presented above have all been on a linear scale while acoustic signals are often presented on a log scale since this is the manner in which the sound is heard by a human observer. Thus the large differences in the acceleration and pressure levels observed between the different honks in Fig. 2 will not appear as great when heard by the human ear. Listening to the recording of the five honks in Fig. 5 the relative volume is easily detected at loud, medium, soft, medium, and loud, respectively. These results show that honking measured with a microphone close to the silo wall is consistent with the measured radial velocity of the wall. This indicates that the acoustical signal can be generated solely by the radial wall vibrations. Thus the honking is generated by the motion of the silo wall acting as a large loud speaker and cannot be likened to a flute or an organ where the sound is generated by resonance inside the object. This conclusion is further strengthened by the fixed frequency with which the honking occurs, irrespective of the fill level. The resonant frequency of the air-column and/or granular solids within the silo will change markedly as the fill level changes; however, no variation in the frequency of honking was observed.

Wall Excitations: Laboratory Study

Excitation Mechanisms

In this section possible excitation mechanisms for the silo walls during discharge are considered. There are a number of possible excitation mechanisms which could potentially be responsible for exciting the silo walls.

1. Slip-stick behavior between pellets and silo walls: The wall friction between the stored solid and the silo walls is an important parameter in the design of a storage structure. This is often measured using a direct shear tester, in which a shallow box containing a sample of the granular solid is sheared against a wall specimen. For some granular solids, the frictional traction needed for the solid to move against the wall material fluctuates considerably. It is possible that the slip-stick fluctuations generate the vibrations that lead to honking.

2. Internal slip-stick behavior within the pellets: The stored solid must go through considerable deformation and shear failure during discharge. Slip-stick behavior can also occur internally within the granular medium. This again can be a significant source of vibration that occurs during discharge.

3. Changing pattern of flow during discharge: In a cylindrical silo with a hopper, the stored solid may flow predominantly either in mass flow or funnel flow. In mass flow, the entire content of a silo is in motion, moving towards the outlet. In funnel flow, only part of the content is in motion while the rest remains stationary. Funnel flow often occurs as an internal flow channel with surrounding zones of stationary solid. Funnel flow occurs when the hopper is too shallow, the hopper walls are too rough, or when a mass flow silo has not been adequately designed. It has been suggested that for some silos, the changes in the properties of the bulk solid during flow can result in alternating flow patterns during discharge (Roberts 1993). The periodic slips against the hopper walls can induce significant vibrations.

4. Dilation of the bulk solid during flow: It has been recognized that most granular solids have to dilate to flow. However, the degree of dilation which is required to move a solid from its storing state to its flowing state varies considerably between different granular solids. The dilation of the solid leads to reduction in bulk density and a corresponding reduction in the magnitude of the stresses within the flow regimes. The reducing stress regimes can then lead to either changing flow patterns or changing flow boundaries. These unstable phenomena can result in significant dynamic effects during flow.

Particulate Solids and Wall Materials

Three different particles were used in the laboratory measurements. PET1 pellets are very uniform in size and each particle has the shape of an elliptical cylinder with an approximately elliptical cross section. The average dimensions are 2.0×3.2 mm and 4.0 mm long. These have been reported to produce honking in thin-walled metal silos. PET2 is a "pillow" shaped PET pellet with similar dimensions which is also known to have a tendency to honk. The third type of particle was blue polypropylene pellets which have not been reported to exhibiting honking. Aluminum plates were used with the same grade and thickness as used in silo constructions. Stainless steel plates were also used for comparison.

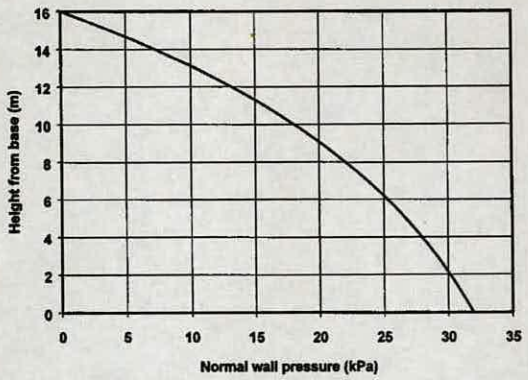

Fig. 9. Normal wall pressure distribution in a typical silo

Evaluation of the Stress State in a Silo

The behavior of particulate solids is highly stress level and stress history dependent. It is thus important to evaluate the stress state in a typical silo, which can then be simulated in the laboratory tests.

The most commonly used theory for calculating stresses in the solid contained in a cylindrical vessel is the Janssen theory (Janssen 1895; Rotter 2001)

$$q = \gamma z_O (1 - e^{-z/z_O})$$

$$P = kq$$

$$\tau = \mu P$$

and

$$z_O = \frac{R}{2\mu k}$$

where q=mean vertical stress in the stored material at depth z, P=normal wall pressure (radial stress), τ=wall frictional traction, γ=unit weight of the stored material, R=radius of the vessel, μ=wall friction coefficient, and $k=P/q$=lateral pressure ratio which is commonly assumed to depend on the angle of internal friction of the solid ϕ, and normally lies between 0.3 to 0.7. In this study k=0.5 is assumed. The following typical silo geometry and pellets properties were used in the calculations: R=2.1 m; μ=0.21; filled height of the cylindrical section, H=16.0 m; and bulk unit weight of the particles γ=8.0 kN/m^3.

Fig. 9 shows the normal wall pressure distribution expected for the cylindrical section of the silo when it is filled to 16 m. The normal wall pressure is zero at the top of the fill (16 m) and increases to a maximum value at the base. The rate of increase in the pressure decreases with decreasing height due to the exponential form of the Janssen theory. The normal wall pressure or the horizontal normal stress in the pellets increases to just over 30 kPa near the hopper transition (at the base of the cylindrical section). The testing of the mechanical behavior of the pellets was therefore conducted with the stress level between 0 and 30 kPa.

Slip-Stick Behavior at the Silo Walls

This section reports a sample of wall friction tests conducted to investigate the shearing behavior of pellets on a wall material. Tests were performed to investigate the effects of shearing rate, stress level, and time under load.

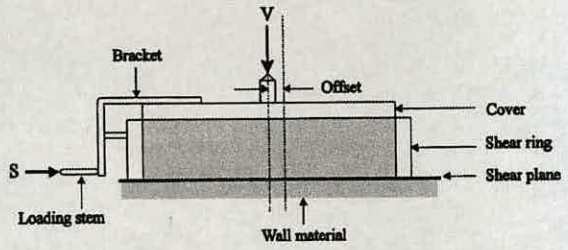

Fig. 10. Jenike shear tester

The wall friction tests were conducted using a Jenike shear tester with a large shear cell of 143 mm in diameter, as shown in Fig. 10 (IChE 1989). In each test, the shear ring was positioned on top of the plate and then carefully filled with the pellets. After leveling the surface of the pellets, a shear lid was placed on top and a normal load was applied before the shearing was initiated. The normal stress levels were chosen to reflect the stress state in the solid during storage. Four levels of normal stress were considered: 2.6, 10.2, 17.6, and 25.3 kPa.

Fig. 11 shows the shearing response of PET1 pellets on the aluminum plate for the four normal stress levels and a shear rate of 1 mm/min. After the initial period when the shear stress increased towards shear failure, there was considerable slip-stick response. The pellets appeared to stick against the aluminum plate until the shear stress reached a certain magnitude, and then a sudden slip occurred, bringing the shear stress down to a lower value before building up again. The shear stress fluctuated between the peaks and the troughs as the pellets slip-stick continually during shearing against the aluminum plate.

The slip-stick response is also noted to be very much stress level dependent, with considerably larger fluctuations at larger normal stress, and very little fluctuations at very low stress levels. Since the stress level in the real silo is governed by the height of fill, this indicates that the slip-stick phenomena at the walls may become significant only when the horizontal stress reaches around 10–15 kPa, which equates to z=11–13 m in Fig. 9. This is in line with the industrial experience that honking occurs only after the silo fill height is above a certain level.

The upper and lower limiting shear stress during the slip-stick shearing were obtained from the shearing response curves in Fig. 11. If it is assumed that the wall adhesion is zero, then the wall

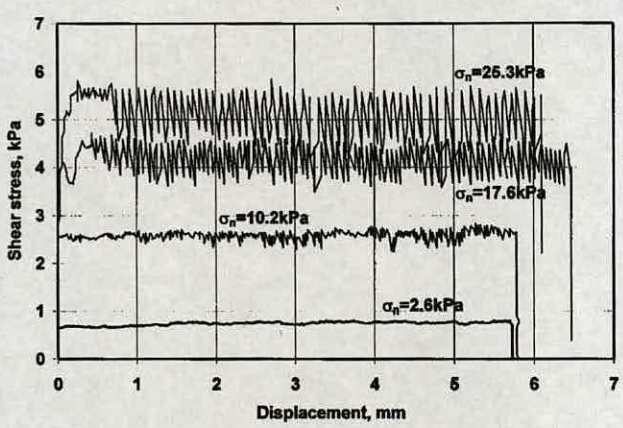

Fig. 11. Shearing response of PET1 pellets on an aluminum wall for a shear rate of 1 mm/min

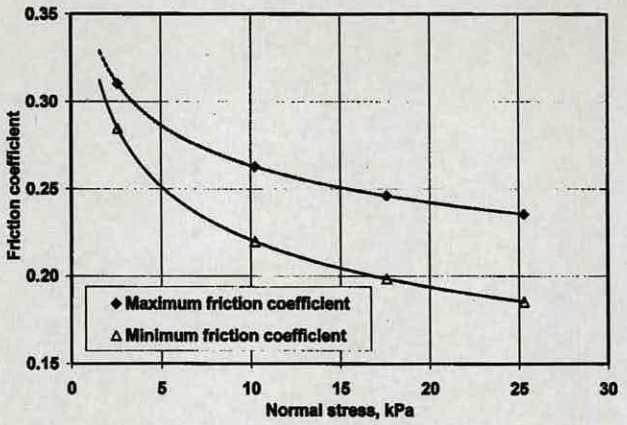

Fig. 12. Stress dependency of wall friction for PET1 pellets on aluminum

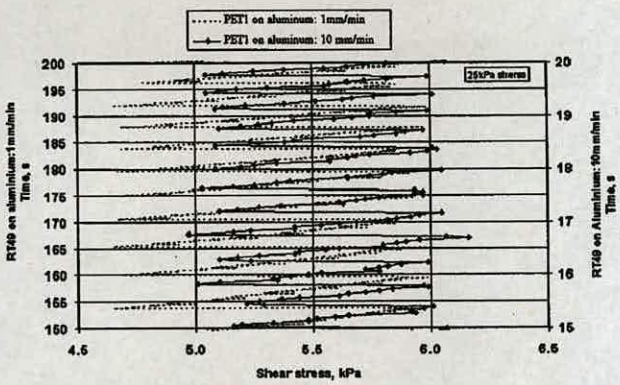

Fig. 14. Wall shear response for PET1 pellets on an aluminum wall for shear rates of 1 and 10 mm/min. The left-hand ordinate is for the shear rate of 1 mm/min and the right-hand ordinate for a shear rate of 10 mm/min

friction coefficient, μ, is simply given by the ratio of the shear stress to the normal stress and is shown in Fig. 12. The upper and lower limiting values of the wall friction coefficient are stress dependent. At medium to high stresses (>25 kPa), the wall friction coefficient fluctuates between 0.185 and 0.235; the median value was used in the calculation of the normal wall pressure distribution in Fig. 9.

Comparison with Other Pellets

Fig. 13 shows the result of a wall friction test on blue polypropylene pellets that have not been reported to exhibit honking. The fluctuating shear stress noted in the PET1 pellets (also shown in Fig. 13) is not seen in these nonhonking pellets. Measurements were also conducted on the PET2 pellets that were thought to have a smaller tendency to honk. The PET2 pellet was found to exhibit a similar slip-stick response to that for PET1 pellets.

Time of Storage

When a silo is not discharging, the stored solid is subjected to the storing stress regime for a significant period of time. Previous studies have shown that the properties of the stored solid can change as a result of the time under stress (see, for example, Schulze 1998a). When a wall friction test was conducted in which the normal stress was applied for a total of 16 h before shearing commenced the results were seen to be indistinguishable from the case where the normal stress was applied immediately before shearing. This suggests that time effect is negligible in this case.

Rate of Shearing

The shear rate is found to vary between different silos and may be an important factor in determining whether honking occurs for a particular silo/pellet combination. Experiments were carried out to explore the effect of rate of discharge on the wall friction response.

Fig. 14 shows the results obtained for the PET1 pellets on an aluminum wall for a shear rate of 1 mm/min (left-hand ordinate) and 10 mm/min (right-hand ordinate). The results show that the frequency of fluctuation increases with increasing shear rate while the magnitude of fluctuation appears to have slightly decreased.

Internal Slip-Stick Behavior Between the Pellets

Jenike direct shear tests were conducted to explore the internal stress-strain response of the honking PET1 pellets using the internal friction test apparatus shown in Fig. 15. The testing procedure involved setting up a sample of the pellets within two split rings, which were then sheared relative to one another under a certain normal stress.

Fig. 16 shows the results of three tests under normal stresses of 5.0, 15.2, and 25.0 kPa, respectively. At higher stress levels, say

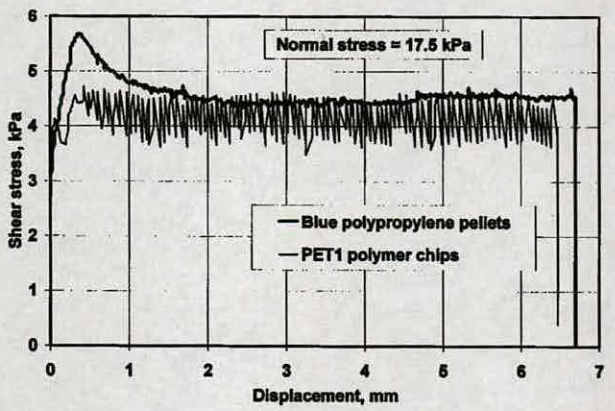

Fig. 13. Shearing response of blue polypropylene and PET1 pellets on aluminum for a shear rate of 1 mm/min

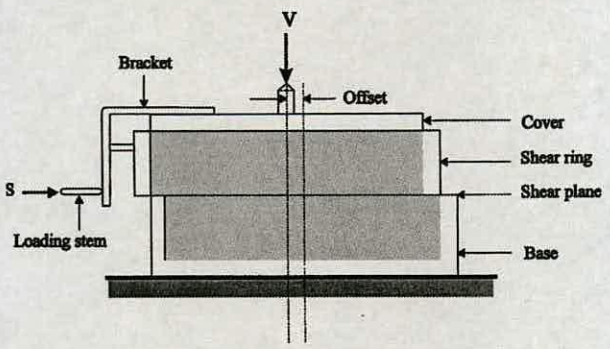

Fig. 15. Jenike shear test apparatus for internal stress-strain measurement

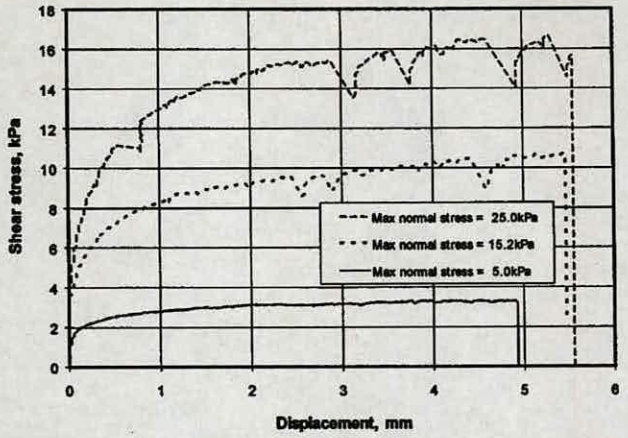

Fig. 16. Interparticle shearing response for PET1 pellets

above 10–15 kPa, the pellets exhibit some slip-stick phenomena, but these do not take place on a regular basis. The results indicate that internal particle–particle slip-stick does take place but is probably not significant in this bulk solid and is certainly less than the particle-wall slip-stick.

Effect of Twisting and Time Consolidation

The effect of twisting the sample, as is often performed during Jenike testing, and of time consolidation were also investigated. The twisting consolidated the specimen and gave rise to a denser packing, resulting in a higher shear stress at failure. A noticeable effect was found at 25 kPa, but only a negligible difference at 5 kPa. The magnitude and the frequency of the slip-stick fluctuations do not appear to change. The effect of time under stress was investigated by conducting a test for which the test specimen was left under the normal stress of 25.3 kPa for a total of 30 h before shearing. The effect of time consolidation was also found to give a negligible difference in the internal slip-stick motion.

Further Discussion

The full scale measurements provided simultaneous measurements of the three components of the wall acceleration during honking as well an acoustic recording of the honk. Since different honks are not identical the simultaneous measurement is essential to obtain a full picture of the phenomenon. Large accelerations were measured of the order of several hundred times the acceleration due to gravity. These were associated with short impulse-like movements of the silo wall and not with the acoustic emissions. During honking the radial and axial components of the silo walls were seen to vibrate within an envelope which grew rapidly over a few hundredths of a second before decaying over a few tenths of a second. The maximum amplitude of this envelope was typically of the order of $10g$, although values of over $100g$ were observed. The circumferential acceleration was relatively small but not negligible. This was thought to be due to irregularities in the symmetry of the silo or asymmetric flow. The relative amplitude of the radial and axial accelerations was seen to vary with the position of the accelerometer but no general relationship was found between the height of the accelerometer and the amplitude. This suggests that the silo is vibrating in a nodal manner; that is, the silo is vibrating with a series of nodes and antinodes along axial and circumferential lines around the silo. Frequency spectra of the three components of the acceleration and of the acoustic emissions all showed a harmonic structure with peaks at the fundamental frequency and integer multiples of this frequency. The acceleration spectra displayed at least 30–40 such harmonic peaks while the acoustic spectrum showed fewer peaks concentrated at the lower harmonic frequencies. A comparison of the acoustic spectra with the wall radial velocity spectrum (obtained by integrating the accelerometer signal in the frequency domain) demonstrated the similarity of the spectra in terms of shape, frequency, and magnitude suggesting that the silo walls were acting as a large loud speaker, rather than the honking arising from resonances within the silo. The most striking feature of the measurements was the constant value of the fundamental frequency of both the acoustic and wall acceleration measurements. This was found to be 333 Hz and was totally repeatable and independent of the position of the accelerometer, the fill level, and other external factors such as temperature and humidity and acts as a signature of the silo/particle combination. This further supports the assertion that the acoustic emission is due to the wall vibrations acting as a speaker since the frequency of an internal resonance would vary with the fill level. Further work is required to determine the relative importance of the silo and the particles in determining the fundamental frequency.

The laboratory measurements concentrated on investigating the slip-stick behavior which can occur between the particles and the silo wall and internally between particles. The measurements were performed at wall pressures typical of those found at different height in a realistic silo. Three different pellets were investigated against an aluminum plate. The two pellets which were known to exhibit honking displayed a slip-stick motion against the wall, while the third pellet which was thought not to exhibit honking showed no slip-stick behavior. The amplitude of the fluctuations in the slip-stick motion was seen to increase with increased normal wall pressure. One of the honking pellets was also tested against a stainless steel plate where it also exhibited a slip-stick behavior. The duration of loading before the test was performed was also investigated but found to have little effect on the measurements. These findings are consistent with the wall slip-stick behavior being the excitation mechanism for honking. Pellets which are known to honk exhibited slip-stick behavior while particles which have not been observed to honk did not. The amplitude of the slip-stick motion reduces with the normal wall pressure, consistent with the fact that (at least on a number of silos which have been studied) honking does not occur when the fill level, and hence the normal wall pressure, is below a certain level. The frequency of the slip-stick motion was seen to increase with increased shear rate, however, the results predict considerably lower frequencies for the slip-stick motion in a silo relative to the observed honking frequencies. Thus the slip-stick motion on the wall is not transferred directly onto the wall vibrations and the manner in which such a transfer could occur requires further investigation. Internal slip-stick between the pellets in the silo was also considered. These showed some slip-stick properties but this was relatively insignificant when compared to the particle-wall slip-stick motion.

Conclusions

The phenomenon of silo honking has been investigated using a two-pronged approach. Full scale measurements have been obtained from a honking silo to evaluate the honking process and laboratory measurements were performed to investigate the pos-

sible excitation mechanism(s) that are responsible for generating the honks.

Wall accelerations greater than $100g$ were measured on the full-scale silo. The acoustical emission or honk was seen to correspond to periods of wall vibration with an acceleration amplitude of the order of $10g$; the frequency of the wall vibration was harmonic with the same structure as the honking sound. Further, a comparison of the radial velocity spectrum of the silo wall and the pressure spectrum of the acoustic emission indicated that the honking was produced by the motion of the silo wall acting as a large loud speaker.

Slip-stick motion was investigated in laboratory measurement both internally between pellets and between the pellets and a wall sample. The internal slip-stick motion was relatively insignificant compared to the particle-wall slip-stick which was investigated for different particles, wall materials, and stress levels. During the tests slip-stick motion was only observed for particles which were known to honk in a full-scale silo. The amplitude of the slip-stick motion was found to increase with increasing normal pressure. These observations are consistent with slip-stick motion between the particles and the wall being an excitation mechanism for silo honking.

Acknowledgments

A preliminary analysis of a portion of this work was presented at the 16th ASCE Engineering Mechanics Conference in Seattle, 2003. The writers would like to thank Mark Astin, Tim Bell, John Carson, Ron Dailey, Paul Dean, Paul Denby, Michael Duerr, Karl Jacob, Paul Mayer, Colin Milton, Peter Moon, and John Thorman for many useful discussions throughout the course of the work. The writers would like to acknowledge the financial and practical assistance of Braby Silos, Dow Chemical Company, DuPont, DuPont Teijin Films, Eastman Chemical Company, Jansens & Dieperink, Jenike & Johanson Inc., and Waeschle and the financial support of EPSRC UK (Grant No. GR/R44263) and an ORS Award (Chavez-Sagarnaga).

References

Gudehus, G., and Tejchman, J. (1992). "Silo music and silo quake." *Silos—Forschung und Praxis Tagung '92*, Karlsruhe, 103–110.

Institute of Chemical Engineers (IChE). (1989). *Standard shear testing technique for particulate solids using the Jenike shear cell*, Institute of Chemical Engineers/European Federation of Chemical Engineering joint publication, England.

Janssen, H. A., (1895). "Versuche uber Getreidedruck in Silozellen." *Z. Vereines Deutscher Ingenieure*, 39(35), 1045–1049.

Kinsler, L. E., Frey, A. R., Coppens, A. B., and Sanders, J. V. (1982). *Fundamentals of acoustics*, 3rd Ed., Wiley, New York.

Levison, B., and Munch-Andersen, J. (1994). "Shocks in coal silos." *Powder Handling Process.*, 6(4), 385–388.

Roberts, A. W. (1993). "Mechanics of self excited dynamic loads in bins and silos." *Proc. Int. Symposium Reliable Flow of Particulate Solids II*, Powder Science and Technology Research, Oslo, Norway, 983–1004.

Roberts, A. W., and Wiche, S. J. (1991). "Silo quaking—a pulsating load problem during discharge in bins and silos." *Proc., Bulk 2000 Conf.*, Institution of Mechanical Engineers, London, 7–12.

Rotter, J. M. (2001). *Guide for the economic design of circular metal silos*, Spon, London.

Schulze, D. (1998a). "Measurement of the flowability of bulk solids." in *Silos—Fundamentals of theory, behaviour and design*, C. J. Brown and J. Nielsen, eds., E&FN Spon, London, 18–52.

Schulze, D. (1998b). "Silo quaking." in *Silos—Fundamentals of theory, behaviour and design*, C. J. Brown and J. Nielsen, eds., E&FN Spon, London, 171–182.

Tejchman, J., and Gudehus, G. (1993). "Silo music and silo quake experiments and a numerical Cosserat approach." *Powder Technol.*, 76(2), 201–212.

Tejchman, J. (1995). "Silo quake—experiments and a polar hypoplastic model." *European Symp: Storage and Flow of Particulate Solids (Janssen Centennial)*, NürnbergMesse GmbH, Nürnberg, Germany, 151–162.

Tejchman, J. (1999). "Technical concept to prevent silo honking." *Powder Technol.*, 106(1-2) 7–22.

PARTEC 2004

Frictional properties of pellets and silo wall materials for the investigation of silo honking

J. Chavez-Sagarnaga[1], J. M. Buick[1,2], J. Y. Ooi[1], Pankaj[1], D. M. Campbell[3] and C. A. Greated[3]

[1] Institute for infrastructure & Environment, School of Engineering and Electronics, The University of Edinburgh, Edinburgh EH9 3JN, U.K.

[2] Department of Physics and Electronics, School of Biological, Biomedical and Molecular Science, The University of New England, Armidale, NSW 2531, Australia

[3] School of Physics, The University of Edinburgh, Edinburgh EH9 3JZ, U.K.

ABSTRACT

Silo honking is a phenomenon in which a loud acoustic emission, not dissimilar to a truck horn, occurs during silo discharge. This phenomenon has been widely reported as occurring in a wide variety of metal silos and with different fills. In this paper we present the result of experiments carried out to explore the particle-particle and particle-wall interactions for the investigation of silo honking. Two types of particles are considered: PET pellets that are known to honk and polypropylene pellets that are not. The measurements were performed using the Jenike shear tester. The shearing response showed that pellets that are known to honk exhibit slip-stick behaviour while particles that have not been observed to honk do not.

1 INTRODUCTION

Thin metal silo structures are used all around the world to store granular bulk solids such as agricultural grains, plastic pellets and mineral ores. It has been suggested that a range of different dynamic phenomena produce vibrations in a silo structure during discharge [1-3]. However, there is no consensus on theories to describe these. A number of these structures are known to emit very intermittent loud sounds similar to a truck horn, known as silo honking [2,4-6]. Although more commonly detected while silos are discharging, honking is also occasionally known to happen after a discharge period. Some of the features of silo honking are: sound pressure levels in excess of 100-110dB, high wall accelerations amplitudes [4-6], and high frequencies. Metal silos designed for mass flow containing polymer granulates [5,6] with high fill levels [5] and often discharging at high outflow rates [6], are known to honk.

The objective of this paper is to study the particle-wall and particle-particle interaction for two different polymer granulates and two different wall materials. The interaction between particles and the wall material is examined for slip-stick, which can be a possible source of excitation in the silo honking phenomenon. The Jenike shear tester was used to investigate this interaction. Different variations were implemented including normal stress variation and sample size variation. The shear response was recorded and plotted against time and displacement.

2 MATERIALS AND METHODS

Two different pellets were tested – PET and blue polypropylene. Industrial experience suggests that PET pellets honk while polypropylene pellets do not. PET pellets considered were in the shape of flattened cylinder with an elliptic cross-section. The typical cross-section of these pellets was 4x1.5-2 mm with 4 mm height and density was in the range 770-890 kg/m^3. The polypropylene pellets were shaped like squat cylinders with 5 mm diameter and 1.5-4 mm height. The density range for these pellets was 550-620 kg/m^3. Two different plate materials were considered: aluminium and stainless steel. The aluminium plate had a thickness of 6.1 mm with a roughness average of 0.88. The stainless steel plate was 4 mm thick with a roughness average of 0.5.

The measurements were performed using a Jenike Shear Tester. Most tests were conducted with a shear ring of 143 mm diameter. Shear ring diameters of 95 mm and 63 mm were used to determine sample size effect. To investigate the particles-wall interaction a shear plane was created between the pellets and the plate (Fig. 1). In these tests the shear ring was placed over the plate and filled with pellets. Once the sample was levelled, a cover was placed on top of the pellets and a vertical force was applied to the cover. Shearing was initiated by applying a horizontal load to the bracket under displacement control [7]. To investigate the particle-particle interaction a shear plane was created between the pellets. The procedure was similar to that described above, except in this case a base container filled with pellets replaces the plate. Base container and shear ring were offset on each

other and the horizontal force was applied to the bracket of the top shear ring, creating a shear plane between particles [7].

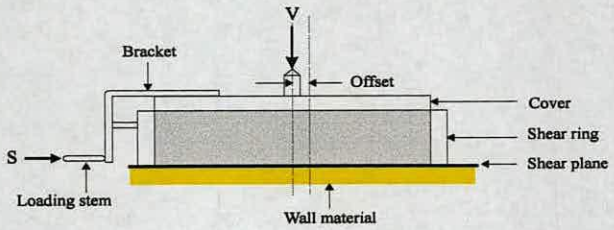

Figure 1: Jenike shear tests for particle-wall interaction.

3 RESULTS AND DISCUSSION

3.1 Effect of stress level and materials

Figure 2 shows the shearing response of PET pellets on the aluminium plate for four different normal stress levels and a shear rate of 1mm/min. The stress levels were chosen to reflect the real conditions in a silo that was known to honk with PET pellets. Considerable slip-stick response, illustrated by fluctuating shear stress, was observed between PET pellets and aluminium plate. The magnitude of these fluctuations increases with normal stress level. The pellets stick against the aluminium plate until a certain magnitude of shear stress is reached. After this a sudden slip occurs, bringing the shear stress down to a lower value. This behaviour is repeated periodically. The same normal stress levels were used with the polypropylene pellets on an aluminium plate and they were sheared at the same rate. The results are shown in Fig. 3. It can be seen that slip-stick fluctuations are absent in this case for all stress levels.

A stainless steel plate was used to perform the same kind of tests with the two pellets. Figure 4 shows the shear response between PET pellets and steel plate. It can be seen that the slip-stick response is present for steel as well. Comparing Figs. 2 and 4 it can be seen that while there is negligible shear stress fluctuation at the lowest stress level considered (5 kPa) for the aluminium plate there is significant fluctuation with the steel plate. Moreover the increase in shear stress fluctuations with normal stress is more gradual with steel in comparison to aluminium. Figures 2 and 4 also show that the typical magnitude of slip displacement of PET pellets is larger for stainless steel than for aluminium. The fluctuation magnitude is also larger with stainless steel. The blue polypropylene pellets were also tested with the stainless steel plate. The results are shown in Fig. 5 and once again exhibit no slip-stick.

By dividing the maximum shear stress value by the normal stress we obtain the maximum wall friction coefficients at different normal stress levels. Similarly the minimum wall friction coefficients can be obtained by using the minimum shear stress values. It was found that the maximum friction coefficients are not influenced by normal stress variations in the PET-aluminium combination. On the other hand, the minimum wall friction coefficients for this combination reduce significantly with increase in normal stress (Fig. 6). For PET–stainless steel combination both, maximum and minimum wall friction coefficients, show a small reduction with normal stress (Fig. 7).

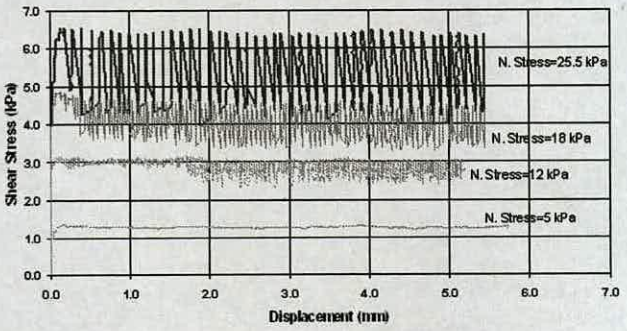

Figure 2: PET-aluminium shearing response.

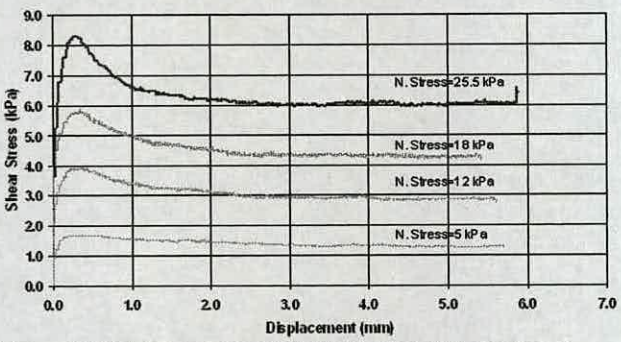

Figure 3: Polypropylene-aluminium shearing response.

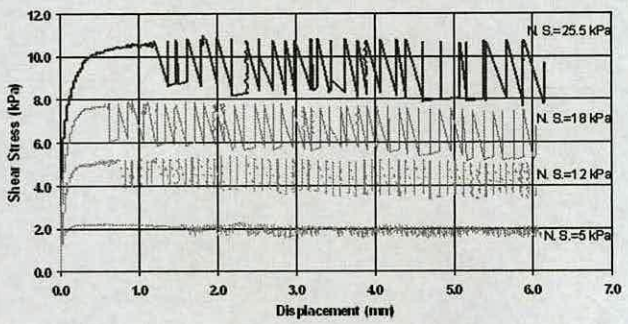

Figure 4: PET-steel shearing response.

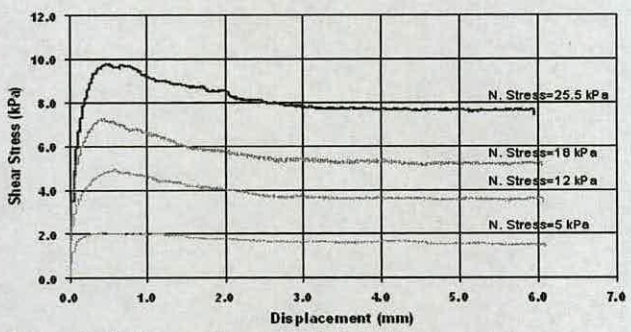

Figure 5: Polypropylene-steel shearing response.

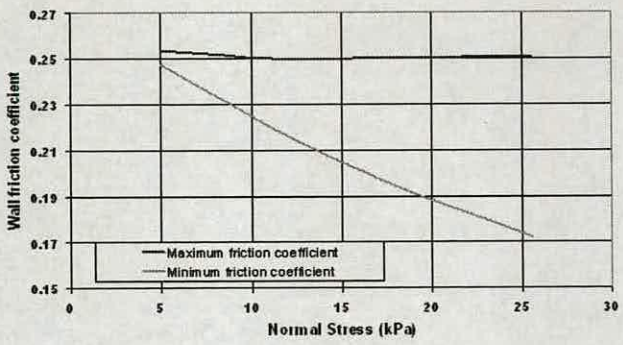

Figure 6: PET-aluminium wall friction coefficient.

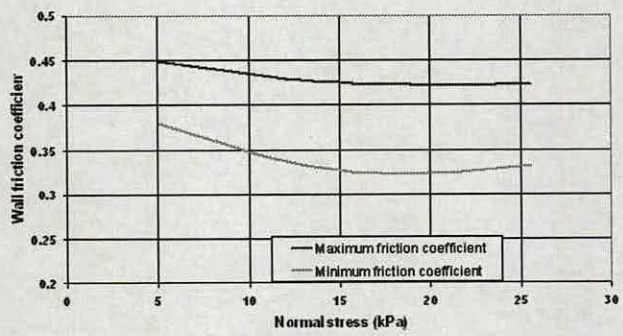

Figure 7: PET-steel wall friction coefficient.

3.2 Slip-stick variation as a function of time

Figure 8 shows the shear stress response of PET pellets on aluminium and stainless steel plates as a function of time for 25.5 kPa normal stress. It can be seen that the frequency of fluctuations for aluminium plate is higher than for stainless steel. Typically in each cycle the duration between the minimum shear stress value to the maximum value (stick zone) is longer in the stainless steel plate than the aluminium plate.

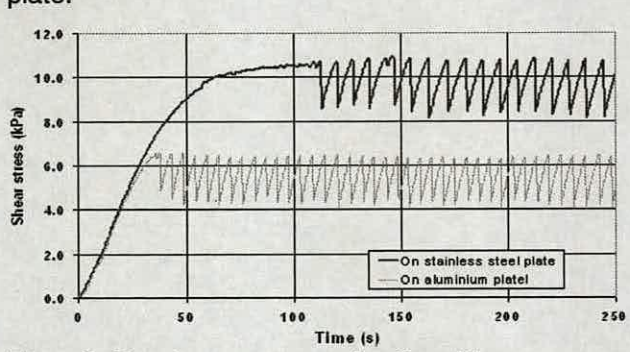

Figure 8: Shearing response as function of time.

3.3 Sample size effect

All the tests described above were conducted with a large ring with 143 mm diameter. To examine the influence of sample size two other ring sizes were included – a standard ring (95 mm diameter) and a small ring (63 mm diameter). It may be noted that for Jenike tests 95 mm diameter ring is standard. Figure 9 shows that for PET–aluminium combination, large slip-stick fluctuations are observed only when pellets were placed in the large ring. The response with standard and small rings is similar and slip-stick is almost absent. In the three tests, the maximum wall friction coefficient is independent of sample size. The normal pressure was then increased from around 25 kPa to about 56 kPa in the standard and small rings. Results are shown in Fig. 10. At this normal stress level, slip-stick response appears in the standard ring sample, but not in the small ring sample. The magnitude of shear stress fluctuations in the standard ring sample is about 3 kPa. The maximum wall friction coefficient reduces slightly from its value at the normal stress of 25 kPa. Further increase of normal stress level (to 126 kPa) in the small ring also showed significant slip-stick fluctuations. This slip-stick dependency on sample size and stress level cannot be readily explained. The same tests were carried out for the blue polypropylene pellets. The behaviour of the pellets was very similar in the three sample sizes. No slip-stick response was observed for any of the ring sizes.

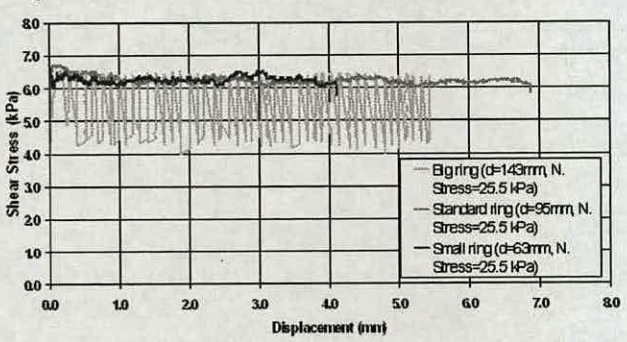

Figure 9: PET-aluminium shearing response for different ring sizes at approximately 25 kPa.

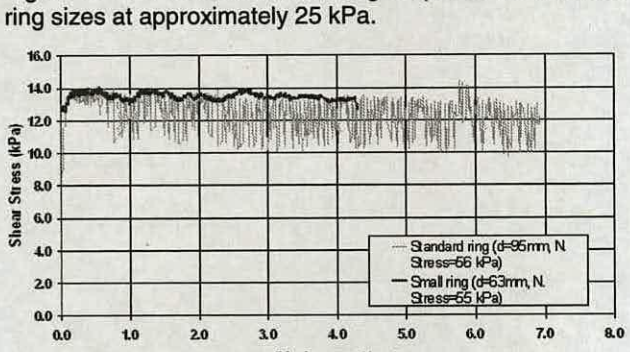

Figure 10: PET-aluminium shearing response for different ring sizes at approximately 55 kPa.

3.4 Internal friction tests

The procedure described in Section 2 for testing particle-particle interaction was carried out for the two pellets. The tests were conducted at a stress level of about 25 kPa. Previous tests on known-to-honk pellets, where normal stress variation has been taken into account, have shown that the slip-stick response between particles is not as cyclic and significant as it is for particle-wall interaction [4,5]. Again, three different sizes of shear rings (large, standard and small) were used. Figure 11 shows that the sample size appears to influence the shear

stress response. Intermittent drop of shear stress was observed. The results show that these drops tend to reduce when the sample size increases. Similar tests, using the large, standard and small ring, were conducted for the blue polypropylene pellets. The results are shown in Fig. 12. Intermittent drops in shear stress were less evident for the three different sample sizes. The effect of sample size is less clear for the interaction between particles in both pellets.

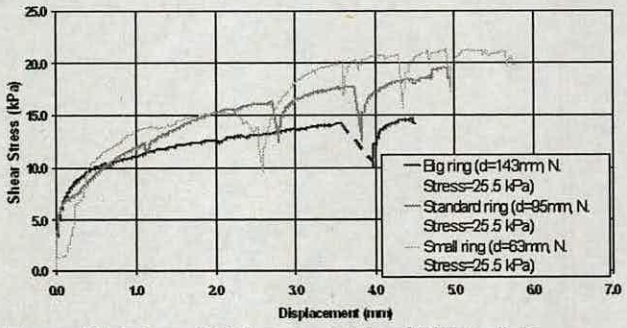

Figure 11: Internal friction response of PET pellets.

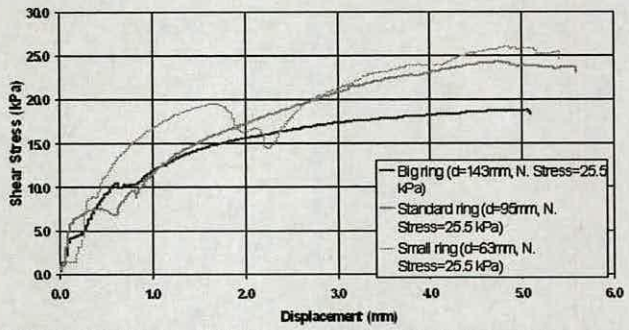

Figure 12: Internal friction response of polypropylene pellets.

4 CONCLUSIONS

The study shows that slip-stick, represented by shear stress fluctuations, is absent when the blue polypropylene pellets are sheared on either aluminium or stainless steel plates. On the other hand shear stress fluctuations are observed with PET pellets for both plate materials. The magnitude of these fluctuations increases with normal stress, indicating these fluctuations would be larger at the lower end of a silo. The magnitude of fluctuations is larger for the stainless steel plate. The maximum friction coefficient for PET–stainless steel is higher than that for PET–aluminium. On the other hand the frequency of fluctuation is higher for PET – aluminium. Stainless steel plate has a longer stick phase. Slip-stick response is also observed with standard and small sample sizes when tested at considerably high normal stresses.

Interaction between PET pellets and wall material (aluminium and stainless steel) is strongly influenced by slip-stick. The slip-stick response between PET pellets and the two metals considered is fairly periodic unlike honking that occurs intermittently [2,4-6]. Slip-stick response was observed to be stress dependent with higher fluctuations at higher normal stress levels. Silo honking too has been reported to occur at high fill levels [5] that induce high stress levels. Silo honking has also been reported to commonly occur at high outflow rates [6]. However, studies suggest that the magnitude of slip-stick fluctuations reduces when shearing rate increases [5,8]. How slip-stick fluctuations lead to honking, if they do, is yet to be fully understood.

ACKNOWLEDGEMENTS

We would like to thank Mark Astin, Tim Bell, John Carson, Bret Cooper, Ron Dailey, Paul Dean, Paul Denby, Michael Duerr, Emily Fraser, G. J. Fons, Mike Gray, Karl Jacob, Paul Mayer, Colin Milton, Peter Moon, Allen Rogers and John Thorman for useful discussions throughout the course of the work. The authors would like to acknowledge the financial and practical assistance of Braby Silos; Dow Chemical Company; DuPont; DuPont Teijin Films; Eastman Chemical Company; Jansens & Dieperink; Jenike & Johanson Inc.; and Waeschle and the financial support of EPSRC UK (grant no. GR/R44263) and ORS Award (Chavez-Sagarnaga).

REFERENCES

[1] A. W. Roberts: Mechanics of self excited dynamic loads in bins and silos. Proc. Int. Symp. Reliable Flow of Particulate Solids II, Oslo, (1993) 983-1004.

[2] A. W. Roberts and C. M. Wenrich: Flow dynamics or 'quaking' in gravity discharge from silos. Chem. Eng. Sci., 57 (2002) 295-305.

[3] J. Tejchman and G. Gudehus: Silo music and silo quake experiments and numerical Cosserat approach. Powder Technology. 76 (1993) 201-212.

[4] J. M. Buick *et al.:* Investigation of silo honking: slip-stick excitation and wall vibration, 16th ASCE Engineering Mechanics Conference, Seattle, 2003 paper 625.

[5] J. M. Buick *et al.:* Investigation of silo honking: slip-stick excitation and wall vibration, submitted to J. Eng. Mech. ASCE. 2003.

[6] J. Tejchman: Technical concept to prevent the silo honking. Powder Technology. 106 (1999) 7-22.

[7] IChE: Standard shear testing technique for particulate solids using the Jenike shear cell. IChE/EFChE joint publication, IChE, England (1989).

[8] T. J. Budny: Stick-slip friction as a method of powder flow characterization. Powder Technology. 23 (1979) 197-201.

PARTEC 2004

Intermittent particle motion on the wall of a model silo during discharge

J.M. Buick[1,2], J. Chavez-Sagarnaga[1], J.Y. Ooi[1], Pankaj[1],D.M. Campbell[3],C.A. Greated[3]

[1] Institute for Infrastructure & Environment, School of Engineering & Electronics, University of Edinburgh, Edinburgh EH9 3JN, U.K.

[2] Department of Physics and Electronics, School of Biological, Biomedical and Molecular Sciences, The University of New England, Armidale, NSW 2351, Australia.

[3] School of Physics, University of Edinburgh, Edinburgh EH9 3JZ, UK.

ABSTRACT

A novel approach is presented for investigating motion of particles on the wall of a model silo. Measurements are presented for a 1.7 m tall and 0.65 m diameter silo with transparent Lexan walls. The motion of PET particles was recorded visually during discharge using a digital CCD camera and analysed using image processing techniques to give quantitative velocity information. The particles are seen to move with intermittent motion. The particles remained stationary against the silo wall for around 0.1 s and then slip against the wall for a further slightly longer period of time. This pattern of motion is repeated in a regular manner. It was also observed that the particles moved in phase over the entire height of the fill, above the transition level.

1 INTRODUCTION

Wall vibrations in full-scale industrial silos have been investigated recently by a number of authors [1-6]. Two different dynamic phenomena have been observed: silo quaking and silo honking. The first mode, silo quaking, is at a low frequency of a few Hertz, while the second mode, silo honking, is at a much higher frequency of several hundred Hertz. Silo honking has been observed in a range of thin walled metallic silos where the high frequency oscillation of the wall is accompanied by an associated acoustic emission, or honk, with an intensity which is often greater than 100 dB. The excitation mechanism is not fully understood for either quaking or honking, however, it has been suggested that silo honking may be generated by a slip-stick motion of the particulate fill against the silo walls. Indeed, it has been shown that PET particles which induce honking in thin walled metal silos exhibit a slip-stick behaviour against a metal wall sample while other pellets which have not been reported to produce honking do not undergo slip-stick motion under similar circumstances [7]. Further, numerical simulations of particle motion in a small-scale silo using the discrete element modelling (DEM) [8] have also shown intermittent particle motion at the wall. In this paper experimental evidence of intermittent motion on the wall of a model silo is presented for PET particles. The motion of the particles against the wall were recorded digitally and analysed to provide quantitative information on particle motion.

2 EXPERIMENTAL PROCEDURE

The experimental system is shown in Fig. 1. The model silo was 1700 mm high with a diameter of 650 mm and was constructed from 1 mm thick transparent Lexan polycarbonate. The silo had a flat bottom and discharged through a central hole with diameter 65 mm. The silo was filled to a height of approximately 1300 mm from a holding box above the silo, which was filled from the silo discharge by an auger. Both the auger and the refill from the holding box were stopped during the period while the measurements were taken. Images of the particles moving against the model silo wall were obtained using a Sony DCR-TRV340E digital camera. These images were analysed to obtain quantitative information about the velocity of the particles at the wall.

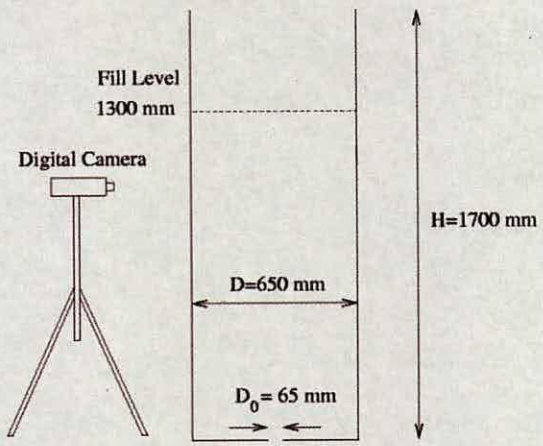

Figure 1: The experimental set-up used to acquire digital images of the PET particles at the silo wall during discharge.

3 ANALYSIS OF IMAGES

The images of the particle motion were analysed to obtain quantitative velocity information about motion

of the granular particles. This was done by dividing each image into small regions. The velocity in each region was then obtained using a cross-correlation routine between successive images. Full details of the technique can be found in [9].

4 RESULTS

Six typical consecutive digital images of the PET particles against the silo wall are shown in Fig. 2. The time separation is $\Delta t = 0.12$ s.

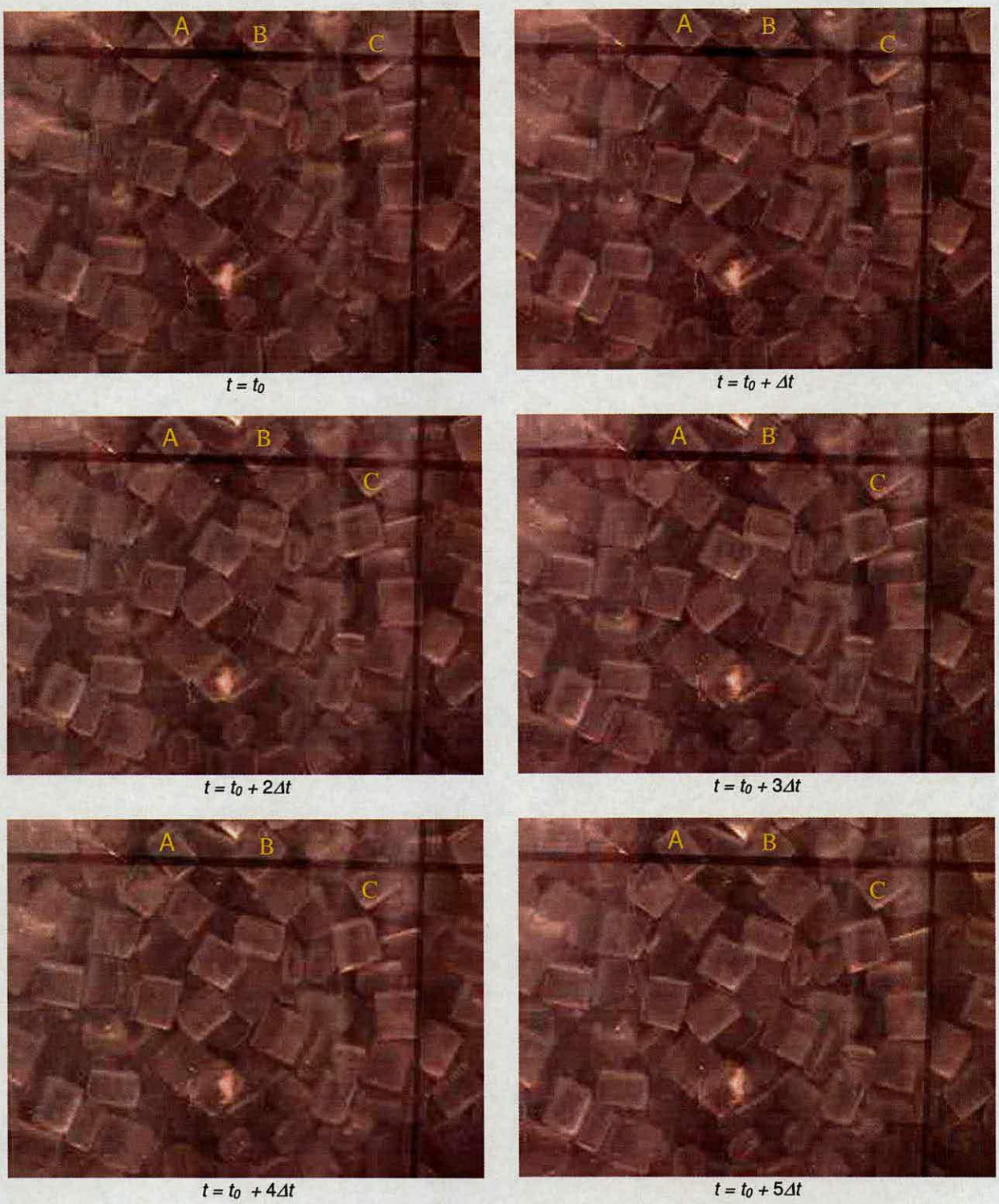

Figure 2: The position of the PET particles in the model silo at successive times. The motion of the particles is best observed in relation to the solid horizontal line which was marked on the outside of the silo wall.

The dimensions of the rectangular region shown in Fig. 2 are approximately 37 mm by 28 mm. The black horizontal line in the images is drawn on the outside wall of the silo and is 1000 mm above the base of the silo which is well above the transition region (between 600 and 700 mm above the base) and significantly below the top of the fill level which was approximately 1300 mm above the base. The motion of the particles can be observed between the six images which are shown. This is best done by comparing particles which are adjacent to, or bisected by, the 1000 mm line on the silo wall. For example, consider particles A, B and C which are marked on the initial picture at $t = t_0$. Both particles A and B are initially sitting just above the horizontal line. During the first four time intervals, Δt, these two particles (A and B) move down steadily. At $t = t_0 + 4\Delta t$ both of the particles are approximately a third of the way past the line. Similarly, it can also be seen that particle C, and any other particle which can be identified, has also moved down the wall by roughly the same distance. Comparing the particles between $t = t_0 + 4\Delta t$ and $t_0 + 5\Delta t$, the motion of the particles can be seen to have stopped. It is also possible to estimate the particle velocity between $t = t_0$ and $t_0 + 4\Delta t$, the particles have moved two to three mm in about half a second.

Clearly direct observation of the particle images can give some qualitative information about the motion of the particles, in particular it is clear that the particles are moving in an irregular manner: sometimes stationary and at other times slipping against the silo wall. However, in order to obtain a more quantitative description of the motion it is necessary to analyze the images further. This was done using the technique outlined in Section 3 [9]. A time series of velocity vector maps was obtained over the region of the silo wall which was imaged. Given the small dimensions of the region it can be assumed to be approximately flat with minimal distortion of the results due to the curved nature of the silo wall. At any time, the value of the velocity over the region considered in Fig. 2 was found to be constant. For this reason the average velocity in each special region was considered at each time interval.

The value of the spatially averaged velocity was, however, found to vary with time as was expected from the visual observations of the particle motion. Figure 3 shows the measured particle velocity as a function of time over a time period of approximately 15 s. There are two distinct modes to the motion: a period where the particles are sliding on the silo wall with a velocity between about 4 ms^{-1} and 6 ms^{-1}; and a shorter period where the particles are stationary against the wall. It is important to realize that the velocities shown in Fig. 3 represent the temporal average of the velocity of the PET particles over the time between images. This may partially account for the range in the measured velocities of the moving particles.

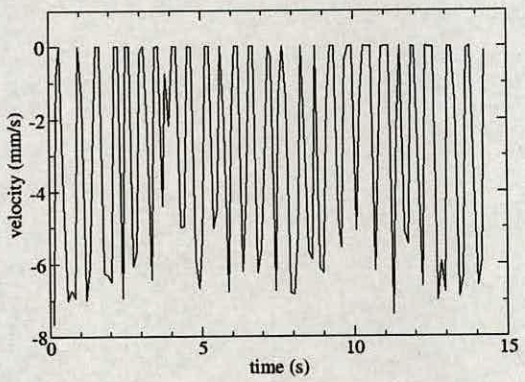

Figure 3: The velocity of the PET particle against the silo wall as a function of time.

Only a small region of the silo wall is shown in Fig. 2, however, other measurements taken over considerably larger areas suggest that the particle motion is in phase over the whole of the silo (from the transition level to the top of the fill).

It is also evident from fig. 3 that the intermittent motion of the particles is relatively regular. To further investigate this the velocity time-series in Fig. 3 was Fourier transformed and the spectrum is shown in Fig. 4.

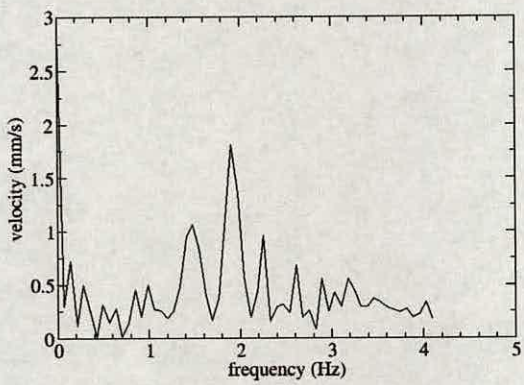

Figure 4: The frequency spectrum of the particle velocity from the results in Fig. 3.

The intermittent nature of the motion is not completely regular; it repeats with a frequency between 1.5 and 2.5 Hz. It is interesting to note that the frequency spectrum is not a smooth Gaussian like distribution; rather there are a number of distinct peaks in the spectrum.

5 DISCUSSION AND CONCLUSIONS

The motion of PET particles against the transparent wall of a model silo has been investigated. This was done by taking digital images of the particles to obtain a qualitative description of the particle motion. The particles were seen to move in an intermittent manner. They remained stationary against the silo wall for a period of time of the order of 0.1 s. The particles then fall abruptly before coming to rest and the cycle is repeated. The images were further analyzed to provide quantitative information about the particle velocity. It was found that the all particles moved in phase. That is, all the particles, over the entire wall of the silo, were either stationary or sliding against the wall at the same time.

This intermittent motion is consistent with DEM simulations [8] on a silo with similar dimensions where similar motion was observed with a higher frequency of around 7 Hz. The motion of the particles is also similar to slip-stick response which has been observed between the same PET particles and aluminum and stainless steel plates with the same grade and thickness as those used in silo construction [7]. This slip-stick motion was observed using a Jenike shear tester and was only observed when a normal stress was applied with a level typical of that found in a full-scale silo. The normal stress level in the model silo considered here is considerable less than the minimum level in [7] at which slip-stick was observed. There are clearly a number of differences between the polycarbonate walls of the model silo and the metal plates used in [7], not least the increased flexibility of the model silo and the different frictional properties of the wall. The results, however, indicate that the particles are moving against the wall with intermittent motion in the model silo which has a lower normal stress level.

Given the significant differences in normal stress between the model silo and those used in [7], it is not evident that the same mechanism is responsible for both motions, although friction apparently plays an important role in both. Before the particulate solid can flow through the silo it is necessary for it to dilate and loosen. In doing this a pressure wave can be set up which can propagate through the fill. The presence of such a pressure wave could account for the intermittent motion which has been observed in the model silo.

It is also interesting to consider that horizontal wall vibrations have also been observed in the model silo during discharge [9]. These have a frequency of around 3 Hz, corresponding to the natural frequency of free vibration of the silo wall. This indicates that vertical motion of the particles is coupled with radial vibrations of the silo wall. Such a coupling is required in a full-scale silo if the slip-stick motion of the particulate fill against the wall is the driving mechanism for silo honking and/or quaking.

ACKNOWLEDGEMENTS

We would like to thank Mark Astin, Tim Bell, John Carson, Bret Cooper, Ron Dailey, Paul Dean, Paul Denby, Michael Duerr, Emily Fraser, G. J. Fons, Mike Gray, Karl Jacob, Paul Mayer, Colin Milton, Peter Moon, Allen Rogers and John Thorman for useful discussions throughout the course of the work. The authors would like to acknowledge the financial and practical assistance of Braby Silos; Dow Chemical Company; DuPont; DuPont Teijin Films; Eastman Chemical Company; Jansens & Dieperink; Jenike & Johanson Inc.; and Waeschle and the financial support of EPSRC UK (grant no. GR/R44263) and ORS Award (Chavez-Sagarnaga).

REFERENCES

[1] A. W. Roberts, O. J. Scott and S. J. Wiche: Silo quaking – a pulsating load problem during discharge in bins and silos. Proc. Bulk 2000 Conference, IMechE, London. 1991 7-12.

[2] G. Gudehus and J. Tejchman: Silo music and silo quake. Silos - Forschung und Praxis Tagung '92, Karlsruhe, October, 1992 103-110.

[3] A. W. Roberts: Mechanics of self excited dynamic loads in bins and silos. Proc. Int. Symp. Reliable Flow of Particulate Solids II, Oslo, 1993 983-1004.

[4] J. Tejchman: Silo quake - experiments and a polar hypoplastic model, European Symp: Storage and Flow of Particulate Solids (Janssen Centennial), March, Nurnberg, 1995 151-162.

[5] D. Schulze: Silo Quaking, Silos - Fundamentals of theory, behaviour and design, eds C.J. Brown and J. Nielsen, E & FN Spon, London, 1998 171-182.

[6] J. M. Buick *et al.:* Investigation of silo honking: slip-stick excitation and wall vibration, 16th ASCE Engineering Mechanics Conference, Seattle, 2003 paper 625.

[7] J. M. Buick *et al.:* Investigation of silo honking: slip-stick excitation and wall vibration, submitted to J. Eng. Mech. ASCE. 2003.

[8] P. W. Cleary: The effect of particle shape on hopper discharge, 2nd Int. Conf. CFD in the minerals and process industries, CSIRO, Melbourne, Australia, December 1999, 71-76.

[9] J. M. Buick *et al.*: Investigation of the motion of granular particles on the wall of a transparent model silo and the associated wall vibrations. In Preparation.

Investigating the causes of silo honking during discharge

Jesus Chavez-Sagarnaga

The University of Edinburgh, School of Engineering and Electronics,
Institute for Infrastructure and Environment, Crew Building, The King's Buildings, Edinburgh EH9 3JN

Project background and objectives

Thin metal silo structures are used all around the world to store granular bulk solids such as agricultural grains, plastic pellets and mineral ores. A number of these structures are known to emit very loud intermittent high frequency sounds, similar to a truck honk, during discharge. As noise pollution becomes increasingly unacceptable, silo honking has become an issue that needs to be urgently addressed. Often honking has sound pressure levels in excess of 100-110dB, which can cause long term hearing damage if hearing protection is not worn.

The objective of the study is to understand the dynamic phenomenon and the fundamental mechanism responsible for the above high frequency sounds in thin metal silos, with an ultimate aim to produce predictive tools and design recommendations to eliminate these unwanted sounds.

Brief description of research

Full-scale measurements of a honking silo, numerical simulation and laboratory experiments were devised and conducted to study the silo honking phenomenon.

To study the vibration and acoustic response during honking a full-scale silo structure that was known to honk was instrumented using one triaxial and several radial accelerometers, a laser vibrometer (to measure radial wall displacements and velocities) and microphones. Frequency analyses of the silo wall motions and sound pressure measurements were conducted. It was found that the frequency spectra of the acceleration and acoustic pressure measurements comprises of harmonic peaks with a fundamental acoustic frequency and higher harmonics at integer multiples of this frequency. Vertical and radial components of wall motion and acoustic measurements gave the same harmonic series of frequencies. This series was totally repeatable for all honks and was independent of the position of the accelerometer. A comparison of the radial velocity spectrum of the silo wall vibrations and the acoustic velocity spectrum (derived from sound pressure measured close to the wall) showed very good agreement. This indicates that the honking is not generated by a resonance inside the silo, as in a flute or organ pipe; but by the vibration of silo walls that act like giant speakers.

A series of Finite Element (FE) analyses were conducted to evaluate the free vibration characteristics (natural frequencies and vibration modes) of the silo structure filled up to different heights and of the empty silo. The aim was to determine the influence of the fill and to determine possible modes responsible for honking. It may me noted that while analytical solutions for simple thin-walled cylindrical structures with constant thickness and without particulate fill exist in literature numerical solutions need to be resorted to for filled variable thickness silos. The available analytical solutions were used, however, to verify the accuracy of FE models. A range of possible modes that may be responsible for honking have been identified. The dynamic excitations that lead to honking are not fully understood. FE analysis is being conducted to evaluate the dynamic response of the silo using different excitations that may exist in a silo during discharge.

A variety of dynamic forces are exerted on a silo structure during discharge. These include forces due to dilatation (which causes flow) creating pressure waves within the solid that are transmitted to the structure and slip-stick excitations between particles and between particles and the silo walls. To evaluate the slip-stick interaction between particles and the silo wall experiments were conducted using a Jenike shear tester with a large shear cell of 143 mm diameter. Different normal stress levels were chosen to reflect the stress state in the solid during storage. Particulate solids that are known to cause honking and those that that do not were considered. The shearing response showed that pellets that are known to honk exhibit slip-stick behaviour while particles that have not been observed to honk do not. The amplitude of slip-stick motion increases with normal pressure. However, the frequency of slip-stick motion is considerably smaller than honking frequencies indicating that the honking phenomenon is not due to steady state harmonic response of the silo.

Potential for application of the results

The fundamental understanding of the honking phenomenon and development of predictive tools will provide a sound methodology for eliminating honking in existing silos and preventing it in those that will be designed in future.

Funding bodies

The study is by supported by the EPSRC (grant no. GR/R44263) and by the ORS Award Scheme. Braby Silos; Dow Chemical Company; DuPont; DuPont Teijin Films; Eastman Chemical Company; Jansens & Dieperink; Jenike & Johanson Inc.; and Waeschle are also providing financial and practical assistance.

INSTITUTE OF PHYSICS PUBLISHING JOURNAL OF PHYSICS D: APPLIED PHYSICS
J. Phys. D: Appl. Phys. 37 (2004) 2751–2760 PII: S0022-3727(04)79851-4

Motion of granular particles on the wall of a model silo and the associated wall vibrations

J M Buick[1,2,3], Pankaj[2], J Y Ooi[2], J Chavez-Sagarnaga[2], A Pearce[2] and G Houghton[2]

[1] Physics and Electronics, School of Biological, Biomedical and Molecular Sciences, The University of New England, Armidale, NSW 2351, Australia
[2] Institute for Infrastructure & Environment, School of Engineering & Electronics, University of Edinburgh, Edinburgh EH9 3JN, UK

E-mail: jbuick@une.edu.au

Received 27 April 2004, in final form 7 July 2004
Published 15 September 2004
Online at stacks.iop.org/JPhysD/37/2751
doi:10.1088/0022-3727/37/19/022

Abstract
Dynamic phenomena during discharge of a silo are not well understood. This study uses a dual approach to quantify the motion of both the particulate solid at the wall of a model silo and the wall itself. The motion of particles was recorded visually using a digital CCD camera. The particles are seen to move with an intermittent motion. Image analysis techniques were then applied to obtain quantitative measurements of the particulate velocity. In relation to the particle motion, the silo walls were observed to vibrate during discharge. These vibrations were measured using a laser vibrometer to obtain independent measurements of the radial displacement and velocity. This enabled comparisons to be made between the particulate motion and the wall vibrations. Results are presented for barley and for polyethylene terephthalate pellets.

1. Introduction

Wall vibrations in full scale industrial silos have been investigated recently by a number of authors and several sources of dynamic excitation in silos have been proposed [1–9]. These include dilation (density changes) in the solid during flow; stick–slip behaviour between stored solids and silo walls; internal stick–slip behaviour within stored solids; alternating flow patterns during flow; and intermittent collapsing arches in the solid. Although in some studies (e.g. [10,11]) silo honking (or music) and silo quaking (or shocks) are considered together, these are two distinct phenomena. Industrial experience shows that silos may both quake and honk, may quake but not honk or may honk but not quake. Silo honking is a high frequency sound, similar to a very loud truck horn, that emanates intermittently from a silo during discharge. While silo honking leads to severe noise pollution, there is little concern that it may cause structural integrity problems. Studies conducted by Buick *et al* [8,9] have shown that honking results from a silo structure vibrating as a giant speaker at high frequencies (a few hundred hertz) in a fixed harmonic set of frequencies (a fundamental acoustic frequency and its multiples). On the other hand, quaking has a predominantly low frequency and a high displacement amplitude response that can be defined as band limited low frequency noise. Industrial silos have been known to fail due to quaking. The excitation mechanism is not fully understood for either quaking or honking; however, it has been suggested [3,12] that stick–slip motion of the particulate fill against the silo walls plays an important role in these dynamic phenomena. Indeed it has been shown that polyethylene terephthalate (PET) particles that are known to honk exhibit stick–slip behaviour against aluminium plates, while polypropelene pellets that are not known to honk do not [9,13]. This paper presents measurements of the wall vibrations that were taken during discharge of a model silo with transparent polycarbonate walls. The motion of the particles against the wall were recorded digitally and analysed to provide

[3] Author to whom any correspondence should be addressed.

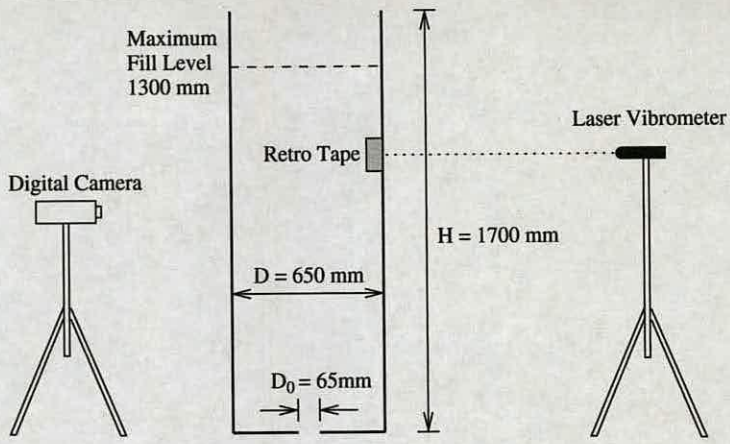

Figure 1. Experimental set-up.

quantitative information on particle motion. The relationship between particle motion and wall vibration is discussed.

2. Experimental procedure

The experimental system is shown in figure 1. The model silo was 1700 mm high with a diameter of 650 mm and was constructed from 1 mm thick transparent Lexan polycarbonate. The silo had a flat bottom and discharged through a central hole with a diameter of 65 mm. The silo was filled to a height of between 1100 and 1300 mm from a holding box above the silo, which was filled from the silo discharge using an auger. Both the auger and the refill from the holding box were stopped during the period while the measurements were taken. This was to ensure that the observed vibration was a result of the silo discharge and was not influenced by the preceding filling process. It is also important to ensure that vibrations do not arise from stopping the fill process. Therefore sufficient time was allowed for any such vibrations to decay before taking any measurements. Silo wall vibrations were measured using a Polytec laser vibrometer, OFV-3001-23/OFV-303, which was directed along the radial direction of the silo onto a piece of reflective retro tape on the silo wall. The retro tape was used to reflect the laser beam, enabling a high quality reflection to be obtained from a transparent material. The laser vibrometer was used to measure the radial velocity and displacement of the wall. The velocity is calculated from the Doppler shift of the reflected light, while the displacement is determined from the phase of the light, which is circularly polarized. This gives two independent measurements of the wall vibrations. Images of the particles moving against the model silo wall were also obtained using a Sony DCR-TRV340E digital camera. These images were analysed to obtain quantitative information about the particle velocity at the wall.

Two different particulate solids were used for the experimental studies: PET and barley. The PET pellets considered were in the shape of flattened cylinders with an elliptic cross-section. The typical cross-section of these pellets was 4 × 1.5–2 mm with 4 mm height and density was in the range 770–890 kg m^{-3}. The barley had a density in the range 714–867 kg m^{-3} and had a typical length of approximately 10 mm.

3. Analysis of particle images

The motion of the granular particles against the model silo wall was observed to be intermittent for both PET and barley. The particles remained stationary against the silo wall for a short period of time. After this the particles moved downwards in a short burst of motion before becoming stationary again. The timescales for the stationary and the moving phases were different for PET and for barley. This motion was captured using a digital camera. This enabled the motion to be viewed and qualitatively assessed as above. To quantitively investigate the particle motion, the successive digital images were analysed using the cross-correlation technique, which is a well established approach to determining the velocity profile of small tracer particles in particle image velocimetry [14, 15] and has also been shown to be applicable to larger-scale objects [16]. The approach is summarized in figure 2.

Two images taken at a small time separation Δt are considered. Each image is divided into small interrogation areas of the same size. In these study regions 32 by 32 pixels were used. Each interrogation region consists of an intensity map, I, over a small region of space. In figure 2, the selected regions show two particles that are clearly seen to move between the images. The two intensity maps are then Fourier transformed using an FFT and the cross-correlation performed in Fourier space. The correlation plane, C, is then obtained through an inverse transform. The position of the peak in the correlation plane, see figure 2, corresponds to the mean displacement between the two intensity maps. The position of the peak in the correlation plane is determined to sub-pixel accuracy using a Gaussian peak fitting algorithm. Finally, the pixel displacement is converted to a velocity vector using the magnification of the image and the time separation of the frames. The magnification, measured in pixels per millimetre, was obtained by taking an image of a metal ruler against the silo wall, while the time separation of the images is determined by the frame rate of the camera. Applying this technique in each interrogation region in the image gives a two-dimensional vector map of the particle velocity. Each vector in the map corresponds to the average velocity within the interrogation region and the velocity vectors lie on a regular grid. This analysis gives the mean translational velocity of the

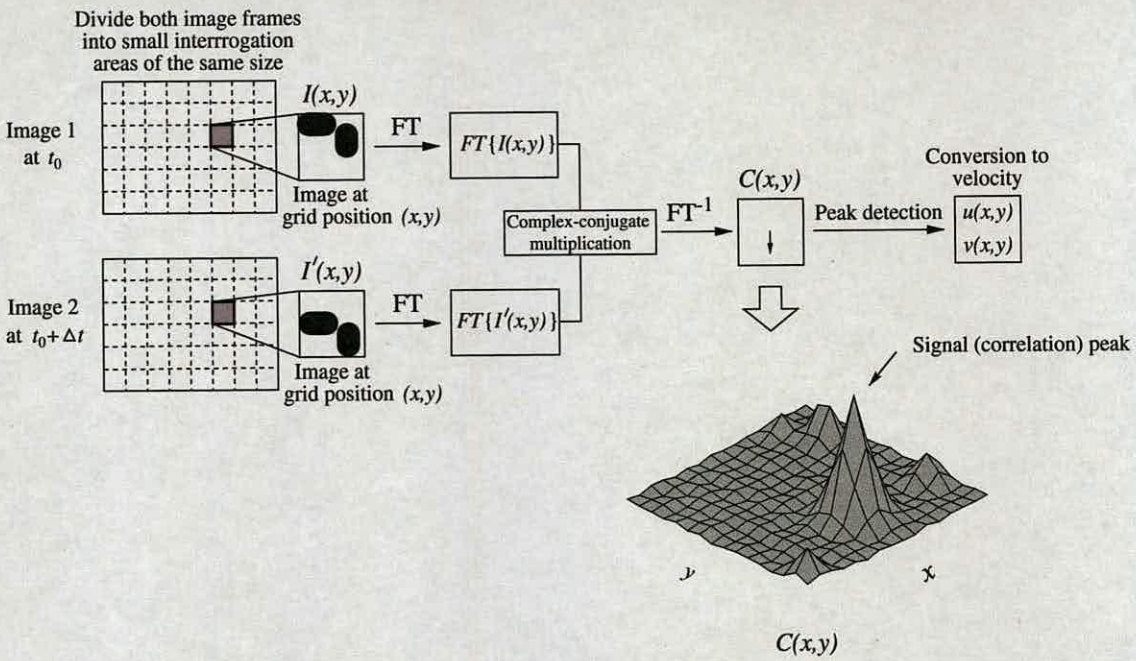

Figure 2. Analysis of the digital images for obtaining velocity information.

particles, and no information concerning particle rotation can be obtained. Two examples are shown in figures 3 and 4 for PET and barley particles, respectively. In figure 3, the PET particles are of a size similar to that of the interrogation region, and thus each velocity vector corresponds approximately to the translational motion of a single particle. Comparing figures 3(*a*) and (*b*) the motion of the individual PET particles can be clearly seen between the images (for example, see particles marked A and B) and appears to be uniform over the whole image. The vector map in figure 3(*c*) confirms this. This shows an approximately constant velocity over the whole of the image with a velocity of around 5 mm s^{-1} at that instant. In figure 3(*c*) there are a number of missing vectors. These arise from outliers that occur when there is no significant peak in the correlation plane. This can occur, for example, when a single particle fills one of the interrogation regions giving very poor contrast between each of the pixels. There is also a slight variation in the magnitude of the vectors in the bottom row of figure 3(*c*), and this may be due to a slight distortion of the image at the bottom edge. All the vectors in figure 3(*c*) are pointing in the negative z direction, indicating that there is negligible horizontal motion of the particles. The time between successive images was 0.12 s; in figure 3 the separation between (*a*) and (*b*) is $3\Delta t$ to highlight the motion of the PET particles.

The images in figure 4 show a larger region of the silo wall with barley as the fill particles. In this case there are several particles in each image and each vector in figure 4(*c*) corresponds to the average velocity in the interrogation region. In figures 4(*a*) and (*b*) there is a considerable amount of glare in the left-hand half of both images. It proved to be difficult to illuminate a large region of the silo sufficiently to obtain good quality images without observing some reflection of the light in the image. The glare on the left-hand half of figures 4(*a*) and (*b*) renders this part of the image unusable for obtaining quantitative velocity information. However, given the curved nature of the silo wall, it was not possible to focus the camera across the variation in the depth of field across the image. For this reason the camera was focused on the region in the right-hand half of figures 4(*a*) and (*b*) and it was therefore not necessary to investigate alternative forms of lighting. This means that the vectors obtained in the left-hand half of figure 4(*c*) are unreliable and only the vectors in the right-hand half of the image can be considered. In this larger region the vectors are still very regular. This was observed in all vector maps for both sets of images and suggests that the temporal variation in the velocity can be investigated by considering the spatially averaged velocity over the whole of the image for which meaningful velocity information was obtained. That is, in images such as those shown in figure 3, the whole vector field is used in the spatial averaging, while for images such as those shown in figure 4 we only use the region where reliable velocity information was obtained.

4. Results

The results are presented in two sections: first the measurements of the particle velocity are considered; and second the wall vibrations measured with the laser vibrometer are discussed.

4.1. Particle motion on the silo wall

The following results, unless otherwise stated, correspond to a spatial average over the whole region for which reliable results were obtained. Each set of results is presented with a schematic representing the region of the silo wall at which the original images were recorded.

Figure 5 shows the temporal variation of the particle velocity at the silo wall over a 13 s time period during the

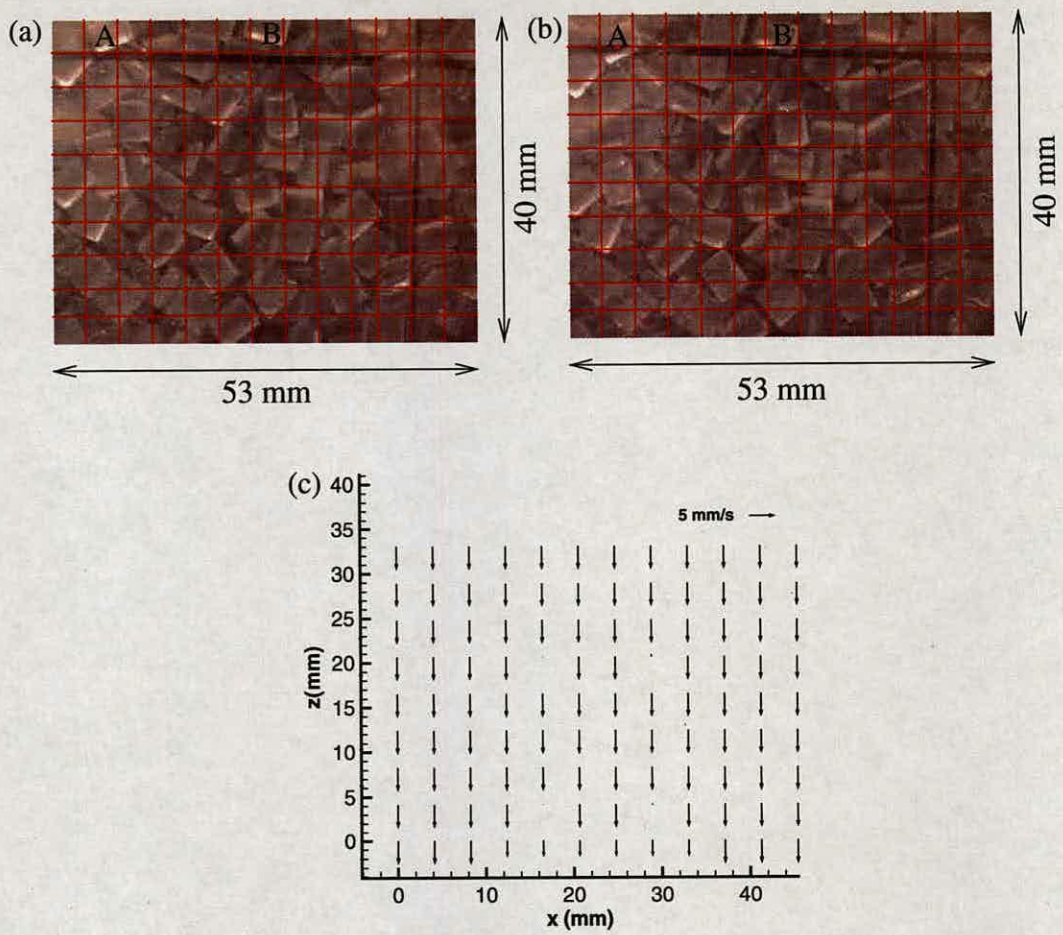

Figure 3. (*a*) Image 1. (*b*) Image 2, a time $3\Delta t$ later. (*c*) The velocity vector map for PET pellets.
(This figure is in colour only in the electronic version)

discharge of PET pellets. The results show short periods of the order of a few tenths of a second during which the particles are stationary. Between these stationary periods the particles are moving along the wall with a downward vertical velocity of the order of 4–8 mm s^{-1}. The frequency spectrum of the averaged particle velocity was also calculated and is shown in figure 6.

As would be expected from the irregular nature of figure 5, the motion does not correspond to a single frequency; however, the predominant frequency of the intermittent motion can be seen to be around 1.5 Hz.

Figure 7 shows the spatially averaged velocity for discharging barley. The region over which the image is taken is significantly larger than the region shown in figure 5. It should be noted that the area marked on the diagram of the silo to the right of the graph in figure 7 corresponds to the area of the full image. Due to problems with reflections on the left-hand side of the image, results are only obtained from the right-hand half of the image. Barley exhibits intermittent motion similar to that of PET. The downward velocity in figure 7 appears not to go to zero but shows a slight upward velocity. Further measurements of the barley velocity over smaller regions of the wall confirmed that the velocity of the particles does drop to zero during the 'stationary' periods. This suggests that the level of noise introduced by the larger length scale may have caused the slightly upward velocity in figure 7. The results are also noisier due to the fact that only half the number of values were available to produce the average. In general, the velocity of the barley is comparable with the velocity measured for the PET pellets, and the main difference between the motion of the two particle types is that the barley remains stationary for a longer time. The frequency spectrum for the barley was also calculated and is shown in figure 8. The frequency spectrum shows a more distinct peak than the spectrum for the PET pellets (figure 6) at a frequency slightly greater than 1 Hz.

It is also of interest to determine the temporal mean velocity for both PET and barley particles. This can be found by integrating the velocity profile in figures 5 and 7 and was found to be 3.8 mm s^{-1} and 1.0 mm s^{-1}, respectively. The discharge rate from the model could have been measured during the experiment, providing further information, but that was not undertaken.

Finally, it is of interest to determine at what length scale the motion of the particles at the wall is in phase. To investigate this, a region of length 500 mm was imaged with the camera during discharge of barley from the silo. In this case the

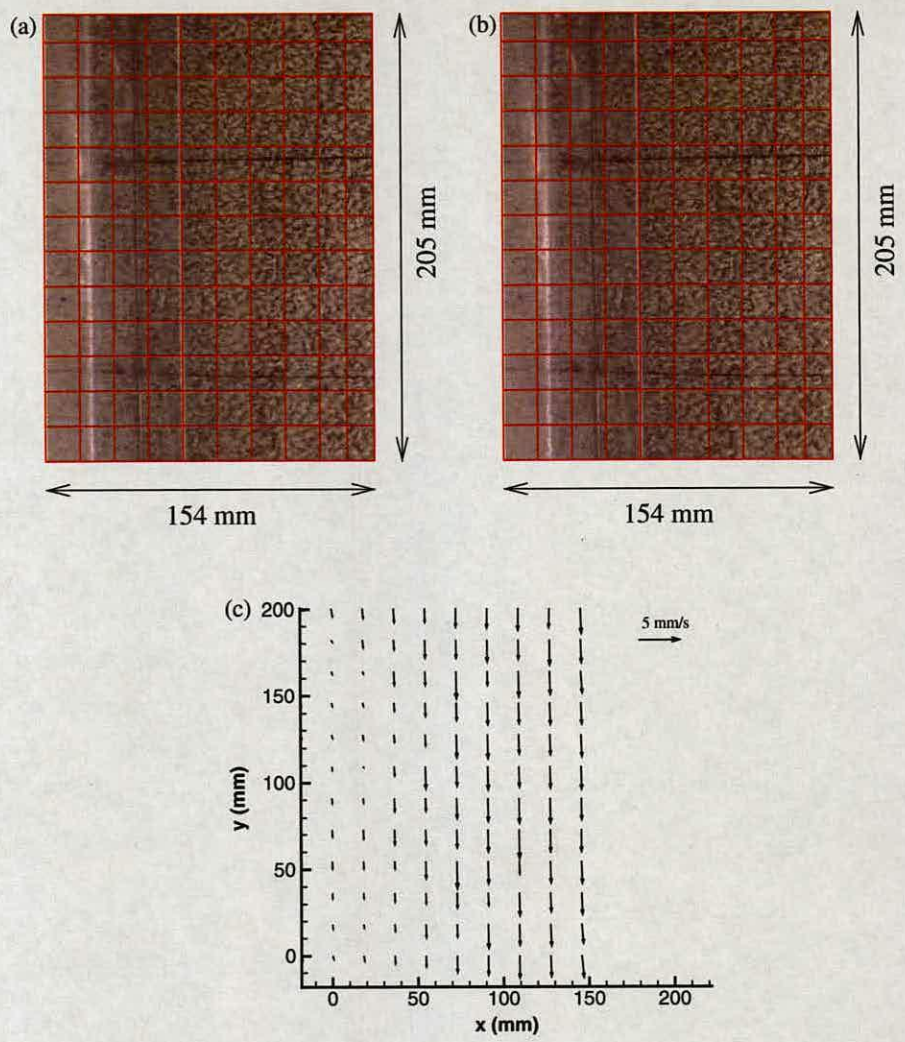

Figure 4. (*a*) Image 1. (*b*) Image 2 a time Δt later. (*c*) The velocity vector map for barley.
(This figure is in colour only in the electronic version)

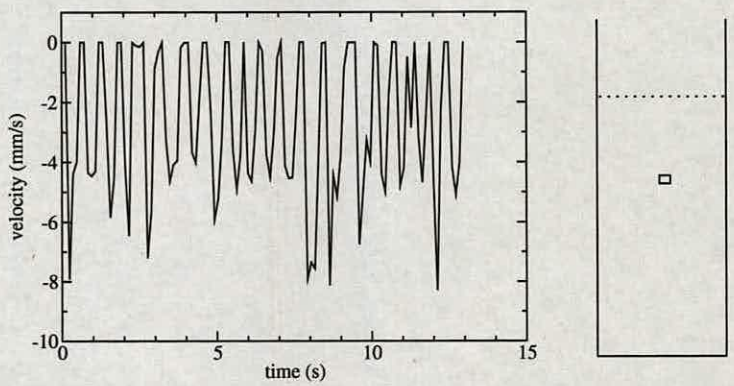

Figure 5. Temporal variation in the spatially averaged velocity for PET pellets. The image to the right of the graph indicates the area of the silo wall where the measurements were taken, the top of the image is approximately 1000 mm above the base of the silo.

velocity at a single point (averaged over an interrogation region) was considered as opposed to the spatial average over the whole length of the image, which is displayed in figures 5 and 7. This is shown in figure 9(*a*) at $z = 950$ mm and at the two extremes of the image: $z = 700$ and 1200 mm. The lower extreme is close to the observed transition region (around $z = 600$ mm), at which the particles stop moving against the wall and the flow becomes internal. The higher

extreme is close to the fill height (around $z = 1300$ mm). The results, although significantly noisier than those obtained over a smaller region, still clearly show the start–stop nature of the motion with a frequency slightly greater than 1 Hz. It is also clear that the motion of the particle is very much in phase over a length scale of 0.5 m. This is further examined in figure 9(*b*), which shows the normalized temporal correlation functions, C_{ij}, where $i, j \in \{t, m, b\}$ and t, m and b represent the top ($z = 1200$ mm), middle ($z = 950$ mm) and bottom ($z = 700$ mm), respectively. Figure 9(*b*) shows no significant time lag, τ, between the three signals. The periodic nature of the signals is also evident in figure 9(*b*) despite the noise.

4.2. *Silo wall vibration*

During discharge, wall vibrations were observed. These were large enough to be felt by touching the wall. A laser vibrometer was used to measure the radial component of the wall velocity and displacement. Figure 10 shows the velocity and displacement of the walls measured 900 mm above the base when the silo was filled to 1300 mm with PET pellet. Figure 10(*a*) shows the normal displacement and velocity over two selected time intervals. In the first time interval, $t = 17$–20 s, the motion does not appear to be periodic, while in the second interval, $t = 21$–24 s, it does.

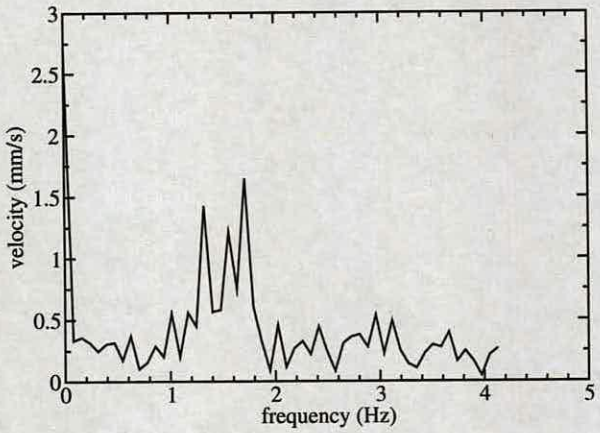

Figure 6. Velocity spectrum during discharge of PET pellets.

This difference between the motions during the two time intervals is confirmed by figures 10(*b*) and (*c*), which show both the displacement and the velocity spectra for the two time intervals, respectively. There is a clear peak in figure 10(*c*) at around 3 Hz, corresponding to the periodic motion between $t = 21$–24 s, but the peak is much smaller in figure 10(*b*). It is also clear that the motion changes rapidly between 20 and 21 s from the non-oscillatory motion observed in figure 10(*b*) to the oscillatory motion observed in figure 10(*c*). This change, from non-periodic to periodic motion, was further investigated. The velocity spectrum as a function of time is presented in figure 11. The spectrum was calculated using a 2048 point FFT. The sampling rate was 2000 samples per second, each FFT corresponding to approximately 1 s of data. The time on the axis of figure 11 corresponds to the central time of the FFT. Figure 11 indicates the nature of the intermittent bursts of periodic motion. In each case the peak initially occurs at approximately 3 Hz. There is also evidence of a peak close to 4 Hz; this is particularly evident towards the end of some of the bursts of periodic motion.

Measurements were also obtained when the silo was discharging barley. In this case wall vibrations were also observed; however, the intermittent periodic and non-periodic feature of the vibrations as observed for the PET pellets was not observed for the barley. We also note that the observed velocities were smaller than those observed for the PET particles by an order of magnitude. During discharge of barley, the walls vibrated continuously in a periodic manner as shown in figure 12. During the discharge of barley the main frequency of vibration is close to 4 Hz, with two smaller peaks at higher frequencies (figure 12*b*).

Multiple measurements were obtained for the peak frequency of the wall vibrations, which were found to be repeatable. The mean value of the peak frequency and the standard deviation were calculated. For the PET particles this was found to be 3.18 Hz with a standard deviation of 0.133 Hz, while for the barley the mean frequency was 3.89 Hz with a standard deviation of 0.159 Hz. From these results it is clear that there is a detectable difference in the frequency of the wall vibrations, depending on the fill particle.

To investigate this further, the natural frequencies of the model silo were measured. This was done using the laser vibrometer when the silo was filled with PET or barley particles

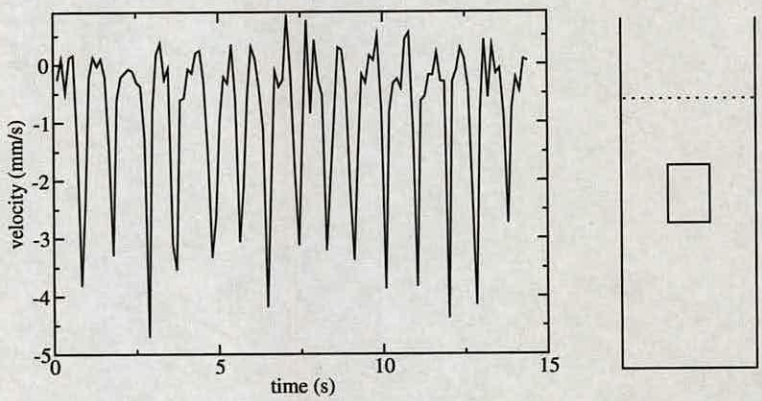

Figure 7. Temporal variation in the spatially averaged velocity for barley.

but not discharging. The silo wall was struck radially with a sharp impulse and the response was recorded. For such an impact the frequency response is expected to be dominated by the lowest natural frequency of the silo fill system. The responses are shown in figures 13 and 14 for the PET and barley particles, respectively. They show that the free vibration response of the model silo is dependent on the particle fill and that the measured peak frequency observed during discharge corresponds exactly to the natural free vibration frequency of the model silo for both barley and PET.

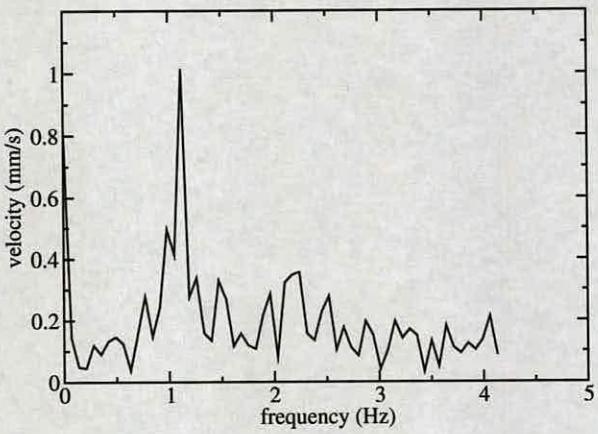

Figure 8. Frequency spectrum for the barley particles against the silo wall.

Finally, it is also of interest to check the ambient vibration response of the silo walls when there is no discharge or applied force on the silo, and vibrations are induced by the surrounding. This was measured for both PET and barley in the silo. In both cases there was a small frequency peak observed at 3 Hz and 4 Hz, respectively. The magnitudes of the peaks were similar for the two fills and were an order of magnitude smaller than the measurements for discharging barley and two orders of magnitude smaller than the results for discharging PET. This indicates that when the silo is not discharging, small wall vibrations are induced by external sources. These background vibrations are, however, considerably smaller than the oscillations observed during discharge. The ambient vibration frequencies as well as the oscillation frequencies during discharge closely match the natural frequencies of the model silo-stored solid system.

5. Discussion

Experimental studies by the authors [8, 9, 13] have shown that stick–slip motion of granular solids on a surface is stress dependant and may not be expected to occur in this model silo, where the horizontal stresses are expected to be 2–3 kPa or smaller. Furthermore, whilst stick–slip has been reported for PET pellets on aluminium or steel surfaces, it has not been reported to occur for barley. Thus the intermittent particle motion observed at the silo wall, for both PET and barley, could be caused by a different phenomenon and not stick–slip frictional response.

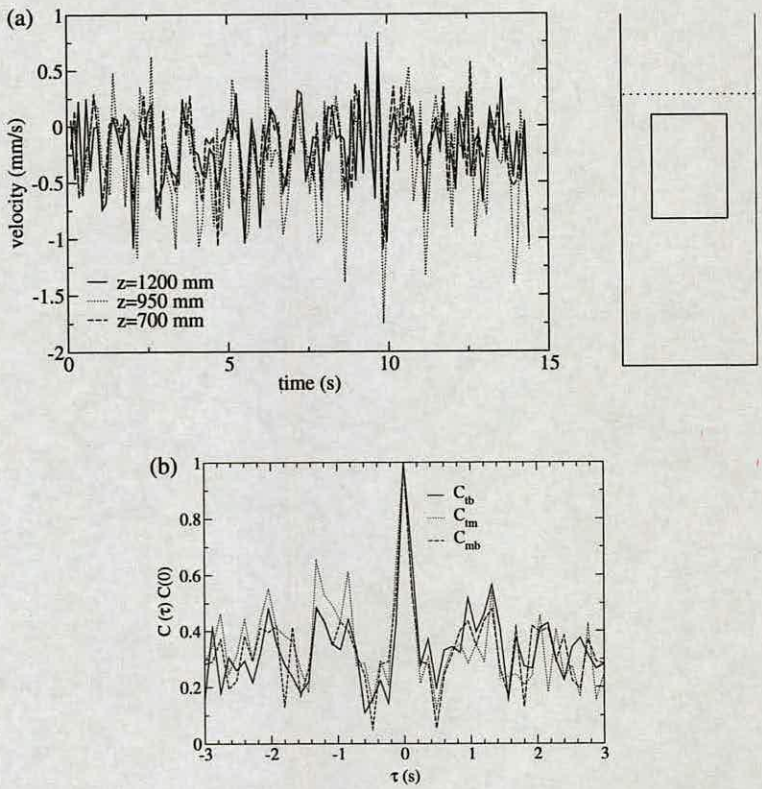

Figure 9. (*a*) Velocity profile of particle motion against the silo wall at three different heights during discharge of barley and (*b*) the correlations between the heights.

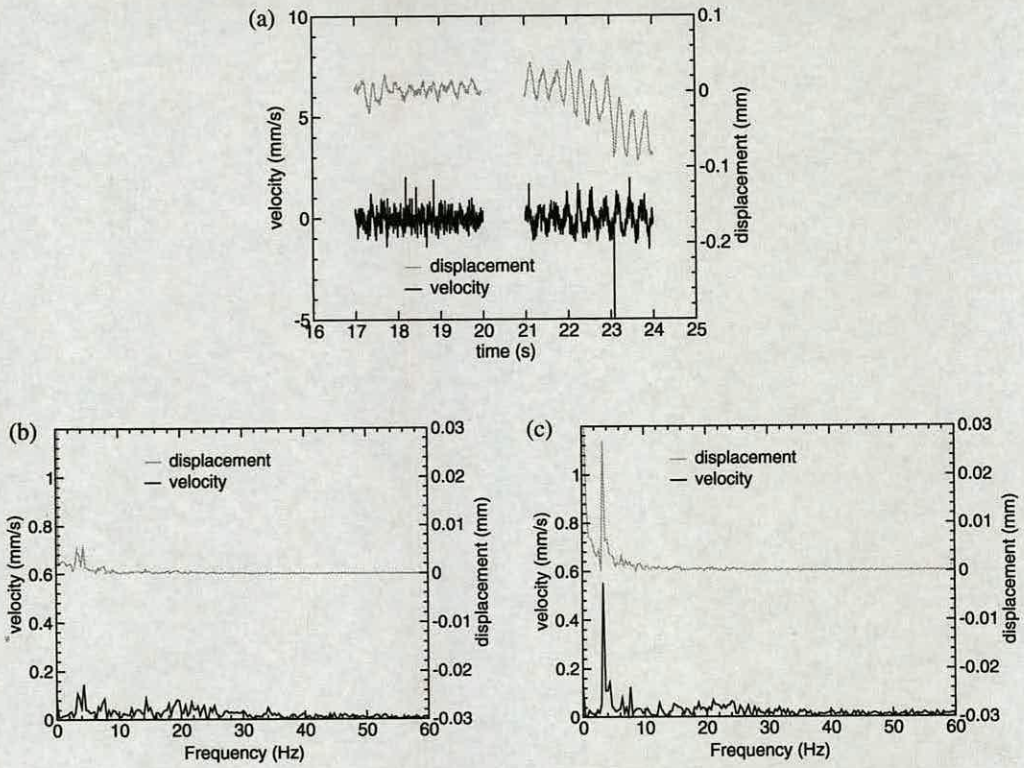

Figure 10. Velocity and displacement measurements during discharge of PET pellets. (*a*) Velocity and displacement at selected times. (*b*) Frequency spectrum for $t = 17$–20 s period. (*c*) Frequency spectrum for $t = 21$–24 s period.

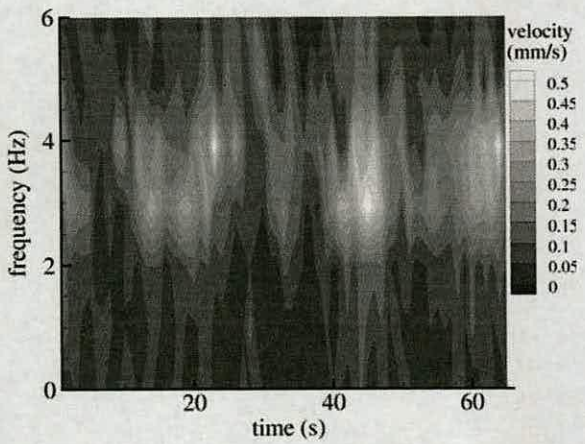

Figure 11. The frequency spectrum as a function of time.

Dynamic effects observed during silo discharge have been discussed earlier. One explanation is that changes in bulk density of the granular medium set up dilation waves that propagate vertically during discharge and that the observed frequency of the intermittent particle relates to this wave propagation. Further work is needed to verify if this can offer a plausible explanation.

What is however incontrovertible is that the dynamic excitation caused by the silo discharge has set the model silo vibrating with its lowest natural free vibration frequency (3.9 Hz for the barley–silo system and 3.2 Hz for the PET–silo system) rather than the frequency of the excitation. For both types of fill particle, the frequency of the time-variations of the particle velocities near the wall are significantly lower than the resulting wall vibrations (by a factor of 2 and 4 for the PET and barley, respectively). It might be expected that coupling at the silo wall would induce vibrations with the same frequency as the particle velocities; however, such vibrations are not supported in the particle–silo system. Rather, the particle–silo system vibrates at its natural frequency. Silo honking has already been shown by the authors [8, 9] and others [7] to exhibit a much higher frequency than the lower natural frequencies of the silo–solid system. Thus the vibration response of this model silo is more akin to the silo quaking/shaking rather than honking. The mechanism that leads to silo honking appears not to have manifested itself here.

It is also worth noting that the magnitude of wall vibrations for PET is an order of magnitude greater than that for barley. This can be attributed to several factors including the difference in properties of the two materials and their interaction with the silo wall. It indicates that PET can generate significantly larger vibrations in silos and is thus more prone to causing undesirable dynamic effects on the silo structure than barley. PET pellets are known to produce honking and quaking in industrial silos and also exhibit strong stick–slip motion in laboratory friction tests under stress levels pertaining to full-scale situations [9, 13]. Barley has neither been reported to cause silo honking nor been found to exhibit stick–slip motion in laboratory friction tests.

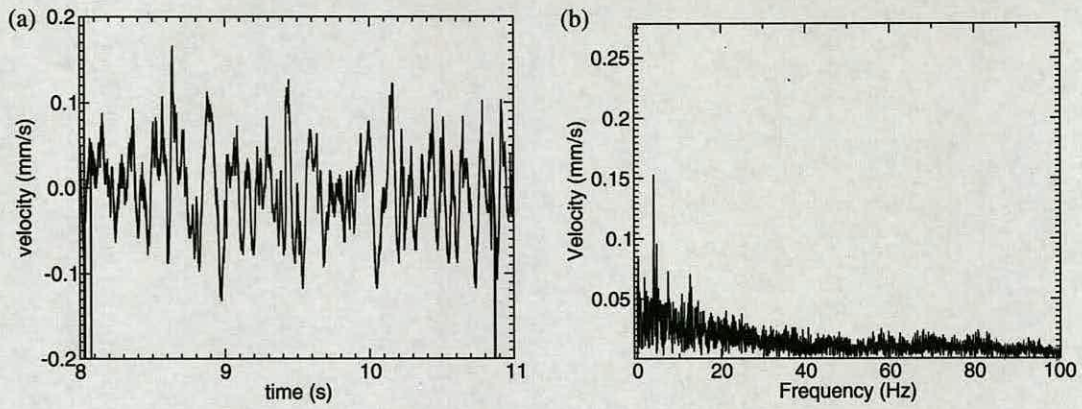

Figure 12. Velocity measurements during discharge of barley: typical velocity variation with (*a*) time and (*b*) frequency.

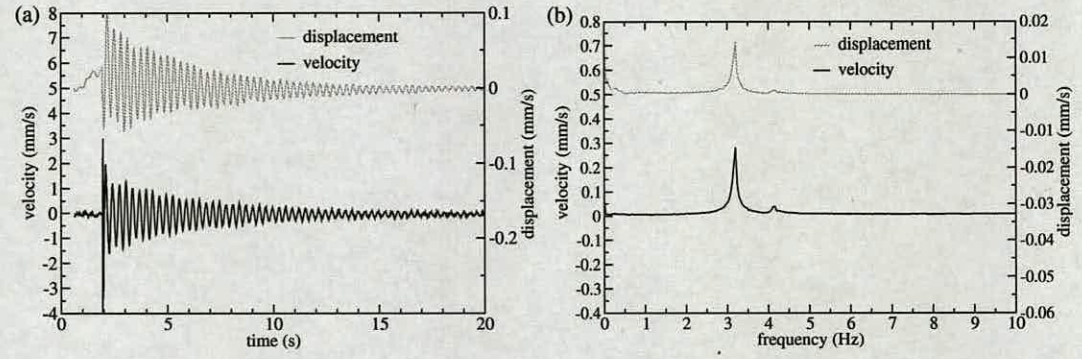

Figure 13. Free vibration of the model silo containing PET pellets.

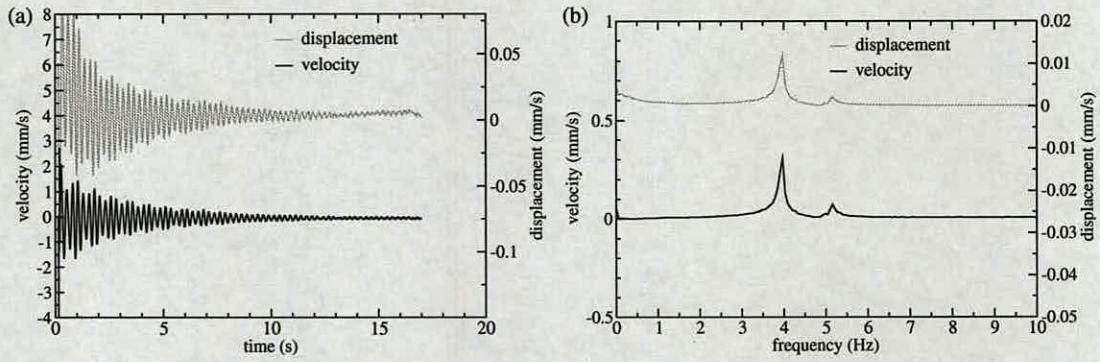

Figure 14. Free vibration of the model silo containing barley.

6. Conclusions

A study of the particle motion and associated wall vibration during discharge of a model silo has been presented. The motion of the particles against the silo wall has been observed to take place in an intermittent fashion. This motion was measured quantitatively, giving a record of the particle velocity as a function of time. The frequency spectra of the intermittent motion were evaluated for the two fill particles: PET and barley. For both fills, the particles were seen to remain stationary at the wall for a time of the order of a tenth of a second and then slide down the side of the wall before returning to rest. The time during which the particles were in motion was several times larger than their stationary period, with an overall repetition frequency of between 1 and 2 Hz. The particles were also observed to be moving in phase over the entire silo wall (above the transition level). The observed motion cannot be readily linked to the natural frequency of the wave propagation in the solid.

Horizontal wall vibrations were observed and measured during discharge. In general the radial vibration response was periodic, though typical durations of non-periodic motion were observed during discharge of PET pellets. The oscillatory motion was found to contain a single peak frequency that corresponded to the natural frequency of free vibration of the full silo. The discharge dynamics has caused the silo to vibrate

in its natural free vibration frequency of 3.9 Hz for barley and 3.2 Hz for PET. The vibration response is thus more akin to silo quaking/shaking than honking.

Acknowledgments

The authors would like to acknowledge the financial and practical assistance of Braby Silos; Dow Chemical Company; DuPont; DuPont Teijin Films; Eastman Chemical Company; Jansens and Dieperink; Jenike and Johanson Inc. and Waeschle and the financial support of EPSRC UK (grant no GR/R44263) and an ORS Award (Chavez-Sagarnaga). The authors would also like to thank C A Greated, D M Campbell and J A Cosgrove for useful discussions.

References

[1] Roberts A W and Wiche S J 1991 Silo quaking—a pulsating load problem during discharge in bins and silos *Proc. Bulk 2000 Conf. IMechE (London)* pp 7–12

[2] Gudehus G and Tejchman J 1992 Silo music and silo quake *Silos—Forschung und Praxis Tagung '92 (Karlsruhe, October)* pp 103–10

[3] Roberts A W 1993 Mechanics of self excited dynamic loads in bins and silos *Proc. Int. Symp. Reliable Flow of Particulate Solids II, (Oslo)* pp 983–1004

[4] Tejchman J 1995 Silo quake—experiments and a polar hypoplastic model *European Symp.: Storage and Flow of Particulate Solids (Janssen Centennial) (Nurnberg, March)* pp 151–62

[5] Schulze D 1998 Silo quaking *Silos—Fundamentals of Theory, Behaviour and Design* ed C J Brown and J Nielsen (London: E & FN Spon) pp 171–82

[6] Ooi J Y, Zhong Z and Hardy M S H 1999 Investigation of vibration and honking in DuPont silos *Confidential Technical Investigation Report* University of Edinburgh

[7] Tejchman J 1999 *Powder Technol.* **106** 7–22

[8] Buick J M, Chavez-Sagarnaga J, Zhong Z, Ooi J Y, Pankaj, Campbell D M and Greated C A 2003 Investigation of silo honking: slip–stick excitation and wall vibration *16th ASCE Engineering Mechanics Conf. (Seattle)* Paper 625

[9] Buick J M, Chavez-Sagarnaga J, Zhong Z, Ooi J Y, Pankaj, Campbell D M and Greated C A 2003b Investigation of silo honking: slip–stick excitation and wall vibration *J. Eng. Mech. ASCE* submitted

[10] Tejchman J and Gudehus G 1993 *Powder Technol.* **76** 201–12

[11] Muite B K, Shandon F, Quinn S F, Sundaresan S and Rao K K 2004 Silo music and silo quake: granular flow induced vibrations *Powder Technol.* submitted http://arxiv.org/ftp/cond-mat/papers/0310/0310086.pdf

[12] Wensrich C 2002 *Powder Technol.* **127** 87–94

[13] Chavez-Sagarnaga J, Buick J M, Ooi J Y, Pankaj, Campbell D M, Greated C A 2004 Frictional properties of pellets and silo wall materials for the investigation of silo honking *Proc. Int. Congress for Particle Technology, PARTEC 2004 (Nuremberg, Germany, March 2004)*

[14] Adrian R J 1991 *Annu. Rev. Fluid Mech.* **23** 261–304

[15] Raffel M, Willert C and Kompenhans J 1998 *Particle Image Velocimetry: A Practical Guide* (Heidelberg: Springer)

[16] Buick J M, Cosgrove J A, Campbell D M and Greated C A 2002 Development of an optical measuring technique for the study of acoustical phenomena *Optical Methods and Data Processing in Heat and Fluid Flow* (London: Professional Engineering Publishing) pp 133–42